Title
A thermodynamic and geochemical evaluation of magmatic processes beneath the Samoan Islands and the thermodynamics of crystalline garnet solutions

Author
Adams, Jenna

Publication Date
2020

UNIVERSITY OF CALIFORNIA

Santa Barbara

A thermodynamic and geochemical evaluation of magmatic processes beneath the Samoan Islands and the thermodynamics of crystalline garnet solutions

A dissertation submitted in partial satisfaction of the
requirements for the degree Doctor of Philosophy
in Earth Science

by

Jenna Victoria Adams

Committee in charge:
Professor Frank J. Spera, Chair
Professor Matthew G. Jackson
Professor Roberta L. Rudnick
Dr. Aaron S. Wolf

September 2020

The dissertation of Jenna Victoria Adams is approved.

Roberta L. Rudnick

Matthew G. Jackson

Aaron S. Wolf

Frank J. Spera, Committee Chair

August 2020

ACKNOWLEDGEMENTS

First and foremost, I would like to thank my advisor, Frank Spera, for his unconditional support and his thirst for knowledge. There was never a topic I could bring to his attention that he would dismiss—his interests and knowledge base are incredibly broad reaching and extremely inspiring. I would like to also thank Aaron Wolf, who I considered a secondary advisor in many ways, for his unwavering patience and the amount of time he devoted to teaching me how to code, among other difficult topics in thermodynamics, that proved to be a steep learning curve for me.

I would like to acknowledge Matt Jackson—one of my committee members and who also gave me the opportunity to work on some incredibly interesting lavas—for teaching me best practices in analytical geochemistry, for his support and encouragement throughout my PhD in general, and for our light-hearted conversations.

Additionally, I would like to thank my committee member, Roberta Rudnick, for her support and feedback on my research over the years. I would like to thank Ellie Price, Ben Byerly, Gareth Seward, and John Cottle for their immense help and patience with analytical work that was instrumental to completing this dissertation.

I would like to thank the Magma Chamber Simulator (MCS) team for their support, encouragement, hard work, and fun times over the years. I would especially like to thank MCS team member and mentor, Wendy Bohrson, for her constant support, encouragement, advice, and fun-loving spirit she provided throughout the years leading up to my PhD and on to the end of my PhD.

A special thanks to all of the UCSB Earth science graduate students, staff, and professors for making graduate school such a fun and supportive experience.

Last but not least, I would like to thank the lifelong friends I made in Santa Barbara in addition to my wonderful family for being so supportive of my decisions and keeping me sane throughout my PhD.

VITA OF JENNA VICTORIA ADAMS

JULY 2020

EDUCATION

Bachelor of Arts in Biochemistry, University of Washington, June 2011

Bachelor of Science in Geology, Central Washington University, June 2015

Doctor of Philosophy in Earth Science, University of California, Santa Barbara, September 2020 (expected)

PROFESSIONAL EMPLOYMENT

2011-2012: Geomicrobiology lab assistant, Department of Earth and Space Sciences, University of Washington

2014-2015: GIS data analyst, Kittitas County Planning Office

2015-2020: Teaching Assistant, Department of Earth Science, University of California, Santa Barbara

2018-2020: Teaching Associate, Department of Earth Science, University of California, Santa Barbara

PUBLICATIONS

Adams, J.V., Spera, F.J., and Jackson, M.G. (2020). Trachytic melt inclusions hosted in clinopyroxene offer a glimpse into Samoan EM2-endmember melts, *submitted.*

Adams, J.V., Jackson, M.G., Spera, F.J., Price, E.A., Byerly, B., Seward, G., and Cottle, J.M. (2020). Extreme isotopic heterogeneity in Samoan clinopyroxenes helps constrain sediment recycling, *in revision.*

Bohrson, W.A., Spera, F.J., Heinonen, J.S., Brown, G.A., Scruggs, M.A, Adams, J.V., Takach, M., Zeff, G. (2020). Diagnosing open-system magmatic processes using the Magma Chamber Simulator (MCS): Part I – Major elements and phase equilibria, *Contributions to Mineralogy and Petrology*, (*accepted*).

Heinonen, J.S., Bohrson, W.A., Spera, F.J., Brown, G.A., Scruggs, M.A, Adams, J.V. (2020). Diagnosing open-system magmatic processes using the Magma Chamber Simulator (MCS): Part II – Trace elements and isotopes, *Contributions to Mineralogy and Petrology*, (*accepted*).

Edwards, M., Jackson, M.G., Kylander-Clark, A.R.C., Harvey, J., Hagen-Peter, G.A., Seward, G.G.E., Till, C.B., Adams, J.V., Cottle, J.M., Hacker, B.R., Spera, F.J. (2019). Extreme enriched and heterogenous 87Sr/86Sr ratios recorded in magmatic plagioclase from the Samoan hotspot. *Earth and Planetary Science Letters, 511(1),* 190-201.

AWARDS

UCSB Alumni Graduate Award in Research Excellence, 2020

Geological Society of American Research grant, 2019

UCSB George Tunnel Memorial Fellowship, 2018

UCSB Richard V. Fisher Scholarship in Volcanology, 2017

UCSB ScienceLine Earth Science Award, 2017

UCSB Earth Research Institute Fellowship, 2016

Tom Ringe Award for Outstanding Undergraduate Research, 2015

NAGT Field Scholarship, 2014

ABSTRACT

A thermodynamic and geochemical evaluation of magmatic processes beneath the Samoan Islands and the thermodynamics of crystalline garnet solutions

by

Jenna Victoria Adams

This dissertation attempts to grapple with the origin and evolution of chemical heterogeneity reflected in lavas erupted in ocean island settings. The approach taken here is to combine analytical geochemistry with thermodynamic, phase equilibria modeling to place better constraints on the composition of heterogeneities contributing to the mantle source region beneath the Samoan Islands, located in the South Pacific Ocean. Additionally, inherent in thermodynamic, phase equilibria modeling are the underlying liquid and crystalline solution models that are built from thermophysical and experimental data. These liquid and solid solution formulations must be adequately calibrated over a broad region of pressure, temperature, and compositional space to be able to successfully model a range of geologically relevant magmatic systems. Therefore, this dissertation also presents a newly calibrated ternary garnet solution model with applications to high pressure igneous processes in addition to updates to the Magma Chamber Simulator (MCS) - a thermodynamically constrained code that allows for simulations of complex magmatic processes, like simultaneous magma mixing, assimilation, and fractional crystallization (RAFC).

This dissertation consists of 5 chapters: (1) analysis of Sr and Nd isotopic heterogeneity in individual clinopyroxenes from a single Samoan lava, (2) major and trace element characteristics of clinopyroxene-hosted melt inclusions from the same lava as in Chapter 1, (3) a new calibration of a solid solution model for ternary garnets applicable to high-pressure igneous processes, (4) applications and new model developments related to major element systematics of combined RAFC processes in the MCS, and (5) the formulation and applications of trace element systematics of combined RAFC processes in the MCS.

Chapters 1 and 2 reveal new insights into the composition and evolution of the enriched mantle 2 (EM2) reservoir, thought to be the result of ancient, recycled continentally derived sediments incorporated into the Samoan mantle plume source. Given the new Sr and Nd isotopic constraints from clinopyroxenes within a single EM2-derived lava and binary mixing theory, EM2 derived mantle melts beneath Samoa are calculated to be trachytic in composition. Fortuitously, trachytic melt inclusions hosted in these clinopyroxenes from the same lava are remarkably similar to the independently calculated trachytic-derived endmember, suggesting they could be direct evidence of EM2-derived mantle melts. However, thermodynamic simulations of mantle sources that could give rise to these trachytic-melts show their formation is not so simple and more work need be done to evaluate their formation and evolution.

Chapter 3 introduces a newly calibrated ternary garnet solid solution model that uses the most up-to-date melt-present phase equilibria data to constrain a model relevant to high pressure igneous processes. The model presented here is shown to be a significant improvement over previously published models. This model is obtained through Bayesian statistical techniques that allow for a comprehensive evaluation of errors among all constrained solution parameters. Using this calibration procedure, the model presented here achieves a pressure-dependent miscibility gap along the pyrope-grossular binary join, in agreement with recent experiments that is not captured by any previously published models.

Chapters 4 and 5 present updates and newly formulated techniques to track the major and trace element and isotopic systematics of open-system processes, pertinent to the first two chapters of this study. Notable features include new geochemical visualizations of magma evolution, the addition of 30 distinct magmatic recharge events, and supplemental calculator that interfaces with the MCS that tracks changes among trace elements and isotopes during combined RAFC process. These types of changes ultimately allow for a detailed quantification of complex magmatic process occurring beneath volcanos.

TABLE OF CONTENTS

Introduction

The purpose of this introduction is to delineate how the several strands of the research I have pursued in the past five years are related and how a computational approach, when used in combination with traditional geochemical and petrological information, can bring new insights into old problems. The geological problem I have been pursuing relates mainly to ocean island basaltic magmatism, also called hot spot volcanism. Ocean Island Basalts (OIB) exhibit bulk compositions (major, minor, and trace elements and isotopes) that are unmistakably different than the dominant basaltic products from global mid-ocean ridge derived basalts (MORB). An important question addressed in this dissertation is why OIB magmas are compositionally distinct from MORB. The common consensus for the past half-century is that the mantle reservoir(s) that give rise to OIBs and their distinctive compositions derive from the addition, to their mantle sources, of materials that were once at or near the earth's surface. These materials (sediments, oceanic crust, mantle lithosphere, volatiles, and possibly older continental crust) are recycled back into the Earth's mantle along convergent plate boundaries known as subduction zones.

Subduction regulates crustal growth, drives arc volcanism including volatile input to the atmosphere, and introduces chemically heterogeneous, volatile-rich material into the mantle. It is important to understand the fate of these subduction-generated chemical heterogeneities because it pertains to the short- and long-term chemical evolution of Earth. It is generally believed that mantle plumes 'sample' such recycled geomaterials leading to a diverse range of geochemical signatures reflected in ocean island basalts at hot spots (e.g., Hofmann and White, 1982; White and Hofmann, 1982; Stern, 2002; White, 2015). These heterogeneous sources and complex chemical signatures are not always easy to distinguish because mixing in the mantle is not well understood. However, studying ocean island basalts (OIBs) provides one very important way to understand the genesis of these mantle heterogeneities and the processes by which they are ultimately and heterogeneously sampled by partial melting and subsequently modified by magma ascent. My research aims to combine large and small-scale observations of magmatic processes—from detailed geochemical studies of individual minerals and melt inclusions, to whole rock geochemistry of suites of lavas erupted onto the surface of the Earth at hotspots—with thermodynamic phase equilibria models to attempt to discern petrogenetic details from the Samoan hotspot located in the South Pacific Ocean. I am studying Samoa because it is known to posess the undeniable signature of crustal recycling.

Extant geochemical models examining mantle heterogeneity are generally based on insights provided by major and trace element and isotope geochemistry. Phase equilibria modeling is an underutilized tool that can help unravel the complex history of magma genesis by simulating magmatic recharge, assimilation, fractional crystallization, and melting processes. My work endeavors to combine constraints from major and trace element and isotope geochemistry with thermodynamic models that provide detailed phase equilibria constraints, i.e., the composition and abundance of coexisting phases in ocean island lavas. The use of computational models in conjunction with geochemical analyses allows one to place more reliable constraints on the identity, abundance, and composition of phases present in the mantle region(s) sampled by partial melting and to grapple with possible subsequent changes in magma during ascent. These characteristics are ultimately a function of pressure, redox conditions, volatiles, and the bulk composition of source materials and control major and trace element and isotopic systematics. Additionally, the underpinnings of thermodynamic models are the liquid and crystalline solution models calibrated from thermophysical and experimental phase equilibria data. These liquid and solid solution formulations must be adequately constrained over a broad range of pressure, temperature, and compositional space to be able to successfully model a given magmatic system. Thus, this work also aims to improve thermodynamic phase equilibria modeling calculations by not only developing the ability to treat magmatic systems as open systems (subject to assimilation, magma mixing, and concurrent fractional crystallization), but also by improving crystalline solution models incorporating new thermophysical and experimental data ultimately in an effort to expand the range of possible magmatic processes and environmental conditions that can be simulated.

The Samoan Islands, located in the South Pacific Ocean, are a volcanically active hotspot setting that is unique given that lavas erupted in Samoa exhibit the enriched mantle 2 (EM2) geochemical signature (Zindler and Hart, 1986; Wright and White, 1987; Weaver, 1991; Farley et al., 1992; Workman et al., 2004; White, 2015). EM2 is thought to be derived by the addition of ancient subducted terrigenous sediment into the plume source (Hart, 1988; Jackson et al., 2007). In particular, lavas erupted specifically from Savai'i Island, western Samoa exhibit the most isotopically enriched (high $^{87}Sr/^{86}Sr$) compositions ever observed in the oceanic mantle (Jackson et al., 2007; Edwards et al., 2019, Adams et al., in review). While the origin and evolution of these lavas and thus EM2 remains uncertain, Chapters 1 and 2 of this dissertation shed new light on the composition of EM2-derived melts and discuss the origin and evolution of the EM2 source. These two chapters use high precision Sr and Nd isotope analyses on individual clinopyroxene grains, in addition to major and trace element data on clinopyroxenes, melt inclusions, and whole rock lavas from Samoa, to help place better constrains on the origin of EM2. These geochemical data are combined with thermodynamic modeling of different EM2 source materials to better understand the EM2-derived mixing endmember playing a role in controlling the EM2 lavas erupted at Savai'i Island.

Ocean island basalts (OIBs) in general exhibit large variability in major and trace element geochemistry and it's thought that for many ocean island settings garnet plays a role in their petrogenesis through partial melting of a source that generally contains residual garnet (e.g., Hauri, 1996; Sobolev et al., 2007, Prytulak and Elliot, 2007; Le Roux et al., 2010, White, 2015). Modeling the source regions of OIBs thus demands the ability to accurately model the behavior of garnet at depth and its effects on major and trace element systematics. Currently, thermodynamic solid solution models constraining mixing of garnet endmembers are not in good agreement, fail to capture significant features of garnet behavior, like the temperature of the spinel-garnet transition zone, only constrain ternary garnet mixing behavior, and rarely consider garnet interactions with liquids. Therefore, Chapter 3 focuses on the important problem of calibrating a new garnet solution model that covers a more representative swath of pressure, temperature, and compositional space than previous published models. Of particular interest to quantifying a new garnet solid solution model is the behavior of Ti-rich garnets. Many OIBS globally exhibit enrichments in TiO_2 (e.g., Prytulak and Elliot, 2007) and garnet is a dominant carrier of Ti at mantle depths. Consequently, many studies have focused on understanding to role of partial melting of garnet-rich lithologies in contributing to this Ti-enrichment (e.g., Yaxley and Brey, 2004; Dasgupta et al., 2005; Kogiso, 2006; Prytulak and Elliot, 2007; Dasgupta et al., 2009; Davis et al., 2011), and yet there exists no accurate thermodynamic models for Ti-bearing garnets;

this is a major motivation for creating and improved more inclusive garnet solution model that incorporates elements like Ti. Prior to performing such a calibration, it behooves us to first understand why the existing ternary garnet models are in such substantial disagreement and thus, to first explore an updated ternary solution model that considers the extensive amount of new phase equilibria data available since the last calibration. Additionally, most natural garnet samples fall within the ternary garnet range, so we find it important to build a robust ternary solid solution model (incorporating Mg, Ca, and Fe endmembers) that can then be built upon to create a 7-component solid solution model that will incorporate endmembers containing Ca, Mg, Fe, Mn, Ti, and Cr.

Chapters 4 and 5 are model development-based studies in which contributions were made towards developing new capabilities for the Magma Chamber Simulator code (MCS) (Bohrson et al., 2014). The MCS is a thermodynamic modeling code that simulates combined open system magmatic processes like magmatic **R**echarge (magma mixing), **A**ssimilation, and **F**ractional **C**rystallization (**RAFC**). RAFC magmatic processes are inherently a function of thermodynamics. Although thermodynamic modeling programs are becoming more widely used tools, as touched on above, many extant geochemical models of RAFC processes are based on major and trace elements and isotope geochemistry only, thus oversimplifying these often-complex thermodynamically-driven processes. In addition, these processes are often occurring concomitantly and are very hard to deconvolve with geochemical constraints alone. Thus, updates to the MCS described in this dissertation make the program more robust and user-friendly in order to more effectively allow for modeling of these complex RAFC processes. Chapter 4 focuses on the utility of MCS major element systematics and visualization tools. Updates to the MCS model in Chapter 4 include the addition of up to 30 magmatic recharge events and new data visualization features, while Chapter 5 focuses on the ability to track trace element and isotope systematics during RAFC processes. I collaborated in this work with other MCS developers to enhance the thermodynamic treatment of assimilation, to streamline/simplify the modeling interface, to extend the magma recharge functionality to include up to thirty discrete magma mixing events in a single magmatic scenario and to develop, build, and test the trace element capabilities of the MCS.

Thermodynamic, phase equilibria modeling combined with geochemistry and petrologic observations is essential to pushing the fields of geochemistry and petrology forward. Thermodynamics quantifies changes in phase equilibria and therefore the evolving chemistry of magmas, minerals, and fluids. Using constraints from geochemistry or petrology alone is not enough to fully describe a magmatic system. The work presented here aims to demonstrate the utility of combining these techniques in addition to the importance of ensuring that models are continuously updated as new data becomes available. Chapters 1 and 2 are mainly case studies, using analytical geochemistry to assess major and trace element and isotopic constraints for lavas erupted at the Samoan Islands. In these studies, modeling using the MCS and MELTS helps to shed light on the origin of these geochemical signatures. Chapters 3-5 are model development studies in which new tools and a thermodynamic crystalline solution model are created, tested, and implemented into existing thermodynamic modeling frameworks to further advance their capabilities.

Chapter 1: Extreme isotopic heterogeneity in Samoan clinopyroxene helps constrain sediment recycling

1 Introduction

Subduction zones are the largest recycling systems on Earth where sediments, oceanic crust, mantle lithosphere, volatiles, and possibly continental crust return to the mantle. It is generally accepted that mantle plumes ‘sample’ such recycled geomaterials leading to a diverse range of geochemical signatures reflected in ocean island basalts (OIB) (White and Hofmann, 1982; Hofmann and White, 1982; White, 2015). Mantle isotopic heterogeneities are clearly observed in OIB lavas from around the world, but the scale, origin, and compositions of the sources and/or derivative melts remain under intense investigation. Many studies that have evaluated isotopic heterogeneity in OIB have done so from the analysis of whole rock or bulk mineral separates (Hauri and Hart, 1994; Hauri et al., 1993; Workman et al., 2004; Jackson et al., 2007; Jackson et al., 2009), but these types of measurements obscure possible broader isotopic heterogeneity present within individual crystals or melt inclusions within a single lava. For example, previous work has shown $^{87}Sr/^{86}Sr$ and $^{143}Nd/^{144}Nd$ isotopic heterogeneity in lower oceanic crust clinopyroxene and plagioclase cumulate crystals (Lambart et al., 2019), and another found $^{87}Sr/^{86}Sr$ heterogeneity in olivine-hosted melt inclusions from a single lava sample, just to name a few (Jackson and Hart 2006; Harlou et al., 2009; Sobolev et al., 2011; Reinhard et al., 2016; Reinhard et al., 2018). Recent work related to the work presented here demonstrated intra- and inter-crystal $^{87}Sr/^{86}Sr$ heterogeneity in plagioclase in Samoan lavas having an enriched mantle 2 (EM2; Zindler and Hart 1986) signature (Edwards et al., 2019). Collectively, these studies suggest that multiple isotopically-distinct melts can contribute to a single lava, and thus magma mixing (Jackson and Hart, 2006) plays an essential role in igneous petrogenesis.

Subduction recycling of sediments into the mantle has been cited to explain the EM2 geochemical signature recorded in lavas erupted at ocean island volcanoes (Jackson et al., 2007; White, 2015). Lavas with elevated $^{87}Sr/^{86}Sr$ (>0.706; Hart, 1988) paired with low $^{143}Nd/^{144}Nd$, sampling an EM2 component, are relatively common among the volcanoes of the Samoan Islands in the South Pacific Ocean. Lavas erupted off the submarine flanks of Savai'i Island, western Samoa (Supplementary Figure S1 of Appendix S1) have whole rock $^{87}Sr/^{86}Sr$ values up to 0.720469 (Jackson et al., 2007), plagioclase up to 0.7224±0.0003 (2SE) and intra-crystal variability of $^{87}Sr/^{86}Sr$ up to ~5000 ppm (Edwards et al., 2019). These studies have invoked mixing between two endmember mantle compositions as the mechanism generating heterogeneity in Samoan lavas, suggesting up to 7% addition of a continental crust-like sediment in the Samoa plume source[16].

This study traces $^{87}Sr/^{86}Sr$ heterogeneity to a fine scale by obtaining coupled, high-precision Sr and Nd isotopes and major and trace elements on individual clinopyroxene crystals from the second-most (at the time of this study) enriched (high $^{87}Sr/^{86}Sr$) Samoan whole rock lava (whole rock $^{87}Sr/^{86}Sr=0.718562$). The clinopyroxenes studied are found within one of the two Samoan lava samples in which Edwards et al. (2019) measured plagioclase $^{87}Sr/^{86}Sr$ profiles from single porphyrocrysts. Consequently, a direct comparison of isotopic heterogeneity observed in clinopyroxene and plagioclase within a single hand specimen provides new constraints on the source of isotopic heterogeneity within the context of magma mixing and phase equilibria constraints. Here we show that extreme $^{87}Sr/^{86}Sr$ heterogeneity observed in individual clinopyroxenes from a single geochemically-extreme oceanic lava is consistent with magma mixing of at least two isotopically-distinct melts—one basaltic and one trachytic.

2 An extreme EM2 sample from Samoa

The sample investigated here is a 5 Ma submarine lava, ALIA-D115-18, dredged off the flanks of Savai'i Island, western Samoa (see Supplementary Figure S1of Appendix S1). This sample is a nepheline-normative trachyandesite with a bimodal crystal population. The larger crystal population is ≥ 25 μm in diameter and includes porphyrocrysts (here we use the term porphyrocryst as a general term implying no direct relation of these crystals with their host whole rock, as compared with phenocrysts, but are still genetically related to the magmatic system, so are not xenocrystic) of clinopyroxene, plagioclase, and ilmenite as well as porphyroclasts ('clots' of porphyrocrysts) consisting of the same three phases with modal abundances corresponding to a microgabbro. This study focuses on clinopyroxene porphyrocrysts, which were analyzed for major (electron microprobe) and trace elements (LA-ICP-MS) prior to dissolution and isotopic analysis by thermal ionization mass spectrometry (TIMS). Seventeen individual clinopyroxene crystals were analyzed for $^{87}Sr/^{86}Sr$ with resulting ratios ranging from 0.716833 (±0.000015, 2SE) to 0.723888 (±0.000015, 2SE), the highest value ever reported in an oceanic lava. Nine of the 17 crystals were also targeted for $^{143}Nd/^{144}Nd$ analysis, and single-crystal values range from 0.512238 (±0.000013, 2SE; $\varepsilon_{Nd} = -7.6$ calculated using $^{143}Nd/^{144}Nd_{chondrite}=0.512630$; Bouvier et al., 2008) to 0.512357 (±0.000013, 2SE; $\varepsilon_{Nd} = -5.3$) (Supplementary Dataset S1). Together, the clinopyroxene Sr and Nd isotopes plot along an extension of the mantle array formed by global OIB, with the $^{87}Sr/^{86}Sr$ variability in this single lava sample spanning ~35% of the variability observed in all Samoan whole rock lavas, and ~30% of the entire oceanic mantle variability (Figure 1).

3 Methods

3.1 TIMS analysis

3.1.1 Sample preparation

Seventeen clinopyroxene grains were plucked from indium mounts. The clinopyroxenes were then leached in concentrated HNO_3 on a 90 ^{o}C hotplate for 2 minutes and then washed once with milli-Q ($18.2*10^6$ Ω•cm) water; this process was repeated twice to ensure that any indium remaining on the grains was removed. The clinopyroxenes were then leached in 6N HCl at 90 ^{o}C for 2 minutes then rinsed 3 times with milli-Q water to remove any remaining surface contamination. Seventeen clinopyroxene samples, together with two aliquots of USGS Reference Material BCR-2 hosting 10.8 ng Sr and 0.88 ng Nd (the first aliquot), and 5.6 ng Sr (the second aliquot, but Nd was not analyzed), respectively, were transferred to vials containing 150 µl concentrated HNO_3 and 225 µl concentrated HF for dissolution. The samples were then set on a 120 ^{o}C hotplate for 2 days for dissolution. All clinopyroxenes and BCR2 aliquots were spiked with ^{84}Sr and ^{150}Nd for determination of the total amount of analyte in the sample by isotope dilution. Samples were then dried down and later brought up in a 500 µl concentrated HNO_3 solution and placed on a 120 ^{o}C hotplate to flux for 24 hours to eliminate fluorides. Following dry-down, the samples were brought up in 1 ml 3N HNO_3 to load on to columns for chemical separation of Sr and Nd; column chemistry follows Koornneef et al. (2015). Total procedural blanks were processed together with sample clinopyroxenes and the BCR-2 through all steps of sample dissolution (beginning with dissolution in HNO_3 and HF), column separations, and mass spectrometry.

Total procedural blanks (including all stages of wet chemistry [e.g., sample dissolution, column chemistry, etc.] and loading on TIMS filaments), varied from 22 to 60 picograms for Sr, and 2.2 to 2.7 picograms for Nd, which are dwarfed by the total amount of Sr (~5.6 to 58.7 nanograms) and Nd (~0.88 to 25.6 nanograms), respectively, in the each clinopyroxene grain and the two BCR-2 aliquots ($[Sr]_{sample}/[Sr]_{blank}$ and $[Nd]_{sample}/[Nd]_{blank}$ ratios for each sample are provide in Supplementary Dataset S1). Thus, while blanks corrections are applied to the samples and the BCR-2 aliquots (assuming a lab blank $^{87}Sr/^{86}Sr$ of 0.711 and $^{143}Nd/^{144}Nd$ blank of 0.5118, obtained by pooling multiple blanks), blank corrections to the $^{87}Sr/^{86}Sr$ and $^{143}Nd/^{144}Nd$ ratios are negligible.

3.1.2 $^{87}Sr/^{86}Sr$ and $^{143}Nd/^{144}Nd$ isotope analyses.

The clinopyroxene grains and the BCR-2 were analyzed for $^{87}Sr/^{86}Sr$ and $^{143}Nd/^{144}Nd$ over two analytical sessions. The separated, dried Sr samples were brought up in 1 µl HNO_3 and each loaded onto outgassed, zone refined rhenium (99.999%) filaments (H Cross, USA) along with a 1 µl $TaCl_5$ emitter solution. For each analytical session, two total procedural blanks were also loaded onto rhenium filaments in addition to a BCR2, all of which passed through the same column chemistry as the clinopyroxene and BCR2 unknowns. In addition, 8 filaments with 1 ng NBS987 were analyzed together with the clinopyroxenes and BCR2 aliquots: average $^{87}Sr/^{86}Sr = 0.710262 \pm 0.000076$ (2SD, N=8). All samples were analyzed by static Faraday collection without amplifier rotation on UCSB's Triton Plus employing 10^{11} Ω amplifiers and using a 3.3 picoamp gainboard, and gains were measured every barrel. Samples were corrected for the offset between the preferred (0.710240) average measured NBS987 $^{87}Sr/^{86}Sr$ from the same analytical session (i.e., the same barrel). Sr isotopes were corrected for mass bias assuming an exponential law and using canonical $^{86}Sr/^{88}Sr$ ratio of

0.1194, and isobaric interferences from Rb were corrected by monitoring mass 85, but correction to the ^{87}Sr/^{86}Sr ratios were negligible.

Only 9 of the above 17 clinopyroxene grains were analyzed for ^{143}Nd/^{144} Nd; these were selected after ^{87}Sr/^{86}Sr was analyzed and were chosen because they spanned the range of measured ^{87}Sr/^{86}Sr values. All of these grains were processed through the same batch of column chemistry with a BCR2 and two total procedural blanks. The dried down, separated Nd samples were brought up in 4 µl 1M HNO_3 and loaded onto outgassed, zone-refined (99.999%, H Cross, USA) double rhenium filaments. Two blanks, six 1 ng JNDi's (average 0.512106 ± 0.000033, 2SD), one 500 ng JNDi (0.512112 ± 0.000011, 2SE), and a BCR-2 (run through the columns) were also loaded onto rhenium filaments and run during the same analytical session (i.e., the same barrel) as the clinopyroxenes. Samples were corrected for the offset between the preferred (0.512099; Garcon et al., 2018) average measured JNdi ^{143}Nd/^{144}Nd from the same analytical session. All samples were analyzed by static Faraday collection without amplifier rotation on UCSB's Triton Plus employing 10^{13} Ω amplifiers and using a 3.3 picoamp gainboard (gains are measured once, at the start of each new barrel). Nd isotopes were corrected for mass bias assuming an exponential law and using a canonical ^{146}Nd/^{144}Nd ratio of 0.7219. Isobaric interferences from Sm were corrected by monitoring mass 147, but correction to the ^{143}Nd/^{144}Nd ratios were negligible.

At UCSB, the long-term reproducibility (up to and including this study) of ^{87}Sr/^{86}Sr for 1 ng and 500 ng loads of NBS987 by static multicollection (without amplifier rotation) using the same methods as this study are 0.710248 ± 0.000061 (2SD, N=69) and 0.710244 ± 0.000014 (2SD, N=39), respectively. For BCR2, multiple runs of aliquots hosting 5.6 to 10.8 ng Sr that were spiked and processed through column chemistry and mass spectrometry (following the same methods as samples here) yield an average $^{87}Sr/^{86}Sr$ value of 0.705018 ± 0.000065 (N=9), which is in line with the $^{87}Sr/^{86}Sr$ of the two BCR2 aliquots analyzed in this study: the 10.8 ng aliquot $^{87}Sr/^{86}Sr = 0.704974 \pm 0.000018$ (2SE), and the 5.6 ng aliquot $^{87}Sr/^{86}Sr = 0.705027 \pm 0.000045$ (2SE). These values are comparable to an average $^{87}Sr/^{86}Sr$ of 0.705005 ± 0.000010 for BCR2 reported by Weis et al. (2006) (following normalization to the same NBS987 value used here). For $^{143}Nd/^{144}Nd$, the long-term reproducibility of 1 ng loads of JNdi by static multi-collection (without amplifier rotation) using the same methods as this study (i.e., 10^{13} Ω amplifiers) is 0.512104 ± 0.000030 (2SD, N=27). For BCR2, 0.50 to 0.88 ng Nd aliquots spiked and processed through column chemistry and mass spectrometry (following the same methods as samples here) yield an average $^{143}Nd/^{144}Nd$ value of 0.512618 ± 0.000023 (N=4), which is in line with the $^{143}Nd/^{144}Nd$ of the BCR2 aliquot analyzed here: a 0.88 ng aliquot $^{143}Nd/^{144}Nd = 0.512634 \pm 0.000032$ (2SE). This is comparable to an average $^{143}Nd/^{144}Nd$ value of 0.512621 ± 0.000012 for BCR2 reported by Weis et al. (2006) (following normalization to the same JNdi value used here, and the La Jolla to JNdi conversion of Tanaka et al., 2000).

3.2 Residence times from diffusion

To obtain an estimate of the *residence time*, defined as the time interval between crystal growth and lava eruption (quenching), of the clinopyroxene porphyrocrysts, the diffusive characteristic of lamellar compositional bands is considered. Examination of compositional profiles revealed that thin lamella of locally higher Mg/Fe were preserved (Supplementary Figure S6 of Appendix S1). Based on Fe-Mg inter-diffusion, we used the thickness of these lamella to obtain an estimate of the maximum residence time of the crystal. That is, if diffusion was active for a period of time greater than the residence, the compositional anomaly would have been erased. ln this one-dimensional diffusion model, a lamella of greater Mg/Fe than its surroundings initially at composition C_0 occupies a region between x=-b and x=+b. The composition outside the lamella is C_1 at all times. The non-dimensional differential equation governing the decay of the lamella compositional anomaly is

$$\frac{\partial \hat{C}}{\partial \hat{t}} = D\frac{\partial^2 \hat{C}}{\partial \hat{x}^2},$$

where the non-dimensional variables are defined as:

$$\hat{C} = \frac{C_1 - C}{C_1 - C_0},\ \hat{x} = \frac{x}{b}, \text{ and } \hat{t} = \frac{Dt}{b^2},$$

where 2b is the lamella thickness, D is species-appropriate diffusion coefficient and t is the time since the start of diffusion. The initial and boundary conditions in terms of the non-dimensional parameters are:

IC: at $t = 0, \hat{C} = 1$ for $-1 < \hat{x} < 1$

BC: at $\hat{x} = \pm 1, \hat{C} = 0$ for $\hat{t} > 0$.

The solution (Carslaw and Jaeger, 1959) recast in dimensional variables is:

$$\frac{C_1 - C}{C_1 - C_0} = 2\sum_{n=0}^{\infty} \frac{-1^n}{(n+\frac{1}{2})\pi} \exp\left[-\left(n+\frac{1}{2}\right)^2 \pi^2 \frac{Dt}{b^2}\right]\cos\left(n+\frac{1}{2}\right)\frac{\pi x}{b}.$$

Based on this solution, we computed the time necessary to eradicate 90% of the compositional anomaly at the centerline of the lamella (see Carslaw and Jaeger, pg.101 for graphical solution) for the thinnest lamella in the clinopyroxenes: ~15 µm (b=7.5 µm). Diffusion calculations were performed at 1150 °C (log $D^{Mg/Fe\ inter\text{-}diffusion}$ = -19.4 m/s^2; Dimanov and Wiedenbeck, 2006) and 1200 °C ($\log_{10} D^{Mg/Fe\ inter\text{-}diffusion}$ = -18 m/s^2; Muller et al., 2013). The effect of varying temperature ±50 K is modest, increasing or decreasing residence times by about 20-30%. The greatest uncertainty is in the laboratory determination of diffusivities.

3.3 Retrieval of magma mixing endmembers

The principles of magma mixing are well established and have been used for decades to decipher magma mixing from assimilation and/or fractionation processes in natural magmatic systems (Langmuir et al., 1978; Juteau et al., 1986; Albarede, 1995; Faure and Mensing, 2004; Spera et al., 2016). The Samoan ALIA whole rock lavas discussed in this study are very likely a result of magma mixing as noted by examination of Figure 3. The mixing trends can be used to estimate the composition of the mixing endmembers given the MgO content of the silicic (S; high $^{87}Sr/^{86}Sr$) and mafic (M, low $^{87}Sr/^{86}Sr$) mixing endmembers. Based on binary mixing theory (Langmuir et al., 1978; Albarede, 1995; Faure and Mensing, 2004), for any two chemical species (major oxides, trace elements, isotopes) the mixing equations may be recast in the ratio-reciprocal form

$$\frac{C_2^H}{C_1^H} = A + \frac{B}{C_1^H} \qquad (1),$$

where C_1^H and C_2^H are concentrations of chemical species 1 and 2 in the mixed (hybrid) magma, respectively and A and B are constants related to the chemical species concentrations in endmembers M and S. The constants A and B in (1) are defined from mixing theory to be:

$$A = \frac{C_2^M - C_2^S}{C_1^M - C_1^S} \qquad (2)$$

and

$$B = \frac{(C_1^M C_2^S - C_1^S C_2^M)}{C_1^M - C_1^S} \qquad (3),$$

where C_1^M and C_2^M are concentrations of chemical species 1 and 2 in the mafic (M) endmember and C_1^S and C_2^S are the concentrations in the silicic (S) endmember. The linear regression of the petrochemical data for the ALIA-D115 lavas gives the intercept and slope that corresponds to A and B. A and B are two equations with 4 unknowns, thus if the concentration of chemical species 1 is known, or can be confidently estimated, in both endmembers, then the concentration of chemical species 2 in both endmembers can be calculated by simple rearrangement of equations (2) and (3). The quality of the computed parameters depends critically on the quality of the fit of the data to equation (1). We have chosen to initially fix values of MgO in both M and S because there is relatively little variability in MgO concentrations in both endmembers based on the array defined by the ALIA-D115 lavas. In other words, Samoan lavas in a SiO_2 vs. MgO plot (see Supplementary Figure 2), shows the linearity expected for mixing, as the ALIA-D115 lavas form a trend with the M endmember sitting in the cloud of data points of "other Samoan shield lavas" and the S endmember extending toward 0 wt% MgO, thus, the MgO in the S mixing endmember must lie between the value of the most evolved and high $^{87}Sr/^{86}Sr$ ALIA lava (ALIA-D115-21) and 0 wt% MgO (see Supplementary Figure S2 of Appendix S1). The M endmember is assigned a value of 10 wt% MgO (similar to the MgO composition one would get if all "other Samoan shield lavas" with less than 50 wt% SiO_2 were averaged) whereas for the S endmember, we have chosen to perform the mixing calculations for three different values of MgO: 3.8 wt% (from ALIA115-21), 2 wt%, and at the low end of the spectrum, 0.5 wt% (which is very close to the MgO content of clinopyroxene-hosted trachytic melt inclusions; see Supplementary Dataset S2) just to cover the possible MgO contents. The method allows one to calculate the oxide compositions of M and S endmembers for each of the three assumed values of MgO in S, given a constant value in M. In detail, we used the A and B

values from the regression of expressions of the following form: C_i/MgO versus 1/MgO space, where C_i are the following chemical species: SiO_2, Al_2O_3, Na_2O, K_2O, and Nd (see Supplementary Figure S4 of Appendix S1).

From these plots we computed an estimate of the M and S bulk compositions for SiO_2, Al_2O_3, Na_2O, K_2O, and Nd (see Supplementary Figure S4 of Appendix S1). As an example, with a linear ordinary least-squares regression equation describing data in K_2O/MgO versus 1/MgO space, with some re-arranging of equations (2) and (3) we can solve for the concentration of K_2O in both the M and S endmembers given our estimated initial values of MgO for each endmember as known values. For the chemical species other than SiO_2, Al_2O_3, Na_2O, K_2O, and Nd we used the computed K_2O concentration as the new denominator value (instead of MgO) to calculate the concentrations of TiO_2, FeO, CaO, MnO, P_2O_5, and Sr. The reason for this is that plots of these elements with K_2O as chemical species 1 in eq. (1) showed much better linearity compared to equivalent plots using MgO in the denominator — we need the best correlations possible to get a best estimate on the two endmember compositions.

According to mixing theory, “companion plots” to the ratio-ratio plot $^{87}Sr/^{86}Sr$ versus $^{143}Nd/^{144}Nd$ should give linear trends and are of the form $^{87}Sr/^{86}Sr$ versus Nd/Sr and $^{143}Nd/^{144}Nd$ versus Sr/Nd (Supplementary Figure S5 of Appendix S1). Thus, these plots are used again with ordinary least squares regression techniques and, given the inferred Sr and Nd concentrations in each endmember derived in the manner described above, we extract $^{87}Sr/^{86}Sr$ and $^{143}Nd/^{144}Nd$ in both endmembers (see Supplementary Dataset S2) using again, equations (2) and (3). The last step of the process is to use the calculated $^{87}Sr/^{86}Sr$ and $^{143}Nd/^{144}Nd$ and Sr and Nd concentrations to obtain a self-consistent mixing curve to the

ALIA-D115 lavas, *in addition* to the new clinopyroxene data of this study, in a plot of $^{87}Sr/^{86}Sr$ versus $^{143}Nd/^{144}Nd$.

The values of the reconstructed major oxide, Sr and Nd concentrations and isotopic ratios for the **M**afic and **S**ilicic magma mixing endmembers for each of the three assumed MgO contents of the R endmember are given in Supplementary Dataset S2. The three high $^{87}Sr/^{86}Sr$ endmember reconstructed compositions (using the three different choices of MgO for the endmember) lie either in the trachyte (two of three) or trachyandesite (one of three) field on the total alkali versus silica diagram.

3.4 Magma Chamber Simulator mixing modeling

Using the calculated mafic (M; low $^{87}Sr/^{86}Sr$) and silicic (S; high $^{87}Sr/^{86}Sr$) mixing endmembers from the above procedure, MELTS (Ghiorso and Sack, 1995; Gualda et al., 2012) and the Magma Chamber Simulator (MCS; Bohrson et al. 2014) were used to simultaneously model the effects of magmatic recharge and fractional crystallization processes on Samoan lavas (RFC in MCS jargon). The metric used to gauge model acceptability was how well the phase equilibria and geochemistry matches the petrology and petrochemistry of the observed Samoa ALIA-D115 lava suite. In the magma mixing calculations, the M endmember composition was the host magma and the S endmember composition, based upon an assumed MgO content of 0.5 wt % (see Supplementary Dataset S2 for details), was the recharge magma. The H_2O content of both M and S endmembers was set at 0.1 wt% along the QFM (quartz-magnetite-fayalite) buffer establishing the ferric to ferrous iron ratio in each endmember. Since the porphyrocrystic clinopyroxenes of this study are in isotopic disequilibrium with the whole rock, clinopyroxene-liquid thermobarometry is not meaningful. Because an independent pressure estimate could not be made, MCS simulations were performed in the range 0.1 to 1 GPa. Upon mixing at low pressures (<0.5 GPa) the stable fractionating mineral assemblage consists of olivine, clinopyroxene, plagioclase, and spinel. Simulations were run for three cases where the high $^{87}Sr/^{86}Sr$ recharge magma (S endmember) was initially either: (1) 100% liquid, (2) possessed a crystallinity of about 15% (15% $An_{22}Ab_{63}Or_{15}$ anorthoclase feldspar, modally) and (3) possessed a crystallinity of 60% (70% $An_{8}Ab_{48}Or_{44}$ alkali feldspar, 23% $An_{20}Ab_{60}Or_{20}$ plagioclase feldspar, 5% spinel, and 2% orthopyroxene, modally) upon addition to the host magma (M endmember). At constant pressure, the difference between these three initial recharge magma thermodynamic states is that as the crystallinity of the recharge magma increases the initial anorthite content of the plagioclase and Mg# of the clinopyroxene that crystallize from the host magma increases upon the initiation of mixing. As an example, at 0.2 GPa, when the recharge magma was 100% liquid, plagioclase (An_{45}) was stabilized at 1107 ^{o}C whereas when the recharge magma was 60% crystalline, An_{50} plagioclase was stabilized at ~1119 ^{o}C. In the case of the ALIA-D115 lavas, the latter case more closely corresponds to observed plagioclase within the lavas (range An_{50-60}; Edwards et al., 2019). Significantly, there are alkali-feldspar inclusions within the clinopyroxene and plagioclase porphyrocrysts of the ALIA-D115-18 lava, suggesting they existed prior to crystallization of these phases and thus, may have grown directly from the S endmember prior to mixing (consistent with the crystal-rich recharge magma simulations in which alkali feldspar was stable prior to mixing). With increasing pressure, the first plagioclase to crystallize from the magma decreased in An content and there was increased stabilization of orthopyroxene in the assemblage over clinopyroxene, which is not observed in the ALIA-D115 lava suite. Thus, MCS simulations favor lower pressures of magma mixing and a partly crystalline recharge magma at the time of mixing. Overall, the modal amounts and phase compositions of the calculations agree quite well with the observed mineralogy. It is important to note that the MCS mixing lines plotted in Supplementary Figures S2 and S3 (Appendix S1) are the evolutionary paths of the *melt* as a result of magma mixing and crystallization (crystals are removed from the system as soon as they form), so the bulk composition is not conserved and thus, one would not expect the mixing lines to end at the EM2-derived endmember, much different than the conservative mixing line based on closed system binary mixing. In addition, the MCS models are thermodynamically constrained models and so the terminus of the mixing line is dictated by where the simulation terminated. In any case, the ALIA-D115 lavas can be explained by the simulations reasonably well given the ubiquitous geological uncertainties in any modeling exercise.

4 Generation of isotopic heterogeneity

Clinopyroxene Sr and Nd isotopes from lava sample ALIA-D115-18 of this study, together with major and trace element and isotopic constraints from other Samoan whole rock lavas from the same submarine dredge as ALIA-D115-18 (referred to as the ALIA-D115 dredge), are used to constrain the composition of the magma mixing endmembers—including the extreme EM2 endmember that contributed to the isotopic variability observed in clinopyroxenes from ALIA-D115-18. This permits us to define the origin and makeup of the high $^{87}Sr/^{86}Sr$ EM2 endmember in the Samoan plume, thereby constraining the petrogenesis of EM2 lavas.

In $^{87}Sr/^{86}Sr$ and $^{143}Nd/^{144}Nd$ space, addition of clinopyroxene data obtained in this study to existing Samoan whole rock data defines a mixing line that exhibits significant curvature (i.e. $r<1$, where $r=[Nd/Sr]_S/[Nd/Sr]_M$ and M and S represent the **M**afic, low- and

Silicic, high-^{87}Sr/^{86}Sr endmembers, respectively) compared with previous suggestions based on whole rock data alone (Langmuir et al., 1978; see also Hauri and Hart, 1994; Figure 1). This implies that the Nd and Sr concentration as well as the ^{87}Sr/^{86}Sr and ^{143}Nd/^{144}Nd values in the two endmembers need to be re-evaluated. It should be noted, however, that the proposed mixing discussed here is not mixing between mantle sources, but mixing between magmas, and therefore differs from the approach in Jackson et al. (2007). Employing an inverse model approach to existing whole rock data from Samoa (see Methods), we argue for an EM2-derived mixing endmember that is not only high in ^{87}Sr/^{86}Sr, but also trachytic in composition. Mixing of the EM2 trachytic magma with more primitive Samoan basalt-like compositions reproduces the mixing trends observed in ALIA-D115 whole rock lavas (Figure 1) as well as the range of ^{87}Sr/^{86}Sr and ^{143}Nd/^{144}Nd in Samoa clinopyroxene.

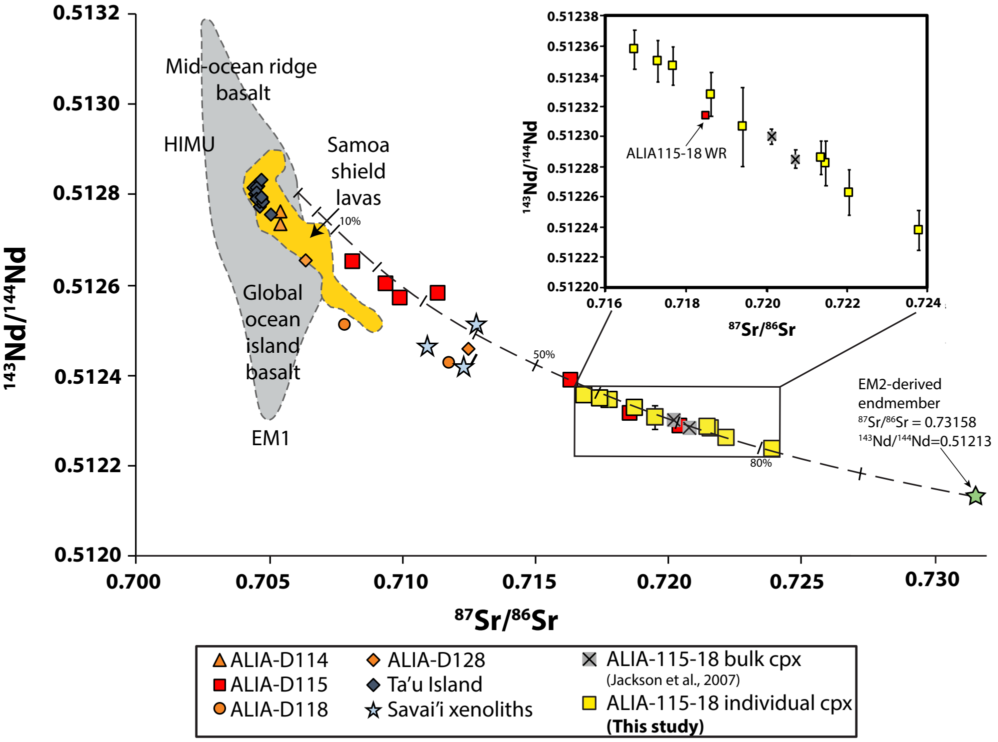

Figure 1: ^{143}Nd/^{144}Nd versus ^{87}Sr/^{86}Sr of new ALIA-D115-18 single clinopyroxene data and prior data on the whole rock and bulk (100's of grains of) clinopyroxene. Fields for Samoa, global ocean island basalts, and mid-ocean ridge basalts, shown in orange and grey fields, respectively. Inset shows a close-up view of the clinopyroxene data collected in this study in addition to the bulk clinopyroxene analyses and the ALIA-D115-

18 whole rock published previously (Jackson et al., 2007, 2009) (errors bars are smaller than symbols except where shown). Note that only 9 of the 17 clinopyroxenes analyzed for $^{87}Sr/^{86}Sr$ also have $^{143}Nd/^{144}Nd$ data, so not all clinopyroxenes analyzed for $^{87}Sr/^{86}Sr$ can be shown on this figure. Samoan shield lavas, ALIA lavas, and Savai'i xenolith compositions are from elsewhere (Hauri et al., 1993; Hauri and Hart, 1994; Jackson et al., 2007). The black dashed line is a calculated binary magma mixing line. The green star denotes the EM2-derived, high $^{87}Sr/^{86}Sr$, trachytic mixing endmember calculated here (see Supplementary Dataset S2). A linear regression analysis was performed on the ALIA-D115 whole rock lavas in element-element and isotope-element space given one assumption about the initial MgO content in both the mafic, low $^{87}Sr/^{86}Sr$ and the silicic, high $^{87}Sr/^{86}Sr$ endmembers. Assuming the MgO content in each endmember, one can use the binary mixing equations derived in the Methods section to calculate a major and minor element composition of the two endmembers and thus, using the derived Sr and Nd concentrations in each endmember, the $^{87}Sr/^{86}Sr$ and $^{143}Nd/^{144}Nd$ can be calculated.

The genesis of this high $^{87}Sr/^{86}Sr$, trachytic magma is an outstanding question and is further explored in the Supplementary Text. This aside, results of this study are consistent with the observation of Jackson et al. (2007) who noted a distinct positive correlation between $^{87}Sr/^{86}Sr$ and SiO_2 concentration among Samoan whole rocks from the ALIA dredge haul, suggesting two-endmember mixing between a highly evolved (high silica, low MgO trachyte), high $^{87}Sr/^{86}Sr$ endmember and a less evolved (basaltic) endmember with low $^{87}Sr/^{86}Sr$. In addition, Edwards et al. (2019) noted a negative correlation between $^{87}Sr/^{86}Sr$ and Sr concentration in plagioclase crystals suggesting the high $^{87}Sr/^{86}Sr$ (the "EM2" component) endmember likely experienced significant loss of Sr due to plagioclase fractionation prior to mixing, consistent with the "EM2" component being highly evolved prior to mixing. If extreme plagioclase fractionation of the radiogenic magma did occur prior to mixing, then a negative correlation should also be observed in the clinopyroxene since they are a direct result of the mixing process. However, there is no clear correlation between clinopyroxene $^{87}Sr/^{86}Sr$ and Sr concentration, which can be best explained if plagioclase fractionation occurred after the onset of mixing. This idea is consistent with MELTS[21] and Magma Chamber Simulator (Bohrson et al., 2014) mixing modeling, which shows that clinopyroxene crystallization begins ~50 °C above plagioclase saturation upon mixing of a mafic, low $^{87}Sr/^{86}Sr$ melt and a silicic high $^{87}Sr/^{86}Sr$ melt. This scenario is also consistent with the observation that the range of $^{87}Sr/^{86}Sr$ in the clinopyroxenes (0.71683 to 0.72389) exceeds that of the range of plagioclase $^{87}Sr/^{86}Sr$ values found in the same hand specimen (0.71791 to 0.72239) by Edwards et al. (2019; Figure 2), suggesting that the system was more homogenized at the time of plagioclase crystallization, compared to the point at which clinopyroxene crystallization initiated.

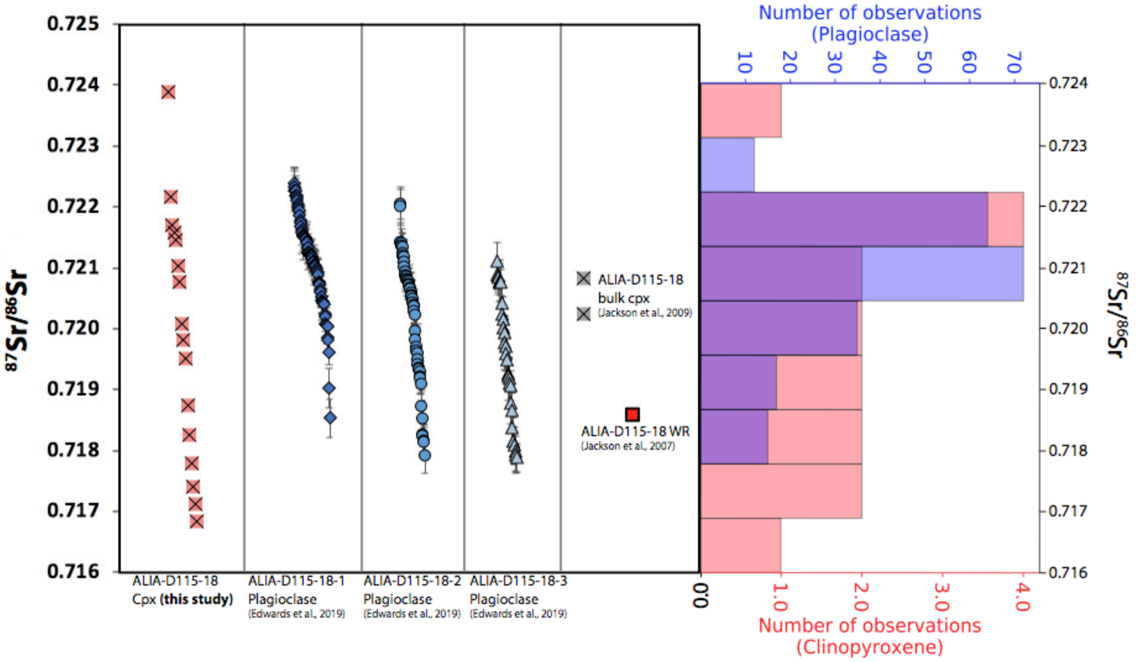

Figure 2: $^{87}Sr/^{86}Sr$ values for single clinopyroxene grains measured in this study, along with LA-ICP-MS spot analyses from three plagioclase grains from the same sample (ALIA-D115-18; Edwards et al., 2019). Previous measurements of bulk clinopyroxene (representing 100's of pooled grains; Jackson et al., 2009) from this same sample are shown together with the whole rock value (Jackson et al., 2007) (error bars are smaller than symbols except where shown). In the histogram, the number of clinopyroxene observations (red bars and figure axis label) span a larger range of $^{87}Sr/^{86}Sr$ than the plagioclase $^{87}Sr/^{86}Sr$ analyses (blue bars and figure axis label); where the clinopyroxene and plagioclase histograms overlap, a purple shade is used. The wider range of clinopyroxene $^{87}Sr/^{86}Sr$ values compared with those of plagioclase from the same sample is consistent with magma mixing modeling using MELTS (Ghiorso and Sack, 1995; Gualda et al., 2012) and the Magma Chamber Simulator (Bohrson et al. 2014) showing that magma mixing between a mafic endmember and a more silicic, trachytic endmember (as derived in this study) precipitates clinopyroxene about 50 ºC above the plagioclase saturation temperature and thus the mixing magmas maybe slightly more homogenized at this point limiting the range of $^{87}Sr/^{86}Sr$ exhibited by plagioclase (see Main text and Methods for more detail).

Figure 3 shows geochemical data from the ALIA-D115 dredge whole rock lavas (red symbols), other whole rock lavas from Savai'i, and lavas (orange) and pillow glasses (purple) from neighboring Samoan islands and seamounts (orange symbols). Mixing is clearly defined by the ALIA-D115 dredge lavas in $^{87}Sr/^{86}Sr$ versus element plots (Figure 3), and in major and select trace element plots (Supplementary Figures S2 and S3 of Appendix S1), spanning compositions ranging from trachybasaltic to trachyandesitic in a single dredge: curved lines define mixing in the ALIA-D115 lavas, while the rest of the Samoan lavas show zero-slope fractional crystallization trends.

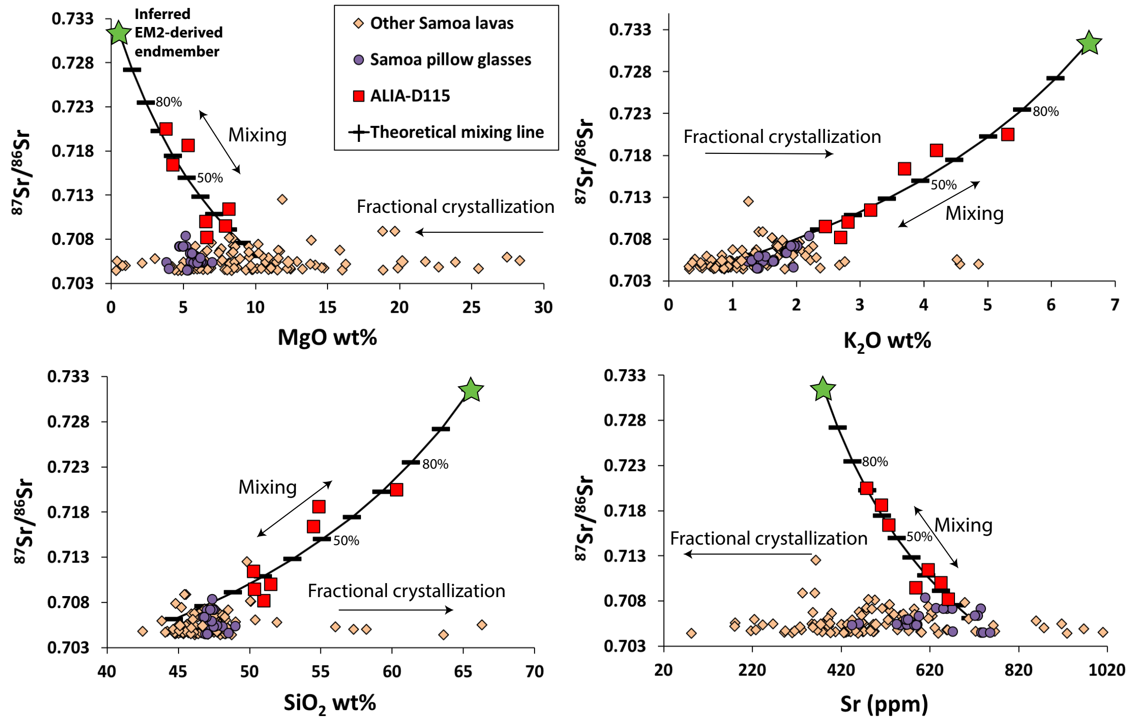

Figure 3: Theoretical mixing of inferred endmember compositions in $^{87}Sr/^{86}Sr$ versus element concentration space. The direction of fractional crystallization is denoted by arrows. The green star denotes the EM2-derived mixing endmember composition (SiO_2 = 65.5 wt%, MgO=0.5 wt%, Al_2O_3=17.1 wt%, FeO=3.8 wt%, CaO=2.7 wt%, TiO_2=1 wt%, and Na_2O+K_2O=11 wt%; See Supplementary Dataset S2), which is calculated in this study (see Methods); the black hatched line shows the path of the calculated mixing curves, where each hatch increases by 10% mixing from the geochemically-depleted mafic endmember to the more evolved EM2-derived endmember (black hatched line is derived from the same methodology as described briefly in Figure 2 and more in depth in the Methods). Mixing is cleared defined by a curve with a non-zero slope unlike the lavas that have been affected only by fractional crystallization.

The Sr, Nd, and major element oxide concentrations, as well as the $^{87}Sr/^{86}Sr$ and $^{143}Nd/^{144}Nd$ of the two endmembers that anchor the ALIA-D115 mixing array are reconstructed using a mixing analysis. The method for defining the endmember compositions (i.e., to reconstruct the composition of both end members), in terms of major elements and Sr and Nd concentrations, requires initial estimates for the MgO content of the endmembers and linear regression analysis of the ALIA whole rock bulk compositions C_i/MgO versus 1/ MgO space (where C_i is the concentration of a major element oxide or a trace element; see detailed description in the Methods section). MgO is estimated, *ab initio*, because it can be best constrained in both mixing endmembers given the limited variability at both ends of the mixing array formed by the ALIA-D115 lavas, which can be observed in plots of SiO_2 vs. MgO, for example (see Supplementary Figure S2 of Appendix S1). Further, according to mixing theory, $^{87}Sr/^{86}Sr$ versus Nd/Sr concentration and $^{143}Nd/^{144}Nd$ versus Sr/Nd concentration (companion plots to the hyperbolic mixing relation in $^{87}Sr/^{86}Sr$ versus $^{143}Nd/^{144}Nd$ space; Langmuir et al., 1978) should give rise to linear arrays in a system described by two-component mixing. Thus, linear regressions were performed on these plots also, and given the derived Sr and Nd concentrations in each endmember, estimates of $^{87}Sr/^{86}Sr$ and $^{143}Nd/^{144}Nd$ were obtained for both endmembers (see Methods for more detail, Supplementary Figures S4 and S5 of Appendix S1for regressions, and Supplementary Dataset S2 for calculated endmember compositions).

Given an initial assumption of 10 wt% and 0.5 wt% MgO in the low (mafic) and high (silicic) $^{87}Sr/^{86}Sr$ endmembers, respectively (which we justify in the Methods), we calculate 380 ppm Sr and 63 ppm Nd in the high $^{87}Sr/^{86}Sr$ EM2 endmember magma (see Supplementary Dataset S2 for composition of 2 other high $^{87}Sr/^{86}Sr$ endmember calculations with different starting MgO concentrations) and retrieve values of $^{87}Sr/^{86}Sr = 0.73158$ and $^{143}Nd/^{144}Nd = 0.51213$. We calculate 712 ppm Sr and 48 ppm Nd in the low $^{87}Sr/^{86}Sr$

endmember and retrieve values of $^{87}Sr/^{86}Sr = 0.70610$ and $^{143}Nd/^{144}Nd = 0.51280$. Figures 1 and 3 illustrate mixing curves (black lines) using these values showing good agreement with the ALIA-D115 lavas and the clinopyroxenes of this study.

The percentage of mixing observed in the $^{87}Sr/^{86}Sr$ vs. $^{143}Nd/^{144}Nd$ plot (Figure 1), consistent with the other major element and isotope plots (Figure 3; Supplementary Figures S2 and S3 of Appendix S1), suggests that the most silica rich ALIA-D115 lava (sample ALIA-D115-21) is composed of ~70-80% of the calculated EM2 endmember melt and ~20-30% of the mafic melt endmember.

5 Preservation of isotopic heterogeneity in the magma chamber

Recent work has shown zoning in pyroxene to be a reliable indicator of magma mixing events (Ubide et al., 2018, 2019). Here, Mg and Fe zoning in clinopyroxene is used to assess magmatic residence times post magma mixing, given relevant temperatures and diffusivities. The eradication of compositional anomalies in the form of thin growth lamella can be computed following a standard one-dimensional diffusion analysis (Carslaw and Jaeger, 1959; details are presented in the Methods section). Attention is focused on the most mobile elements in clinopyroxene that exhibit zonation and for which diffusivity data exists at the inferred temperature range relevant to petrogenesis. Fe/Mg inter-diffusion in clinopyroxene is ideally suited in this analysis, and we select two magmatic temperature intervals for analysis: 1200 °C ($\log_{10} D^{Mg/Fe\ inter\text{-}diffusion} = -18\ m/s^2$; Muller et al., 2013), and 1150 °C ($\log D^{Mg/Fe\ inter\text{-}diffusion} = -19.4\ m/s^2$; Dimanov and Wiedenbeck, 2006). The thinnest Fe and Mg lamella observed in clinopyroxene is about 15 μm thick (see Supplementary Figure S6 of Appendix S1). The residence time of clinopyroxene (i.e., time needed to eradicate anomalous compositional lamella) bands is <45 years using a temperature of 1150

°C to <2 years using 1200 °C. Although there are uncertainties in the assumed temperature and in the experimental values of Fe/Mg inter-diffusion in clinopyroxene, we argue these estimates are accurate to within an order of magnitude, and potentially within 20-30%, based on experimentally-determined activation energies and reasonable estimates for magma temperatures that are constrained by phase equilibria (Zhang and Cherniak, 2010). The elemental concentration field observed in the clinopyroxenes exhibit no coherent zoning pattern, and along with the $^{87}Sr/^{86}Sr$ zoning in plagioclase from Edwards et al. (2019), are suggestive of at least one magma mixing event. The preservation of elemental zoning in clinopyroxene suggests that the eruption occurred relatively rapidly after magma mixing. The short timescales between mixing of geochemically-distinct melts and the eruption of the mixture was sufficiently short to permit preservation of the heterogeneous $^{87}Sr/^{86}Sr$ and $^{143}Nd/^{144}Nd$ in the magmatic clinopyroxenes, which reflect the heterogeneity represented by the heterogeneous magmas that contributed to the mixture.

6 Thermodynamic modeling of the evolution ALIA-D115 lavas

Using the two endmember compositions described above—the mafic, low $^{87}Sr/^{86}Sr$ and the trachytic, high $^{87}Sr/^{86}Sr$ endmembers—thermodynamically-constrained mixing simulations using MELTS (Ghiorso and Sack, 1995; Gualda et al., 2012) and the Magma Chamber Simulator (MCS; Bohrson et al. 2014) at ~0.2 GPa best capture the major element and isotope characteristics of the Samoan lavas (see Supplementary figures S2 and S3 of Appendix S1) and validate the mixing endmembers proposed in this study. In addition, the mixing calculations approximately reproduce the dominant mineralogy of clinopyroxene ($Mg\#_{71-80}$; natural clinopyroxene range from $Mg\#_{71-82}$ from Jackson et al., 2009; see also Supplementary Table 1) and plagioclase (~$An_{45;}$ natural plagioclase range from An_{50-60} from

Edwards et al., 2019) observed in the ALIA-D115-18 lava (see Methods for model parameterizations). It is important to note that the MCS mixing lines plotted in Supplementary Figures S2 and S3 (Appendix S1; plotted in grey) are not expected to follow the same path in compositional space as the binary mixing models, nor end at the "EM2"-derived endmember (see Methods). This is because the former tracks the predicted melt composition whereas the latter tracks the bulk composition of the mixture. It is expected that mixing would produce crystal populations with heterogeneous major, trace, and $^{87}Sr/^{86}Sr$ and $^{143}Nd/^{144}Nd$ compositions since the hybridization of the mixing endmember magmas is not instantaneous and most likely incomplete, even after decades of magma co-mingling (Jackson and Hart, 2006).

The petrogenetic modeling presented here shows that a silicic endmember EM2 magma is consistent with the geochemical array formed by the ALIA-D115 lavas from Samoa. An important outcome of this effort is the determination that the extreme EM2 magma endmember in Samoa is trachytic in composition. While the presence of this trachytic endmember (with $^{87}Sr/^{86}Sr$ up to 0.73158) is inferred from the mixing calculations presented here, it has not (yet) been found in pure form in lavas examined from the ALIA-D115 dataset. However, geochemical interrogation of the highest $^{87}Sr/^{86}Sr$ Samoan lavas—ALIA-D115-18 and ALIA-D115-21 (with whole rock $^{87}Sr/^{86}Sr$ of 0.718592 and 0.720469, respectively; Jackson et al., 2007)—reveals that single clinopyroxene crystals ($^{87}Sr/^{86}Sr$ up to 0.723888; this study, Supplementary Table 1) and zones in plagioclase ($^{87}Sr/^{86}Sr$ up to 0.7224; Edwards et al., 2019) sample even more extreme EM compositions than the host whole rocks and trend towards the endmember EM2 melt calculated here. More intriguingly, reports of high-SiO_2 (65 to 69 wt%) trachytic melt inclusions (Adams et al., 2017) hosted in the same ALIA-D115-18 clinopyroxene grains examined in this study raise the possibility that the EM2 endmember may be preserved in relatively pure form as glassy melt inclusions in the clinopyroxenes from a high $^{87}Sr/^{86}Sr$ lava (see Supplementary Dataset S2 for example melt inclusion compositions). Unfortunately, these melt inclusions are too small for analysis of $^{87}Sr/^{86}Sr$. Nonetheless, the presence of trachytic melts representing the EM2 endmember composition raises important questions about the origin of melts sampling this source. While the new radiogenic isotopic compositions support models advocating for a large fraction of recycled terrigenous sediment into the Samoan plume (Jackson et al., 2007; Edwards et al., 2019), constraining the residence of this sediment in the deep mantle is important for understanding its long-term survival during convective attenuation. EM mantle domains have been found to correspond geographically with the large low shear-wave velocity provinces (LLSVPs) (Castillo and Batizat, 1989; Jackson et al., 2018), suggesting that sediment-rich domains can survive in the LLSVPs over geologic timescales, and have been sampled by the Samoan plume.

Chapter 2: Trachytic melt inclusions hosted in clinopyroxene offer a glimpse into Samoan EM2-endmember melts

1 Introduction

Melt inclusions (MIs) have been used for decades to provide a glimpse into the petrogenetic evolution of lavas (e.g., Anderson & Wright, 1972; Danyushevsky et al., 2002; Kent, 2008; Kent & Elliott, 2002; Lowenstern, 1995; Melson, 1983; Plank et al., 2013; Sobolev, 1996). Melt inclusions are liquids present in evolving magmas that are captured by growing phenocrysts and they can be used to better understand the evolution of a magma. Conceptually, these captured melts are physically isolated from the effects of subsequent (post-entrapment) magma mixing, assimilation, or fractionation that ultimately modify magma compositions. They present compositional snapshots in time, although following entrapment MI compositions may be modified by post-entrapment crystallization (PEC) or by post-entrapment diffusive exchange with their host crystal (PED). MIs often reveal very heterogenous compositions, or distinct compositions not realized by the associated erupted products (e.g., Kamenetsky, 1996; Kamenetsky et al., 1997; Kent et al., 1999; Reinhard et al., 2018; Saal et al., 1998; Sobolev & Shimizu, 1993; Sobolev et al., 2000; Sours-Page et al., 1999; Wallace, 2005). Compared with the whole rock, these differences in composition are likely a direct result of sampling different time frames during melting and mixing processes, or even melts from different mantle sources than are present in whole rock lavas (e.g., Jackson & Hart, 2006; Saal et al., 1998; Sobolev, 2007), and can thus be used to better understand lava petrogenesis.

Here we focus on major and trace element compositions of uniformly trachytic clinopyroxene-hosted melt inclusions found within the second-most-enriched (high $^{87}Sr/^{86}Sr = 0.71856$) whole rock lava from the Samoa hot spot. This lava, ALIA-D115-18, was dredged off the submarine flanks of Savai'i Island, western Samoa, and similar to other lavas from the same dredge haul, exhibit the "enriched mantle 2" (EM2) geochemical signature (Jackson et al., 2007). The EM2 signature is believed to be the result of addition of ancient subducted terrigenous sediment to the mantle source region (White & Hofmann, 1982; Jackson et al., 2007; Edwards et al., 2019; Adams et al., in review). Sample ALIA-D115-18 hosts clinopyroxenes that have trapped melt inclusions with trachytic compositions. A recent study by Adams et al., in review (see also Chapter 1) uses binary mixing theory, high precision single-crystal magmatic clinopyroxene $^{87}Sr/^{86}Sr$ and

$^{143}Nd/^{144}Nd$ isotopes, and major and trace element data of clinopyroxenes within the ALIA-D115-18 sample to calculate the EM2 magma mixing endmember. Notably, the calculated EM2 endmember melt is predicted to be trachytic and bears a remarkable resemblance to the clinopyroxene-hosted melt inclusions reported in this study.

We suggest below that the clinopyroxene-hosted trachytic MIs are EM2-endmember melts captured during the mixing process. The clinopyroxene-hosted MIs are silicic (64-68 wt% SiO_2), depleted in MgO (0-1 wt%), and exhibit much of their chemical variation in the alkali elements (Na_2O+K_2O varies from 8.2 to 11.6 wt.%). In addition, one clinopyroxene-hosted MI has two partially resorbed Fo_{73} olivine crystals, suggesting interaction of the trachytic melt with a mafic magma, as the olivines and trachyte melt inclusions are not in equilibrium, consistent with two-component mixing between a mafic magma and a much more evolved magma that has been inferred from relationships between major-trace element compositions and radiogenic isotopic ratios in the Samoan magmatic suite (Jackson et al., 2007; Edwards et al., 2019; Adams et al., in review). This raises several important questions: what is the origin of these high-silica MIs? What is their relationship to the ALIA-D115-18 whole rock and the EM2 source? Do they represent relatively primary high-silica partial melts that were trapped in growing clinopyroxenes at depth during magma mixing, or is their compositional array a result of post-entrapment modification? These questions are addressed in the following sections.

2 Samples and Methods

Melt inclusions of this study are hosted in clinopyroxenes from a single Samoan hotspot lava (ALIA-D115-18), dredged off the submarine flanks of Savai'i Island, western Samoa.

Twenty-two MIs were studied with diameters ranging from ~15-100 μm. The MIs are generally spherical or ellipsoidal in cross-section and are glassy; some contain minor amounts of crystal inclusions consisting of clinopyroxene ~ ilmenite >> olivine (Figure 1). Of the 22 inclusions, vapor bubbles are observed in two MIs occupying between 11 and 26 vol% of the MI, one shows significant amounts of crystal inclusions consuming about 10 vol% of the MI (Figure 1a), one has about 2 vol% of ilmenite (Figure 1b), and, most significantly, twenty MIs (91%) show less than 1 vol% of crystal inclusions. The crystal volume estimate was made assuming an ellipsoidal geometry for both the MI and the crystals.

For volatiles and trace element analyses of the melt inclusions by ion microprobe, the sample surface was pre-sputtered prior to analysis. Volatile elements (H_2O, Cl, F, S) in the melt inclusions were analyzed on the Cameca IMS 6F ion microprobe housed at the Department of Terrestrial Magnetism (DTM), Carnegie Institution of Washington following methods from Hauri (2002), where uncertainties are ± 10% (2σ) for volatile element concentrations. Trace element (Sc, Sr, Nd, Y, Zr, Ba, Ce, Dy, Nb, La, Yb, Hf, Gd) analyses of the melt inclusions were also carried out on the DTM Cameca IMS 6F, following techniques in Peterson et al. (2017), where precision on trace element analyses is better than 10% (2σ). Major element concentrations in the melt inclusions were measured on the JEOL Superprobe housed at the Geophysical Laboratory, Carnegie Institution of Washington, and methods and uncertainties follow Hauri (2002): a 15 kV accelerating voltage was used, and a 10 nA, defocused (10 micron) beam was employed during analysis. Lastly, it's important to note these melt inclusions were never heated (e.g., by heating stage or furnace) for rehomogenization. New major, trace, and volatile element data on melt inclusions are shown in Supplementary Dataset S5.

We measured 17 compositional profiles in 4 clinopyroxenes hosting melt inclusions and the major and trace element data can be found in Supplementary Datasets S6 and S7. Major and trace element analyses were carried out at the University of California Santa Barbara (UCSB) for several transects across a 4 clinopyroxenes, extending from near the clinopyroxene-melt inclusion boundary to distal regions of the clinopyroxene. Major elements were analyzed on the EPMA at UCSB; an accelerating voltage of 15 kV was used with a 20 nanoAmp beam with a spot size of 2 microns. Trace element concentrations were analyzed by LA-ICP-MS at UCSB using a Photon Machines Excite 193 Excimer laser coupled to an Agilent 7700 quadrupole ICPMS; a 15 micron spot size was used and the reference material NIST612 was analyzed every 8-10 unknown analyses.

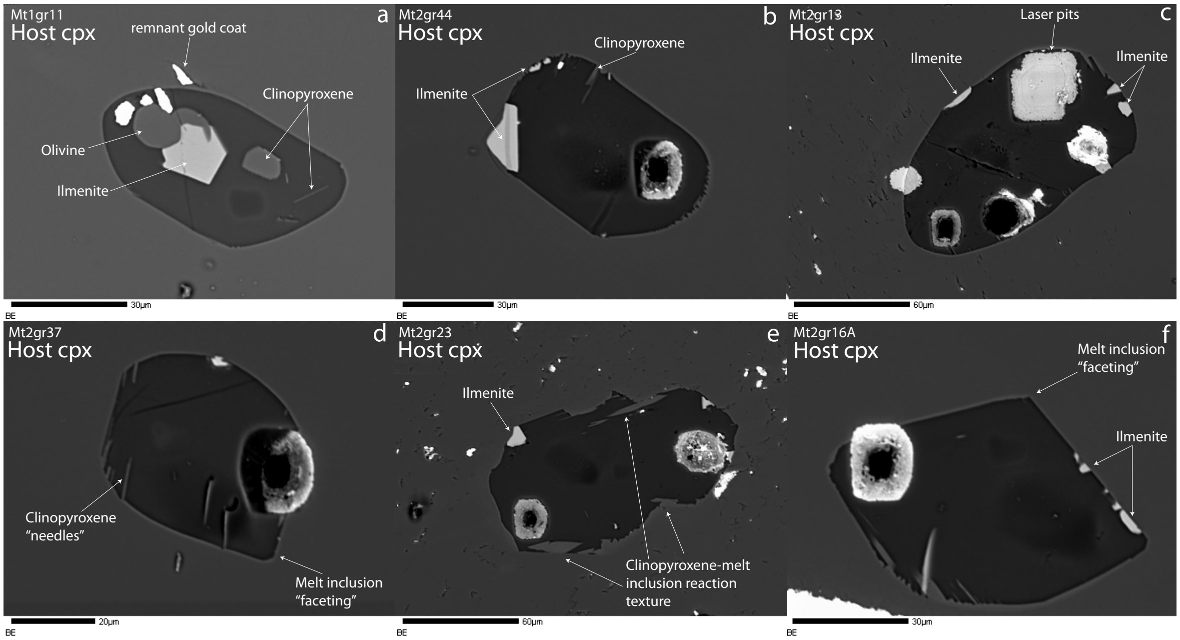

Figure 1: Back-scatter electron (BSE) images of select melt inclusions. (a) Melt inclusion with the largest amount and variety of crystal inclusions. (b) and (c) relatively pristine melt inclusions with some ilmenite crystal inclusions nucleating on the melt inclusion walls. (d) Relatively pristine melt inclusion showing clinopyroxene needles that have nucleated in the inclusion in addition to the beginning stages of "faceting"

(see text for details). (e) the only melt inclusion that shows direct reaction of the melt inclusion walls with the surrounding clinopyroxene. The reaction texture is denoted by the jagged appearance of the melt inclusion wall. In addition, there is a slightly brighter region around the melt inclusion edge compared with the rest of the host clinopyroxene, indicative of compositionally distinct clinopyroxene. (f) Melt inclusion exhibiting somewhat evolved faceting, but shows very minimal post-entrapment crystallization. Some of the above inclusions also show laser and ion probe pits.

3 Results

3.1 Major elements

The melt inclusions are orthoclase-normative and show limited variability in the major elements with the exception of silica, Na_2O, and K_2O. The melt inclusions lie between ~64.0-68.0 wt% SiO_2, 0-1 wt% MgO, 0.5-1.5 wt% FeO, and 8.2-11.6 wt% total alkalis ($Na_2O + K_2O$) (see Supplementary Dataset S5 for full compositions).

3.3 *Trace elements*

Trace elements were measured in sixteen of the twenty-two inclusions. The incompatible trace element compositions show extreme variability, particularly, for the LREE, Zr, Sr, and Ba compared with the HREE. In particular, Ba and Zr show the largest compositional variability with a range of 777 ppm (from 248 to 1025 ppm; one relative standard deviation=27% variability) and 374 ppm (from 211 to 585 ppm; one relative standard deviation=28% variability), respectively. Yb and Dy show the smallest variability with a range of 1.8 ppm (from 0.5 to 2.3 ppm; one relative standard deviation=43% variability) and 3.7 ppm (from 1.3 to 5 ppm; one relative standard deviation=39% variability), respectively (see Supplementary Dataset S5 for range and standard deviation of all other elements). A comparison of the melt inclusions with the ALIA-D115 whole rocks and average Ta'u and Ofu lavas, which represent the least geochemically-enriched lavas from Samoa, shows the ALIA-D115-18 MIs have a strong enrichment of LREE and depletion of HREE compared with other Samoan whole rock lavas (Figure 2).

3.4 Volatiles

Water, sulfur and the halogens have been measured in 18 of the 22 MIs. The MIs have H_2O contents ranging from 0.4-1.06 wt%, S ranging from 67-504 ppm, Cl ranging from 781-2916 ppm, and F ranging from 19-2674 ppm. A plot of any volatile element versus melt inclusion size shows no correlation, suggesting the variation in volatile concentrations, and in particular H_2O, has not been affected by diffusive loss (Kent 2008; Cabral et al., 2014). F concentrations are highly variable across the MI suite. In the H_2O, Cl, and S dataset, one MI has anomalously low volatile concentrations compared with the rest of the MIs, and this inclusion is also the MI that shows the most faceted shape (Mt2gr16A; Figure 1f). We do not have an explanation for the low volatile concentrations in this inclusion, except to suggest that the inclusion may have ruptured during ascent, allowing some volatile loss, prior to reannealing.

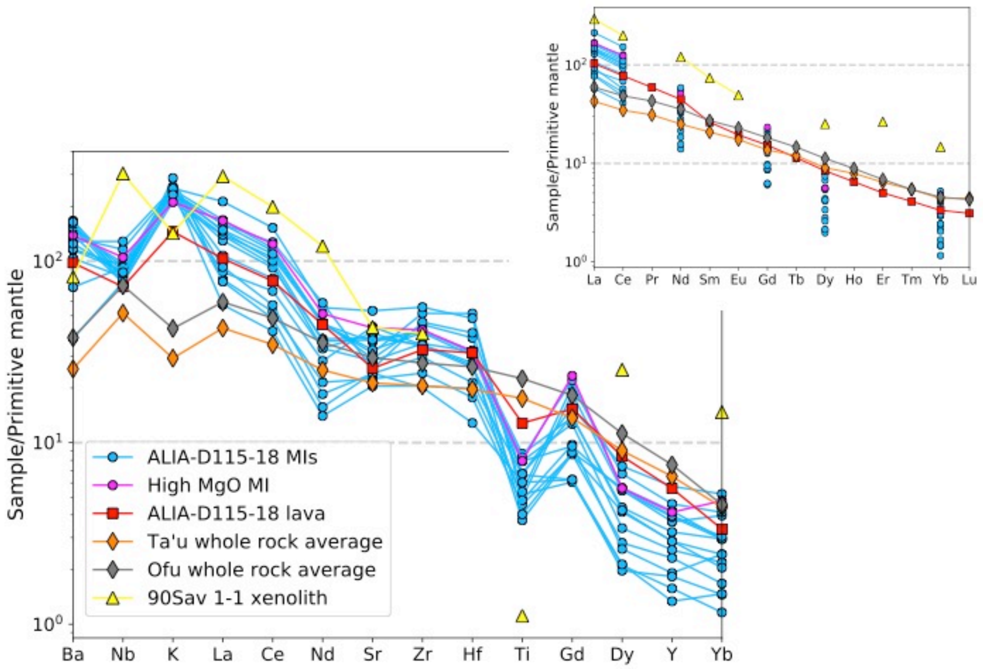

Figure 2: Primitive mantle normalize trace element patterns of clinopyroxene-hosted melt inclusions (MIs) (blue circles) from the ALIA-D115-18 whole rock lava (red squares). The data are shown in comparison with other Samoa whole rocks (average compositions for Ta'u and Ofu whole rocks). The highest MgO MI is denoted by the magenta circles. The orange and grey diamonds represent average Samoan lava compositions from Ta'u and Ofu Islands, respectively, which are the most geochemically-depleted shield volcanoes in the eastern Samoan region. The yellow diamonds are a Savai'i xenolith glass, 90SAV1-1, from Hauri et al. (1993). The inset spiderdiagram shows rare earth elements only. An enrichment of the MIs in LREE and depletion in HREE compared with the other Samoan lavas indicates that their source likely had residual garnet.

4 Discussion

4.1 Post-entrapment modification

Modification processes affecting MIs post-entrapment have been studied extensively (Baker, 2008; Bucholz et al., 2013; Cottrell et al., 2002; Danyushevsky et al., 2000; Danyushevsky et al., 2002; Gaetani et al., 2012; Gaetani & Watson, 2000, 2002; Kent, 2008; Kress & Ghiorso, 2004; Nielsen et al., 1998; Portnyagin et al., 2008; Qin et al., 1992;

Schiano & Bourdon, 1999; A. v. Sobolev, 1996; Spandler et al., 2007). The two main ways by which MIs can be chemically modified post-entrapment are by: (1) nucleation and growth of the host mineral on the MI walls, either by reaction between the edge of the melt inclusion and host clinopyroxene, or nucleation and growth of phases that are different than the host mineral (e.g., ilmenite), and (2) diffusive re-equilibration of the MI with external melt mediated by the host crystal. These modification processes and their effects on the MIs of this study are evaluated, in turn.

4.1.1 Diffusive modification

A key indicator of diffusive modification is MI morphology. It has been noted that round melt inclusions are disequilibrium features. As diffusion proceeds between a MI and its host, inclusions begin to take on negative crystal shapes of the host mineral, becoming "faceted" (e.g., Pamukcu et al., 2015; Soldati, 2011; Wortis, 1988). The melt inclusions of this study are quite rounded with the exception of three inclusions that exhibit incipient faceting (See Figure 1d and 1f and Appendix S2 Figure S10p), but these three inclusions show no significant differences in major and trace element chemistry from the other MIs (not including the volatiles, which are highly variable among all MIs). This suggests there has been minimal modification of the melt inclusion compositions via diffusion through the host clinopyroxene.

In addition, if diffusive re-equilibration has played an important role in modifying melt inclusion composition, there should be a correlation between MI size and composition, with the smallest inclusions closest to equilibrium due to greater diffusive equilibration compared with large melt inclusions (e.g., Qin et al., 1992; Sinton et al., 1993; Nielsen et al., 1998; Cottrell et al., 2002; Baker, 2008). Figure 3 shows a series of plots of melt inclusion size versus composition for selected major and trace elements, for several incompatible (e.g., K_2O, Cl, La, Sr) and two compatible elements (e.g., CaO, Sc) in clinopyroxene. These plots show no correlations. Additional comparisons (not shown) of other chemical species, including both major and trace elements, also show a lack of correlation with melt inclusion size. This is consistent with the argument that post-entrapment diffusive (PED) modification of the melt inclusions has been negligible.

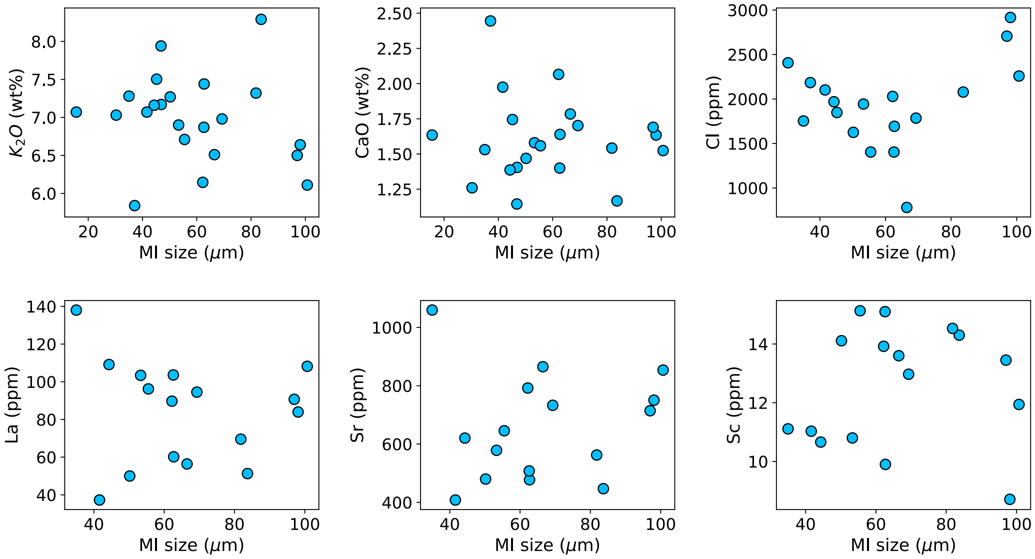

Figure 3: Melt inclusion size (diameter of MI) versus composition. If diffusive modification has played a significant role in modifying melt inclusion chemistry, a positive, linear trend will be observed between incompatible element concentration versus melt inclusions size, as smaller inclusions will be affected more rapidly by diffusion compared with larger inclusions. Full melt inclusion sizes and compositions can be found in Supplementary Dataset S5.

Additionally, boundary-layer driven diffusion can also be assessed as a means of altering MI composition using a simple test of plotting element diffusivity in melt versus trace element standard deviation measured using the composition of all 22 MIs (Kent, 2008; Michael et al., 2002). Accordingly, fast diffusing elements should show little variation (low standard deviation) because diffusion will rapidly reduce ("smooth out") trace element variability in the clinopyroxene, while slow diffusing elements should show the most variability (high standard deviation). We test this in Appendix S2 Figure S11 with a comparison of compositional standard deviation versus known diffusivities in trachytic melts at 1150 °C for MI trace elements, and we observe no correlations. This also supports the hypothesis that diffusion has played a negligible role in modifying the MIs.

4.1.2 Post-entrapment crystallization

Of the melt inclusions in this study, 20 out of 22 show 2 vol% or less crystallinity. Of the 20 MIs with 2 vol% crystallinity or less, two show <<1 vol% crystal inclusions, but contain vapor bubbles. These two MIs (mt2gr9 and mt2gr8b; Appendix S2 Figure S10i and S10h, respectively) are also the only two MIs that are surrounded by clinopyroxene "halos", which are rings of clinopyroxene with distinct mean atomic number observed only in BSE imaging. The halos range from ~10-30 μm wide and encircle the MIs. These halos could be related to post-entrapment crystallization from the MIs or to diffusion processes, but the origin remains ambiguous. If either of these two processes were at play, these two inclusions would be geochemically distinct from the other MIs, which is not the case. In addition, compositional gradients in the clinopyroxene going away from the MIs, including clinopyroxenes hosting halos (discussed in the Appendix S2 text and denoted by a grey dashed line in Appendix S2 Figures S3 and S4), are inconsistent with the aforementioned two hypotheses. The MIs with crystal inclusions have predominately clinopyroxene and ilmenite. Two MIs obviously exhibit evidence of reaction with the host clinopyroxene at the inclusion-clinopyroxene boundary: in one inclusion, this resulted in formation of orthopyroxene (melt inclusion Mt1gr12; see Appendix S2 Figure S10e), and in another inclusion, the result is a jagged MI rim surrounded by compositionally distinct clinopyroxene (indicated by the brighter region surrounding the MI in the BSE image compared with the slightly darker host clinopyroxene) that returns to the host clinopyroxene composition with distance from the MI edge into the clinopyroxene (Mt2gr23; see Figure 1e).

Of the two MIs that show greater than 2 vol% crystallinity, one shows about 2.5 vol% of predominantly ilmenite (Mt2gr44: Figure 1b). The second of the two MIs with >2 vol% crystallinity (Mt1gr11; Figure 1a) contains crystals of Fo_{73} olivine + ilmenite+ clinopyroxene representing a crystallinity of about 10 vol% of the MI. However, we argue that these phases did not crystallize directly from the melt inclusion post-entrapment, but were rather trapped along with the melt simultaneously. Crystal inclusions that have grown directly from MIs post-entrapment tend to nucleate at the melt inclusion-host contact (the walls of the MI). This single MI that exhibits olivine, ilmenite, and clinopyroxene *appear* isolated within the bulk volume of the MI and have not grown from the MI walls (e.g. Roedder, 1984, Sobolev, 1996; Kent, 2008; Kress & Ghiorso, 2004). Additionally, if these crystals did precipitate from the melt inclusion, one expects that the MI would significantly differ in major element composition compared to other melt inclusions with little to no daughter crystals, but this is not the case. Furthermore, the presence of Fo_{73} olivine in the trachytic melt inclusion provides further evidence that the olivine did not grow post-entrapment, as the olivine is far out of equilibrium with the trachytic melt; additionally, the olivine could not have grown from a more mafic precursor that evolved into the trachyte (via post-entrapment crystallization) because very little post-entrapment crystallization occurred, as we show in the Appendix S2 text. To summarize, all but two MIs show much less than 2 vol% crystallinity with two showing >2 but <10 vol%. We argue that some of the crystallinity in the MIs is not related to PEC but was present upon entrapment. Regardless, this small amount of PEC would not significantly modify the major and trace element compositions of the MIs.

Additionally, we used the Fe-Mg exchange between olivine and ilmenite and clinopyroxene and ilmenite in inclusion Mt1gr11 (Figure 1a) to estimate an equilibration temperature based on thermodynamic data and ideal ionic mixing of Fe and Mg. Computed temperatures for both olivine-ilmenite and clinopyroxene-ilmenite were very low, ~ 600 ^{o}C, and suggest that olivine and clinopyroxene were never in equilibrium with the ilmenite, as this temperature is much too low for Fo_{73} to be in equilibrium with either clinopyroxene or ilmenite.

As a comparison with other clinopyroxene-hosted MIs, a study looking at clinopyroxene-hosted MIs by Frezzotti (2001) suggests these types of MIs can often evolve to trachytic liquids with significant fractionation of clinopyroxene on the melt inclusion walls under slow cooling conditions. An example from Mt. Etna clinopyroxene-hosted melt inclusions suggests the inclusions were originally alkali-basaltic in composition and experienced 30% crystallization of clinopyroxene resulting in volatile saturation and precipitation of water-rich phases like amphibole as well as a distinct clinopyroxene-rim around the MIs. If melt inclusions presented here experienced a similar history, we would expect to see abundant daughter crystals as well as a compositionally distinct clinopyroxene compositions surrounding the melt inclusions in the BSE images (see Figure 1). This is not the case for the Samoan melt inclusions with the exception of *one* inclusion shown in Figure 1e (i.e., Mt2gr23), that does show some compositionally distinct clinopyroxene that has clearly grown from the MI walls creating a jagged MI rim texture. This further suggests that the MIs investigated here have undergone very little PEC.

Finally, compositional profiles were analyzed in four clinopyroxene grains hosting melt inclusions (two of which show MIs with the clinopyroxene halo feature described above) in search of chemical gradients indicative of PEC. Assuming negligible diffusion, consistent with the diffusion analysis discussed previously, then PEC of compositionally distinct clinopyroxene directly from the MIs, driving them to more evolved compositions, should be observed in the form of chemical gradients going away from the MI edge and into the host clinopyroxene. If this is the case, compatible element concentrations should increase going away from the MI edge, while incompatible elements should decrease in concentration going away from MI edge (see Appendix S2 Figure S1 and text for more details). An analysis of all major and trace element profiles (17 profiles have major element characterization and 13 of these profiles have trace elements) across four clinopyroxenes show that only 2 out of the 13 profiles (~15%) show evidence of PEC (see Appendix S2 text for further discussion). The fact that 11 out of 13 (85%) of the profiles are inconsistent with PEC suggests that PEC has not significantly influenced the composition of the melt inclusions (see Appendix S2 Figures S2-S9 for profiles). If we were to consider major elements only (17 transects performed), just 2 out of 17 (12%) are consistent with PEC.

Based on this analysis, it would appear that the PEC was not an important process in modifying the composition of the MIs.

4.2 Origin of trachytic melt inclusions

Several recent studies have shown the ALIA-D115 lavas—a suite of lavas from the same submarine dredge of a Samoan volcano (Savai'i) as the ALIA-D115-18 lava studied here—to be a result of magma mixing between a low $^{87}Sr/^{86}Sr$, mafic endmember and one that is high $^{87}Sr/^{86}Sr$, and evolved, representing the EM2-derived endmember (Jackson et al., 2007; Edwards et al., 2019; Adams et al., in review). The origin and composition of the EM2-derived mixing endmember remains uncertain. Adams et al. (in review) present high precision Sr and Nd isotope measurements on individual clinopyroxene porphyrocrysts from the ALIA-D115-18 whole rock lava, discovering the highest $^{87}Sr/^{86}Sr$ (0.723888) ever recorded for the oceanic mantle (for comparison, the highest $^{87}Sr/^{86}Sr$ for an ALIA-D115 whole rock is 0.720469; Jackson et al., 2007). Thus, the EM2-derived endmember melt must have a $^{87}Sr/^{86}Sr$ at least as high as this value. Adams et al. (in review) used the compositions of ALIA-D115 whole rock lavas, together with magma mixing theory, to derive estimates of the compositions of the two mixing endmembers. The generation of the ALIA-D115 lava compositions requires a mafic, low $^{87}Sr/^{86}Sr$ endmember and one that is high in $^{87}Sr/^{86}Sr$, and high in silica (the EM2-derived endmember). The EM2-derived mixing endmember calculated by Adams et al. (in review) is trachytic in composition (SiO_2=65.5 wt%, MgO = 0.5 wt%, Na_2O+K_2O=11 wt%) with an estimated $^{87}Sr/^{86}Sr$ value of about 0.7316. Remarkably, the modeled EM2-derived endmember melt composition bears a close resemblance to the measured trachytic MIs presented in this study. Figure 4 shows major element plots versus SiO_2 showing that this EM2-derived endmember melt overlaps with the MI compositions quite well. Thus, the question remains, what is the origin of these MIs? Are they melts formed by fractional crystallization of a mafic parental melt that was enriched in radiogenic Sr? Or do they represent partial or total melts of a more silica-rich and Sr-radiogenic source material? In the case of the latter, the reactivity of such relatively high-silica melts in an ultramafic (peridotitic) mantle is problematic for their mobility. In either case, the MI bulk compositions are intimately associated with the EM2 source and were captured during the magma mixing process that formed the ALIA-D115 lavas.

Our results suggest the MIs have undergone little modification since entrapment and are remarkably similar to the independently derived EM2-mixing endmember proposed by Adams et al. (in review). In order to assess this hypothesis, we can compare the MI chemistry with that of the ALIA-D115 whole rocks, other Samoan whole rock lavas, and Samoan pillow glasses to gain insights on the mixing process. Figure 4 shows major element plots of the ALIA-D115-18 MIs with whole rock lava compositions from the ALIA-D115 and other Samoan whole rock lavas and pillow glasses. The ALIA-D115 lavas form an array extending from the more primitive Samoan whole rocks towards the ALIA-D115-18 melt inclusions. Also plotted are the two mixing endmembers proposed by Adams et al. (in review), in which the black star represents the mafic endmember and the green star represents the EM2-derived mixing endmember. The major element composition of the EM2-derived mixing endmember overlaps with the major element composition of the melt inclusions of this study, with the exception of FeO, which is about 1 wt% lower in the ALIA-D115 MIs than the inferred EM2-derived endmember and Al_2O_3, which is about 1% higher. This suggests that the MIs could in fact be representative of the EM2-derived mixing endmember predicted by Adams et al., (in review). However, the trend formed by ALIA-D115 whole rock lavas could be mistaken for a fractional crystallization trend (Figure 4). Nevertheless, unequivocal evidence of the MIs being a mixing endmember of the ALIA-D115 lavas is seen in trace element and isotope data (see below). These trends are inconsistent with fractional crystallization.

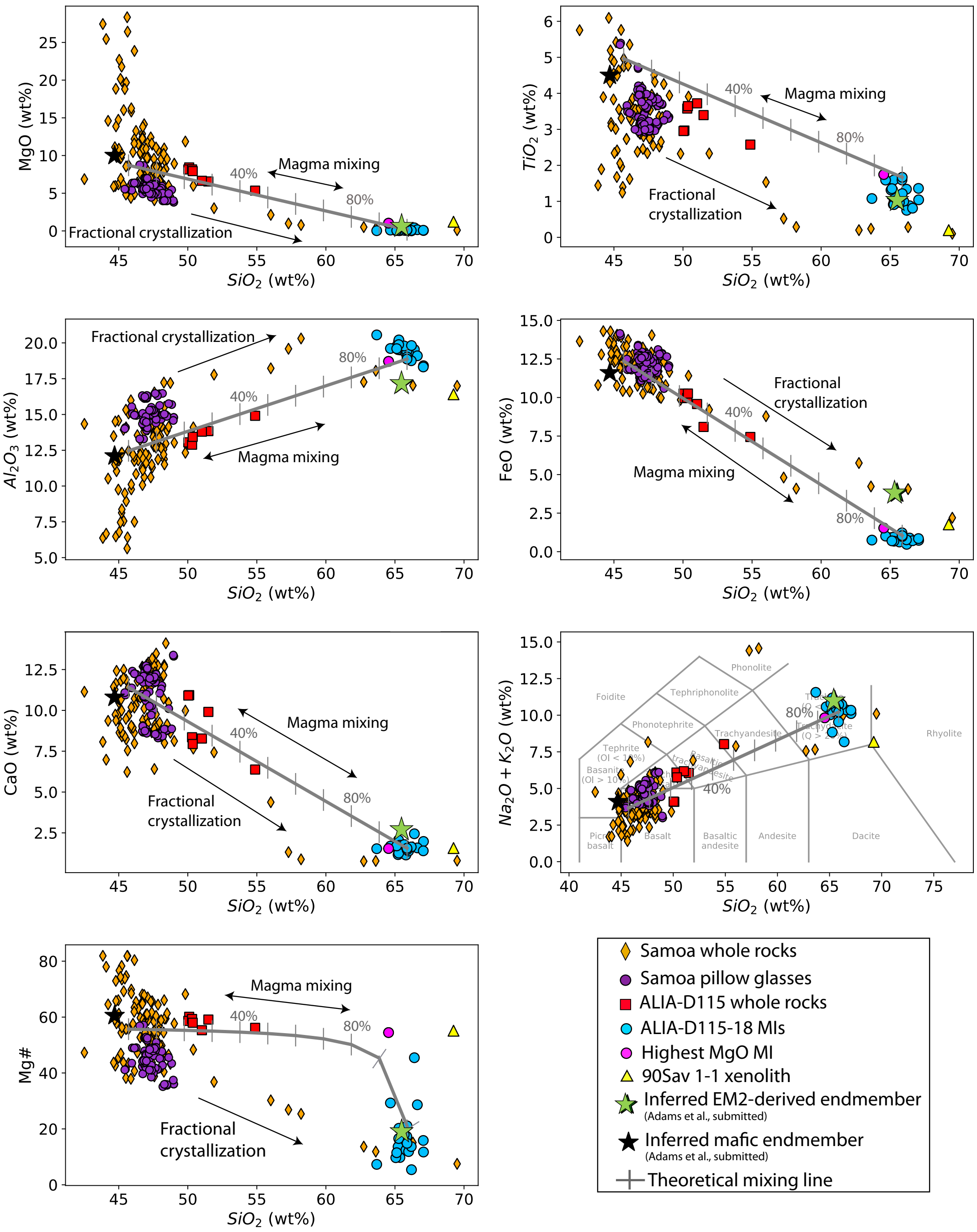

Figure 4: Major element versus major element plots showing the relationship between the ALIA-D115 lavas (red squares), other Samoan whole rock lavas (orange diamonds), Samoan pillow glasses (purple circles), and the ALIA-D115-18 melt inclusions (blue circles). Also plotted for reference are the inferred mafic (black star) and silicic (green star) mixing endmembers calculated by Adams et al., (in review). The highest MgO MI is denoted with a magenta circle. The silicic Savai'i xenolith glass from Hauri et al. (1993) is also shown for reference as a yellow diamond. The ALIA-D115 lavas show a mixing trend extending from more primitive Samoan lavas and pillow glasses to melt inclusions suggesting the melt inclusions could be a mixing endmember. The rest of the Samoan lavas (orange diamonds) that are more evolved show fractional crystallization trends. This can be seen particularly well in the plot of Mg# vs. SiO_2, in which other Samoan whole rock lavas show a linear trend while the ALIA-D115 lavas and MIs show a mixing trend in which there is little decrease in Mg# with decreasing SiO_2, which is consistent with the EM2-derived mixing endmember

(the green star) being trachytic in composition. In addition, a mixing line (grey hatched line) has been calculated using a melt inclusion (mt2gr44; SiO_2 = 65.9 wt%, TiO_2=1.7 wt%, Al_2O_3 = 18.9 wt%, FeO = 1.0 wt%, MgO = 0.16 wt%, CaO = 1.6 wt%, Na+K = 10.2 wt%, and Mg# = 21) and a primitive Samoan whole rock lava composition (OFU-04-05; SiO_2 = 45.7 wt%, TiO_2=5.0 wt%, Al_2O_3 = 12.5 wt%, FeO = 12.4 wt%, MgO = 8.7 wt%, CaO = 11.4 wt%, Na+K = 3.7 wt%, and Mg# = 56; Konter & Jackson, 2012) as endmembers. The mixing line captures the ALIA-D115 lavas quite well with the exception of TiO_2 versus SiO_2 space. The amount of mixing of a MI composition with a more primitive Samoan whole rock lava is about 70-80% mixing, which is consistent with that proposed by Adams et al. (in review).

Plots of LREE and K versus Y (Figure 5) show that the Samoan whole rock lavas and pillow glasses form a linear, positively-sloping fractional crystallization trend, whereas the ALIA-D115 lavas form an orthogonal (negatively-sloping) trend connecting the array formed by Samoan lavas with the array formed by the Samoan MIs. The orthogonal trend in the K versus Y plot (where both elements are incompatible in the suite of phases observed in the host lava and melt inclusions) cannot be the result of fractional crystallization. We argue that the trend formed by the ALIA-D115 lavas is the result of magma mixing in which the MIs are a silicic mixing endmember, and the Samoan basalts reflect the mafic mixing endmember; this is consistent with the results of Adams et al. (in review), who identified the ALIA-D115 lavas to be the result of mixing between a mafic (low $^{87}Sr/^{86}Sr$) and a silicic (high $^{87}Sr/^{86}Sr$ endmember). Although we cannot yet measure the $^{87}Sr/^{86}Sr$ in the melt inclusions due to their small size, the isotopic compositions can be inferred by extrapolating existing trends in the Samoan magmatic suite. Figure 6 shows $^{87}Sr/^{86}Sr$ versus SiO_2 and K_2O for the ALIA-D115 whole rocks, other Samoan whole rocks, and the two mixing endmembers of Adams et al. (in review). The data support a mixing trend for the whole rock lavas from dredge ALIA-D115, where lavas associated with higher SiO_2 and K_2O have higher $^{87}Sr/^{86}Sr$. Using this trend, we can also extrapolate $^{87}Sr/^{86}Sr$ compositions by employing the SiO_2 and K_2O concentrations of the melt inclusions. An extrapolation of the ALIA-D115 mixing trend into the region (grey shaded area) representing the MI chemical range and meeting the average MI value (the thick grey line) for both the SiO_2 and K_2O plots show that, on average, the MIs could have $^{87}Sr/^{86}Sr$ of about 0.729, which is only slightly lower than the value predicted by Adams et al. (in review) of 0.7316 (Figure 6). Lastly, further evidence that the MIs likely represent a mixing endmember is that one melt inclusion hosts two Fo_{73} olivines, not in equilibrium with a trachytic liquid, and indicative of interaction with a more mafic magma. Thus, there are multiple lines of evidence that interaction of mafic and silicic magmas played a central role in the formation of the ALIA-D115 lavas, and the melt inclusions provide us with the first glimpse of actual melts that match the trachytic composition of the EM2 endmember predicted by Adams et al (in review).

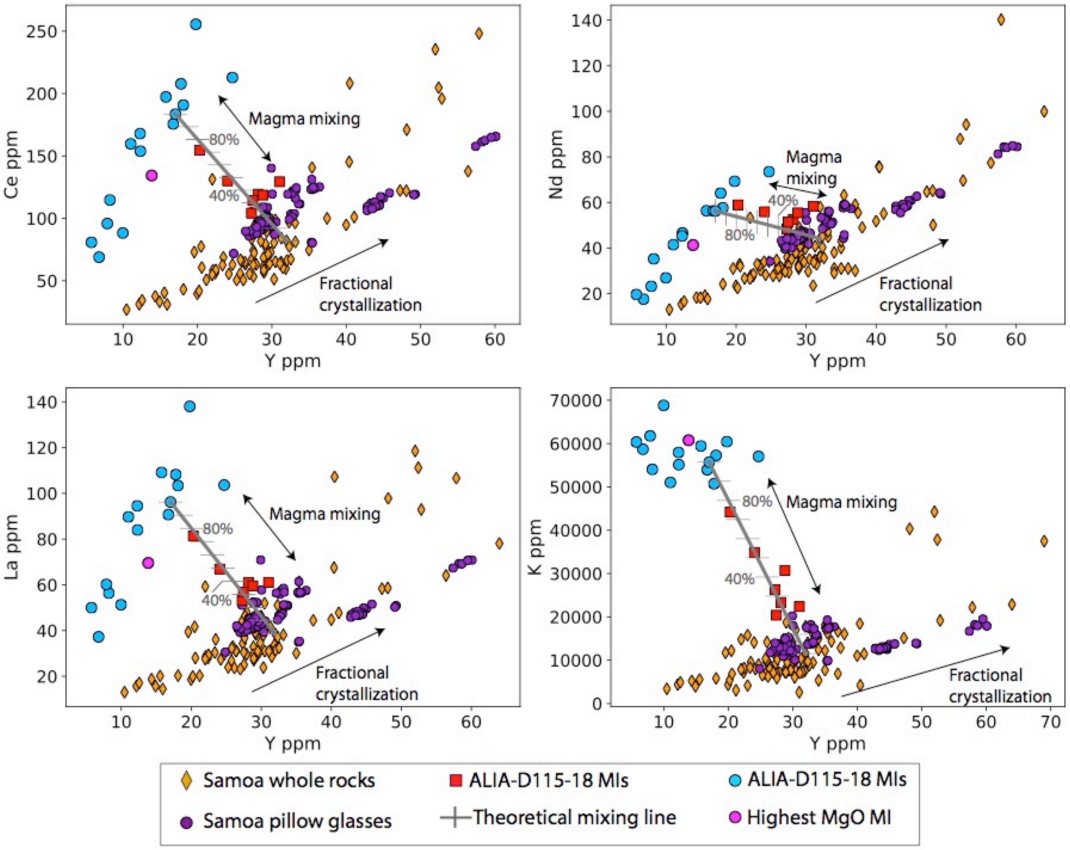

Figure 5: Select trace element plots comparing the ALIA-D115 lavas (red squares), other Samoan whole rock lavas (orange diamonds), Samoan pillow glasses (purple circles) and the ALIA-D115-18 melt inclusions (blue

circles). In trace element space, the ALIA-D115 mixing trend is very clearly extending between more primitive Samoan whole rock lavas (or glasses) and the trend of the MIs of this study. The Samoa whole rock lavas show a clear fractional crystallization (positive slope in plots) trend while the ALIA-D115 lavas form an orthogonal trend (negative slope in plots) extending toward the MIs. Using the same two mixing endmembers as in Figure 4: the mt2gr44 melt inclusion (Y=17.0, La=96.2, K=55,699.7, Nd=56.2, Ce=183.5) and a primitive Samoan whole rock lava (OFU-04-05; Y=32.0 ppm, La=38.5, K=11,539.0 ppm, Nd=44.1, Ce =81.9), a mixing line has been calculated for trace elements (grey hatched line) that explains the ALIA-D115 mixing trend quite well and again suggests about 70-80% mixing of a more primitive Samoa whole rock with the melt inclusions of this study.

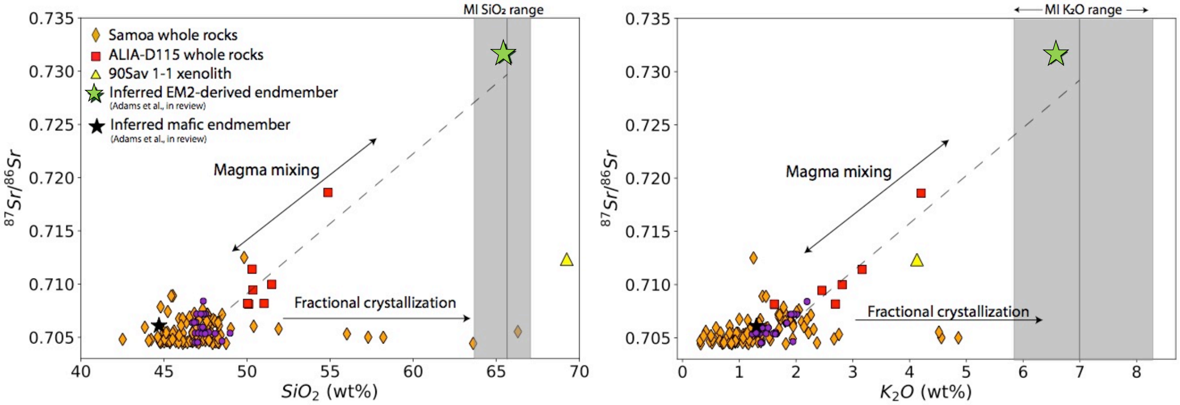

Figure 6. ^{87}Sr/^{86}Sr versus SiO_2 and K_2O comparing Samoan whole rock lavas (orange diamonds) ALIA-D115 whole rock lavas (red squares), Samoa pillow glass (purple circles), a Savai'i xenolith glass, 90SAV1-1, from Hauri et al. (1993) (yellow diamonds), and the inferred mafic and silicic mixing endmembers (black and green stars, respectively) derived by Adams et al. (in review). The figure allows an estimate of the ^{87}Sr/^{86}Sr compositions of the melt inclusions (not yet measured) using whole rock trends and melt inclusion major element compositions. The grey shaded region is the range of SiO_2 and K_2O values observed in the MIs of this study. The thick grey line within grey shaded region is the average MI value. The dashed line is a best fit line through the ALIA-D115 lavas, which is shown to illustrate an extension of this mixing array into the MI composition space (grey shaded region). The dashed line meets the average MI value at a ^{87}Sr/^{86}Sr value of ~0.729 for both the SiO_2 and K_2O plots. This value is slightly lower than that calculated by Adams et al. (in review) of 0.7316.

We have considered and rejected the hypotheses that the MI chemical variation was generated either by PEC or PED, leaving us with the hypothesis that the Si-rich nature observed in the MIs was present upon capture of the MIs. If the MIs are in fact melts that ultimately derived from an EM2 source, what process(es) has controlled their composition? There are two obvious potential options that could explain the observed variability: 1) the EM2-derived liquids began as mafic primarily liquids that experienced significant fractional crystallization prior to entrapment and the MIs were captured by growing clinopyroxene, or 2) the MI formed as a result of partial melting, to different degrees (strongly affecting the trace element compositions), of the EM2-derived source directly, with little subsequent pre- or post-entrapment fractional crystallization (i.e., the primary mantle melts were silicic). In reality it's likely a combination of both, but a few points seem clear: 1) the variability and enrichment in LREEs compared HREEs is indicative of garnet in the petrogenesis of the melt inclusions (Figure 2), and 2) if the melt inclusions were a result of originally mafic melts that underwent significant fractional crystallization, we expect that their trace element signatures would reflect this process. Trace element compositions in Figure 2 shows that the MIs exhibit depletions in Nb and Ti, which could be related to removal of Ti-rich phases, like ilmenite, during crystallization after partial melting from the source. In addition, the MIs are depleted in Sc (Supplementary Dataset S5) relative to the ALIA-D115 lavas (Jackson et al., 2007), suggesting that they could have had significant clinopyroxene removal as well. Both seem reasonable, as ilmenite and clinopyroxene are common phases in the ALIA-D115 lavas. However, another very common phase in the ALIA-D115 lavas is plagioclase, which is not observed in any of the MIs of this study. If the MIs had undergone significant differentiation prior to entrapment, plagioclase would likely have been removed, but this is certainly not the case as the MIs are quite enriched in Sr; while some inclusions exhibit negative Sr anomalies—the hallmark of plagioclase crystallization—many do not (showing either a positive anomaly or no anomaly; Figure 2). This suggests that plagioclase removal is not responsible for the high silica nature of the inclusions. Thus, it seems as though hypothesis 1 is not supported by all of the observations, and perhaps does not fit the MI geochemistry. Alternatively, if the trachytic liquids in the MIs are a result of partial melting of a hybridized source (i.e., the primary mantle-derived melts were trachytic), how have these liquids survived without reacting with the surrounding peridotite mantle during ascent through the asthenosphere and oceanic mantle lithosphere?

There are a few possibilities that could explain the origin of the trachytic MIs. One of perhaps the simplest explanations is that they are derived from partial melting of a sediment or sediment-enriched source. These melts then mix with more primitive Samoan basaltic melt (derived by partial melting of peridotite) to create the ALIA-D115 mixing trend. Problematically, this requires silicate melts to remain isolated from the ambient ultramafic mantle—including during ascent through >60 km of Pacific mantle lithosphere—until the time of mixing with the basaltic magmas in shallow magma chambers. As is well known, siliceous melts are highly reactive with ultramafic bulk compositions. Nevertheless, there is evidence that such processes could occur. Mantle xenoliths found in alkali basalts from Tallante, Spain show isolated high-silica veins (quartz-diorites) that are interpreted to be the result of slab melts. These melts were isolated from the surrounding mantle through an initial reaction between the silicate melt and olivine that generated an orthopyroxene reaction barrier at the contact between the silicic melts and the peridotite wall rock (Arai et al., 2003; Bianchini et al., 2011, 2015; Shimizu et al., 2004). However, the Tallante xenoliths record a process that occurred at the cm-scale. In order for the process to operate to transport trachytic liquids out of the mantle source, it would have to operate on a much larger scale, allowing the trachyte liquid+peridotite reaction to create opx-rich wall rock to buffer the silicate melts, allowing them to be transported >60 km through the peridotite oceanic mantle lithosphere without completely reacting with the surrounding peridotite. However, if this process did occur at Samoa, then why do we not see these silicic primary liquids erupted at other hotspot locations, like Hawaii, where partial melting of Si-saturated eclogite yields Si-rich liquids (Hauri, 1996; Sobolev, 2007; Sobolev et al., 2000, 2005; Yaxley & Sobolev, 2007)?

Another explanation for the formation of the trachytic MIs is a scenario in which ancient recycled sediment, captured by the Samoan plume source, partially melts and fertilizes the surrounding mantle to form a hybridized peridotite + sediment mixture. Thermodynamic phase equilibria modeling by Adams et al. (in review) of various hybrid peridotite + sediment bulk compositions suggests that the partial melts are basanitic to phonolitic (depending on the extent of melting) and that subsequent differentiation of these melts does not lead to trachytic liquids. nevertheless, the exploratory model space is quite large and these models capture a small parameter space in terms of starting compositions, pressures, percentage of source melting prior to differentiation, etc. Some experimental studies however that show partial melting of hybridized peridotite+sediment-like bulk compositions can in fact produce trachytic liquids similar to the MIs of this study (Gao et al., 2019; Wang et al., 2017). However, the same problem remains as noted above: how are silicic liquids transported through the peridotitic mantle lithosphere to the surface without reacting with the wall rock?

Lastly, there is evidence that the EM2 source beneath Samoa has been enriched not only by addition of sediments, but also carbonatitic melts (Ashley, 2019; Ashley et al., 2020; Hauri & Hart, 1994; Hauri et al., 1993). Evidence for carbonatite metasomatism is clearest in Samoan mantle peridotite xenoliths that show LREE enrichment and Zr and Ti depletions in clinopyroxene (Hauri et al., 1993; Hauri and Hart, 1994). More recently, Ashley et al. (2020) performed an analysis of water systematics and major and trace element systematics on Samoa peridotite xenoliths, focused on orthopyroxene, revealing variable depletions in water contents of nominally anhydrous minerals (e.g., orthopyroxene) and their trace element characteristics are indicative of metasomatism of carbonatitic and silicate liquids. Further, previous studies have suggested that partial melting of mantle enriched with carbonatitic liquids can result in phonolitic to trachytic liquids (Hauri et al., 1993; Tsuno and Dasgupta, 2011; Ashwal et al., 2016; Loges et al., 2019). Hauri et al. (1993) found rhyolitic-trachytic glass (69% SiO_2, 8% total alkalis; see main text Figures 3 and 6 for plotted compositions of the glass) hosted in a carbonatite metasomatized peridotite xenolith from the Samoan island of Savai'i—the same volcano that erupted the ALIA-D115-18 melt inclusions examined here—which they interpreted to be a partial melt of carbonated peridotite. Critically, this liquid has high $^{87}Sr/^{86}Sr$ (0.712344) and is similar in major element composition to the MIs of this study, further suggesting a role for carbonatitic metasomatism in the origin of EM2 and supporting the presence of high silica melts in the mantle. An important question is whether sufficient trachytic melt can be generated in metasomatic peridotites, and sequestered into crustal magma chambers, to give rise to the Si-rich Samoan EM2 endmember lavas and the trachytic melt inclusions they host.

5 Conclusions

Three important questions were raised in this work: 1) Have the MIs been significantly modified by post-entrapment processes, 2) how are the MIs related to their host whole rock and the other ALIA-D115 lavas, and 3) what is the origin of the MIs? We show that the MIs have not been modified significantly by post-entrapment processes and thus, could represent liquids derived directly from an EM2 source. In both major and trace element compositions, the MIs lay at one end of the ALIA-D115 mixing array, suggesting that the MIs are the silicic and high $^{87}Sr/^{86}Sr$ mixing endmember with an affinity to EM2, consistent with previous studies suggesting that the EM2 mixing endmember beneath Samoa is highly evolved and enriched (high in $^{87}Sr/^{86}Sr$). Projecting the ALIA-D115 mixing trend in $^{87}Sr/^{86}Sr$ versus SiO_2 and $^{87}Sr/^{86}Sr$ versus K_2O plots shows that the trend intersects the average MI composition at $^{87}Sr/^{86}Sr$ values of about 0.729 (consistent for both SiO_2 and K_2O), close to the independent value predicted by Adams et al. (in review) of 0.7316.

The origin of the MIs is not completely clear, but their trace element variability is most consistent with the presence of garnet in their source. Trace element signatures suggest the MIs may have undergone some fractionation prior to entrapment in the clinopyroxenes, but the current composition of the MIs suggests that plagioclase should also have been removed, and it very clearly has not. Alternatively, the MIs could be representative of melts derived directly from the EM2 source with little pre-fractionation prior to entrapment. Further partial melting thermodynamic calculations of potential EM2 source compositions as well as laboratory studies of partial melting of various mafic and ultramafic sources subject to sediment addition or modification by metasomatism should be explored to understand the formation of these trachytic melt inclusions. It is clear that these MIs offer a unique snapshot into the complex history of EM2 magma genesis beneath Samoa.

Chapter 3: A thermodynamic solid solution model for (Ca, Fe, Mg)$_3$Al$_2$Si$_3$O$_{12}$ garnets relevant to high pressure igneous systems

1 Introduction

Garnets capture significant petrological, geochemical, and geochronological information during their growth over a wide range of pressure (P)-temperature (T) conditions and compositions (X). Unsurprisingly, many studies over the last few decades have attempted to quantify the thermodynamic and diffusive properties of garnet crystalline solutions for implementation in phase equilibria and transport models with applications to geothermometry, geobarometery and geospeedometry (e.g., Ganguly and Saxena, 1984; Dasgupta et al., 2004; Tirone et al., 2005; Dasgupta et al., 2009; Ganguly, 2010 and references therein). Garnet group minerals can accommodate many different cations with a range of size and charge allowing for stability over a wide range of P-T-X conditions.

The general garnet formula is typically represented as $X_3Y_2Z_3O_{12}$ with eight formula units in the unit cell. There are three kinds of coordination polyhedra in the garnet structure at low to moderate pressure. The X-cation (Ca, Mn, Fe^{+2}, Mg with minor Y and Na) is coordinated by eight oxygens in a triangular dodecahedron arrangement, the Y-cation (Al, Cr, Fe^{+3} with minor Ti^{+4}, Fe^{+2} and Si) is in six-coordination with oxygen as distorted octahedrons and the Z-cations (Si with minor Al, Ti, Fe^{3+}, Fe^{2+}) are four-coordinated with oxygen in a distorted tetrahedron. In this study, attention is focused on the thermodynamics of multi-component garnet crystalline solutions. Earlier thermodynamic studies have quantified garnet models of binary systems (e.g., **pyrope-grossular**: Ganguly and Kennedy, 1974; Hensen et al, 1975; Green et al., 2012a, **spessartine-grossular**: Koziol and Newton, 1987, **almandine-grossular**: Cressy, 1978, **almandine-spessartine**; Powenceby et al., 1987), ternary garnets (e.g., pyrope-grossular-almandine; Berman and Koziol, 1991, Berman and Aranovich 1996, Mukopahdyay et al., 1997, White et al., 2014) or quaternary garnets (e.g., spessartine-pyrope-grossular-almandine; Berman, 1990, Ganguly et al., 1996). A few other studies also quantify >4 endmember garnets (e.g., Holland and Powell, 1998, 2011, Holland et al., 2013; White et al. 2014; Jennings and Holland, 2015). The range in calibration conditions in P-T-X space of each of the above-mentioned garnet solution models are highly variable and this makes comparisons difficult or impossible in some cases.

Despite research on garnet stability for almost a century (Menzer, 1928), a robust multi-component solid solution model is not available for high-temperature *igneous* systems. In particular, phase equilibria experiments used in constraining previous garnet solution parameters rarely involve interactions with silicate liquids, meaning most experimental constrains were sub-solidus, univariant reaction experiments. The experimental constraints also capture only a limited range in garnet composition as a function of pressure and temperature. This is a major problem when trying to quantify garnet phase equilibria at temperatures and pressures in which liquid coexists with garnet, which are the pressures and temperatures directly relevant to igneous processes. Holland et al. (2013) have more recently taken the approach of using experimental data and regression techniques to constrain a high-pressure model of garnets in the Na_2O-CaO-FeO-MgO-Al_2O_3-SiO_2 system specialized for ultramafic to mafic compositions, but this model is tuned to high pressures and low silica compositions and is only applicable to sub-solidus reactions. Recent garnet solid solution models by White et al. (2014) and Jennings and Holland (2015) do contain some liquid-present data, but the White et al. (2014) asymmetric model calibration is really geared towards metamorphic pressure and temperature conditions, include ferric Fe, and is focused on metapelitic bulk compositions, while Jennings and Holland (2015) is a 5-component, symmetric regular solution model focusing on peridotite melting down to the transition zone. A ternary garnet model constrained at melt present conditions (relevant to igneous systems) over a broad range of temperatures and pressures is not yet available and is the objective of this study.

Extant garnet solid solution models are not in agreement in terms of their endmember excess Gibbs energy interaction parameters and hence component activity coefficient values (e.g., Geiger, 1999; Holdaway et al., 2000). They utilize different calibration methods (e.g., mathematical programming, MINUIT optimization, weighted regression, regularization) and types of data (e.g., phase equilibria experiments, reversed equilibria experiments, equilibrium displacement reactions). Perhaps most importantly, none of the previously published models (with the exception of Mukhopadhyay et al., 1997), quantify errors on the endmember excess Gibbs energy solution parameters.

Silicate liquid-present sxperiments used in this study are derived from the Library of Experimental Phase Relations (LEPR) to form a comprehensive calibration dataset with greatly improved coverage in pressure, temperature, and composition space. This database allows us to calibrate a garnet solid solution model specifically designed for high-temperature (T>900 K) and high-pressure (0-4 GPa) phase equilibria applications in igneous systems. The current study is the first of a two-part study on garnet solid solution thermodynamics. In this study, a 3-component, ternary garnet model of Ca-Mg-Fe garnets is developed and calibrated. In the second study, a seven-component garnet model in the system MgO-FeO-CaO-MnO-Al_2O_3-Cr_2O_3-TiO_2-SiO_2 is developed. The value of performing a ternary garnet solid solution model prior to the 7-component system is to take the large amount of ternary garnet-specific experimental data and gain a better understanding of existing limitations of ternary garnet models, with a special focus on resolving some substantial disagreements. Additionally, many natural garnets, and experimental garnets, lie close to or fall within the ternary garnet system Mg-Ca-Fe (pyrope-grossular-almandine). Equipped with the large amount of new phase experimental data now available, we are inclined to first derive a better solution model for ternary garnets, which then forms the foundation for a robust 7-component solid solution model.

Calibration of our newly developed ternary garnet solution model combines the latest melt-present phase equilibria experiments (in contrast with previous studies that rely primarily on sub-solidus experimental constraints), thermophysical data, and Bayesian statistical techniques. Bayesian statistics provides methods for combining uncertainties from a variety of sources—including experimental, standard state, and thermophysical data used in model calibration yielding a robust approach to thermodynamic solution model calibration. Ultimately, the goal of performing this new calibration is to improve the accuracy of garnet stability in thermodynamic modeling software, particularly the MELTS algorithm (Ghiorso and Sack, 1995; Ghiorso et al., 2002; Gualda et al., 2012; Ghiorso and Gualda, 2015).

2 Asymmetric solution model formulation for ternary garnets

In this study, we adopt a 3-component, asymmetric (sub-regular) solution model for the garnet crystalline solution following the Margules formulation. The importance of using an asymmetric solution model derives from the fact that previous studies have shown asymmetry in the miscibility gap along the pyrope-grossular binary in addition to the potential for short-range ordering along (e.g., Bosenick et al., 1995, 1999, 2000; Dachs and Geiger, 2006; Vinograd and Sluiter, 2006), requiring asymmetric solution terms. For clarity, each binary is treated as a sub-regular solution and no ternary terms are included in the excess Gibbs energy expression below. We must quantify the energy, volume, and entropy of interactions between different cations in terms of the excess Gibbs free energy. Focusing on just a binary (relevant to the final solution formulation of this study), the following formulations apply:

$$G_{real} = G_{ideal} + G^{EX} \tag{1}$$

where,

$$G_{ideal} = \sum X_i G_i^o + RT \sum X_i ln X_i \tag{2}$$

and

$$G^{EX} = \sum_{i \neq j} X_i X_j \left(W_{G_{ij}} X_i + W_{G_{ji}} X_j \right) \qquad (3).$$

W_G is described as:

$$W_G(P,T) = W_H(1\ bar, T) - T W_S(1\ bar, T) + W_v \Delta P \qquad (4).$$

Combining equations (3) and (4) gives a means of relating the Margules parameters (W) and G^{EX}, and W_G can be retrieved by fitting the phase equilibria data to extract the Margules coefficients. The Margules parameters define the equation that describes G^{EX} as a function of pressure, temperature, and composition. Activity coefficient expressions for each component are related to the Margules parameters as well. For the complete formulation of ternary garnets, the explicit form of G^{EX} and activity coefficient expressions are included in Appendix S3.

3 Comparison of existing ternary garnet models.

Four ternary garnet solid solution models calibrated in the 90's, related to igneous systems, are compared below (Berman and Koziol, 1991; Berman and Aranovich, 1996; Ganguly et al. 1996; Mukhopadhyay et al., 1997). These solution models are in poor agreement with one another (e.g., Geiger, 1999; Holdaway, 2000). Perhaps more importantly, all of them use phase equilibria constraints that focused on sub-solidus reactions only at narrow pressure-temperature-composition conditions. As an example, all models, except Berman and Aranovich (1996), use the GASP (**GA**rnet-**S**ilica-**P**lagioclase) univariant reaction of 3 anorthite = grossular + 2 Kyanite + quartz as a constraint for determining solution parameters. This was the only reaction used as a constraint in Ganguly et al. (1996), along with calorimetric measurements, to formulate the solution parameters. In addition, many previous studies focused on experiments constraining binary garnet compositions only (e.g., almandine (Fe)- pyrope (Mg) garnets), and few constrain garnets with the pyrope (Mg), grossular (Ca), and Almandine (Fe) endmembers. In addition, no previously published models take into account prior constraints on the garnet excess solution parameters, such as the excess volumes for each binary, which are fairly well constrained today, and any ternary garnet solution model should be consistent with these data.

Berman (1990) is one of the earlier models constraining binary interaction parameters in the Ca-Mg-Fe garnet system. Berman (1990) uses mathematical programming techniques to analyze reversed phase-equilibrium data in conjunction with calorimetric and volumetric data of garnets. There are five reactions constraining the phase equilibrium of garnets at a narrow range of pressure, temperature, and compositions space, but the author uses these data in conjunction with standard state properties of Berman (1988) and an asymmetric solution model formulation to constrain binary interaction parameters only (i.e., Ca-Mg, Ca-Fe, Fe-Mg), and includes no ternary interaction terms. Berman & Koziol (1991) build on earlier work by seeking the effects of ternary mixing parameters on the binary parameters. Berman & Koziol (1991) again used reversed equilibrium data, but on an anorthite breakdown reaction (Koziol and Newton, 1989). New binary mixing properties were determined, but a ternary solution parameter could not be well-constrained.

Unfortunately, these solution parameters are again based on data within a very limited range of P-T-X space. In later work, Berman & Aranovich (1996) used a more refined approach, applying mathematical programming techniques to 15 garnet-bearing experiments (univariant reactions) and thermophysical data to constrain ternary garnet mixing parameters in the P-T range of 0.1–4.5 GPa and 700-1400 ^{o}C. In addition to extracting garnet solution parameters, endmember thermodynamic properties from model fitting were also extracted. This was an improvement over previous techniques, but the experimental database was still quite limited and this approach did not allow for incorporation of errors on experimental measurements or standard state properties. Ganguly et al. (1996) produced a garnet solution model constraining binary garnet mixing parameters based on experimental data and standard state data from Berman (1990). These workers used approximately 34 new experiments at a range of Fe-Mg-Ca garnet compositions, pressures (2.4-4 GPa), and temperatures (1000-1400 ^{o}C). Lastly, Mukhopahdhyay et al. (1997) published an additional model for garnet solution parameters but did not incorporate the new standard state properties of Berman & Aranovich (1996). Instead, they used standard state values from Berman (1990) and different experimental phase equilibria data. The advantage of the Mukhopahdhyay et al. (1997) model was the use, for the first time, of weighted regression techniques on about seven garnet-bearing experiments allowing for incorporation of uncertainties on garnet solution parameters, a feat not achieved in earlier work. However, only one of the seven experiments constrained ternary garnet compositions while all others only constrained binary garnet endmembers.

In summary, the previously published garnet models use variable types and a limited amount of data to calibrate ternary models over a range of P-T-X conditions, likely explaining the disagreement between them. The ternary garnet model of this study aims to use the newest, liquid-bearing, garnet phase equilibria, standard state, and thermophysical data to calibrate a self-consistent solid solution model. The approach in this study uses Bayesian statistical techniques to incorporate known data constraints (as described below) in the model fitting procedure and provides robust uncertainties on the final garnet solution parameter values.

4 Data constraints

4.1 Phase equilibria experiments

The experimental garnet phase equilibria data published before 2011 used in this study come from the Library of Experimental Phase Relations (LEPR) database (the last time the database was updated). Experiments performed after 2011 were added manually to the dataset. The data and references to all of the experiments used to calibrate the model of this can be found in Supplementary Dataset S8. The data were filtered based on a number of criteria: phase equilibria experiments were removed if (1) the oxide totals for liquids or solids present were less than 98%, (2) there was no reported oxygen fugacity, and (3) if the garnet compositions contained more than 5% non-ternary garnet components, in order to limit projecting non-ternary garnets into the ternary space. After filtering, the total number of acceoptble experiments was 192 (out of 950), with 54 being liquid-present reactions and 138 being sub-solidus reactions involving garnet (both types of reactions involve garnet in addition to other solid phases). The experimental temperatures and pressures range from ~600-1600 ^{o}C and ~0.2 to 4 GPa, respectively and the spread of ternary garnet compositions covered by the experiments, color-coded by the experimental pressure, is shown in Figure 1. Figure 2 shows the range of experimental starting compositions.

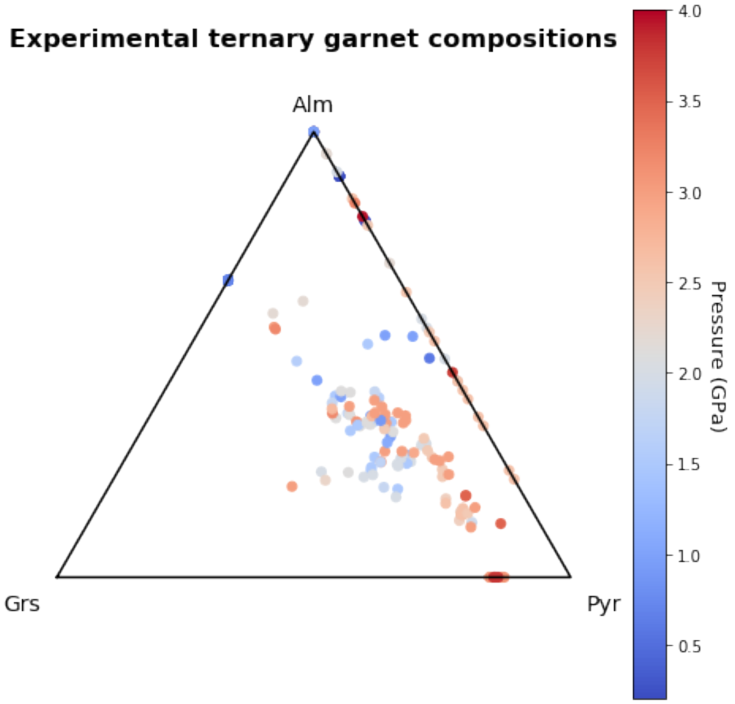

Figure 1. Ternary garnet compositions of experiments used in this study for the model calibration. There are 54 total experiments and each point represents the garnet composition for an individual experiment and are color coded by the experimental pressure. Hot colors are high pressures (>2 GPa) and cold colors are low pressures (<2 GPa). Each experimental garnet composition is >95% ternary composition (i.e., Mg (pyrope) -Fe (Almandine) -Ca (grossular)). Abbreviations are as follows: Grs = grossular (Ca), Pyr = pyrope (Mg), and Alm = almandine (Fe).

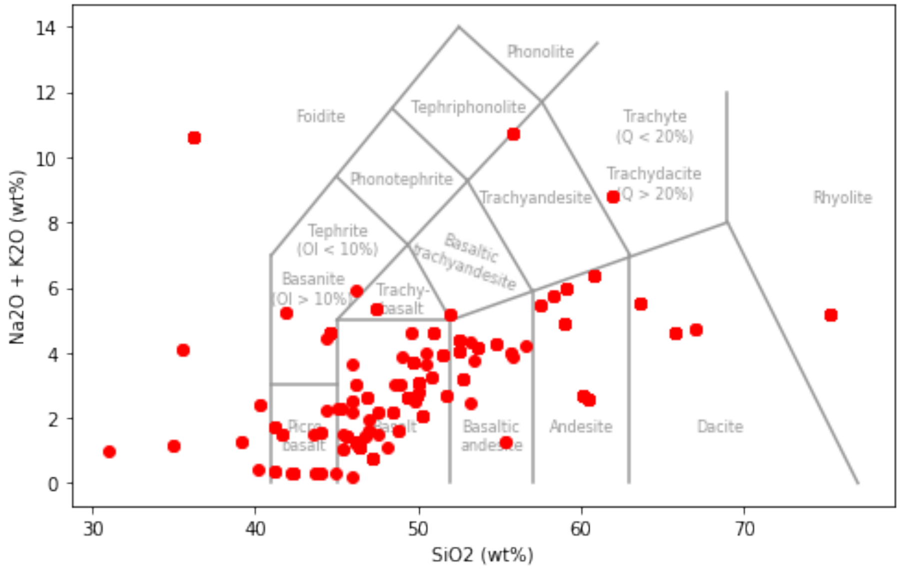

Figure 2. Total alkali vs Silica diagram showing starting bulk compositions for each experiment (n=54) used in this study. The complete starting bulk compositions and experimental data references can be found in Supplementary dataset 1.

4.2 Endmember standard state properties and binary excess enthalpies

All of the affinity calculations described above are based upon equations (1-4) above with specified standard state thermodynamic properties (e.g., enthalpy, entropy, volume, heat capacity) of each garnet endmember. We chose to use standard state properties derived from the Berman and Aranovich (1996) thermodynamic database as it is self-consistent with the MELTS liquid model, is robust in terms of their derivation procedure, and is consistent with experimental observations. They also used the broadest set of univariant reactions to constrain their model parameters in terms of P-T-X space. The self-consistency with the MELTS model allows us to make a direct comparison of the garnet model of this study to the model currently used in the MELTS algorithm.

4.3 Binary excess volume data

Binary excess volume properties of garnets have been studied extensively, particularly for the almandine, grossular, and pyrope binary joins (e.g., Newton et al., 1977; Geiger et al., 1987; Wood, 1988; Ganguly et al., 1993; Ungaretti et al., 1995; Bosenick et al., 1995, 1996; Bosenick and Geiger, 1997; Geiger and Feenstra, 1997; Geiger, 1999, Vinograd and Sluiter, 2006; Dachs and Geiger, 2006; Freeman et al., 2006; Hamecher, 2013; Hamecher et al., 2013; Du et al., 2015, 2016). This information is extremely valuable because it constrains the changes in volume, and therefore the pressure-derivative deviations from ideality, along the binaries. This is crucial for calculation of high pressure, high temperature phase equilibrium. The deviations from ideality are most likely the result of large cation size differences on the dodecahedral site for garnets (Du, 2011; Freeman et al., 2006).

In previous studies, excess volume parameters have been constrained experimentally using piston-cylinder, multi-anvil, or diamond-anvil techniques and measured using powder XRD methods (Newton et al., 1977; Geiger et al., 1987; Wood, 1988; Koziol, 1990; Ganguly et al., 1993; Bosenick et al., 1995, 1996; Bosenick and Geiger, 1997; Geiger and Feenstra, 1997; Geiger 2000; Dachs and Geiger, 2006) or using computational modeling techniques (Berman, 1990; Ganguly et al., 1996; Mukopahdyay et al., 1996; Berman and Aranovich, 1996; Bosenick et al., 2001; Ungarettie et al., 2005; Vinograd and Sluiter, 2006; Hamecher, 2013). In general, there is agreement among these studies that there is a positive deviation from ideality in terms of volume for the pyrope-grossular and almandine-grossular join, while the pyrope-amandine join is nearly ideal (no excess volume of mixing). The near-ideality of the pyrope-almandine join is rationalized by noting that Fe^{2+} an Mg^{2+} have very similar ionic radii, while the difference between the atomic radii of Ca^{2+} and Mg^{2+} and Fe^{2+} is quite large.

A robust synthesis of previous work on garnet volumes and a model calibration constraining excess volumes with errors for the pyrope-grossular and almandine-grossular joins (using 766 experimental data points) was performed by Hamecher (2013). We chose to use their binary almandine-grossular excess volume and uncertainty as a constraint on the model fit of this study. The contemporaneous evaluation of excess garnet volume along the pyrope-grossular join by Du (2011) and Du et al., (2015, 2016) were not taken into account by Hamecher (2013), but provide new and important information on the pyrope-grossular excess volume constraint. Both studies predict non-ideal, asymmetric positive excess volumes of mixing (see Table 1 for excess volume prior values), but the Du (2011) and Du et al. (2015, 2016) values are about three times larger and we propose they are more robust as they were experimentally derived and immiscibility along this join was directly observed in their experiments. Therefore, for the pyrope-grossular excess volume and uncertainty constraint, we chose to follow Du (2011) and Du et al. (2015, 2016). For the pyrope-almandine join, we use the value of Geiger and Feenstra (1997), as they are the only authors to constrain an excess volume and uncertainty for this binary join.

Table 1. Description and range of prior values used in model fitting procedure. For a full explanation of "priors", see section 5.1.

Prior	Description	Prior value	Uncertainty (or range of values tested)[c]
Exchange reaction affinities	Affinity calculated considering an exchange reaction of ions between each garnet endmember and the liquid reaction phases (e.g., Fe^{2+} - Mg^{2+} exchange between garnet and the liquid)	N/A	5–100 kJ
Saturation reaction affinities	Affinity calculated considering the solid and liquid are in complete equilibrium	N/A	5–100 kJ
Wh_{ij}[a]	Enthalpy of mixing	N/A	10-100 kJ/mol
ΔWh_{ij}	Enthalpy of mixing perturbation	N/A	1-10 kJ/mol
Wv_{12}[b]	Volume of mixing for the almandine-grossular binary	0.1073 J/bar	0.05-0.0893 J/bar
Wv_{13}	Volume of mixing for the almandine-pyrope binary	0 J/bar	0.005 J/bar
Wv_{23}	Volume of mixing for the grossular-pyrope binary	0.1 J/bar	0.01-0.1 J/bar
Critical point temperature	Highest temperature on the solvus. Prior value here is the average value of the range provided by the many studies evaluating garnet miscibility. See text for more details	873 K	10-200 K
Critical point almandine composition	Fraction of almandine in the critical point composition, which is the composition at which the critical point occurs.	0	0.03 (3% almandine endmember)
Univariant reaction temperature	The midpoint temperature of the experimental reaction performed by Bohlen et al. (1983a).	1173 K	10-100 K
Univariant reaction slope	dP/dT of the experimental reaction boundary of Bohlen et al. (1983a).	0.14	0.01-0.001

[a] Subscripts i and j refer to arbitrary endmember garnet binaries (e.g., i and j could refer to the almandine-pyrope binary)
[b] subscripts 1, 2, and 3, refer to the distinct garnet endmember almandine, grossular, and pyrope, respectively.
[c] See Appendix S3 Table A1 for final uncertainty values in the final model fit.

4.4 Ternary garnet miscibility gap constraints

The excess volume constraints described above are important because they dictate garnet immiscibility at temperatures and pressures that are relevant to igneous processes. Thus, in addition to constraining excess volumes, we must also ensure that our model captures the known behavior of garnet immiscibility. Many studies have evaluated garnet immiscibility mainly along the pyrope-grossular binary. Mixing on the pyrope-almandine binary likely deviates little from ideality and is not expected to exhibit immiscibility, especially at temperatures relevant to this study as previously noted (Hensen et al., 1975; Geiger and Feenstra, 1997; Geiger, 1999; Lavrentiev et al., 2006; Hamecher, 2013). Although Ganguly and Kennedy (1974) suggest a miscibility gap could exist along the pyrope-almandine join, the critical temperature of ~ 479 +/- 63 °C, is much lower than magmatic values and are outside the range pertinent to this study. The almandine-grossular join has received considerably less attention than the pyrope-grossular join and thus, no miscibility gap has been firmly established along this join. Cressey (1978) suggest a solvus may exist along the almandine-grossular join but, again, it is likely at temperatures much lower than magmatic temperatures. Ganguly et al. (1996) modeled ternary garnet immiscibility and suggests that immiscibility occurs in almandine-poor garnets, which is consistent with the study of Wang et al. (2000), which is the only study to definitively demonstrate garnet immiscibility in a natural sample, and suggests that immiscibility occurs in garnets with $X_{alm} < 0.14$-0.19 at temperatures between 400 and 600 °C. There are many studies evaluating the miscibility gap along the grossular-pyrope join, but predicted critical temperatures are not in agreement. There is *some* agreement on the following: 1) immiscibility can occur at magmatic temperatures relevant to this study, 2) immiscibility is pressure dependent, and 3) the solvus is asymmetric. Given the availability of data, we focus here on constraining only the miscibility gap related to the pyrope-grossular join.

The critical temperatures predicted for the pyrope-grossular join by various studies are highly variable and have been predicted using different methods, like theoretical modeling, the use of calorimetry and volume data, or by experimental synthesis of garnets to measure excess volumes and/or observe exsolution. In a binary crystalline solution of components pyrope (pyr) and grossular (grs), the variation of the chemical potential of the pyr component as a function of composition in a *symmetrical* regular solution is given by

$$\mu_{pyr} - \mu^{*}_{pyr} = nRT\ln(1 - X_{grs}) + nW_G X^2_{grs} \tag{5}$$

The critical temperature, and its variation with T and P can be determined by differentiating equation (5) with respect to composition and setting the resulting expression equal to zero. This gives the critical temperature

$$T_c = \frac{2W_G X_{gr}(1 - X_{gr})}{R} \tag{6a}$$

Since, for a symmetric regular solution the consolute point occurs at X_{gr}=0.5, equation (6a) simplifies to

$$T_c = \frac{W_G}{2R} \tag{6b}$$

The variation of T_c with T and P are given by

$$\left(\frac{\partial T_c}{\partial p}\right)_T = \frac{W_V}{2R} \quad \text{and} \quad \left(\frac{\partial T_c}{\partial T}\right)_p = \frac{-W_S}{2R} \tag{7}$$

These expressions are useful in relating the critical temperature to the Margules parameters. For a sub-regular solution, the method remains the same although equation (5) is modified to include two distinct Margules parameters. Details of computing the critical temperature and composition for a binary sub-regular solution may be found in Thompson and Waldbaum (1969) and are not repeated here for brevity.

Ganguly and Kennedy (1974) use a mix of theoretical calculations and high-pressure experimental constraints for the reaction: pyrope + grossular → $\text{garnet}_{(\text{solid solution})}$ to predict a critical temperature along the pyrope-grossular binary of 694 +/- 55 °C and an absolute upper limit of the critical point of 750 °C at 4 GPa. Hensen et al. (1975) predict a critical temperature of 629 +/- 90 °C by experimentally constraining activity coefficients for grossular in a mixed pyrope-grossular garnet using a divariant reaction assemblage at 1.5-2.1 GPa. Haselton and Newton (1980) use calorimetric and volumetric activity formulae to constrain the critical temperature from 1 bar to 6 GPa and show a range of critical temperatures from ~430 °C (1 bar) to 1300 °C (6 GPa) that shift towards increasing pyrope contents with increasing pressure. In contrast, Berman and Aranovich (1996) predict critical temperatures that are essentially insensitive to changes in pressure. These authors determined experimentally the equilibrium displacement of the reaction: Grossular + 2 Kyanite + Quartz = Anorthite as a function of garnet composition. Results of this experimental study along with other observational and experimental data from the literature were used to determine binary garnet mixing parameters. Using these newly derived thermodynamic parameters, Berman and Aranovich (1996) quantified binary and ternary miscibility gaps showing a pyrope-grossular critical temperature of ~625 °C at 4 GPa and a composition of approximately $Py_{70}Grs_{30}$ and they show a very negligible pressure dependence of the critical temperature. The reason for the pressure dependence discrepancy between the work of Aranovich and Ganguly (1996) and Haselton and Newton (1980) is a difference in the volumetric properties used. Dachs and Geiger (2006) suggest a critical temperature in the range of 850-1300 °C at a composition of ~$Py_{65}Gr_{35}$ using experimentally derived heat capacity measurements on a range of pyrope-grossular garnet compositions; these authors also show no pressure dependence. Vinograd and Sluiter (2006) perform lattice dynamics calculations and Monte Carlo simulations to constrain the volumes of mixing for pyrope-grossular and suggest critical temperatures that are pressure dependent and range from about 694 °C at 1 bar to 764 °C at 4 GPa with compositions ranging from $Py_{66\text{-}70}Grs_{30\text{-}34}$. Lastly, Du (2011) and Du et al. (2015, 2016) directly observed pyrope-grossular immiscibility experimentally by performing high-pressure (6 and 8 GPa) annealing experiments on a $Py_{65}Gr_{35}$ garnet composition. These workers observed garnet immiscibility at 8 GPa and 1200 °C confirming that the critical temperature must be greater than 1200 °C. Their experiments also demonstrated that the critical temperature at 6 GPa is between 1100 °C and 1200 °C consistent with the idea that critical temperature decreases with decreasing pressure. They also suggest that based on their results of excess volumes constrained experimentally, critical temperatures along the grossular-pyrope join increase from 0.5 to 4 GPa by about 100 °C, which is higher than the 30 °C change in critical temperature calculated by Ganguly and Aranovich (1996) and other published ternary garnet models over the same pressure change.

Figure 3 summarizes the literature critical temperature estimates discussed above including the calculated miscibility gap of the Berman and Aranovich (1996), Berman and Koziol (1991), Ganguly et al., (1996), and Mukhopadhyay et al., (1996) ternary garnet solution models. Although there is much uncertainty on the pyrope-grossular critical temperature, the general consensus of the most recent studies is that, at 1 bar, the critical temperature lays somewhere between about 450 and 700 °C. There is quite good agreement from all studies that the composition of the critical temperature is skewed towards pyrope-rich garnets at pressures from 1 bar to 8 GPa. Perhaps most importantly, some studies suggest a strong pressure dependence of the critical temperature, but most do not. We do not constrain this feature directly in our model fitting procedure, but instead chose to simply constrain the critical temperature at 1 bar, since there seems to be a general consensus on the temperature and composition at this pressure. Thus, considering the most recent and robust experimental studies, we set a prior critical point composition constraint that limits the amount of almandine present in the critical point composition at 1 bar to be less than 3% (since we are only focusing on the binary) and we set a critical point temperature value to approximately the average value of the above temperature range, at 600 ^{o}C, with an uncertainty ranging from 10-150 ^{o}C.

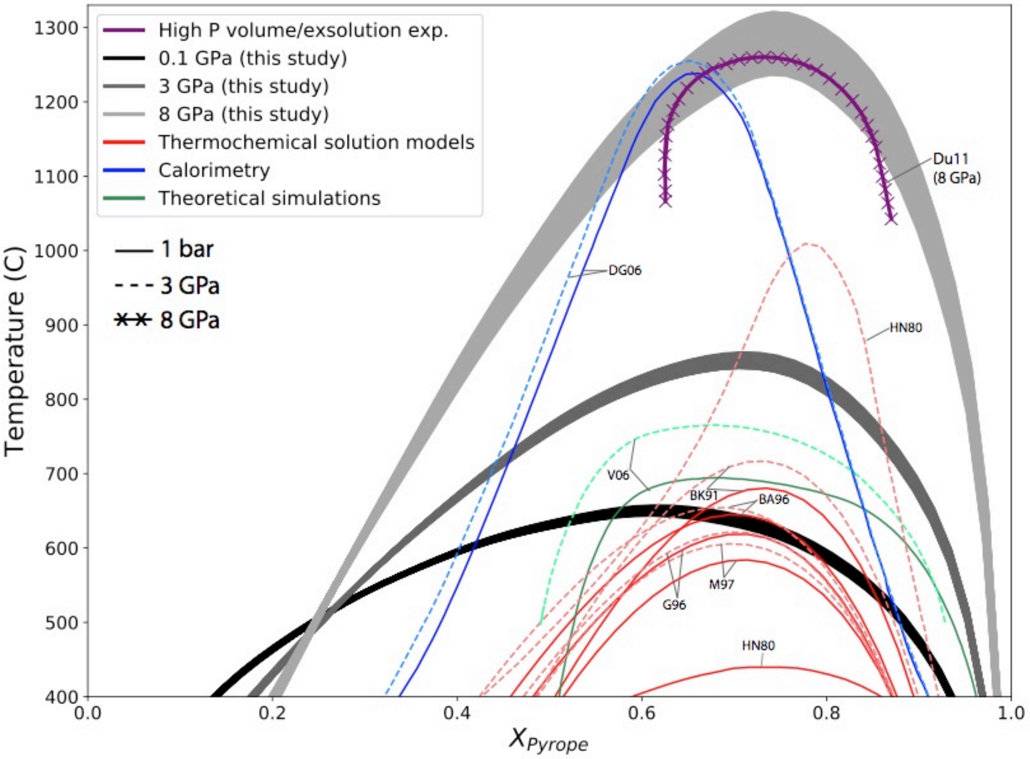

Figure 3. Calculated solvi (miscibility gap) along the pyrope-grossular binary join for the fitted model of this study at 1 bar, 3 GPa, and 8 GPa in comparison to previously published models. The fitted model is shown by the thick black (1 bar), dark grey (3 GPa), and light grey (8 GPa) boundaries, where the thickness of the regions are the 1 sigma uncertainties. The published models are shown for each pressure, if available, and are broken up into data type. The study plotted in dark purple is based on an experimental study using XRD in which unit cell parameters were measured and multi-anvil experiments were performed to directly observe immiscibility in garnets at 8 GPa. The studies plotted in red are all thermochemical solution models constrained using thermochemical and phase equilibria data. The blue solvi reflect calorimetric studies along the pyrope grossular join and the green study was derived via theoretical techniques using lattice dynamics

calculations and Monte Carlo simulations. Solid lines indicate a solvus calculation at 1 bar, dashed lines indicate 3 GPa, and the hatched line indicates 8 GPa. The 1 bar critical temperature and composition were the only data constraints imposed on the model fit of this study. Most notably, our model captures the strong miscibility gap pressure dependence suggested by Du (2011) and Du et al., (2015, 2016). Abbreviations are as follows: HN80=Hasleton & Newton, 1980; BK91=Berman & Koxiol, 1991; BA96=Berman & Aranovich, 1996; G96=Ganguly et al., 1996; M97=Mukhopadhyay et al., 1997; DG06=Dachs & Geiger 2006; Du11=Du, 2011.

4.5 Univariant reaction constraints

Another constraint imposed in this model calibration is the univariant equilibrium reaction of Bohlen et al. (1983a): Grossular ($Ca_3Al_2Si_3O_{12}$) + 2 Pyrope ($Mg_3Al_2Si_3O_{12}$) $\rightarrow$ 3 Anorthite ($CaAl_2Si_2O_8$) + 3 Fayalite ($Fe_2Si_2O_4$). This is a well-constrained reaction in the pressure-temperature range relevant to this study. The calculated equilibrium reaction using previous published ternary garnet models (i.e., Berman, 1991; Berman and Aranovich, 1996; Ganguly et al., 1996; and Mukhopadhyay et al., 1996) do not capture the low (<900 ^{o}C) and high temperature (>900 ^{o}C) regions of the univariant reaction well (see Figure 4). Thus, this reaction is used as a Bayesian ‘prior’ (see Methods below for discussion of Bayesian ‘priors’) in this study to ensure the model better captures the slope of this reaction in pressure-temperature space. We performed a least squares regression on the data presented in Bohlen et al. (1983a) to obtain a reasonable reaction boundary slope that averages the experimental data. We then imposed an uncertainty on this slope as well as constraints on the middle temperature of the P-T space to anchor the slope to the correct location. We imposed an uncertainty on the temperature based upon the experimental uncertainty of the reaction boundary temperatures of ± 10-50 ^{o}C. For information on the range of uncertainties and real values used as priors, see Table 1.

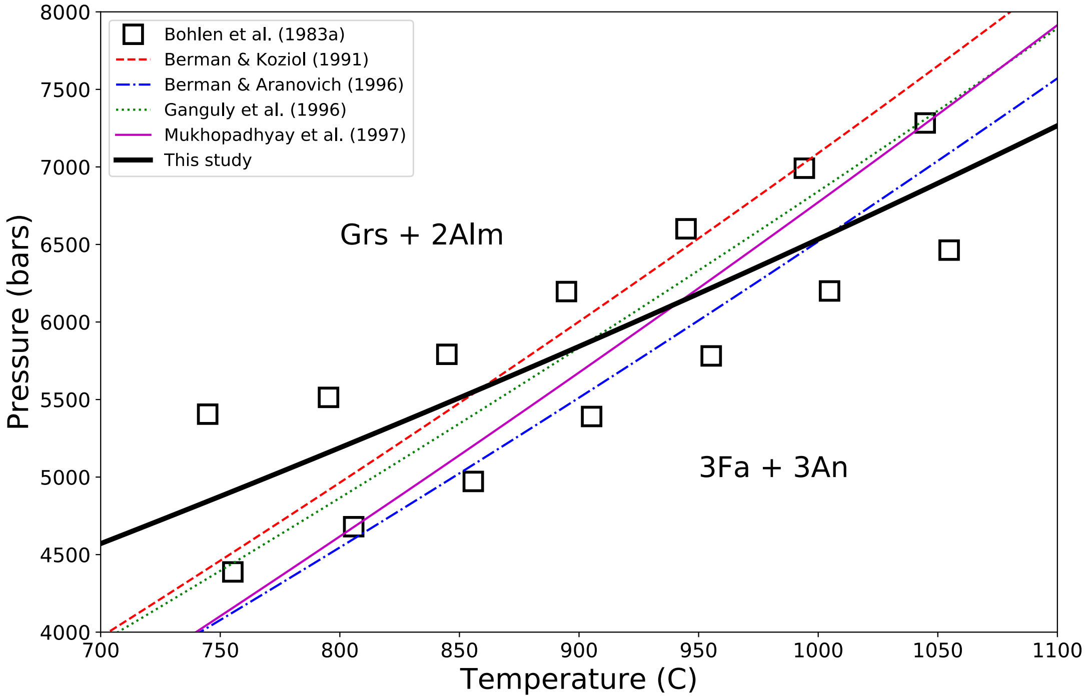

Figure 4. Calculated equilibrium reaction boundaries for the univariant reaction: Grossular (Grs) + 2 Almandine (Alm) →3 Fayalite (Fa) + 3 Anorthite (An) of Bohlen et al. (1983a). Experimental data points are denoted by unfilled squares. The following previously published model equilibrium reaction boundaries are calculated and plotted: 1) Berman and Koziol, 1991 (red dashed line), 2) Aranovich and Berman, 1996 (blue dot-dashed line), Ganguly et al., 1996 (green dotted line), and 4) Mukhopadhyay et al., 1997 (magenta line). The model fit of this study is shown by the heavy black line, where the uncertainty on the reaction boundary is shown by the thickness of the line. The reaction boundary was imposed as a constraint on the model fit of this study and is satisfied by the best fit model, which is the only model to capture the reaction slope in contrast with previously published models.

5 Methods

5.1 Bayesian statistical approach

Bayesian statistical methods offer a sophisticated generalized approach to deriving parameters and uncertainties that can be applied to crystalline solution models. This method uses prior knowledge, or probability distributions summarizing relevant data, to allow for a more accurate calibration and quantification of errors on the computed fit parameters. Bayesian statistical methods are used in this study to derive ternary garnet solution mixing parameters given existing data constraints and errors on available standard state properties, mixing parameters (W's – Margules parameters), experimental reactions involving garnet, and miscibility gaps within the ternary garnet system.

Bayesian statistics, as applied to parameter estimation, is used to determine the probability of a model given data constraints and prior knowledge on its parameters. Bayes' theorem is described as follows:

$$P(\vec{\theta}|\vec{d}) = P(\vec{d}|\vec{\theta}) \cdot P(\vec{\theta}) \ / \ P(\vec{d}) \qquad (5),$$

where $P(\vec{\theta}|\vec{d})$ (the posterior probability) is the probability of the model summarized by the vector of parameter values $\vec{\theta}$ given the data, $\vec{d}$. $P(\vec{\theta})$ (the prior probability, or the initial degree of belief in $\vec{\theta}$) is the probability of parameter values, $\vec{\theta}$, before collecting new data, $\vec{d}$, and $P(\vec{d})$ is the evidence for the model, which is merely a normalization constant that plays no role in parameter estimation. The most important (and familiar piece) of Bayesian model calibrations is the *likelihood* ($P(\vec{d}|\vec{\theta})$) term, which describes the probability of the data given a particular set of parameter values, which is readily calculated directly from the model. In this study, we use melt-present phase equilibria experiments to provide constraints for the likelihood, while the aforementioned data constraints from the literature (discussed in the previous section) provide additional *prior* information ($P(\vec{\theta})$). These impose crucial extra constraints on the model that help to control poorly-constrained parameters of the model (the posteriors) and thus, prevent unphysical results. The *posteriors* provide the final fitted model parameters and uncertainties ultimately consistent with the combined constraints from the data and prior information as discussed above.

5.2 Model fitting procedure

The foundational data constraints for this study are provided by the phase equilibria experiments (described in the previous section), which give us pressure, temperature, and composition constraints on the stability of garnet under various magmatic conditions. The phases involved in the experiments, involving at least solid garnet plus a liquid, should be in equilibrium and thus, the reaction affinity, described as:

$$A = -\left(\frac{\partial G}{\partial \xi}\right)_{P,T} = -\Delta_r G \qquad (6),$$

where G is the Gibb Free Energy, ξ is reaction extent, and r stands for reaction, should be equal to zero – these are saturation affinities. In reality, reaction kinetics are slow and may be too slow for some reactions performed in a laboratory setting to come to equilibrium. One way to circumvent this experimental uncertainty is to consider exchange reaction affinities. Exchange reaction affinities may more accurately reflect reaction equilibrium as they rely only on the exchange of ions (like Mg^{2+} and Fe^{2+}) between the solid and liquid phase, which generally occur more rapidly than solid-solid reactions (Swalin, 1972). In addition, calculations of saturation affinities may be biased because reaction affinities are calculated using the liquid model of the pMELTS modeling software (Ghiorso et al., 2002). The liquid model itself is a model based on data that may not entirely cover the liquid compositions observed in the experiments used in this study. Further, pMELTS was trained on a very limited set of garnet-present experiments and thus, saturation affinities are expected to possess an overall energy bias of order ~10 kJ or more (see section 6.6: *Model limitations* for further details); despite this systematic offset, pMELTS still provides accurate information on the relative stabilities of different garnet compositions, and is thus an imperfect yet crucial tool in deriving this new calibration. Furthermore, incorporating exchange reaction affinities in addition to saturation affinities partially mitigates the effects of a potentially biased pMELTS silicate liquid model.

Ultimately, the idea is to constrain the ternary garnet model so that it obeys the constraints extracted from the experiments by assuming reactions are in equilibrium and therefore the two types of reaction affinities discussed above should adopt zero values. In order to impose these constraints, we calculate reaction affinities for each published experimental constraint and these are used in addition to other “prior” constraints to derive ternary garnet solution parameters. Fortunately, we can use the pMELTS algorithm (Ghiorso et al., 2002) to perform affinity calculations. One caveat is that in order to impose equilibrium on every possible reaction requires knowledge of the thermodynamic parameters of each phase present in the experimental run product and thus, all the experimental reaction phases would have to also be present in the MELTS thermodynamic database (Berman and Koziol, 1991). Because this is not necessarily the case (e.g., one reaction might contain zircon, which is not a phase present in the MELTS thermodynamic database and we cannot include it in the affinity calculation), a work-around is to use only the liquid-present experimental reactions (most relevant to magmatic temperatures and pressures) and treat the liquid as an omni-component phase (Ghiorso, 2013). An omni-component phase is one in which all of the components of the system can be found and so we can create relevant reactions only between the solid garnet phase and this omni-component phase (i.e. the liquid). Once we have the relevant reactions compiled, we can use the liquid model of pMELTS (Ghiorso et al., 2002; most relevant to starting compositions and pressures of the experiments) together with a thermodynamic model for garnet to calculate reaction affinities.

The *initial guess* for the thermodynamic mixing parameter values used (that are initially handed to a least-squares solver) for the garnet phase is taken from of Berman and

Aranovich (1996) as their derived values are based on extensive phase equilibria data constraints and are thermodynamically self-consistent with the MELTS model database. In addition, previously published information regarding univariant reactions involving garnet, miscibility, excess volumes, and relevant uncertainties on all of these values are considered initially as well (see Table 1 for values used). All of this information is packaged into a vector that is handed, with the initial guess for the garnet solution parameters, to a least-squares solver that finds the best solution that minimizes the reaction affinities. In order to perform approximate Bayesian estimation, we apply a least squares solver simultaneously to the join set of constraints derived from the primary (affinity) data as well as the prior constraints on model parameters and model predictions (e.g. the critical temperature), vastly improving model behavior. Additionally, at the end of the model calibration, we use a Bayesian Monte Carlo technique to explore model predictions across the family of acceptable parameter combinations found in the posterior. In practice, what this looks like is that the classic goodness-of-fit metric, chi-square (χ^2), is directly related to the log-posterior value, χ^2= -2 log $P(\vec{\theta}|\vec{d})$ from equation (5). This allows us to adopt the Bayesian approach of maximizing the posterior and exploring its shape in the region around the best fit by using standard chi-square minimization techniques (as long as the chi-square metric includes both the likelihood and prior terms). For this study, we adopt the following form for the chi-square metric:

$$\chi^2 = \sum r_i^2\{Exchange\ affinites\}$$

$$+\sum r_i^2(saturation\ affinites)$$

$$+\sum r_i^2(priors\ on\ \theta) + \sum r_i^2(univariant\ reaction\ constraints)$$

where,

$$r_i = \frac{y_i - y_{i\,modified}}{\sigma_i}$$

The output of the algorithm implementing all constraints discussed above are the best fit solution parameters that minimize the residual vector. We tested four different types of fitting procedures in which not all of the garnet mixing parameters are actually fit and those that are not being fit are fixed at zero in the model, consistent with ideal behavior (see Table 2 for model fit types). This was done in order to assess the impact of some parameters being consistent with ideal behavior and some exhibiting non-ideality. For example, we can explore how the fitted model behaves without considering the added complications of non-ideality for the ternary excess parameters. Perhaps most importantly, this allows us to ensure that we are fitting the simplest model possible and not over-fitting the data, ensuring confident and accurate prediction for geological applications.

Table 2. Types of model fits performed in this study. Parameters left out of a given type of fit show empty cells and were set equal to 0, or ideal values. To control for overfitting, we considered the fit types in the 3 right-hand columns. The bold model is the favored model of this study based on numerous fitting procedures. Each numerical value in each cell indicates how many of each parameter was fit (e.g., if 3 Wh$_{ij}$ values are fit, that indicates that 3 garnet binary Wh values were fit) and the last row indicated the total number of parameters fit for that model type.

Mixing parameter	**No ternary parameters**		All parameters	No entropy parameters	No entropy or ternary parameters
Whij	**3**		3	3	3
ΔWhij	**3**		3	3	3
Wvij	**3**		3	3	3
ΔWvij	**3**		3	3	3
Ws$_{ij}$	**3**		3	-	-
ΔWsij	**3**		3	-	-
Wh123	**-**		1	1	-
Wv123	**-**		1	1	-
Ws123	**-**		1	-	-
Total fitted parameters	**18**		21	14	12

6 Results and Discussion

6.1 Arriving at the best fit solution

The uncertainties considered in this study consist of four independent data types being the phase equilibria experiments, solution parameters, critical point constraints, and univariant reaction boundary constraints. This provides a challenge in fine-tuning uncertainties on the priors in that the relative weighting of uncertainties has a direct impact on the model solution. Thus, we tested a range of uncertainty values (see Table 1) in order to drive the model towards a physically realistic model that balances the misfit among the different data types. In fine-tuning the uncertainties, each model output was evaluated to make sure that the data constraints maintained physical values and through many iterations of fine-tuning, we were able to hone in on the relative uncertainties that allowed the model to be well-behaved across the four distinct types of data measurements. We report the final uncertainties that were adopted to produce the best fit model in Appendix S3 Table S1.

6.2 Chi-square and Monte Carlo analysis of best-fit model

A careful analysis of the least-squares residuals for the best fit model was performed in order to ensure model convergence and to evaluate posterior model uncertainties. To begin, the residuals and best fit solution parameters were used to evaluate the curvature of chi-square about the minimum, providing an estimate of the covariance matrix of the model fit. To ensure the optimizer fully reached a minimum, a Monte Carlo was subsequently performed on the covariance matrix of the best fit model returned by the optimizer. Prior to the Monte Carlo, the absolute model errors were calculated by scaling the covariance matrix by the best fit reduced chi-squared (χ^2) value, which was 2.22. The covariance matrix was then randomly sampled (in 10,000 independent draws) and for each random draw, new model residuals and chi-square values (sum of the square of the residuals) were calculated. The model exhibiting the lowest chi-square value was selected as the final best fit model. This model essentially agrees with the one returned by the optimizer, but returning a modestly lower value of chi-square and slightly perturbed parameter estimates. Using this fast Monte Carlo approach (occupying <10 minutes of computing time), we ensure that the true best-fit model is obtained in spite of any potential optimization convergence issues. The covariance matrix for this final solution can be found in Supplementary Dataset S9.

6.2 Best fit solution parameters and experimental reaction affinities

Table 3 gives the best fit solution parameters derived in this study compared with other previously published ternary garnet models. For each of the four model fit types described in Table 2, about 100 model fits were performed under different parameterizations of the priors, like changes in the average critical temperature prior or uncertainties on the Wv solution parameters. The best fit model achieved in this study was of the type that included no ternary interaction parameters (W_{123}), consistent with most other previously published models. Exchange and saturation affinities for the best fit model of this study are greatly enhanced over previously published models as can be seen in Figure 5. It should be noted that the saturation affinities for the model fit of this study are not centered on zero, but achieve much lower saturation affinities than those of previously published model. As described more fully in the model limitations section below, the bias away from zero of the saturation affinities is a result of inherent bias of saturation affinities in the pMELTS model. Nevertheless, the model of this study greatly reduces that bias, as the bias according to Ghiorso et al. (2002) on the almandine endmember alone is on average about 8 kJ but the errors on that average suggest 10's of kJ. The model of this study shows an average bias of about 14 kJ, better than the previously published models that range from average saturation affinities of ~18-21 kJ (see Figure 5).

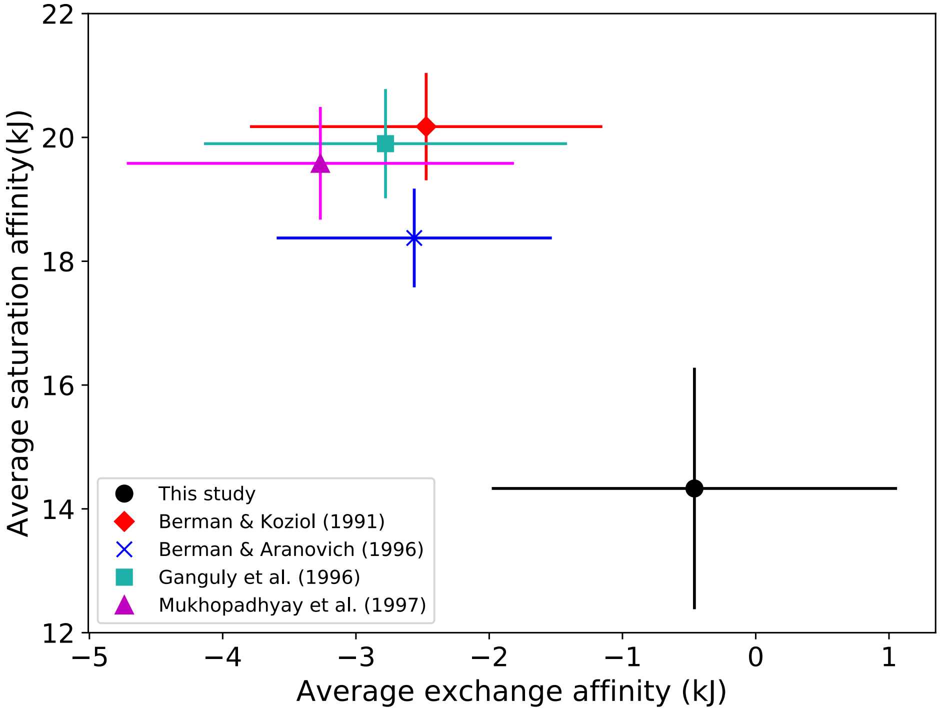

Figure 5. Comparison of *average* calculated saturation and exchange reaction affinities with previously published models. Plotted averages and associated uncertainties (1 sigma) are the result of many repeated measurements that individually suffer from significant noise, but on average the model of this study performs better than previously published model. Assuming each experimental reaction is in equilibrium, the saturation and exchange reaction affinities should be centered on zero. Given the inherent bias in garnet saturation affinities (~10 kJ on average with errors suggesting 10's of kJ) in the pMELTS model used to calibrate the model of this study (see discussion in model limitation section), our model achieves a minimized bias on saturation affinities that ultimately controls the temperature of garnet crystallization.

Table 3. Garnet solution parameters for the best fit model of this study compared with previously published values. Subscripts 1, 2, and 3 refer to the (1) almandine, (2) grossular, and (3) pyrope endmembers, respectively.

Mixing parameter	**This study**	**Uncertainty (2 sigma)**	Berman & Koziol (1991)	Aranovich & Berman (1996)	Ganguly et al. (1996)	Mukhopadhyay et al. (1997)
[1]Wh_{12} (J)	51910.4	7.2	11470	16766.5	11469	-293.5
Wh_{13} (J)	10011.1	19.8	1975	5666.8	4218	-950.5
Wh_{23} (J)	59874.2	19.8	45380	50875	47182	39744
Wh_{123} (J)	0	-	0	73298.3	0	0
[2]ΔWh_{12} (J)	9280.3	2.0	-8850	-5185	-8850	-17820
ΔWh_{13} (J)	1221.6	2.0	1745	602.3	2133	23216
ΔWh_{23} (J)	-2330.0	2.0	-23820	-17405	-17690	-25438
Wv_{12} (J/bar)	0.121	1.8 x10^{-4}	0.13	0.13	0.015	0.086
Wv_{13} (J/bar)	0.033	1 x 10^{-7}	0.035	0.08	0.035	0.008
Wv_{23} (J/bar)	0.049	1 x 10^{-6}	0.1	0.105	0.035	0.104
Wv_{123} (J/bar)	0	-	0	0.281	0	0
ΔWv_{12} (J/bar)	-0.45	0.011	-0.04	-0.04	-0.015	-0.048
ΔWv_{13} (J/bar)	-0.69	0.016	0.025	-0.02	0.035	0.042
ΔWv_{23} (J/bar)	-0.42	0.023	0	0.0685	0.023	0.036
Ws_{12} (J/K)	32.2	0.038	5.08	9.43	5.07	-0.5
Ws_{13} (J/K)	-8.72	0.023	0	4.11	0	-4.84
Ws_{23} (J/K)	18.2	0.030	18.8	18.8	17.3	11.7
Ws_{123} (J/K)	0	-	0	32.3	0	0
ΔWs_{12} (J/K)	36.8	0.13	0	0	0	-15.0
ΔWs_{13} (J/K)	1.75	0.22	0	0	0	17.2
ΔWs_{23} (J/K)	6.21	0.29	0	0	0	-9.17

[1]Represented in delta notation in which Wh_{12} is equal to (Wh_{112} + Wh_{122})/2. See Appendix 1 for further details

[2]Represented in delta notation in which ΔWh_{12} is equal to (Wh_{112} - Wh_{122})/2. See Appendix 1 for further details

6.3 Excess thermodynamic properties

Figure 6 shows the excess thermodynamic properties of the fitted model and those of previously published models. The model of this study shows a distinct asymmetry in the excess volume behavior along each binary, not seen in any other published model (see section 6.4 for implications for the miscibility gap). The asymmetry becomes very important when considering immiscibility in garnets and is driving the pressure dependence along the pyrope-grossular binary in our model. This asymmetry is not observed in many other previously published models (Figure 3) and is a remarkable finding of this study. Previous studies have also suggested the potential for short-range ordering along the pyrope-grossular binary (e.g., Bosenick et al., 1995, 1999, 2000; Dachs and Geiger, 2006; Vinograd and Sluiter, 2006). The excess entropies in this study, specifically along the pyrope-grossular join are consistent with these findings and are in fact within error of the Dachs and Geiger (2006) calorimetric excess entropy measurements (similar to all other ternary garnet models). The positive and slightly asymmetric excess entropy suggest that a more detailed configurational ordering model, which accounts for ordered states, may be needed to completely capture the behavior of this system. However, there is nowhere near enough experimental data currently available to adequately constrain the additional parameters required for such a model, and therefore prediction accuracy would suffer greatly. Given the available data, we are quite satisfied with the predictive accuracy of our model across a broad range of experimental techniques.

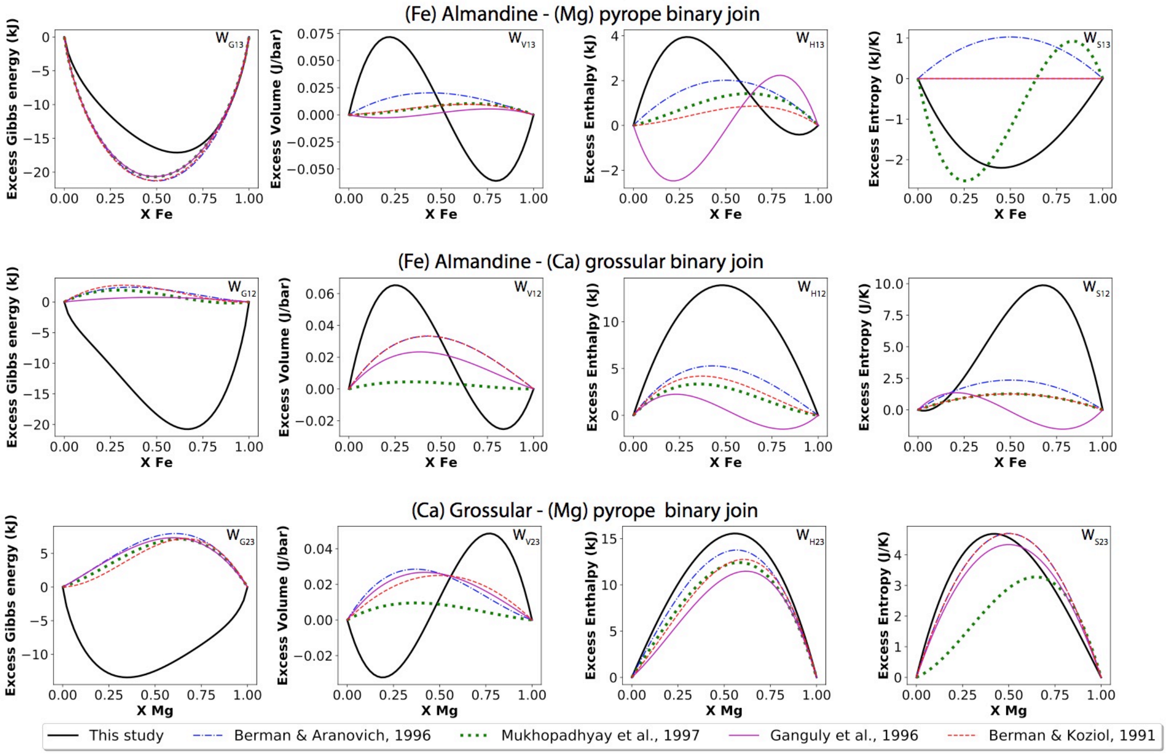

Figure 6. Excess thermodynamic properties (deviations from ideality) for the best fit model of this study compared with previously published models.

6.4 Univariant reaction

An imposed constraint on the best model fit was the position of the univariant reaction boundary of Grs + 2Alm → 3Fa + 3An from Bohlen et al. (1983a). Although no sub-solidus reaction constraints were imposed on this model, this constraint acts as good control on how well our model handles non-liquid-present reactions. Figure 4 shows the final result of the univariant reaction boundary as constrained by the best fit model of this study in relation to how well the boundary is captured by previously published models. All previously published models have similar slopes that are all skewed from the actual reaction boundary slope. The best fit model of this study captures the approximate slope and temperature of the reaction boundary quite well. The 1σ uncertainties on the temperature and pressure estimates are represented by the width of the best fit line in Figure 4.

6.5 Miscibility gap

Most previous studies suggest there is no significant pressure dependence in terms of the miscibility gap along the pyrope-grossular binary and that the immiscibility that does exist will not be realized at magmatic temperatures relevant to igneous processes (see Figure 3 for summary of miscibility gap calculated or observed by previous studies). However, a relatively recent experimental study by Du (2011) and Du et al., (2015, 2016) has shown that in fact at 6 and 8 GPa, immiscibility is observed at temperatures relevant to igneous processes (>1100 °C; see discussion in section 4.2.3). Further evidence of the potential for immiscibility to manifest at magmatic conditions, Wang et al., 2000 observed immiscibility in an almandine-poor garnet in an ultramafic diatreme. Remarkably, our model captures the critical temperature predicted by Du (2011) and Du et al., (2015, 2016) as seen in Figure 3 at 8 GPa. The critical temperature at 1 bar predicted by the model of this study is 649 °C ± 4

°C (2 sigma) at a binary composition of $Pyrope_{62}Grossular_{38}$, was constrained tightly by the model priors, and agrees well with previously published ternary garnet models (see Figure 3). Significantly, calculation of the critical temperature at 3 and 8 GPa were not constrained by our model, but using the best fit model were calculated at 854 ± 8 °C (2 sigma) with a composition of $Pyrope_{70}Grossular_{30}$ and 1281 ± 37 °C (2 sigma) with a composition of $Pyrope_{75}Grossular_{25}$, respectively. The 8 GPa critical temperature predicted in this study agrees very well with that of the aforementioned Du studies that suggest a critical temperature at 8 GPa of 1260 °C at a binary composition of $Pyrope_{73}Grossular_{27}$. Pressure dependence is not captured by any other ternary garnet models except for that of Haselton and Newton (1980), which captures the pressure dependence but does not capture the actual critical temperatures and compositions from 1 bar to 3 GPa well. The model presented here captures the pressure dependence and the critical temperature and composition constraints at 1 bar and 8 GPa according to previously published models.

According to our model, the critical temperature along the almandine-grossular is not present at magmatic temperatures until at least 5 GPa, where the critical temperature reaches temperatures above 800 °C. Regardless, the miscibility gap does show a similar pressure dependence to that observed along the pyrope-grossular join, which is perhaps unsurprising given the similar difference in cation size between Fe^{2+} and Ca^{2+} compared with Mg^{2+} and Ca^{2+}. No miscibility gap exists for our model along the almandine-pyrope binary join.

6.6 Model limitations

It's important to point out that the affinities, and thus the derived ternary garnet solution parameters of this study, are underpinned by the liquid solution model calibration in pMELTS. Sources of bias can creep in owing to the fact that the pMELTS liquid model is a model calibrated using liquid-bearing experimental data that does not entirely cover the liquid compositions observed in the experiments used in this study. Additionally, the garnet-present experimental data used to calibrate pMELTS were very limited. Therefore, according to Ghiorso et al. (2012), saturation affinities (directly affecting the saturation temperature of a phase), particularly for Fe-rich garnet endmembers, are biased by an average of about 8 kJ, but the errors are large suggesting this could be 10's of kJ. Therefore, the bias exhibited by the model of this study (~14 kJ) is actually an improvement.

An additional limitation to the model is the lack of incorporation of ordering between Ca^{2+} and Mg^{2+} ions on the dodecahedral site. Short range ordering has been suggested by numerous authors (e.g., Bosenick et al., 1995, 1999, 2000; Dachs and Geiger, 2006; Vinograd and Sluiter, 2006), but incorporating ordering into the model of this study would require better data constraints that do not exist currently. For a more complete discussion of ordering, see section 6.3.

7 Conclusions

Previously published ternary garnet models lack agreement among their solution parameters and excess thermodynamic properties. In addition, many of these previously published models have been calibrated using disparate data types, covering variable P-T-X conditions, and calibration methods. Most of these studies were performed in the 90's and since this time, copious experimental data have become available. The more recent garnet solution models formulated over the last decade are focused on metamorphic types of P-T conditions and additionally mainly focus on sub-solidus reactions. We present here an updated ternary garnet solution model calibrated using the latest *liquid*-bearing, garnet-present experimental phase equilibria data with hopes of implementation particularly into the MELTS family of thermodynamic models.

The ternary garnet model presented here is applicable to high pressure igneous systems, and is well-constrained by data in the temperature range of about 600-1600 °C and pressures of 0.2-4 GPa, with most data laying between 1 and 4 GPa. There are a number of improvements made in this study over previously published ternary garnet models. 1) The use of Bayesian statistical techniques in our model calibration allows for a robust quantification of uncertainties on all solution parameters. 2) Our model captures the significant pressure dependence of the pyrope-grossular miscibility gap, observed experimentally by Du (2011) and Du et al., (2015, 2016), which has not been captured by previously calibrated ternary garnet models. 3) The inherent bias observed in the average garnet saturation affinities calculated using our model has been greatly reduced compared with previously published garnet models and thus will increase stability of the garnet phase, particularly in thermodynamic modeling software like MELTS (Ghiorso and Sack, 1995). 4) Slightly asymmetric, excess entropies along the pyrope-grossular binary join are consistent with calorimetric and theoretical studies on the behavior of excess volumes and entropies along this join, which have suggested short-range ordering of Ca and Mg ions at low to moderate temperatures.

These improvements have important implications for use of the garnet model as a thermobarometer, for example, as our model shows that un-mixing of Ca^{2+} and Mg^{2+} ions on the dodecahedral site is energetically favorable at magmatic temperatures and pressures, contrary to previously published models. Additionally, the consistency of the model presented here with previous experimental constraints on garnet immiscibility, cation ordering, and excess thermodynamic properties provide confidence that our model is robust and will be a useful tool in high-pressure igneous phase equilibria modeling. Lastly, this new, accurate high P-T ternary garnet model provides the necessary solid foundation to expand to the complete 7-component garnet model proposed in the Introduction needed to better understand mantle and OIB lithologies. The 7-component garnet model will include the Ti-bearing garnet endmember (in addition to the Cr-bearing endmember and the high-pressure form of garnet, majorite) necessary for understanding the role of garnet in the source of OIB lithologies and the enrichment in TiO_2 observed in many OIB lavas.

Chapter 4: Diagnosing open-system magmatic processes using the magma chamber simulator (MCS): Part I – Major elements and phase equilibria

1 Introduction

The Magma Chamber Simulator (MCS) is a rigorous self-consistent thermodynamic model that quantifies the evolution of a composite magmatic system that interacts by exchange of matter and energy following the constraints imposed by local thermodynamic equilibrium. In MCS, the Magma subsystem (M), initially a finite mass of melt in a well-defined thermodynamic state, is coupled to its host sub-system or Wallrock (WR) *via* a diabatic and semi-permeable boundary. During AFC processes, sensible (melt cooling) and latent heat (formation of cumulates by fractional crystallization, FC) flows across the M-WR boundary, heating up and *potentially* partially melting wallrock. If partial melting does occur and the melt fraction in wallrock exceeds a rheologically-determined, user-specified critical threshold (f_m^o or fmzero), partial melt from WR mixes with and equilibrates with melt in the M sub-system (herein called M subsystem melt or M melt for brevity). Earlier formed cumulates are chemically isolated from M melt, but remain in thermal equilibrium. This coupled AFC process is at the core of the MCS.

The extent of matter transfer between WR and M is governed by key parameters connected to ambient geological conditions and initial bulk compositions. For example, was WR cold and dry, warm and wet, refractory or easily fusible? What are the bulk composition and temperature of the M sub-system? In addition to contamination of M melt by wallrock partial melt (i.e., AFC), contamination can simultaneously or solely occur by the process of stoping (S). In stoping, wallrock in a well-defined thermodynamic state (bulk composition, phase abundance and composition, and temperature) is added *en masse* to M melt, and the contaminated system comes to a new equilibrium state at a new temperature. The stoping event may cause crystalline solids or a fluid to precipitate, and naturally, the contaminated M melt will assume a different bulk composition. MCS is able to handle simultaneous partial melt assimilation (classical AFC in the MCS jargon) and contamination by stoping (S).

A final process that MCS accounts for is magma mixing by recharge (R). During MCS recharge, a finite mass of internally equilibrated recharge magma (in a well-defined thermodynamic state) is added to M melt, and the new mixture attains chemical potential equilibrium. This operation is computationally identical to the stoping operation. The initial state of recharge (R) magma is controlled by fixing its bulk composition and temperature, which then defines its pre-mixing equilibrium phase state of crystals ± melt ± fluid. A finite mass of such R magma is then added *en masse* to M melt, generally at a different temperature, and the new bulk composition is allowed to attain chemical potential equilibrium to form a new hybridized magma, typically at a new temperature.

The current version of MCS allows up to thirty distinct events of the S or R type. The user-defined condition that triggers an R or S event is either a specified M melt temperature, a temperature decrement from the last S or R event, or a set temperature of M melt below its starting (liquidus) temperature. These inherently open system processes are collectively termed RASFC processes (RASFC for brevity) that can be arranged by the user to be serial or simultaneous in order to emulate the open system behavior of natural magmatic systems.

The MCS generates compositional and other information on all melts, solids, and fluids that characterize each step of RASFC. This output can be compared to natural system petrological and geochemical information, including whole-rock, melt inclusion, and mineral major and trace element and isotopic data, in order to establish the most significant RASFC processes involved in the formation of a suite of plutonic or volcanic rocks. Used in forward-model mode, MCS also documents the relative impact of a host of parameters (e.g., initial temperature of wallrock, composite system pressure and redox conditions, mass of recharge magma, volatile content of magma and wallrock, etc.) on the evolution of open-system magmas. To the critic who argues that 'there are too many parameters' in MCS, it's important to note that nature is complicated and variable, and so the models must be as well.

The theoretical underpinnings and an AFC example of the MCS are provided in Bohrson et al. (2014), and a complete description of the MCS along with the code, examples, tutorials, and related tools may be found at https://mcs.geol.ucsb.edu, the MCS website, which is regularly updated with the latest MCS developments. The architecture of MCS includes a Visual Basic interface that couples with any of four MELTS engines (v 1.2.0, v 1.1.0, v 1.0.2 or pMELTS; Ghiorso and Sack 1995; Ghiorso et al. 2002; Gualda et al. 2012; Ghiorso and Gualda 2015; http://melts.ofm-research.org/). MCS calculations are undertaken in two parts:

(1) MCS-PhaseEQ: the major element and phase equilibria computation of the RASFC evolution, and (2) MCS-Traces: the trace element and isotopic (Sr, Nd, Hf, Pb, Os, and O) consequences of the RASFC scenario from (1). This bipartite structure to the MCS simulation recognizes that robust trace element/isotopic calculations are necessarily built upon an accurate major element solution that quantifies phase abundances, compositions, and temperatures. A researcher may iterate in step (1) by comparing observables with predicted results before investing effort into trace element and isotopic modeling. Conversely, because of the bipartite structure, a researcher can run multiple trace element and isotopic ratio calculations using, for example, different initial trace element compositions and/or mineral-melt, mineral-fluid partition coefficients for M, WR, S and R but using the same part (1) RASFC solution. This bipartite approach maintains maximal flexibility in the pursuit of a 'best-fit model' and aids in understanding the sensitivity of a full solution (phase equilibria, trace elements and isotope) to the initial conditions and parameters.

It is envisioned that the MCS can be utilized in two mutually inclusive ways. The first is forward modeling of different RASFC scenarios. Results of such models show how phase equilibria, major and trace elements, and isotopes respond to different open-system processes. Repeating a sequence of RASFC operations with variable initial conditions and MCS parameters enables one to understand how magmatic system evolution depends on and responds to different compositional, mass, and thermal characteristics of the composite system. For example, other factors remaining constant, how do RASFC results depend on composite system pressure and redox state, or initial H_2O content of the M melt? How do small changes in wallrock bulk composition affect the contaminated magma? What if, instead of a CO_2-absent recharge magma, the R magma bulk composition includes 1 wt. % CO_2?

Many similar questions can be addressed by forward modeling. Understanding the sensitivity of various parameters is especially important in petrological and geochemical modeling because, in general, process and parameter uncertainties loom large. However, such uncertainties should not be seen as a limitation but instead viewed as an *opportunity* to develop empirically based intuition of open system magmatic evolution.

The second way MCS can be used involves modeling informed by an array of data—whole-rock, mineral, and melt inclusion, major and trace element and isotope—from individual magmatic (i.e., volcanic and plutonic) systems. Among the goals for such modeling are defining what processes dominate a particular igneous rock record. A first-order issue affecting many detailed geochemical studies on igneous rocks from many different petrotectonic environments (arcs, MORBs, OIBs, LIPs) is understanding the time-transgressive balance of mantle versus crustal contributions to a particular magma (e.g., Cox and Hawkesworth 1984; Asmerom et al. 1991; Moore et al. 2018), and exploring what conditions favor large versus small magma bodies. *In situ* crystal evidence suggests that some recharge events may (directly or indirectly) catalyze eruption, whereas other recharge events do not (e.g., Tepley et al. 2000; Tepley et la. 2013; Wark et al. 2007; Scruggs & Putirka 2018, Ubide and Kamber 2018). Furthermore, some magma systems show evidence of staging in shallow crust, whereas others are dominated by deeper residence (e.g., Walker et al. 1993; Mangiacapra et al. 2008; Becerril et al. 2013; Weber and Castro 2017). What parameters distinguish these systems? Both modes of modeling also serve another very important function; they help identify potential enhancements that allow us to continue to build MCS so that it better addresses the complexity of the natural world.

Finally, it's important to emphasize that MCS is a *thermodynamic* model that, while allowing for open system behavior, assumes local thermodynamic equilibrium. Because MCS is a thermodynamic and not a transport model, thorough and complete mixing is assumed when magmas mix or partial melts are assimilated. There are no compositional gradients within WR, R/S, M sub-systems. Because the MCS is based on thermodynamic methods, time is not explicit. In a RASFC scenario, the sequence of events *does* follow the 'arrow of time,' but there is no implication regarding *rates* of processes. On the one hand, one might argue that magma mixing is often imperfect or that perfect thermodynamic equilibrium is a limit that is never attained. In real systems with dissipation (entropy generation) and non-equilibrium effects, kinetic factors are undoubtedly important. To *model* such systems, a great deal of additional information regarding initial conditions and magma transport phenomena (e.g., diffusion rates and viscous effects) would have to be known in order to apply and solve the conservation equation for mass, species, momentum, and energy. Nevertheless, magma evolution is an archetypical example of a chaotic system, and the utility of thermodynamics becomes clear when viewed through such prism. Even for complex RASFC scenarios, unique final states exist and can be computed. *These solutions serve as reference states to which natural system data can be compared.* Then, initial conditions can be altered and simulations run again with new parameters, with the goal of more closely approximating nature and hence enhancing one's understanding of how open magmatic systems evolve.

In this contribution, an overview of operational details of MCS to implement the major element and phase equilibria part of the code (MCS-PhaseEQ) is provided. In addition, five illustrative RASFC forward models are discussed (FC, R_2FC, AFC, S_2FC, and R_2AFC where the subscript defines the number of "events") to showcase the capabilities of the MCS. The purpose is to provide perspective on how melt, cumulates, wallrock and recharge masses, temperatures, and compositions evolve in open-system environments. Key outcomes show that magmatic markers of open-system processes vary as a function of characteristics of the composite system. The simultaneous effects of partial melt assimilation and fractional crystallization leave a robust signal that can be deciphered *a posteriori* even when concurrent AFC is interrupted by multiple recharge (magma mixing) events. MCS models can inform one regarding the relative roles of mantle *versus* crustal contributions by leaving a distinct geochemical signal in melt and mineral chemical compositions and in the relative masses of anatectic melt, recharge magmas, cumulates and stoped blocks. In paper II, trace element and isotopic characteristics for these same five cases are presented along with the theory and code logistics for such computations in the MCS framework (MCS-Traces; Heinonen et al. submitted). Examples of the use of MCS in studies of natural systems are given elsewhere (e.g., Borisova et al. 2017; Heinonen et al. in press).

2. Architecture and Operational Details of the MCS

2.1. How does MCS work?

MCS-PhaseEQ is the union between a computational thermodynamic *engine* and an executive *brain* (Bohrson et al., 2014). These two keystones are detailed briefly below. The thermodynamic engine implemented in the MCS-PhaseEQ is one of four MELTS codes currently available. These are enumerated as pMELTS, and rhyolite-MELTS versions 1.0.2, 1.1.0, or 1.2.0 (Ghiorso and Sack 1995; Ghiorso et al. 2002; Gualda et al. 2012; Ghiorso and Gualda 2015; http://melts.ofm-research.org/). Details of the MELTS software can be found in these original references. Here a brief summary is given, since a full understanding of the capabilities of MCS requires an understanding of the underlying computational infrastructure.

A centerpiece of the MELTS family of phase equilibria models is the thermodynamic model for the dependence of Gibbs free energy of silicate liquids as a function of melt composition, temperature (roughly 850-1900 K), and pressure (roughly 0-4 GPa). For numerical calculations, the laws of thermodynamics, which are rigorously adhered to in MELTS, are not sufficient and must be adjoined with the thermodynamic properties of the materials composing the composite system. Any thermodynamic model is only as good as the data upon which it is based. Hence, so long as there are inaccuracies in experimental data, there will be uncertainties in the computational model. In this sense, the model is approximate. As more experimental data become available to calibrate the thermodynamic database, computational models like MELTS and MCS will improve.

The executive command and control aspects of the MCS-PhaseEQ, informally referred to as the MCS executive *brain*, are built with Microsoft's Visual Basic programming language. The brain is responsible for implementing the particular R_nAS_nFC scenario specified by the user by (1) sending instructions to the chosen MELTS engine, (2) performing additional internal calculations based on values returned from MELTS, (3) making the conditional and sometimes complex sequential executive decisions required to carry out the user-defined R_nAS_nFC petrological scenario, (4) producing a variety of real-time and archived graphical and numerical output, and (5) archiving input and output in a systematic manner enabling a synoptic view of the results. Rapid analysis is essential because generally one may wish to compute many cases to determine the parameters that play primary, secondary, or minor roles.

2.2. Overview of Computational and Installation Requirements, Operating Instructions, and MCS Input and Output

Because of coordination between the Visual Basic code and the selected MELTS engine, the MCS comes with some specific requirements for the computational environment. The platform must be able to run standalone MELTS, so graphical operating system Macintosh OS X 10.11 (El Capitan) or later is needed. The version of MCS that is available with this publication runs in either Excel 2016 (version 16.16) or 2019 (version 16.20). Because MCS relies on the Visual Basic infrastructure provided by Microsoft, the website will post updates as needed. As Microsoft introduces changes to Excel, support for MCS in newer versions may be undermined. As a consequence, a parallel development of a platform-independent version of MCS that will not rely on Excel is being pursued.

Below, a brief overview of the five major steps that are followed to run a MCS-PhaseEQ simulation is provided, and the input and output is described. For complete and updated information about the Magma Chamber Simulator, see the MCS website (http://mcs.geol.ucsb.edu), which includes written and YouTube step-by-step instructions for installation and use.

After preparation of an input file (MES file, see below) and successful installation and launch of MCS-PhaseEQ in Excel, an interface appears that guides one through the following steps: Step 1 (*MELTS Terminal Commands*) initiates MCS communication with MELTS through a maximum number of three terminal windows (for Magma, Wallrock, and Recharge/Stoping). Step 2 (*Select MES input file and create new MCS output file*) involves choosing an output file name and input MES file from those available. Step 3 (*Find Wallrock (WR) Solidus*) is a preliminary calculation that prepares the WR sub-system by computing a solidus or near solidus thermodynamic state for wallrock for eventual coupling with the M sub-system, a requirement for AFC scenarios, and Step 4 (*Run MCS*) launches and runs the

MCS-PhaseEQ simulation. A simulation will run until the magma and wallrock are at or very close to thermal equilibrium or until a user-specified "hard stop" temperature or M melt mass is reached. Finally, Step 5 (*Export Run Results*) involves exporting the simulation results to an Excel workbook. The workbook tabs record the input and the masses and temperatures of melt, fluid phase, and all solid phases in the magma, wallrock, and each recharge magma/stoped block subsystem. Melt major oxide compositions are archived for magma, wallrock, and recharge magma/stoped block, and mineral formulae and some useful graphs are also provided. Additional steps (e.g., Step 3 (alt)) provide enhanced capability for running MCS, and these are detailed on the website.

A standardized input file is required for all MCS-PhaseEQ runs, and the default name for these files must begin with MES_ (e.g., MES_FC.xlms). Composite system parameters such as a single pressure (i.e., each run is isobaric), fO_2 and the wallrock percolation threshold (i.e., the fraction of melt that must be sustained in wallrock; any fraction above this threshold is transferred into the magma, see Bohrson et al., 2014 for details) are required, as are the temperature, mass, and composition for parent magma melt, recharge magma(s)/stoped block(s), and wallrock. The output file contains 10 tabs that echo input and archive various forms of output including the masses and temperatures of melt, fluid phase, and all solid phases of magma, wallrock, and each recharge magma/stoped block. In MCS-PhaseEQ, melt major oxide compositions are archived for magma, wallrock, and recharge magma/stoped block, and mineral identities and formulae are also provided. A variety of x-y plots (like those shown in real-time in MCS-PhaseEQ runs) illustrates the compositional evolution of magma melt, and an additional series of diagrams illustrates various ways of interrogating the masses and mass fractions of melt, fluid phase, and minerals in the resident magma (e.g., mass fraction of melt, fluid phase, and each mineral in the magma body (resident melt + cumulate reservoir)) during the R_nAS_nFC scenario.

3 Comparison of Closed (Fractional Crystallization) and Open-System Magma Evolution Illustrated by MCS

Five MCS-PhaseEQ simulations are presented that compare the major oxide and phase equilibria evolution of a magma body undergoing fractional crystallization (FC), recharge (two events)-fractional crystallization (R_2FC), assimilation-fractional crystallization (AFC), fractional crystallization accompanied by assimilation through stoping (two events) (S_2FC), and recharge (two events)-assimilation-fractional crystallization (R_2AFC).

For each simulation, the parental magma is depleted mantle-derived continental tholeiite from the ~180 Ma Karoo Large Igneous Province (sample P27-AVL, Luttinen et al., 1998) (Table 1a). Initial H_2O was set at ~2 wt. %, and the Fe^{2+} to Fe^{3+} ratio was initially calculated at FMQ; each simulation was then run under fO_2-buffer absent conditions. This means that the system is closed with respect to the addition or subtraction of oxygen; during the run, the fugacity of oxygen will rise or fall according to the dictates of Gibbs energy minimization of the composite system.

Each simulation has a user-chosen magma temperature decrement of 5°C, which means that the state of the system (magma and wallrock melt, minerals, fluid phase) is determined and archived at 5°C temperature decrements for the FC case (Table 1b). Within these 5-degree decrements, the M subsystem can be envisaged to evolve by equilibrium crystallization after which the formed minerals are fractionated to the cumulate pile before the next step. MCS-PhaseEQ internally adjusts M temperature to values other than the user-defined decrement in response to the homogenization of recharge magma(s), stoped block(s), or anatectic melt with M melt; these processes are explained in more detail below. For the cases involving recharge (i.e., R_2FC, R_2AFC), the recharge magma composition (including initial H_2O wt. % and fO_2) are the same as the parent magma. Wallrock composition is average upper continental crust from Rudnick and Gao (2003), with initial fO_2 also calculated at FMQ, initial H_2O of ~2 wt.% and initial CO_2 of ~1 wt. % (Table 1a). The fixed composite system pressure for all five simulations is 0.1 GPa. The percolation threshold is 0.1 (mass fraction), which means that before anatectic melt can be transferred from wallrock to resident magma melt, 10% melt must be present in wallrock; any mass above this threshold is transferred and equilibrated with M melt. For all simulations, the mass of wallrock involved is twice (200 mass units, m.u.) that of the initial magma (100 m.u.), yielding a wallrock/initial resident magma mass ratio of 2. All simulations discussed here were run using Rhyolite-MELTS v1.2.0. Tables 1a and 1b list compositions and other initial conditions for the five simulations.

The models are discussed and compared in detail below. Electronic Appendix 1 provides all input variables for each case described in this study, Electronic Appendix 2 provides mass and temperature outcomes for the cases, and Electronic Appendices 3, 4, and 5 present detailed comparison data for mineral assemblage, fluid saturation, and selected melt compositional parameters for resident magma, wallrock and recharge magmas for each case. Figures 2-5 illustrate selected mass, thermal, and compositional data for melt and minerals for resident magma and wallrock.

Note that all model output is presented in Electronic Appendices 6-10, and it's recommended that the output files (concentrating on the "RunSummary" tab) be viewed simultaneously when reading the following sections. The structure of the output files is uniform across all cases and, hence, time invested in learning the structure of the output will be amply rewarded and makes the assimilation of data relatively easy after an investment of effort. By way of introduction, the different tabs of the output that store the relevant information are specifically named in the discussion of the first FC case (section 3.1). Note also that the MES input files are included in Electronic Appendices 11-15; this means that all the cases discussed here can be replicated.

3.1 Case 1: Fractional Crystallization (FC)

The parent magma, the Karoo basalt (~2 wt. % initial H_2O) specified above, has a liquidus temperature of ~1131°C at 0.1 GPa. The FC simulation ends at a user-chosen temperature of ~900°C. *Via* fractional crystallization, the melt composition evolves from tholeiitic basalt to dacite, with the dacitic melt forming through ~76% fractional crystallization (see Electronic Appendix 6, tab ChartTAS for graphical view of the simulation; all percentages listed are wt. % unless otherwise noted). Magma melt becomes H_2O-saturated at ~1026°C. At the end-temperature (~900°C), the H_2O-fluid phase constitutes ~1% of the magma system, with melt composing the remaining ~23% (Figure 2) as noted by examination of columns I through L on row 53 of the *RunSummary* tab (all tab references for the FC case can be found in Electronic Appendix 6).

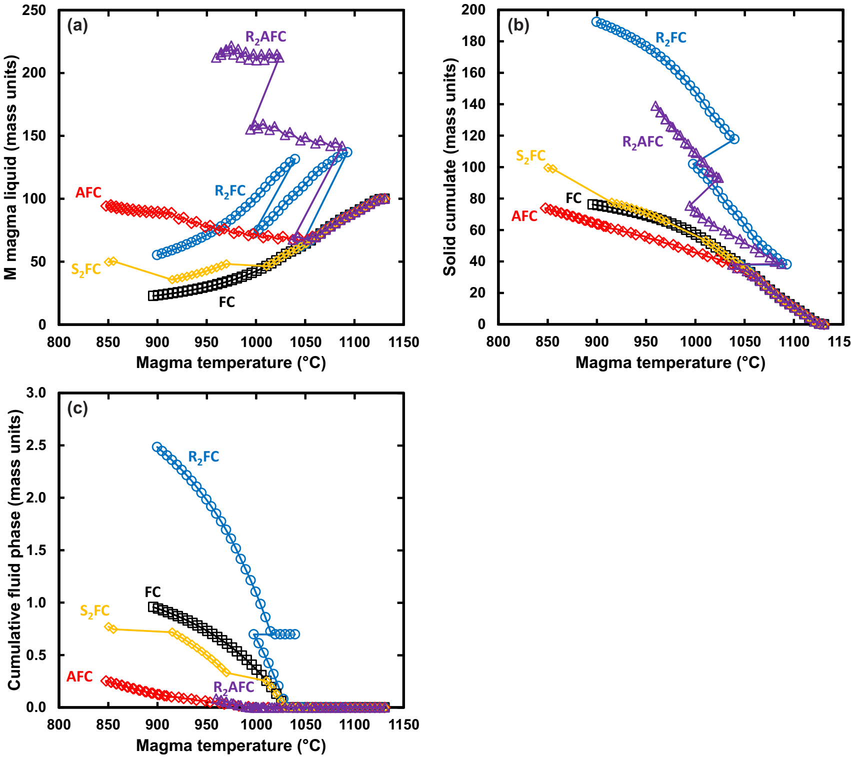

Figure 2 Results of MCS-PhaseEQ simulations for five cases (FC, AFC, R_2FC, S_2FC, R_2AFC). Magma temperature (°C) versus (a) M magma liquid (melt) mass, (b) total cumulative mass of crystals removed to the cumulate reservoir, and (c) total cumulative mass of fluid phase. Each simulation runs from parent magma liquidus temperature to the end of the simulation. For cases involving assimilation, the simulation ends when magma and wallrock are at or close to thermal equilibrium. For cases that do not involve assimilation, the simulation ends at a user-defined "stop" temperature. See text, tables and appendices for additional details.

Olivine is the first liquidus phase (see column Z of the *RunSummary* tab), and its composition is Fo_{82} (line 84, *SolidFormulas* tab, color code darker blue). Olivine is followed by clinopyroxene (first appearance at ~1121°C) and plagioclase (first appearance at ~1086°C, An_{84}). Additional phases include spinel (first appearance at ~1071°C) and rhombohedral oxide (first appearance at ~981°C). By the end of crystallization, the cumulate is dominated by clinopyroxene and plagioclase, each of which composes ~39% of the bulk cumulate mineral mode; olivine constitutes ~15%, spinel ~5 % and rhombohedral oxide < 1% (Figure 3).

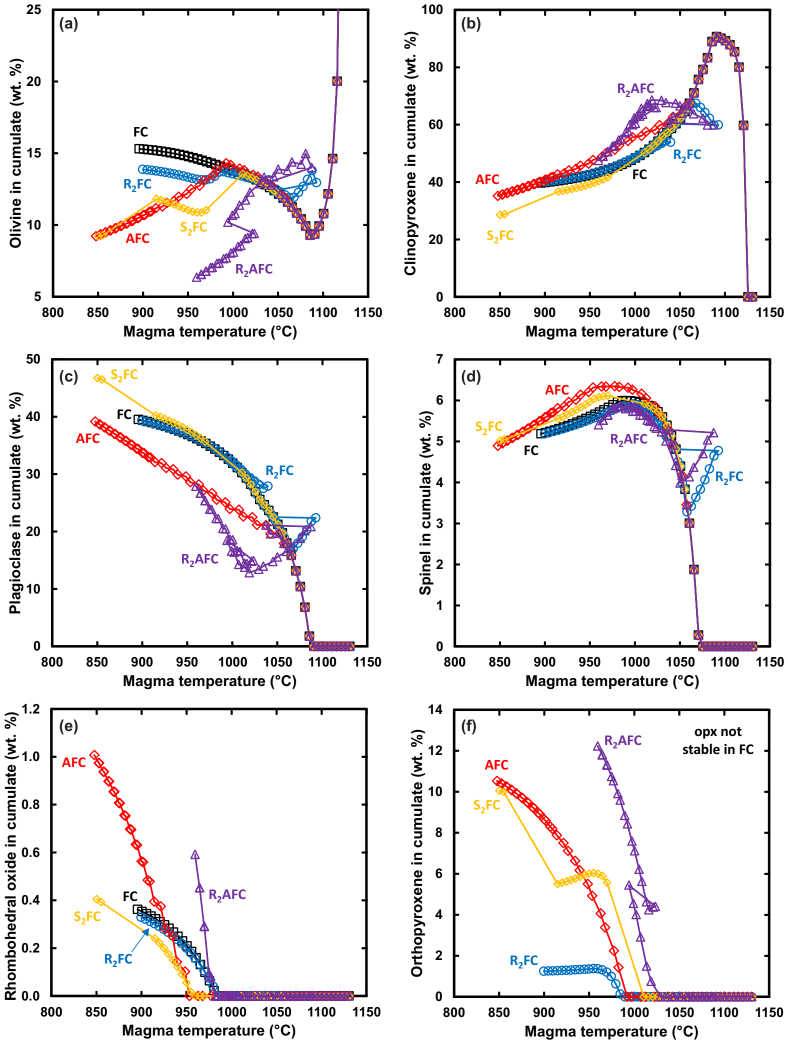

Figure 3. Magma temperature (°C) versus modal percent of minerals in bulk cumulate in the five MCS simulations (FC, AFC, R$_2$FC, S$_2$FC, R$_2$AFC). (a) olivine, (b) clinopyroxene (cpx), (c) plagioclase, (d) spinel, (e) rhombohedral oxides, (f) orthopyroxene (opx).

This information is graphically portrayed on the tabs labeled *ChartMassFrac*, *ChartPPD and ChartPMD*. The compositional range of minerals is large (see *SolidFormulas* tab and Electronic Appendix 3), as anticipated for a parental basaltic melt that evolves to dacitic after significant fractional crystallization. For example, olivine Fo ranges from 82 to 22, plagioclase anorthite (An) contents range from 84 to 46, and clinopyroxene Mg# from 84-49.

As SiO_2 increases, MgO and CaO decrease. FeO, Fe_2O_3 (not shown), TiO_2 and Al_2O_3 initially increase, but eventually decrease after ~60 to 80 °C of cooling from the liquidus.

Na_2O, K_2O, P_2O_5 and H_2O wt. % increase in the melt with increasing SiO_2 (Figure 4). Similar information is displayed graphically on MgO versus oxide diagrams on the tab *Charts*.

The initial wallrock temperature for this simulation is 100°C. Enthalpy transferred from magma due to cooling and crystallization yields a final wallrock temperature of ~330°C (Table 2), too low for any partial melting to occur. Thus, although the wallrock heats up, it remains below its solidus temperature, and no mass transfer occurs.

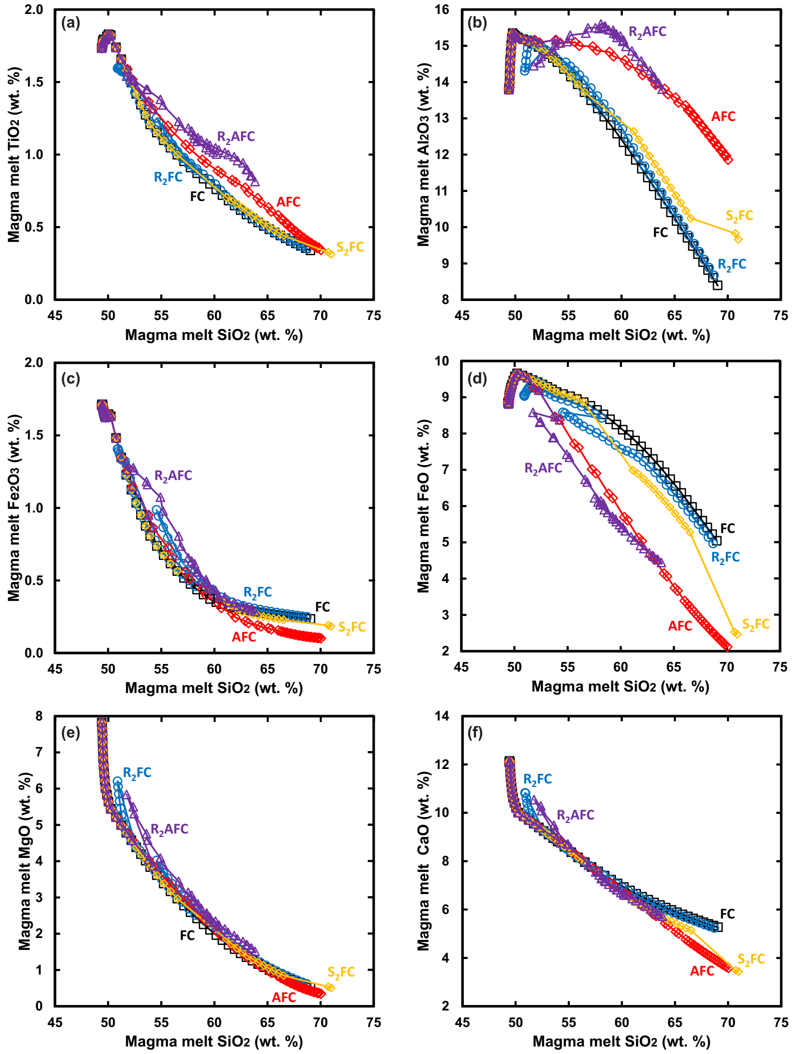

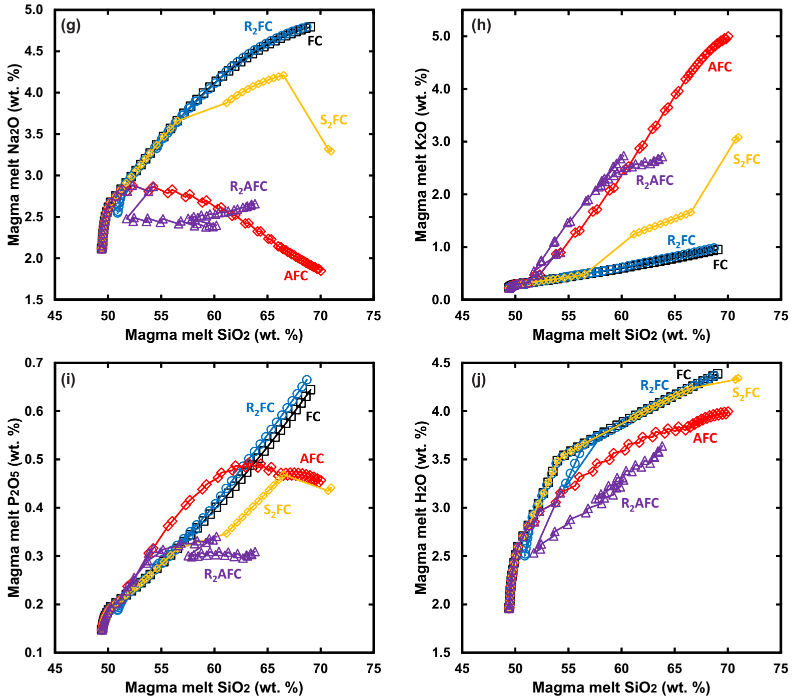

Figure 4. Results of MCS simulations for five cases (FC, AFC, R2FC, S2FC, R2AFC). Magma melt SiO2 versus wt. % MgO, CaO, Al2O3, FeO, TiO2, K2O, Na2O, P2O5, H2O (component).

3.2. Recharge-Fractional Crystallization (R2FC)

Two recharge events simulate intrusion of mantle-derived magma into resident magma melt as it evolves by fractional crystallization in an upper crustal (0.1 GPa) magma storage system. The first recharge event involves a recharge magma/initial magma mass ratio of 0.75 (that is, for an initial parent melt mass of 100 m.u., 75 m.u. are added by recharge, Table 1b). This recharge magma at ~1131°C (100 % melt) intrudes into and fully hybridizes with resident melt that is at ~1046°C (Table 1, Electronic Appendix 5). Note that the temperature at which recharge actually occurs differs slightly from that reported in the input (Table 1, 1050°C) because the recharge event occurs in the step after that target temperature is reached. Prior to the first recharge event, the resident magma had been crystallizing a mineral assemblage of olivine (Fo_{68}) + clinopyroxene (Mg_{74}) + plagioclase (An_{81}) + spinel (i.e., the same assemblage as in the FC case at this temperature). Immediately following the recharge event, the new, equilibrated state of hybridized M melt yields a new temperature of 1093°C (Electronic Appendix 2), and crystallization of clinopyroxene, plagioclase, and spinel is suppressed. Thus, in response to mixing, resident magma (melt + cumulates) temperature increases by almost 50°C, and the new hybridized magma crystallizes only olivine that is more magnesian (Fo_{77}) than the olivine that was crystallizing just prior to the recharge event. With 5°C of cooling, clinopyroxene (Mg_{82}) returns to the M crystallizing assemblage, and with an additional ~25-30°C of cooling, plagioclase (An_{82}) and spinel also return to the M mineral assemblage. For most major oxides, the first recharge event has only a subtle effect on resident melt composition: the most pronounced changes are an increase in MgO from ~4.4 to 6.2 wt.%, and a decrease in SiO_2 from 52.6 to 50.9 wt.% (Figure 4).

The second recharge event is compositionally identical to and has the same mass constraints as the first (75 m.u.), but for this recharge event, the temperature of the recharge magma is ~1080°C, which is below the liquidus for this composition. Thus, the recharge magma is 21% crystalline at the time recharge is triggered. Of this crystal assemblage, ~12% is olivine (Fo_{76}), ~82% is clinopyroxene (Mg_{81}), and ~6% is plagioclase (An_{83}). As a consequence of the second recharge event, the temperature of M increases from ~998°C to ~1040°C (Table 2), and plagioclase and spinel crystallization is once again suppressed. However, after M has cooled a further 5°C, plagioclase and spinel return to the crystallizing assemblage, but with expected changes in mineral compositions: olivine ($Fo_{55} \rightarrow Fo_{68}$) + clinopyroxene ($Mg_{69} \rightarrow Mg_{76}$) + plagioclase ($An_{71} \rightarrow An_{78}$). Resident melt reaches volatile saturation at ~1028°C, similar to the temperature of saturation in FC (~1026°C). At 985°C, orthopyroxene joins the mineral assemblage, followed shortly by rhombohedral oxide at ~980°C; orthopyroxene crystallization ceases at 955°C (Electronic Appendix 3). Importantly, some of the major oxide changes pre- and post-recharge are more profound compared to the first recharge event, because the contrast in some major elements between resident melt and recharge magma is greater. For example, from pre- to post-recharge, SiO_2 decreases from ~58 to 54.5 wt.% (as opposed to a decrease of <2 wt.% SiO_2 in M following Recharge event 1; see also Figure 4).

The final temperature of the R_2FC simulation is ~896°C, and the final melt composition is dacitic. The final R_2FC melt major oxide compositions are similar to the final melt compositions formed in the FC case; that is, the record of the increases in MgO and decreases in SiO_2 is not preserved in the final melt composition (Figure 4). The proportion of crystals, melt, and fluid phase at the final simulation temperature is similar between R_2FC and FC (~77% crystals, 22% melt, 1% fluid for R_2FC and ~76% crystals, 23% melt, 1% fluid for FC, respectively). The proportions of phases in the final cumulate are similar, with the obvious exception of orthopyroxene, which makes up ~1% of the final cumulate in R_2FC. The general range of mineral compositions is also similar (Electronic Appendix 3).

What is distinctly different between FC and R_2FC is the overall mass of the system, which is ~2.5 times greater in R_2FC because the recharge events add 150 (2 x 75) m.u. into the system. Thus, the total mass of the R_2FC system is 250 m.u., compared to 100 m.u. in the FC case. The masses of melt, cumulates, and fluid are also proportionally larger, as anticipated. Finally, the larger magma system mass significantly affects the wallrock temperature, with a final wallrock temperature of ~654°C, compared to ~330°C for FC alone (Electronic Appendix 4). The hotter wallrock is, of course, due to the added enthalpy of recharge magma intruding into resident melt. This suggests that recharge systems are more prone to induce partial melting in their host rocks due to this ‘enthalpy-pumping’ effect (all other conditions remaining constant).

3.3. Assimilation-Fractional Crystallization (AFC)

All other parameters being identical, the initial conditions of the AFC simulation contrast with those of the FC case with regard to the initial temperature of wallrock; it is 700°C compared to 100°C. This case reflects assimilation of upper continental crust by a depleted continental tholeiite evolving in an upper crustal (0.1 GPa) magma storage system. The elevated wallrock temperature is intended to maximize the assimilation signature and simulates assimilation in crust that has been thermally primed by previous episodes of magmatism.

As resident melt cools from its liquidus, it first evolves in like manner to the FC case. For a wallrock/initial magma mass ratio of 2, anatectic (wallrock) partial melt begins to contaminate magma melt at a magma temperature of ~1061°C. At this point, the wallrock is ~746°C (Electronic Appendix 2) and its percolation threshold (10%) for anatectic melt has been exceeded. Anatectic melt above this limit is transferred into, and thoroughly hybridized and equilibrated with M melt. In each subsequent magma temperature decrement step, only the mass of anatectic melt above the percolation threshold in wallrock is transferred and equilibrated with M melt. Note that because incoming anatectic melt is at a lower temperature and different specific enthalpy than M melt, the assimilation of wallrock partial melts drives M melt to a slightly lower temperature. This is a consequence of the isenthalpic AFC process. That is, the energy for partial melting of wallrock is derived by the cooling and crystallization of the M sub-system. The new, lower magma temperature following assimilation can catalyze crystallization of the contaminated melt. These crystals, like all crystals in MCS-PhaseEQ, become part of the cumulate reservoir, where they remain in thermal contact with M melt.

At the onset of assimilation, the assemblage that crystallizes continues to be olivine + clinopyroxene + plagioclase + spinel, albeit in slightly smaller proportions than before AFC onset. Contaminated melt becomes fluid saturated at ~992°C, which is ~34°C lower than the FC case. At magma temperature ~983°C, olivine becomes unstable in the mineral assemblage, and is replaced by orthopyroxene as a cumulus phase. At ~962°C, clinopyroxene crystallization ceases, and at ~948°C, rhombohedral oxide joins the stable mineral assemblage (Electronic Appendix 3).

By the terminus of the run (M-WR equilibration temperature of ~848°C), contaminated resident melt has evolved to a dacitic composition (Electronic Appendix 3); at that temperature, the final wt.% SiO_2 produced by the FC and AFC runs are within 1 wt.% (69 versus 70 wt. %, Figure 4) of each other. At the same SiO_2, AFC Al_2O_3 and K_2O have distinctly higher concentrations, whereas Na_2O, H_2O, FeO, and Fe_2O_3 are lower compared to FC. CaO, MgO, and TiO_2 are similar between the two scenarios. P_2O_5 behavior is more complicated; it is first higher, then lower at the same SiO_2 compared to FC (Figure 4).

The effect of assimilation on crystallization is marked; the proportion of crystals in the cumulate reservoir of the AFC magma system (44%) is much smaller than that associated with FC (76%); the proportion of fluid phase in AFC is also smaller than FC (0.1 versus 1%) (Figure 2, Electronic Appendix 2). The final AFC cumulate is different than the FC one; there are slightly less olivine and clinopyroxene, very similar percentage of plagioclase, and in AFC, orthopyroxene makes up ~12% of the final cumulate mode. In addition, the total ranges in olivine and plagioclase compositions are different (Electronic Appendix 3). The last olivine to crystallize in AFC is Fo_{57} (compared to Fo_{22} in FC) and the final plagioclase to crystallize is slightly more anorthitic (An_{53}) compared to FC (An_{46}). Thus, addition of anatectic melt changes not only the crystallizing assemblage (e.g., orthopyroxene precipitates, and olivine and clinopyroxene disappear as cumulus phases) but also changes the balance of melt versus cumulate. AFC also delays the onset of fluid saturation by tens of degrees, and the total proportion of the magma system that is an exsolved fluid phase is smaller (Electronic Appendix 2).

The mineral abundances of wallrock at its solidus are plagioclase >> quartz > alkali feldspar > orthopyroxene; spinel + rhombohedral oxide + apatite are accessory phases (Electronic Appendix 4). Wallrock reaches its percolation threshold temperature at ~746°C; in the first instance of partial melting above the percolation threshold, apatite reacts and ceases to be a part of the wallrock residual mineral assemblage. The restite assemblage of plagioclase + quartz + alkali feldspar + orthopyroxene, with accessory spinel + rhombohedral oxide, persists until wallrock temperature ~783°C, at which point, alkali feldspar is totally consumed (Figure 5). The remaining minerals persist in wallrock restite to the equilibration temperature.

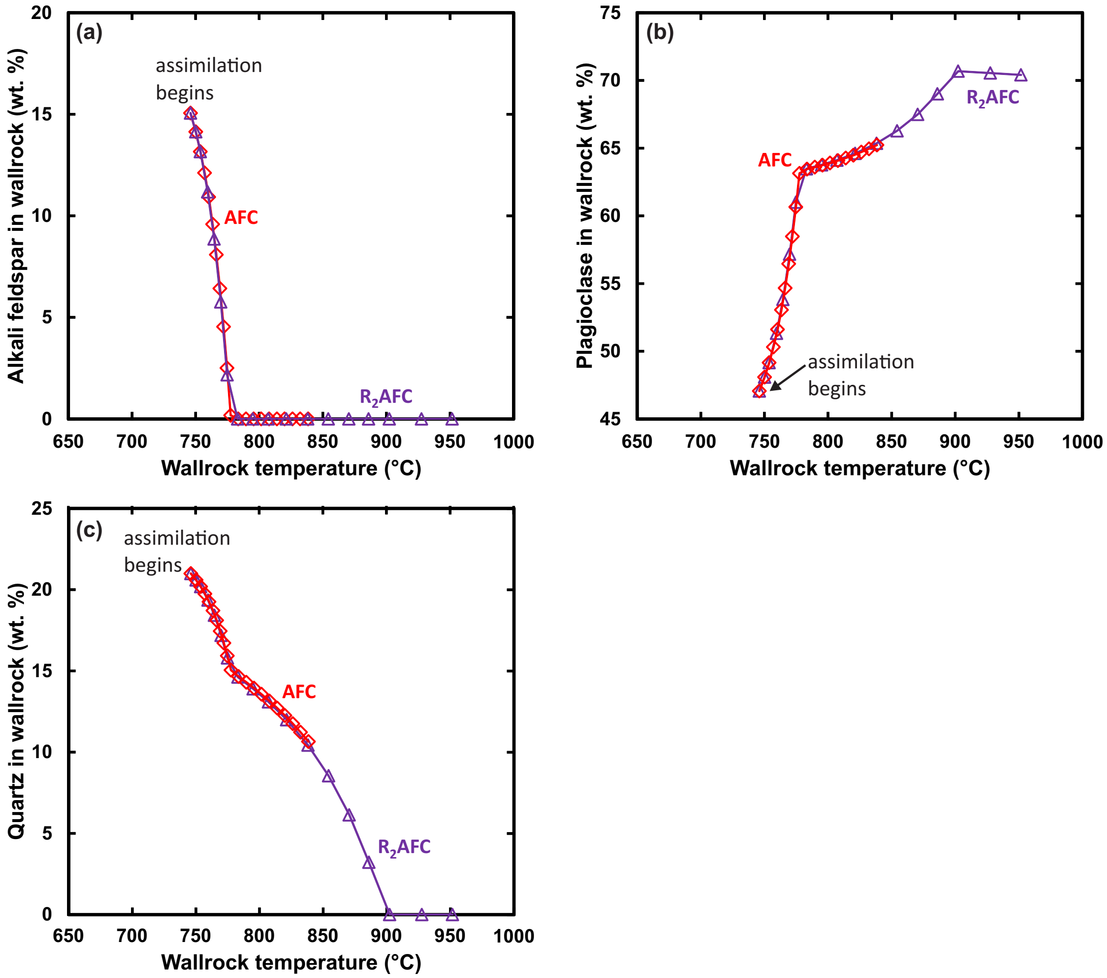

Figure 5 Wallrock temperature (°C) versus modal percent of minerals in wallrock solids (restite after partial melt is transferred to magma) for two MCS cases involving assimilation of wallrock anatectic melt (AFC, R_2AFC). Wallrock initial temperature is 700°C, and wallrock heats up to the end of the simulation, where magma and wallrock temperature are at or close to thermal equilibrium. (a) alkali feldspar, (b) plagioclase, (c) quartz. Alkali feldspar and quartz react preferentially such that they contribute less to the modal makeup of wallrock solids as wallrock heats up and partially melts. Plagioclase becomes proportionally more abundant as wallrock heats up.

For each step of anatectic melt transfer into magma melt (except the first one), the size of anatectic melt increment is ~2-3% (by mass) of the initial mass of the wallrock system (i.e., mass transfer involves ~4 to 6 m.u. of the initial 200 m.u. of wallrock). This mass rate of melt transfer changes when alkali feldspar completely dissolves. After this (wallrock T ~783°C), wallrock melt productivity decreases, and the size of the increments transferred goes down to <1% of the initial wallrock mass (<2 mass units) (Figure 6, magma T ~910°C where slope changes slightly). Anatectic melt that is transferred and homogenized with resident magma melt is mostly rhyolitic, varying in SiO_2 between ~70 (at onset of assimilation) and 76 wt. % (at the equilibration temperature). The cumulative percent anatectic melt added to the magma system can be viewed in two different ways. The total proportion of the wallrock system that was assimilated into resident magma is ~34% (~68 m.u. of the initial 200). When assessed as a part of the resident magma, this assimilated mass represents about 41% of the final magma (melt + crystals + fluid phase) body mass: ~68 m.u. of the final 168 m.u. system). By the time thermal equilibrium is attained, the wallrock has melted ~41%; this value is different than the total amount of wallrock assimilated because 10% anatectic melt remains within the wallrock system). See Electronic Appendix 2 for details of these mass relations.

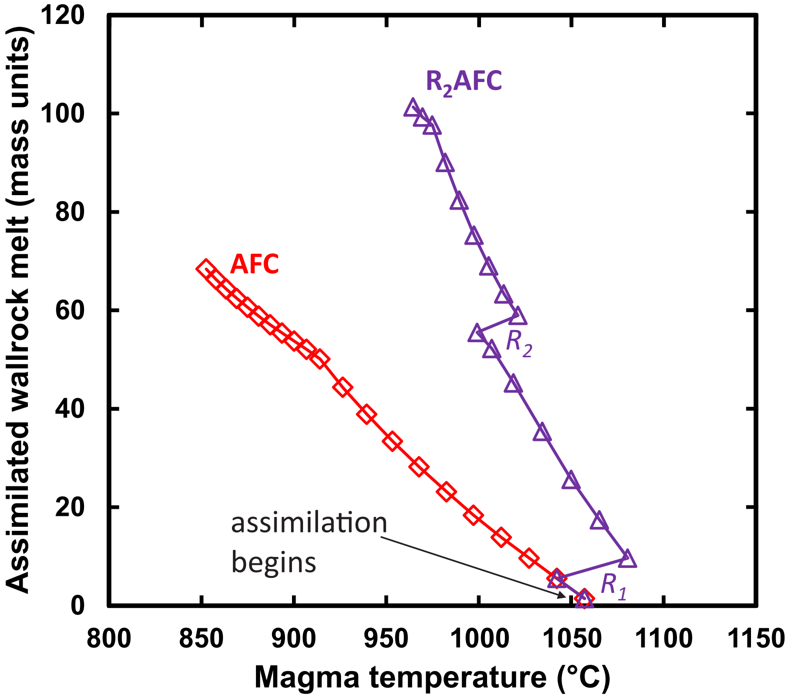

Figure 6. Magma temperature (°C) versus cumulative anatectic melt assimilated into magma once assimilation begins shown for two MCS cases with assimilation of wallrock anatectic melt (AFC, R_2AFC).

3.4. Assimilation through Stoping-Fractional Crystallization (S_2FC)

Stoping in MCS is considered as a process whereby crustal contamination occurs *via* reaction of a block (or blocks) of wallrock incorporated wholesale into magma melt. The temperature of the stoped block dictates its mineralogical and phase state; that is, the block can be stoped with different proportions of crystals, melt, and fluid phase. The S_2FC case presented here involves two stoping events, with all other parameters being identical to those of the FC case.

In MCS, stoped blocks are incorporated using the recharge function of the computer code because the thermodynamics of stoping are best replicated in MCS by the processes of recharge and hybridization. The initial (bulk) composition of the stoped blocks is identical to that of initial wallrock in the AFC case (Table 1a). Stoped block temperatures and masses were chosen to provide relevant comparison with the AFC case. For stoping event 1, the mass of the stoped block was chosen to reflect the cumulative mass of anatectic melt assimilated by M by that M temperature in the previous AFC simulation (14 m.u.; the ratio of stoped block to initial magma mass is 0.14); the temperature of the stoped block was chosen to reflect the wallrock temperature at that point as well (~760°C). At 760°C, the block is composed of ~79% crystals, 19% melt and 2% fluid phase, and its mineral assemblage is plagioclase > quartz > orthopyroxene > alkali feldspar, with spinel and rhombohedral oxide as accessory phases. The co-existing melt is rhyolitic and fluid-saturated. Prior to the first stoping event, resident magma temperature was ~1011°C, and it was crystallizing olivine + clinopyroxene + plagioclase + spinel. Following complete homogenization of the stoped block, the resident magma temperature decreased to 970°C, and orthopyroxene becomes stable in the cumulate assemblage over the range 970°C to 945°C. Rhombohedral oxide is the final phase to join the crystallizing assemblage at a magma temperature of 955°C. Upon stoping, resident magma melt SiO_2 increases from ~57 to ~61 wt. % (Figure 4 and Appendix 5).

The second stoped block reflects the conditions of the wallrock in the AFC run at M temperature ~915°C; at this temperature where the wallrock is ~778°C and cumulative anatectic melt assimilated is ~50 m.u. (ratio to initial magma mass is ~0.50). Stoped block 2 has a temperature of ~778°C and its mass is 36 units (50 – 14 that was assimilated in the first stoping event). Stoped block 2 is hotter than stoped block 1, and therefore it has proportionally more melt: crystal, melt, fluid phase percentages are 62, 36, and ~2, respectively. Its mineral composition is plagioclase >> orthopyroxene > quartz, with accessory spinel and rhombohedral oxide. Note that at ~778°C, alkali feldspar is not a part of the stoped block mineral assemblage, and, in comparison with stoped block 1, quartz is proportionately less abundant than orthopyroxene (Electronic Appendix 5). Like stoped block 1, the co-existing melt is rhyolitic and fluid saturated. For stoping event 2, the magma temperature before stoping is 915°C and after stoping is 855°C. Prior to the second stoping event, resident magma was crystallizing olivine + clinopyroxene + plagioclase + spinel + rhombohedral oxide. Following assimilation of the second stoped block, olivine and clinopyroxene cease to crystallize, and orthopyroxene becomes a part of the cumulate assemblage. Upon the second stoping event, SiO_2 increases from ~66 to ~71 wt. % (Figure 4).

This simulation ends at ~850°C, which is a similar end temperature to that of the AFC case. Compared to assimilation of anatectic melt ('classical' AFC), stoping favors crystallization, as the resultant proportion of crystals in the magma system is higher in S_2FC (66%) than AFC (44%; see Figure 2). The percent fluid phase is also slightly higher in S_2FC (Figure 2, Electronic Appendix 3). The final cumulate shares some characteristics with those of the AFC case: similar percentages of olivine, spinel, rhombohedral oxide, and orthopyroxene, slightly less clinopyroxene and slightly more plagioclase. The range of olivine composition is more similar to the FC case. Interestingly, plagioclase in S_2FC is the most albitic of all the simulations (Electronic Appendix 3). The final melt at ~850°C is on the boundary between dacitic and rhyolitic. Oxide concentrations are more similar to the FC case than the AFC case. For example, the distinct enrichment in Al_2O_3 seen in the AFC case is absent in the stoping case. Na_2O and K_2O are enriched compared to FC, but less so than AFC (Figure 4).

The final temperature of wallrock is 294°C. This is the lowest final wallrock temperature of the five simulations. Upon stoping, in the new equilibrium magma melt, quartz and alkali feldspar (where present in the stoped block) are not stable. Hence, there is an enthalpy cost to resorbing/reacting these phases, which decreases enthalpy available for transfer into the wallrock.

3.5. Recharge-Assimilation Fractional Crystallization (R_2AFC)

The two recharge events from the R_2FC case were imposed on the AFC case; recall that the wallrock initial temperature is high (700°C). For the two recharge events, like R_2FC, the recharge magma/initial magma mass ratio is 0.75, and the temperatures of the recharge magmas at the instance of recharge are 1131°C and 1080°C for recharge events 1 and 2, respectively. Also, like R_2FC, recharge magma 1 is 100% melt, and recharge magma 2 is 21% crystalline, with a mineral assemblage of clinopyroxene >> olivine > plagioclase. Assimilation begins at magma temperature of ~1061°C as in the AFC run, and by recharge event 1, M has assimilated ~5.5% anatectic melt (where percent is calculated based on the initial mass of resident magma - i.e., cumulative addition of 5.5 m.u. of anatectic melt).

Immediately preceding recharge event 1, the magma temperature is ~1037°C, with a crystallizing mineral assemblage of olivine + clinopyroxene + plagioclase + spinel. In response to recharge event 1, the resident magma temperature increases to ~1087°C, and plagioclase and spinel stop crystallizing. SiO_2 decreases from ~54 to 52 wt.% and MgO increases from 3.9 to 5.8 wt.% (Figure 4, Electronic Appendices 1-5).

After the first recharge event, AFC continues; at ~1050°C, spinel rejoins the crystallizing assemblage, and at magma temperature ~1019°C, orthopyroxene starts to crystallize and at ~1014°C, plagioclase rejoins the crystallizing assemblage. Recharge event 2 is triggered after the resident magma has cooled to 994°C, and heats the resident magma, increasing its temperature to ~1024°C. Olivine crystallizes for a short temperature interval, and plagioclase and orthopyroxene stop crystallizing. After ~10°C of cooling, the mineral assemblage returns to its pre-recharge assemblage of clinopyroxene + plagioclase + spinel + orthopyroxene. At 992°C, clinopyroxene ceases to crystallize, and magma melt reaches fluid saturation (with a mixed H_2O + CO_2 fluid), but the proportion of fluid phase in the magma system is quite small (<0.1). At 977°C, rhombohedral oxide joins the assemblage. A modest change in melt composition is noted; upon recharge, SiO_2 again decreases, this time from ~60 to 57.5 wt.% and MgO increases from 2.2 to 3.1 wt.% (Figure 4).

The equilibration temperature for R_2AFC is ~960°C. The final magma melt composition is distinctly lower in SiO_2 compared to the other four simulations and plots at the low SiO_2 end of the dacitic field. R_2AFC manifests a similar enrichment in Al_2O_3 and K_2O compared to AFC; likewise, the depletions in FeO, H_2O and Na_2O are similar to AFC (Figure 4). P_2O_5 is the least enriched among all cases. Like AFC, R_2AFC suppresses crystallization. Crystals make up only ~40% of the magma body mass in the R_2AFC run, compared to ~76%

in FC, and R_2AFC expresses the smallest degree of fluid saturation. The range of olivine and plagioclase compositions is more similar to AFC than FC, with the most Fe-rich olivine being Fo_{65} and the most Na-rich plagioclase being An_{69}.

For each step of anatectic melt transfer into magma melt (except the first one), the size of anatectic melt increment is ~2 to 5% of the initial mass of the wallrock system (i.e., 4 to 10 m.u.). This changes after alkali feldspar completely reacts and ceases to be part of the wallrock solid assemblage. After this (wallrock temperature of ~783°C, magma temperature ~1007°C, Figure 6), melt productivity decreases, and the size of the increments transferred decreases to 1-2% of the initial wallrock mass (3 m.u.). Like the wallrock melt in AFC, the anatectic melt that is transferred and homogenized with resident magma melt is mostly rhyolitic (~70 to 76 SiO_2).

At the equilibration temperature of ~960°C, ~51% of the wallrock system has been assimilated into the resident magma. Thus, substantially more anatectic melt was assimilated due to recharge, consistent with more enthalpy being available from magma cooling and crystallization to heat wallrock compared to AFC. However, when assessed as a percentage of the resident magma system, this assimilated mass represents only ~29% of the final magma body (melt +crystals + fluid phase) mass - in contrast to 41% of the final magma body in the AFC case (Electronic Appendix 2). Like the R_2FC case (compared to FC), the size of the magma body system (melt + cumulate + fluid phase) is substantially greater than AFC, and considering the larger mass assimilated, the addition of recharge magma “dilutes” the crustal signature.

4 Discussion

It is instructive to compare outcomes of the cases described above (FC, R_2FC, AFC, S_2FC, R_2AFC) to illustrate how fractional crystallization, recharge, and assimilation (by wallrock melts or stoped blocks) affect the evolution of the composite shallow crustal magma system. The compositions of M, WR, and R magmas are intentionally kept constant in order to focus upon process and sequence rather than sub-system compositions. These cases reflect a very small fraction of possible RASFC scenarios, but they do underscore some of the challenges petrologists face in trying to diagnose processes that dictate magma compositions.

4.1 Comparison of Thermal and Mass Characteristics

The final modeled wallrock temperature is related to the overall size of the magma body, the mass of cumulates formed, and the mass and thermodynamic state of the recharge magma/anatectic melt/stoped blocks added to the magma system. AFC and R_2AFC provide a contrast that illustrates the impact of magma recharge; the final wallrock temperature of R_2AFC (951°C) is higher than that of AFC (844°C), reflecting the addition of recharge magma with its attendant enthalpy. All other parameters of these simulations are the same, including the initial wallrock temperature of 700°C. The added enthalpy from hotter recharge magma into resident magma yields a larger increase in wallrock temperature during resident magma cooling and crystallization. Not only is there more resident magma to cool, but the mass of crystals formed in R_2AFC is also greater, adding more latent heat of crystallization available for wallrock heating and partial melting. The higher final wallrock temperature also means that wallrock melts to greater extent for R_2AFC than AFC (56% versus 41%, respectively). More anatectic melt is transferred into the magma body per decrement of magma cooling (Figure 6), and thus, the cumulative amount of wallrock partial melt transferred is larger in

R_2AFC: of the total mass of wallrock, 51% anatectic melt is added to resident melt in R_2AFC compared to 34% in AFC (Electronic Appendix 2). However, while the total mass of anatectic melt added to resident melt is larger in R_2AFC than AFC (~101 versus 68 m.u.), the percentage of the magma system mass that comes from anatectic melt is smaller (29% in R_2AFC versus 41% in AFC) due to the added recharge magma mass that makes the R_2AFC total magma system mass larger (~351 versus 168 mass units for R_2AFC versus AFC, respectively, Electronic Appendix 2). These collective differences, although perfectly clear in hindsight, are neither trivial nor easily predicted. Furthermore, the enhancement of assimilation in systems with significant recharge might not be obvious geochemically due to the effects of recharge in diluting the signature of assimilated partial melt. Even in this simple comparison, one notes the complex feedbacks that can take place. The magnitude of these non-linear compositional effects varies depending on most of the sensible variables of a given simulation.

The final wallrock temperatures for FC, R_2FC and S_2FC are 330°C, 654°C, and 294°C (Electronic Appendix 2), respectively. The lowest temperature of the stoping case is due to addition of cold blocks of wallrock. In addition, minerals in the blocks such as quartz and alkali feldspar are not stable after the blocks equilibrate with resident melt. The energetic cost of resorbing these is debited to the magma, and thus magma has less enthalpy available to transfer to wallrock. The higher wallrock temperature of R_2FC of 654°C (compared to FC and S_2FC) is a function of added enthalpy due to recharge and underscores the energy impact and thermal priming potential that recharge can have: with two recharge events of modest recharge to initial magma mass ratio (0.75), the wallrock temperature increases from its initial (100°C) to a temperature that reflects a relatively high geothermal gradient akin to the assimilation cases presented here. Different wallrock/initial magma mass and recharge/initial magma mass ratios as well as different compositions will yield different outcomes, but the thermal impact of recharge may be profound in some cases.

The total size of the magma system (which does not include the residual wallrock) is an obvious outcome of MCS, and one that is simple to contrast. FC, a "closed-system" process, yields the smallest magma body size, where the magma body includes resident magma melt + cumulates + fluid phase. The AFC and S_2FC cases are ~1.5 to 1.7x bigger than the FC magma body, R_2FC is ~2.5x bigger, and R_2AFC is ~3.5x the biggest (Electronic Appendix 2; these comparisons relate masses upon completion of the simulation). These differences are obviously related to addition of recharge magma, anatectic melt and/or stoped crustal blocks and have implications for the sizes of potential eruptions, the growth of the crust (i.e., mass of magma added to the crust), its state of stress, and local geotherms.

Another difference, not necessarily obvious, is the percent melt versus crystals among these different magma systems. AFC and R_2AFC suppress crystallization, compared to the other cases. In the AFC and R_2AFC cases, the cumulate reservoir composes about 40-44% of the resident magma system, whereas it is ~76% of the magma body mass in the FC and R_2FC cases; S_2FC yields approximately 66% crystals (Electronic Appendix 2). Suppression of crystallization is caused by addition of anatectic melt, which changes the temperature-composition relationships such that the mass of crystals that form per decrement of cooling of resident melt is lower when assimilation is ongoing (e.g., the slope of the magma temperature versus percent cumulative crystals is lower for AFC and for the assimilation-influenced parts of the R_2AFC compared to FC and R_2FC, Figure 7). Thus, in the two cases that invoke assimilation, the total magma system is dominated by melt: 56% for AFC and 60% for R_2FC (Electronic Appendix 2). The higher equilibration temperature for R_2AFC plays a role in the high proportion of melt, but even if the slope of the R_2AFC magma temperature versus percent cumulative crystals trend (Figure 7) is extrapolated to a higher final magma temperature, the percent crystals is still lower than the R_2FC and FC cases. Note that although the proportion of crystals in R_2AFC is smaller than in FC and S_2FC, the total mass of crystals is larger, as expected from the larger total system mass. This outcome leads to the prediction that basaltic systems recharged with magmas similar to the initial parent magma will build large cumulate piles whereas basaltic systems that experience contamination by average upper crust will be melt dominated systems.

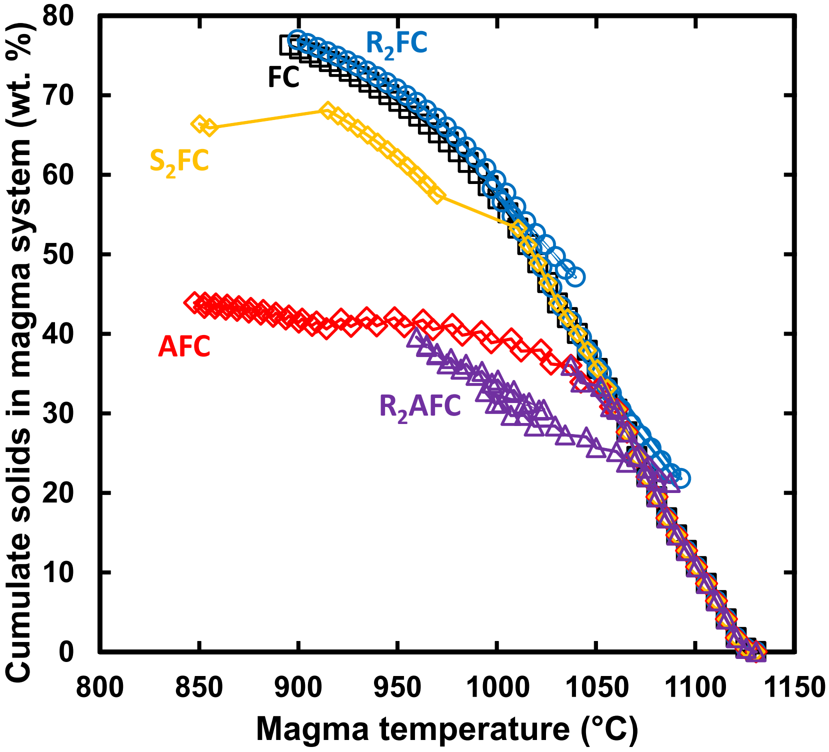

Figure 7 Magma temperature (°C) versus percent cumulative crystals in magma system in the five MCS simulations (FC, AFC, R_2FC, S_2FC, R_2AFC). Thus, of the total mass of the magma system (that has potentially undergone assimilation of partial melts or wholesale stoped blocks of wallrock and/or magma recharge), crystals compose ~40% of the AFC and R_2AFC cases whereas the other three cases are more crystal-rich systems (~65% and greater).

Explicit tracking of instantaneous and cumulative masses of minerals crystallized and anatectic melt assimilated (versions of the DePaolo (1981) “r” constant) provides a platform by which to examine the mass ratio of anatectic melt assimilated to the mass of cumulates formed during AFC. Here, *instantaneous* refers to the ratio of the mass of anatectic melt assimilated divided by the mass of crystals formed in a single (circa 5 °C) AFC magma temperature decrement (i.e., crystallization followed by assimilation), in the case when recharge occurs (R_2AFC), the crystal mass includes crystals formed upon recharge added to those that form in a fractional crystallization "event.". Cumulative refers to the total mass of anatectic melt divided by the mass of crystals from the first step in the simulation to the present temperature step. For AFC, instantaneous and cumulative "r" values vary from 0.4 to 3.0 and 0.05 to 0.94, and for R_2AFC from 0.16 to 1.9 and 0.05 to 0.78, respectively (values reflect start of assimilation to end of the simulation, Figure 8). For the first part of the AFC instantaneous and cumulative trends (from ~1057°C to 914°C), the productivity of melt in wallrock is relatively high; this leads to systematically increasing values of instantaneous "r" as magma temperature goes down. The marked change in instantaneous "r" between ~914°C and 907°C reflects decreased anatectic melt productivity as alkali feldspar fully reacts, and this change is reflected in the change in slope of the cumulative plot as well (Figure 8).

For the R_2AFC case, instantaneous and cumulate "r" are the same as AFC until the first recharge event. Upon recharge (event 1, R_2AFC, Figure 8a, labeled "recharge event 1 complete"), instantaneous "r" increases very little compared to the AFC case. This is because the first recharge event does not yield abundant crystal formation, and it also does not significantly change the mass of crystals fractionated in a magma temperature decrement. The decrease in R_2AFC instantaneous "r" at temperatures between ~1019°C and 999°C (before recharge event 2) occurs because alkali feldspar in the wallrock is fully reacted, and anatectic melt productivity decreases as a result. A consequence of the second recharge event (that brings the magma temperature up to ~1023°C, Figure 8a, labeled "recharge events 2 complete"), is a short-lived pulse of crystallization, and both instantaneous and cumulative "r" decrease. Following this, the somewhat complex trend seen in the instantaneous "r" is the result of changes in crystallization as the magma system responds to being heated by recharge as well as the changing mineral composition of wallrock and the associated consequences on wallrock melt production.

Three outcomes of the analysis above are that (1) crystallization and assimilation "rates" are difficult if not impossible to predict in the absence of thermodynamic treatment, and thus, (2) quantitative thermodynamic treatment of RAFC processes is absolutely essential to characterize these processes. The exact response of wallrock to melting and magma to recharge are dictated by the thermal, mass, and compositional character of the players, and these in turn influence the "rate" of mass assimilated to mass crystallized. (3) These rates are therefore neither predictable nor constant, and models that use constant "r" values do not reflect the complexity of RAFC processes. Given the availability of computational tools that provide thermodynamic estimations of magma systems, using tools that lack phase equilibria treatment of igneous systems may, at best, provide only rough estimates of natural processes and therefore should be used with considerable caution. In addition, one should be wary of conventional arguments and inferences often applied when analyzing petrological and geochemical data. Many of these notions are based on closed system behavior, despite the now common understanding that closed magmatic systems are generally the exception rather than the rule.

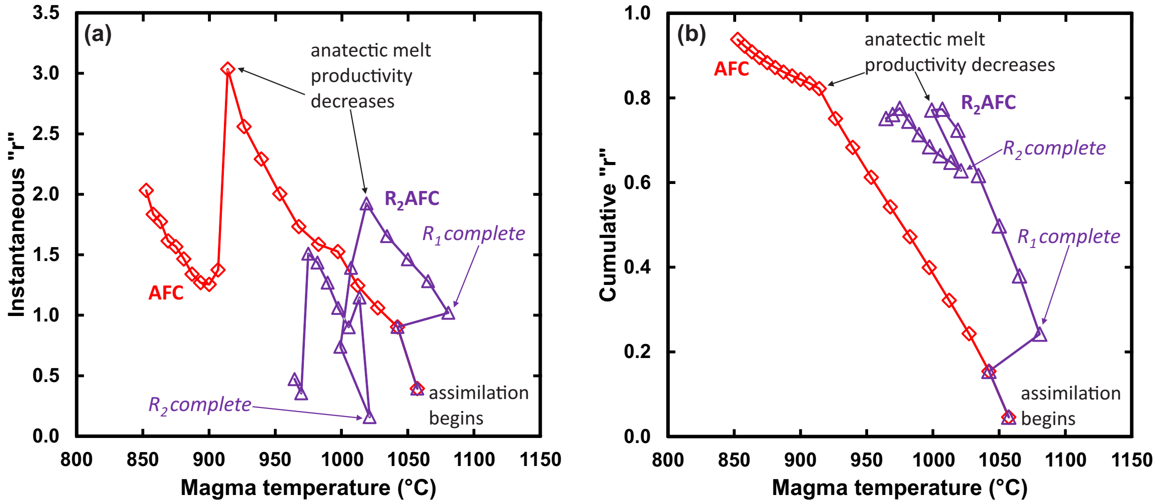

Figure 8. Magma temperature (°C) versus (a) instantaneous “r”, and (b) cumulative “r” shown for two MCS cases with assimilation of wallrock anatectic melt (AFC, R_2AFC). The definition of “r” is based on DePaolo (1981) and is the mass of anatectic melt assimilated/mass of crystals formed. Instantaneous refers to those masses for each individual temperature step where assimilation ± recharge occurs, and cumulative refers to the total mass of anatectic melt assimilated/total mass of cumulates produced from the start of the simulation to the magma temperature shown. The value of “r” is zero before assimilation begins, and for simplicity, this part of the AFC or R_2AFC is not shown. Instantaneous and cumulative “r” after completion of recharge events 1 and 2 labeled, as are the values at which anatectic melt productivity decreases due to complete reaction of alkali feldspar. See text for discussion.

4.2 Geochemical and Petrological Indicators of Open-System Processes

The major oxide signatures of open-system magmatic processes manifest in ways that may not be obvious or intuitive. Among the best indicators of open-system processes are radiogenic and stable isotopes, assuming that there is isotopic contrast between resident magma, crust, and recharge magma. Why then toil to identify or quantify fingerprints of RASFC using major element data? The first reason is practical; typically, many more samples are analyzed for major elements than for isotopes and some trace elements. Being able to identify key samples that have potentially undergone open-system processing based on major elements (and/or mineral chemical compositions and identities) enables judicious choice of samples for more expensive and time-consuming trace element and isotopic analysis. Second, careful reconstruction of major element characteristics as well as the crystallizing mineral assemblage is required for accurate calculation of trace element and isotopic signatures of an open-system magma *via* the use of mineral/melt and mineral/fluid distribution coefficients. *Thus, to document trace element and isotopic open system signatures, one must know the open-system history of melt, minerals, and fluids*. The third reason is that a higher number of constraints (major oxides, trace elements, isotopes) leads to better models, and better models lead to more refined interpretations. More quantitative constraints on individual magmatic systems will lead to enhanced understanding of a broad range of issues that are not only important for academic study, but may also have broader societal implications. For example, assimilation of distinctive anatectic melts potentially produces different resident magma major element and mineral responses, and identifying the most likely wallrock may aid in narrowing the location of the resident magma system. In turn, determining whether a magma storage system is more likely located in the shallow versus deep crust has implications for volcanic eruption monitoring and hazard mitigation. All such models should naturally always be assessed in relation to MCS-independent evidence such as geophysical constraints.

What, then, are definitive major element and/or phase equilibria markers of RASFC processes? Indicators of these processes vary depending on the relevant masses, temperatures, and compositions of resident magma, recharge magma(s), and wallrock(s). Below, major element and phase equilibria comparisons are highlighted that illustrate the complexity of identifying open-system processes and emphasize the value that thermodynamic computational modeling brings to identifying such processes.

4.2.1 Identifying the Fingerprint of Magma Mixing from Melt and Mineral Data

Classic linear trajectories often ascribed to binary mixing are not present in many of the R_2FC major element plots (e.g., SiO_2 versus MgO, Na_2O, TiO_2; Figure 4). This is because homogenization is followed by crystal removal through fractional crystallization. The inverse is also true; there are segments of some of the FC oxide arrays that are approximately linear (e.g., K_2O, P_2O_5, H_2O, Al_2O_3 at SiO_2 > ~55 wt. %), and thus may resemble mixing trends.

For FC and R_2FC, most of the oxide trends (plotted versus MgO) are very similar, and these trends underscore the difficulty of diagnosing process via some major element trends (Figure 4). But some oxides can show distinctive behavior with recharge. In the simulations highlighted here, MgO is the most telling. Its concentration changes beyond analytical uncertainty when recharge with a more primitive magma occurs, but the difference between FC and R_2FC is subtle and might be difficult to detect in a suite of samples that lack stratigraphic control. Sampling with excellent stratigraphic (i.e., age) control may reveal excursions to higher MgO after recharge events (Figure 4a), but sampling frequency, field exposure, and analytical uncertainty will play a role in capturing (or not) the record of recharge events.

As recognized in numerous studies, crystal cargo (e.g., Davidson et al. 2007; Streck 2008, and references therein; Edwards et al. 2019, Ubide et al. 2019; Ubide and Kramer 2018; Streck et al. 2008; Ginibre et al. 2007; Davidson et al. 1997) can provide a rich inventory of mixing histories, but the modeling results presented herein indicate that in some cases, these records may be selective. For example, in R_2FC, the complete record of mixing is not preserved in plagioclase, which is not stable upon mixing, but returns to the stable assemblage within ~30°C of cooling after the first recharge event and ~10°C of cooling after the second. Its compositional change is small after the first event (An_{81} to An_{82}) but larger and detectable after the second (~An_{71} to An_{78}). In stark contrast to plagioclase behavior, olivine crystallizes both before and after mixing, thus potentially recording a complete phase equilibria record of the effects of mixing. The mineral changes composition abruptly from Fo_{68} to Fo_{77} after the first recharge/mixing event, and from Fo_{54} to Fo_{68} after the second event. These changes are easily detected by electron microprobe analysis, provided the zoning is preserved.

Crystals produced during mixing may also preserve a record of temperature changes. For R_2FC, the temperature of the magma increases 40-50 degrees after each recharge/mixing event. That record may be preserved in mineral geothermometry, depending on the uncertainty of the calibration, and with the caveat that minerals (as noted) may selectively preserve evidence of the temperature increase. In R_2FC, olivine and clinopyroxene would be the best indicators of the temperature change, as they preserve the most complete record of mixing. In contrast, plagioclase would not likely record heating associated with the first recharge event for the reasons discussed in the previous paragraph. The takeaway lesson from this single example is that in order to fully document temperature excursions associated with recharge that are recorded in minerals, one needs a complete picture of the phase equilibria changes that occur in response to the mixing event. Even with such data, documenting temperature changes may be challenging given the equilibrium requirements and uncertainties of many geothermometers (e.g., Putirka 2017).

The presence or absence of distinctive recharge signatures is, of course, a function of the magma mixing scenario. In the cases highlighted here, the same parent magma is mixed into its evolving counterpart. Different scenarios will, of course, lead to different mixing fingerprints. For example, the mass of the recharge event compared to the resident magma/melt mass will influence the extent to which pre- and post-recharge magmas change composition, and a substantial compositional contrast between resident melt and recharge magma may yield recharge signatures that are more obvious than those presented here. Myriad forward modeling case studies can be done in MCS to examine the temperature, composition, and mass landscape of mixing and crystallization processes.

4.2.2 Identifying the Fingerprint of Crustal Assimilation from Melt and Mineral Data

Similar to the FC *versus* R_2FC comparison, some major elements do not show evidence of crustal assimilation. For example, AFC and R_2AFC are generally similar to FC and R_2FC in SiO_2 versus MgO (with the exception of the notable change immediately after the recharge events for R_2AFC and R_2FC) and CaO. This is an interesting result given the anatectic melt and recharge magma have very different concentrations of these oxides, and yet, the SiO_2 versus CaO and MgO trends are indistinguishable for these 4 cases at >55 wt.% SiO_2 (Figure 4).

In contrast, three major elements that show quite distinct differences are K_2O, Na_2O, and Al_2O_3. Once assimilation begins, Al_2O_3 is more concentrated in AFC and R_2AFC than in their non-assimilation equivalents (at the same SiO_2). Because these cases contrast with respect to not just the bulk composition of the “added” material, but also in the mass and identity of cumulus phases, there could be a number of explanations for these differences. The total final percentage of cumulus plagioclase in FC and AFC is similar (~39%) whereas for R_2AFC, it is smaller (~28%) (Electronic Appendix 3). Thus, for FC and AFC, about the same final proportional amount of plagioclase was removed as a fractionating phase, but that final tally obscures differences as the systems evolve. Reference to Figure 3 shows that plagioclase makes up a smaller proportion of the cumulate assemblage in AFC, compared to FC, for most of the simulation. The reason the final proportions are similar is because the end temperature of AFC (~848°C) is lower than that for FC (~896°C), which provides a longer crystallization temperature interval for plagioclase in the AFC case. For most of the AFC simulation, for each cooling step, less plagioclase forms, and thus the resident melt is not debited in Al_2O_3 as extensively as in the FC case. In the case of R_2AFC, Al_2O_3 is slightly higher at the same wt.% SiO_2 than in the AFC case and reflects the lower cumulate plagioclase proportion, compared to AFC (Electronic Appendix 3). Thus, less Al_2O_3 is removed from resident melt. R_2AFC and AFC have distinctly lower Na_2O at the same SiO_2 (once assimilation begins), whereas K_2O is distinctly higher than FC and R_2FC. The bulk composition of wallrock and the way it melts are responsible for these differences. Alkali feldspar melts disproportionately into anatectic melt, enriching the melt in K_2O. Plagioclase (~$An_{37\text{-}35}$), on the other hand, disproportionately increases in abundance in wallrock restite, and thus, anatectic melt addition dilutes Na_2O in resident magma melt (Electronic Appendix 4).

The remaining oxides also show differences, but they are less pronounced. FeO is slightly lower for the two assimilation cases, compared to FC and R_2FC, due to dilution by the anatectic melt. Fe_2O_3 in AFC is similar to slightly lower than FC due to minor dilution, and R_2AFC is slightly higher because of the recharge events. TiO_2 is modestly enriched in AFC and R_2AFC compared to FC and R_2FC. For R_2AFC, the TiO_2 concentration of the recharge magma is higher than that of resident melt when recharge occurs, and thus addition of recharge may explain the enrichment. But anatectic melt is less enriched in TiO_2 compared to resident melt when assimilation begins, which might suggest the opposite effect—that contaminated magma would have lower TiO_2 concentrations relative to FC. The most likely reason for the slight enrichment of AFC compared to FC is the delay of crystallization of rhombohedral oxide, which does not join the crystallizing assemblage until ~948°C, compared to 981°C for FC. P_2O_5 is initially slightly elevated in the AFC case (i.e., once assimilation begins), and then is lower compared to FC and R_2FC. The reason is twofold. First, the initial

P_2O_5 in wallrock is higher than the magma probably because the small amount of apatite in wallrock is depleted (i.e., reacts) early. Eventually however, anatectic melt addition dilutes P_2O_5 in magma melt. Likewise, in R_2AFC, P_2O_5 is initially slightly elevated compared to FC and R_2FC because of the reasons noted above. The first recharge event has a very slight dilution effect on P_2O_5, compared to AFC. As assimilation continues, P_2O_5 begins to be diluted, and a second recharge event reduces P_2O_5 even more compared to FC and AFC. The subsequent relatively flat R_2AFC SiO_2-P_2O_5 slope signals an even competition between enrichment due to crystallization versus dilution due to assimilation. Resident melt H_2O is less concentrated in AFC and R_2AFC compared to FC and R_2FC. While wallrock is fluid-saturated upon initiation of melting, the fluid phase is not incorporated into magma melt in MCS although H_2O dissolved in anatectic melt is. Once assimilation begins, dilution due to anatectic melt addition is evident, and lower rates of crystallization (i.e., mass of crystals fractionated per decrement of cooling in resident magma) of anhydrous minerals in the AFC case lessens the amount of enrichment. R_2AFC parallels the AFC trend until the first recharge event, which dilutes H_2O. The second causes additional dilution. The combination of lower rates of crystallization and recharge yields the lowest magma melt H_2O contents of all the cases by the termination of the simulation.

Based on the analysis above, for the AFC and R_2AFC cases presented here in which a depleted basalt is being contaminated by anatectic melt from average upper continental crust, the only major element and phase equilibria indicators that are likely to be diagnostic is the resident melt K_2O, which is enriched by ~5x (by the end of the AFC versus FC simulation, Electronic Appendix 3) compared to the concentration expected for a basalt that has undergone ~76% fractional crystallization (Electronic Appendix 2, Figures 3 and 7). In the context of the comparison of AFC/R_2AFC and FC, the source of the enrichment is obvious, but incomplete sampling, especially of the more mafic end of the samples might obscure the degree and source of enrichment. In addition, an expectation that crustal assimilation would lead to more profound and obvious changes in other oxides might yield a misinterpretation of these data that attributes the geochemical signals to mantle heterogeneity. Likewise, depletion of Na_2O might be easily misinterpreted as representative of mantle heterogeneity and/or alteration. While the AFC/R_2AFC Al_2O_3 versus SiO_2 trends are distinct from those of FC, Al_2O_3 may be difficult to interpret as its concentration is partly a function of the amount of plagioclase crystallization, and plagioclase stability is controlled not only by composition, but also pressure and H_2O content. Thus, the higher Al_2O_3 may not be easily connected to assimilation. We emphasize that these results are case specific, and underscore the importance of open-system models that evaluate phase equilibria.

Mineral fingerprints of assimilation are potentially preserved in the cumulate assemblage (Electronic Appendix 3). The most obvious is the presence of orthopyroxene, which is not stable in FC and is in much smaller proportion in R_2FC (~1%) compared to >10% for AFC and R_2AFC. Orthopyroxene is likely stabilized by SiO_2 added by anatectic melt; on the other hand, fractionation of orthopyroxene enriches M melt in SiO_2 less than crystallization of olivine so the effect of adding SiO_2 into the system by assimilation is counteracted (Figure 4a). Other modal differences for the cumulate assemblages are evident. For example, olivine and clinopyroxene do not crystallize for the full AFC simulation whereas they do in FC.

Similar to predictions about the effects of magma recharge and mixing, the case studies involving assimilation bring into focus the difficulty of postulating *a priori* the patterns expected on Harker variation diagrams and in mineral compositions and identities. Major element and mineralogical responses to these processes may not be easily predicted or distinguished. The overarching conclusion of the recharge and assimilation case studies is that using closed system reasoning may produce misleading and spurious conclusions because the effects of these processes are non-linear and non-intuitive.

4.2.3 Distinguishing the Mode of Crustal Contamination: Crustal Assimilation versus Stoping

Here, we compare and contrast AFC and S_2FC to illustrate a possible range of effects from different mechanisms of crustal contamination. Evidence of bulk assimilation of stoped blocks compared to assimilation of anatectic melt is preserved in some oxide trends, but not in others.

In the S_2FC scenario, SiO_2 versus MgO and CaO are quite similar to AFC, and TiO_2, Fe_2O_3, and P_2O_5 show only subtle differences (Figure 4). In contrast, Al_2O_3, FeO, K_2O, Na_2O, and H_2O are markedly different for AFC versus S_2FC. For the first stoping event, Al_2O_3 versus SiO_2 has a slope that is rather similar to FC and R_2FC trends, and thus is much lower in concentration (at the same SiO_2) compared to AFC. While the Al_2O_3 content of the stoped block is slightly higher than resident melt, this addition is apparently offset by a "pulse" of plagioclase crystallization (described in the next paragraph) that removes Al_2O_3. While intuition may dictate that adding an Al-rich stoped block would lead to increased Al_2O_3 in M melt, this will not always be the case and the given example again illustrates how simplistic reasoning can be misleading (e.g., polyphase mixing is *not* identical to melt-melt mixing). Likewise, Al_2O_3 remains at lower concentrations compared to AFC during and after the second stoping event for the same reason. Spinel also experiences a pulse of crystallization with both stoping events, and likely contributes to the lower Al_2O_3 in the S_2FC case. Na_2O has values that are higher than AFC; by the first stoping event, Na_2O in M sub-system melt is more concentrated than the bulk composition of the stoped block, and thus resident melt Na_2O is lower because of dilution. FeO behaves like Na_2O; it is diluted slightly by stoping. K_2O is not as enriched as in the AFC case because the stoped block K_2O concentration is lower than that of anatectic melts. This is a direct result of the difference in style of contamination. Through assimilation by stoping, bulk wallrock contaminates resident melt, whereas the process of partial melting in the AFC model changes the K_2O content (as well as other oxides) of anatectic melt, thus significantly enriching the resident melt in it. H_2O is more enriched at a given SiO_2 in S_2FC than in AFC because all of the fluid phase is transferred into resident melt via stoping, as opposed to remaining in wallrock restite in the AFC case. The aspect of allowing fluid phase to remain in wallrock rather than travel with the fluid-saturated anatectic melt is a feature that may be modified in a future version of the MCS by including an option regarding the mobility of the fluid phase.

Assimilation by stoping also has an effect on the cumulate assemblage. Upon homogenization of the first stoped block, all of the quartz and alkali feldspar react away. As noted above, a “burst” (i.e., large mass) of plagioclase crystallizes (Figure 3) (x7 more than had been crystallizing in prior magma temperature decrements) in response to assimilation of the stoped block. Spinel also experiences a crystallization “burst” (increase by x6), but the total mass is much smaller than plagioclase. Similar to stoping event 1, during homogenization of stoped block 2, quartz completely reacts, and, plagioclase and spinel crystallization “bursts” occur, and these are proportionally much larger than after stoping event 1 (e.g., for plagioclase, ~x28 more than had been crystallizing in prior magma temperature decrements). While plagioclase continuously crystallizes in both AFC and S_2FC, the mass, thermal and compositional records are quite different. In AFC, each set of fractional crystallization-assimilation "events" yields about the same mass of plagioclase, and its composition varies smoothly from An_{82} when assimilation begins to An_{53} at the simulation's termination. The temperature record is also smoothly varying with decreases of ~15°C per fractional crystallization-assimilation "event". For the stoping events 1 and 2, there is a dramatic increase in the rate of plagioclase crystallization and plagioclase Na content (from An_{75} to An_{66}, and from An_{52} to An_{42}), and the melt temperature decreases are ~41°C and 59°C, respectively. Both of these changes would be detectable by modern analytical methods. By the end of the simulation, plagioclase in S_2FC is distinctly more albitic than that in AFC (An_{41} versus An_{53}), consistent with the addition of Na_2O from stoped blocks compared to the "dilution" effect seen in AFC. The difference in plagioclase composition highlights the difference in bulk addition of a stoped block versus partial melting of wallrock. Partial melting favors reaction of alkali feldspar over plagioclase, and thus the resulting anatectic melts substantially enriches resident melt in K and depletes it in Na. These elemental differences influence the M melt phase equilibria response.

4.3 Quantifying Mantle versus Crustal Contributions to Magma Systems

A key goal in petrology and geochemistry — to distinguish and quantify how mantle versus crustal contributions to a magma system change in space and time — informs models of crustal growth and evolution, models of mantle evolution, and mass and thermal fluxes between these reservoirs. The literature abounds with studies of magmatic systems in which geochemical and petrologic signatures are quantitatively or qualitatively attributed to mantle versus crust (e.g., Hildreth and Moorbath 1988; Asmerom et al. 1991; Arndt et al. 1993;

Wooden et al. 1993; Baker et al. 2000). Modeling results presented here illustrate the complexity associated with this enterprise and some potential pitfalls. The FC case assumes that mantle-derived magma intrudes the crust and undergoes fractional crystallization without involvement of any crust. Thus, the entire compositional signal derives from the mantle. Magmas that have undergone only fractional crystallization without interaction with crust and/or recharging magmas are likely uncommon given the realities of moving low-viscosity materials through large sections of crust of contrasting composition as well as the episodic nature of magma intrusion. The case of FC only is therefore admittedly a simplification but serves as a point of comparison. Based on many thousands of MCS models collectively run over the past several years, it seems a top-down rather than bottom-up strategy be employed when addressing the crust heterogeneity *versus* mantle contribution question. Once plausible and potential RASFC scenarios are fully explored (i.e., running many MCS models), remaining discrepancies between model results and data from the natural system might then be postulated to be caused by mantle heterogeneity of the M subsystem magma.

5 Magma Chamber Simulator: Assumptions and Limitations

The main limitation (by design) of the MCS is that it is a thermodynamic model. Paradoxically, this is also its greatest strength, as elaborated in this study. Kinetic, microscopic, and macroscopic time-dependent transport phenomena are not accounted for explicitly in the MCS. Heat and matter are instantaneously exchanged (although serially or concurrently ordered, according to user input) between wallrock, magma (melt + cumulates) and recharge/stoping subsystems. Although the criterion that a threshold fraction of melt be attained in wallrock before partial melt is added to and equilibrated with resident melt is informed by the rheological properties of crystal-liquid mixtures (Lesher and Spera 2015), the mass of partial melt added is simply the difference between the evolving local melt fraction in wallrock and a user-defined threshold value. There is no Darcy percolation *per se*. Transport details justifying melt extraction dynamics are given elsewhere (Spera and Bohrson 2001; Bohrson et al. 2014). Because the MCS is a thermodynamic model, no absolute timescale beyond the ‘arrow of time’ defined by the user-specified RASFC scenario is implied. A specific RASFC scenario produces an evolutionary record of melt composition, cumulate petrology, anatectic melt composition, wallrock residual mineralogy and pre-mixing state of stoped blocks and recharge magmas. MCS results are deterministic in a temporally ordered way, but the absolute flow of time is not addressed. Quantification of timescales can be approximated using simple scaling arguments based on observed petrographic and mineralogical features such as mineral zoning and magma mixing times (Oldenburg et al. 1989; Costa et al. 2008; Spera et al. 2016) in consort with MCS results. A critic might object to the purely thermodynamic approach noting that many irreversible processes with concomitant entropy production (heat conduction and convection, chemical diffusion, transport of momentum by the action of viscosity) surely come into play during the evolution of magmatic systems. Although this may be true, experience has shown that local equilibrium is indeed often attained in high temperature petrologic systems. The very existence of a host of useful geothermometers, geobarometers, and geohygrometers (e.g., Putirka 2008, 2017; Wade et al. 2008; Coogan et al. 2014; Neave and Putirka 2017) frequently applied with success to estimate temperature, pressure, and volatile contents of magmas as well as the consistency of laboratory experiments with observed features in natural magmatic systems (e.g., Bowen 1928; Yoder and Tilley 1962; Grove et al. 1992; Villiger et al. 2007) supports the notion that a thermodynamic approach serves as a reference standard. Natural systems in all their rich observational detail can be compared to predictions of models based on the assumption of local equilibrium. Deviations between prediction and observation leads to refined input parameters, further simulations, and eventually valuable insights into magmatic evolution. Using the MCS in this iterative mode allows one to sort out the sequence of RASFC processes and put constraints on end-member compositions and thermodynamic intensive variables such as temperature, pressure, redox conditions, volatile compositions and contents.

A second, and somewhat more prosaic limitation of the MCS is the quality of the thermodynamic data that underpins the rhyolite-MELTS computational engine. These data include the standard state properties of all phases, activity-composition relations for all crystalline solutions defined by end-members with known standard state properties, the mixing properties of H_2O-CO_2 supercritical fluids and the Gibbs excess free energy model for silicate liquids. The latter gives the excess Gibbs energy of silicate melt as a function of composition, temperature, and pressure for multicomponent silicate melt. *Any thermodynamic model is no better than the data upon which it is based*. On the other hand, the MELTS thermodynamic database is the best available model for MCS purposes. Examples of limitations of MELTS in this context are thermodynamic models of activity-composition relations for garnet, trioctahedral mica, and amphibole family phases. Hence in volcanic and plutonic rocks where these phases are modally abundant, the predictions of system evolution are relatively more uncertain. A final limitation is the coverage in p-T space for which the MELTS engines are optimized. This range is roughly 1000-2000 K and 0 to 3 GPa, limiting modeling to the outer ~ 100 km of Earth and deeper on smaller bodies such as the Moon, Mars, Venus, Mercury and the asteroids. Fortunately, this coverage is sufficient for a great variety of igneous environments that may be modeled with MCS. For additional details on the

MELTS family of codes, the reader should refer to the MELTS website (http://melts.ofm-research.org/) and primary MELTS literature cited earlier.

6 Magma Chamber Simulator: Future Developments

The MCS has undergone continuous development and improvement since its first incarnation and its functionality is being continually expanded. Here, four major extensions presently under development are reviewed.

A critical enhancement of MCS is to free it from its dependence on Mac Excel, which is a temperamental platform on which to build and sustain development. A high priority for MCS is to port the code to a new platform with an accessible web user interface.

The second extension is to allow some fraction of earlier formed cumulates in the M sub-system to react with melt. Currently, in MCS, once cumulates form, although they remain in thermal equilibrium with M melt, no chemical reaction is permitted. However, it is not unreasonable to imagine that ambient M melt can be quite reactive with earlier formed cumulates. The concept of crystal resorption has been part of the petrological literature for a long time (e.g., Fries 1939; Wiebe 1968; Couch et al. 2001; Ginibre et al. 2007; Erdmann et al. 2012); orthopyroxene rims on olivine-cored crystals is perhaps the type example (e.g., Ambler and Ashley 1977). Such ‘back-reactions’ are currently not enabled in MCS, and this extension would enable some or all of previously formed cumulates to react with ambient melt.

A third MCS future development is to implement a Monte Carlo version of the MCS. For example, to run a single RAFC simulation, circa 50 parameters should be specified in the MES input file. In attempting to model a natural system, one recognizes that there are inherent uncertainties in these parameters. To acknowledge and address these when modeling magmatic systems, the MCS algorithm can be extended by adoption of a Monte Carlo approach. The concept is to acknowledge that each input parameter should be specified as a possible *range* of values (e.g., SiO_2 of the wallrock lies between 67 and 69 wt.% etc.). Once ranges for *all* input parameters have been defined, the algorithm will select randomly or by Bayesian methods a *particular* set of initial conditions. These conditions are then used in an MCS simulation and results are archived in a searchable database. In this manner, thousands or even tens of thousands of MCS models can be run, each with a unique set of input parameters and associated output. Once archived in a searchable database, the user can then ask questions such as: Of the thousands of simulations run, which ones compare best to the data from the particular natural system under study? Using this Monte Carlo approach, solutions can be filtered to find the best fit to observables using some objective criterion such as the residuals of the squared differences between the model and the observations.

Finally, a fourth extension to the MCS model is to attach to the RASFC back-end calculation a front-end calculation to determine the initial M sub-system melt composition. This would be a calculation that would allow a wholly crystalline source to be decompressed along some p-T path. For instance, the p-T path could be an isentropic one or some other dp/dT path set by the user. Additional parameters could be set to constrain the style of partial melting (e.g., batch, fractional, or incremental batch). In addition to the decompression p-T path mode, partial melting could also be isobarically triggered by the addition of heat or volatiles. Then, melt could be extracted once a critical fraction has formed. In all cases, the state of residue and melt would be tracked in composition-p-T coordinates as appropriate. This addition would allow a user to thoroughly explore, within the confines of the available thermodynamic treatments (e.g., MELTS family of models), how chemical and mineralogical heterogeneity in the mantle, and variability introduced during mixing and partial melting in the crust, influence the igneous products under study.

7 Conclusions

Magmatic processes are recorded by high fidelity elemental and isotopic records derived from integrated studies of the petrography, petrology, mineralogy, geochronology and geochemistry of magmatic products including whole-rock bulk compositions, glasses, melt inclusions, crystal cargo, and lithic inclusions, both cognate and xenolithic. Textures and compositions of magmatic products from many well-documented volcanic and plutonic systems suggest that open system exchange of material and energy is more the rule than exception. Analysis of these attributes suggests that open system behavior is dominated by crystal fractionation, magma mixing, and the interaction of magmas with their host environments *via* partial melting and stoping of wallrock. This collection of processes is referred to as RASFC, and an important task for the petrologist and geochemist is to unravel the most important processes by quantification and temporal ordering. Establishing a magmatic 'arrow of time' is intrinsically a complex task due to the vast range of time and spatial scales involved—from microns to kilometers and from hours to several million years. Deciphering such records demands a variety of approaches.

The Magma Chamber Simulator was developed as a rigorous open system thermodynamic tool for addressing RASFC processes governing the evolution of multicomponent-multiphase composite systems of wallrock, resident magma, and recharge/stoping reservoirs. RASFC scenarios are computed in the primary MCS tool (MCS-PhaseEQ) by minimization or maximization of appropriate (constraint-dependent) thermodynamic potentials using one of four MELTS engines coupled to a Visual Basic interface that performs executive, logical, computational and graphical functions for each sub-system. Heat derived by cooling and crystallization of resident magma passes to wallrock that heats up and potentially undergoes partial melting. Wallrock partial melt above a percolation threshold passes through the wallrock-magma boundary and achieves chemical potential equilibrium with magma. Crystals that form in response to magma cooling and anatectic melt contamination of resident magma become part of a cumulate reservoir that is chemically but not thermally isolated from resident magma. In addition to AFC, discrete instances of magma mixing and contamination by recharge and/or stoping can occur in a single RASFC scenario. Each recharge magma or stoped block has a unique pre-mixing thermodynamic state of bulk composition, melt composition, phase identity and modal abundance, and temperature. Recharge magmas and stoped blocks hybridize and equilibrate with resident magmas to yield a new magma composition and temperature. Crystals present in recharge magmas or in stoped blocks may resorb upon mixing, and any new crystals that form during the equilibration process join the cumulate reservoir. The MCS output includes a plethora of information on all materials in the sub-systems in an organized format, including many tables and graphs. There are countless applications of the MCS. Model constraints on natural systems and forward modeling results provide quantitative insight into mantle versus crustal contributions to terrestrial magmas, and the chronology of magma mixing by recharge, the assimilation of partial melts or of stoped blocks (solid or mushy) and fractional crystallization. RASFC processes are recorded by *in situ* crystal data, the record of magmatism preserved in cumulates, and in exsolved or trapped fluids. Case studies of FC, R_2FC, AFC, S_2FC, and R_2AFC illustrate the range of information provided by MCS and illustrate the distinctive signatures of RASFC processes. The trace element and isotope MCS computational tool (MCS-Traces) and its implications on the same cases presented here are described in part II.

Chapter 5: Diagnosing open-system magmatic processes using the magma chamber simulator (MCS): Part II – Trace elements and isotopes

1 Introduction

Phase equilibria in magmatic systems at given P-T-conditions is controlled by the major element composition and thermodynamic properties of the magma. Major (± minor) elements are usually reported as oxides in geochemical datasets and are primary stoichiometric constituents of mineral phases that are stable in the magma. Modeling of phase equilibria and major element evolution of an igneous system requires knowledge of the thermodynamic properties of the liquid + solid + fluid phases present in the system. These include the standard state properties of all end-member components in all phases as well as the activity-composition relations of all phases.

The Magma Chamber Simulator (MCS; Bohrson et al., 2014) is a computational tool that uses the family of MELTS engines (Ghiorso and Sack, 1995; Ghiorso et al., 2002; Gualda et al., 2012; Ghiorso and Gualda, 2015) to numerically quantify these parameters in an open-system resident magma body subsystem (M: melt ± solids ± fluid) that evolves by fractional crystallization (FC) and can simultaneously experience magma recharge/mixing (R) and assimilation of either anatectic melts (A) and/or stoped blocks (S) of wallrock (WR). The utilization and application of *MCS-Majors* and its bearing on the evolution of phase equilibria and major elements has been described in a companion paper (Bohrson et al., submitted).

Trace elements are found in dilute quantities (usually ≤ 0.1 wt.%) and are not primary stoichiometric constituents of common phases in magmatic systems. They generally do not influence phase equilibria, but their relative concentrations and isotopic compositions can nevertheless record important information about the sources and evolution of magmatic systems. The activities of trace elements vary in direct relation to their concentrations, and their behavior is controlled primarily by their relative compatibility among melt, solids (i.e., minerals) and fluid. This behavior is defined by a partition coefficient (K), which in igneous petrology is a ratio of the concentration of an element in a mineral versus the concentration of the element in the melt (K_{sm}) or fluid (K_{sf}) in equilibrium with the mineral. Because information on the composition and relative amounts of stable phases in a magmatic system is required to constrain bulk partition coefficients (D_{sm} and D_{sf}), detailed modeling of trace elements is not possible without a record of phase equilibria of the system.

In this study, we describe the *MCS-Traces* Visual Basic tool that uses primary *MCS-Majors* output as input and adds equations for modeling up to 48 trace elements in a R_nAS_nFC system. In addition to quantitative results from *MCS-Majors*, program input includes initial trace element concentrations for the M parental melt, R_n ($n \leq 30$), and WR, and K_{sm} (± $K_{s/H2O}$ ± $K_{s/CO2}$ for possible fluid phases) values for M and WR. For more advanced modeling, an option to take account the T-dependence of K values is available. In addition to trace elements, *MCS-Traces* computes radiogenic isotope ($^{87}Sr/^{86}Sr$, $^{143}Nd/^{144}Nd$, $^{176}Hf/^{177}Hf$, $^{206}Pb/^{204}Pb$, $^{207}Pb/^{204}Pb$, $^{208}Pb/^{204}Pb$, and $^{187}Os/^{188}Os$ as defaults) and stable O isotope ($\delta^{18}O$) compositional evolution of the open-system resident melt based on user-input isotope ratios for the parental resident melt, WR, and each R magma. A description of the tool is provided along with results and comparisons of case studies that correspond to the ones introduced in the companion paper. An example of *MCS-Traces* applied to a natural magmatic system (continental flood basalts) is given in Heinonen et al. (2019).

2 Architecture and Operational Details of *MCS-Traces*

2.1. How does MCS-Traces work?

MCS-Traces utilizes the output ("RunSummary") of the *MCS-Majors* modeling tool (Bohrson et al., submitted). This output is read as the manual for what is going on in the R_nAS_nFC system (in terms of phase equilibria and mass balance) and *MCS-Traces* executes the trace element and isotope calculations based on it and user-input initial concentrations, isotope ratios, and K values. Fluid composition primary output is used by the *MCS-Traces* tool to calculate K_{sf} values and temperature information is required for runs with T-dependent K values. Because of these utilizations, *MCS-Traces* cannot be used without output from a successfully executed *MCS-Majors* model. The MCS-derived trace element solution has the advantage of being self-consistent and more complete in the sense that a proper reckoning is made between trace elements and isotopes and major element phase compositions, modal abundances, pressure, and temperature.

The tool itself is composed of two main parts: 1) the user interface built in Visual Basic environment, and 2) the trace element and isotope engine that is a separate Excel worksheet, in which all the computations are performed. In short, the user interface feeds input into the engine and, after the calculations have been performed, collects the output in an easily accessible and digestible form that is then amalgamated as a set of additional worksheets with the original *MCS-Majors* output. Consequently, the entire petrological-geochemical solution to a complex RASFC scenario is given in one workbook with multiple tabs. More detailed descriptions are given in the following sections and on the MCS website (https://mcs.geol.ucsb.edu/).

2.2. Trace element and isotope equations

The basic framework of modeling trace elements and isotopes in *MCS-Traces* is described in Bohrson et al. (2014); we will complement and update that description here. The trace element equations for equilibrium crystallization in a melt ± solid ± fluid system developed by Spera et al. (2007) form the backbone of the trace element engine:

$$\frac{C_m}{C^0} = \left[f_m(1 - D_{sm}) + D_{sm}\left(1 - f_f\right) + \frac{f_f D_{sm}}{D_{sf}}\right]^{-1} \tag{1}$$

$$\frac{C_s}{C^0} = D_{sm}\left[f_m(1 - D_{sm}) + D_{sm}\left(1 - f_f\right) + \frac{f_f D_{sm}}{D_{sf}}\right]^{-1} \tag{2}$$

$$\frac{C_f}{C^0} = D_{sm}/D_{sf}\left[f_m(1 - D_{sm}) + D_{sm}\left(1 - f_f\right) + \frac{f_f D_{sm}}{D_{sf}}\right]^{-1} \tag{3}$$

In equations 1–3, C_m, C_s, and C_f stand for trace element concentration in the melt, solid, and fluid, respectively, whereas C^0 is the initial trace element concentration in the system in internal equilibrium. D_{sm} and D_{sf} are solid/melt and solid/fluid bulk partition coefficients for a given element, and f_m and f_f mass fractions of melt and fluid, respectively. D values for M (D_{sm}^{M} and D_{sf}^{M}) and WR (D_{sm}^{WR} and D_{sf}^{WR}) are calculated on the basis input element-specific K values and the mass fractions of stable equilibrium phases (x) for each step, as shown below:

$$D = \sum_i^n x_i K_i \tag{4}$$

Note that magma recharge/mixing and assimilation by stoping involve homogenization of bulk R magma or WR, and thus, the partitioning of elements into solid, melt and fluid is not relevant to the mass balance of the recharge/mixing and stoping trace element and isotope calculations; therefore, constraints on $K_{sm} \pm K_{sf}$ are only needed for M and, in the case of AFC, for WR.

If a separate fluid phase consisting of either H_2O or CO_2 or both (possible in *MCS-Majors* runs using rhyolite-MELTS 1.1.0 or 1.2.0 engines) is saturates in M and/or WR, respective K_{sf} values have to be input. When the fluid phase contains both components, the effective K_{sf} is computed according to:

$$K_{sf} = \frac{w_{H2O}}{K_{s/H2O}} + \frac{1-w_{H2O}}{K_{s/CO2}} \tag{5}$$

in which w_{H2O} is the mass fraction of H_2O in the fluid phase and $K_{s/H2O}$ and $K_{s/CO2}$ are the solid-H_2O and solid-CO_2 partition coefficients, respectively.

Also, T-dependence of K_{sm} and K_{sf} can be invoked in *MCS-Traces*. The engine calculates the K at a given temperature [°C] logarithmically based on A and B values, which, in turn are calculated based on two user-input K values at two different temperatures [°C]:

$$K(T) = e^{\left(\frac{A+BT}{T}\right)} \tag{6}$$

$$A = \frac{T_1 T_2 \ln\left(\frac{K_2}{K_1}\right)}{T_1 - T_2} \tag{7}$$

$$B = \ln K_2 - \frac{A}{T_2} = \ln K_2 - \frac{T_1 \ln\left(\frac{K_2}{K_1}\right)}{T_1 - T_2} \tag{8}$$

The temperature-dependence of K is identical in form to that of any reaction with the isobaric heat capacity change of the reaction set to zero. Note that for many elements and solid phases, the effects of composition (of melt and the solid phases themselves) and temperature (and other physical and chemical factors) on K values are difficult to distinguish from each other (e.g., Blundy and Wood, 2003). These effects, however, are also effectively intertwined in magmatic systems, and, for example, T-dependency can thus be used to approximate the compositional dependency with some caution (e.g., Blundy and Wood, 1991).

For M, each temperature step is considered to be an equilibrium crystallization step. At the end of the step and before the model proceeds, however, the newly formed solid phases are fractionated from M in a solid cumulate reservoir. Similarly, newly formed fluid is fractionated in a "cumulate" fluid reservoir. In equations 1–3 for M, C^0 thus represents the composition of M melt initially or at the end of the previous fractionation step. In equations 1–3 for WR, which is always in internal equilibrium, C^0 represents the bulk composition of WR initially or after the previous anatectic melt removal event. When a mass of WR melt, R, or S is added to M melt, simple mixing equations are utilized to calculate the resulting hybridized composition of M melt:

$$C_M = f_M C_M^{prev.\ step} + (1 - f_M) C_{WR\ melt/R/S} \tag{9}$$

In the case of assimilation of WR partial melt, the assimilated mass of the trace element is then removed from the WR reservoir.

In the case of isotopes, isotopic equilibrium within the subsystems (M, WR, R) and high-T isotope fractionation during melting and crystallization is not taken into account. Minor high-T fractionation of relatively light O isotopes during melting and crystallization is a well-known process, but the geochemical effect of this fractionation is generally quite small (usually <1 ‰ in a magmatic series) compared to that of adding isotopically distinct components into resident melt (e.g., Eiler, 2001). Therefore, and because additional input of such fractionation factors would be needed for each stable phase, high-T fractionation of O isotopes is not considered in *MCS-Traces*. Simple mixing between the subsystems is assumed in the case of all isotope compositions (ε):

$$\varepsilon_M = f_M\left(\frac{C_M^{prev.\ step}}{C_M}\right)\varepsilon_M^{prev.\ step} + (1 - f_M)\left(\frac{C_{WR\ melt/R/S}}{C_M}\right)\varepsilon_{WR\ melt/R/S} \quad (10)$$

For O isotopes, O mass fractions are calculated for the M melt, R, and WR melt (or S) on the basis of MCS major element output at each step.

2.3. General overview of using MCS-Traces

For detailed instructions on the operation and input and output of both MCS tools, the reader is referred to written instructions and instructional videos on the MCS website (http://mcs.geol.ucsb.edu); a generalized overview of the *MCS-Traces* is presented here.

MCS-Traces should be run with the same Macintosh platform and Macintosh Excel version that was used to run *MCS-Majors* (see Bohrson et al., submitted). *MCS-Traces* should never be updated or configured separately from *MCS-Majors* and, in the case of possible updates, we always recommend downloading the most up-to-date versions of both programs from the website. An internal compatibility check performed by the Visual Basic software will prevent use of outdated or otherwise incompatible *MCS-Majors* output in the *MCS-Traces* tool. If one has used *MCS-Majors* to produce output required for *MCS-Traces*, the installation of the whole MCS package has been successful.

2.3.1. Input

The general layout of *MCS-Traces* Visual Basic interface is presented in Figure 1. The command buttons are set so that the default work flow proceeds primarily downwards and secondarily from left to right. Note that the worksheet should never be saved, even when the worksheet suggests it when closing Excel.

After selecting the desired *MCS-Majors* output, trace elements to be modeled can be selected from the periodic table. Selecting Sr, Nd, Hf, Pb, Os, or O will enable isotopic modeling by default. Titanium, Cr, Ni, Mn, and Co are disabled as trace elements if these were modeled as respective oxides in *MCS-Majors*.

The third and fourth row of buttons are used to set phase- and element-specific K values and initial trace element concentrations and isotopic ratios for the M parental melt and WR. The solid phases available for K input correspond to ones listed in the *MCS-Majors* output file (Bohrson et al., submitted); all solids are defined by the MELTS algorithms and are related to how MELTS treats solid-solutions. Input of $K_{s/H2O}$ and/or $K_{s/CO2}$ values is only possible if fluids are present in the model (either in M or WR or both). For all K values, it is possible to input constant or T-dependent values.

The fifth row of buttons (for a run involving R or S) is used to set trace element concentrations and isotopic ratios for the R magma(s) and stoped WR blocks. The concentration input is not bound to a unit so the user can input the concentrations in ppm, ppb, or any other unit as long as the unit is uniform across the different subsystems. Isotope ratios can be input in the case of Sr, Nd, Hf, Pb (three ratios), Os, and O. This fifth row of buttons will appear only if the *MCS-Majors* output file for that particular run has one or more recharge/stoping events.

MCS-Traces provides an option to load pre-defined sets of concentrations, isotope ratios, and K values or save the values input in the form of so-called PAR files. The user can filter what data, and for which subsystem, is loaded or saved. It is also possible to modify and build PAR files manually in Excel. Some recommended sources for K_{sm} values for igneous systems are Rollinson (1993) and the Geochemical Earth Reference Model (GERM) Partition Coefficient Database (https://earthref.org/KDD/). A compilation of K_{sf} values is available in Spera et al. (2007), and the reader is also directed to the original publications that support this compilation.

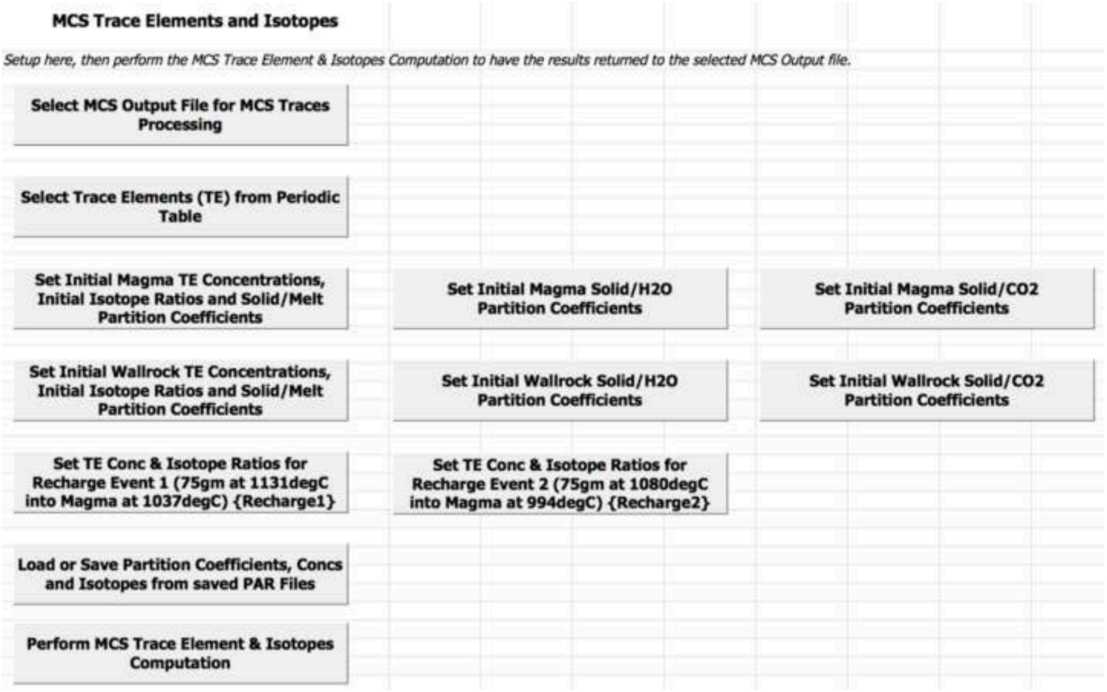

MCS Trace Elements and Isotopes

Setup here, then perform the MCS Trace Element & Isotopes Computation to have the results returned to the selected MCS Output file.

Figure 1. The user interface of the *MCS-Traces* tool. The number of buttons on rows 3–5 vary according to the uploaded *MCS-Majors* output. In this run, which is the R$_2$AFC case analyzed in this study (see section 3.5), both M and WR contain a fluid phase composed of a mixture of H_2O and CO_2, and two R events took place.

2.3.2. Output

Once the computation is complete, the *MCS-Traces* output can be accessed by opening the original *MCS-Majors* output file in any version of Excel on Macintosh or PC capable of opening .xlsx files: two to three new tabs in the *MCS-Majors* output worksheet have been produced. Note that *MCS-Traces* can be run multiple times against the same *MCS-Majors* output file, the double/triplet tab sets are then distinguished by numbers (X = 1, 2, 3…, see below) as they are introduced.

The tab "Traces_X_Magma" tabulates all the information regarding the trace element and isotope budget in the magma chamber (namely melt, fluids, and cumulate pile). The topmost rows echo the *MCS-Traces* input (trace element concentrations, isotope ratios, and *K* values) regarding the parental and recharge magmas. Selected columns from the primary *MCS-Majors* output are also echoed, and *MCS-Traces* output for each temperature step is presented in thematic clusters. Note that any possible negative solid and fluid masses (these are related to how MELTS algorithm performs the calculations; see MCS website) have been approximated as zero for the trace element calculations. This ensures that these very small negative masses of mineral phases do not cause negative trace element concentrations for those elements which have high K_{sm} or K_{sf} values. The effect of this approximation on the trace element model results was determined to be negligible (<0.1% difference in regards to total masses, i.e., less than the analytical error of any major and trace element geochemical data). The tab "Traces_X_Wallrock", which is only included in cases involving A, tabulates all the information regarding the trace element budget in the WR (i.e., melt, fluids, and residual WR) and has a similar structure to the "Trace_X_Magma" tab. Finally, tab

“Traces_X_OUTPUT” tabulates the full output from the *MCS-Traces* computation. This data compilation allows the user access to all the values calculated by the *MCS-Traces* engine.

3 Comparison of Closed (Fractional Crystallization) and Open-System Magma Evolution Illustrated by MCS

We present and compare trace element (Ni, Sr, Zr, Ba, La, Nd, and Yb) and isotopic ($^{87}Sr/^{86}Sr$, $^{144}Nd/^{143}Nd$, and $\delta^{18}O$) results of the same five MCS simulations presented in the companion paper (Bohrson et al., submitted). These models are: fractional crystallization (FC), fractional crystallization + assimilation of wallrock anatectic melts (AFC), fractional crystallization + recharge (n = 2) (R_2FC), fractional crystallization + assimilation by stoping (n = 2) (S_2FC), and fractional crystallization + recharge (n = 2) + assimilation of wallrock anatectic melts (R_2AFC). The input and results of *MCS-Majors* modeling are only briefly outlined here to place the trace element and isotope results in context. The reader should refer to Bohrson et al. (submitted) for details of initial conditions and thermal, mass, phase equilibria, and major element output.

The *MCS-Majors* models used a depleted mantle-derived tholeiite from ~180 Ma Karoo large igneous province as the initial melt and recharge magma (sample P27-AVL; Luttinen and Furnes, 2000) with ~2 wt.% of H_2O added. Initial redox conditions were set at quartz-fayalite-magnetite (QFM) buffer, but the run itself was closed for oxygen, i.e., oxygen fugacity was determined by the relevant internal chemical equilibria of the system. This tholeiite has the following trace element composition used as input in the *MCS-Traces* tool: Ni = 154 ppm, Sr = 226 ppm, Ba = 70 ppm, Zr = 86 ppm, La = 4.97 ppm, Nd = 10.53 ppm, and Yb = 1.73 ppm. The radiogenic isotope composition was set to that of mean modern MORB ($^{87}Sr/^{86}Sr = 0.702819$ and $^{144}Nd/^{143}Nd = 0.513074$; Gale et al., 2013) and O isotope composition was also adopted based on representative analyses of MORB glasses ($\delta^{18}O$ = 5.5 ‰; Eiler et al., 2000).

Wallrock and the stoped blocks represent the granodioritic average upper continental crust of Rudnick and Gao (2003) with ~2 wt.% of H_2O and 1 wt.% of CO_2 added and initial Fe oxidation state set at QFM. It has the following trace element composition: Ni = 47 ppm, Sr = 320 ppm, Zr = 193 ppm, Ba = 628 ppm, La = 31 ppm, Nd = 27 ppm, and Yb = 1.96 ppm. The radiogenic isotope composition has been constrained on the basis of global river waters ($^{87}Sr/^{86}Sr$ = 0.716 and $^{144}Nd/^{143}Nd$ = 0.51178; Goldstein and Jacobsen, 1988) and the O isotope composition is within the range of felsic crustal rock types ($\delta^{18}O$ = 12 ‰; Eiler, 2001). In the models involving assimilation of wallrock partial melts (AFC and R_2AFC), the mass of WR was twice that of the initial M, and the percolation threshold (fmzero) of the WR was set to a melt mass fraction of 0.1. The degree of contamination of the resident magma can be presented in two sensible ways in the models: 1) relative to the mass of the parental melt or 2) relative to the mass of the resident magma chamber (the whole M subsystem). The former may be relevant for cases without recharge, but here we use the latter approach that is in line with the companion paper. Note that the models that do not involve assimilation of WR anatectic melts (FC, R_2FC, and S_2FC) still included WR in the modeling for the purpose of studying its thermal evolution due to heat released by the cooling and crystallizing magma (Bohrson et al., submitted). Therefore, initial composition and K_{sm}^{WR} values were part of the input in *MCS-Traces* modeling also in these three cases. Because the temperature of the wallrock does not reach its solidus, and hence no anatectic melt forms or is assimilated by the resident melt, however, the input values do not affect the outcome of these models, and can thus be ignored.

Models were run at 0.1 GPa with an M temperature decrement of 5 °C. K values used in the models have been compiled from Drake and Weill (1975), Bacon and Druitt (1988), Ewart and Griffin (1994), Boudreau (1999), and Kessel et al. (2005) and are listed in Table 1. We selected consistent sets of K_{sm} values widely used and appropriate for the modeled compositions. K_{sf} values (for H_2O and CO_2) are 1000 for all general runs to minimize incompatible element concentrations in the fluid phase. We also ran a FC trace element model that utilized more realistic D_{sf}^{M} values (Kessel et al., 2005), and illustrates the partitioning of mobile elements (D_{sf}^{M} for Sr, Ba, La, and Nd < 1) into a separate fluid phase in the resident magma. Two additional trace element models were constructed for the FC case to illustrate the effects of using elevated $K_{ol/m}^{M}$(Ni) and $K_{cpx/m}^{M}$(Ni) (Norman et al., 2005) and K_{sm} T-dependence ($K_{plg/m}^{M}$(Sr); Drake and Weill, 1975). The latter effect was also studied for the AFC case (T-dependent $K_{plg/m}^{M}$(Sr) and $K_{plg/m}^{WR}$(Sr)). The total number of *MCS-Traces* runs illustrated and discussed below is thus nine (four FC models: default, T-dependent $K_{plg/m}^{M}$(Sr), element-specific D_{sf}^{M} values, and high $K_{ol/m}^{M}$(Ni) and $K_{cpx/m}^{M}$(Ni); one R_2FC model; two AFC models: default, T-dependent $K_{plg/m}^{M}$(Sr) and $K_{plg/m}^{WR}$(Sr); one S_2FC model; and one R_2AFC model).

Table 1. Element- and phase-specific K_{sf} values used in the MCS simulations.

Resident Magma	ol	cpx	plg	spl	opx	rhm
Ni	**3[a]; 38[*b]**	**1[a]; 5.42[*b]**	0.04[a]	**10[a]**	**1[a]**	**17[a]**
Sr	0.0004[a]	0.1283[a]	**3.2487[a]**	0.0006[a]	0.0012[a]	0.7[a]
Sr (T-dep)			1.29 @ 1400 °C, 3.19 @ 1153 °C[#c]			
Zr	0.001[a]	0.05[a]	0.03[a]	0.015[a]	0.032[a]	0.33[a]
Ba	0.0003[a]	0.0007[a]	0.459[a]	0.0005[a]	0.0005[a]	0.09[a]
La	0.0003[a]	0.0536[a]	0.124[a]	0.0006[a]	0.0008[a]	0.0023[a]
Nd	0.0002[a]	0.1873[a]	0.068[a]	0.0006[a]	0.0056[a]	0.0012[a]
Yb	0.0052[a]	0.43[a]	0.0097[a]	0.0045[a]	0.22[a]	0.057[a]

Wallrock	opx	plg	ksp	qtz	spl	rhm	apa
Ni	**15[d]**	**1.1[d]**	0.18[d]	0	**5.2[d]**	**3.8[d]**	0.4[a]
Sr	0.068[d]	**7.6[d]**	**2.11[d]**	0	0.063[d]	0.043[d]	**2[e]**
Sr (T-dep)		1.29 @ 1400 °C, 3.19 @ 1153 °C[#c]					
Zr	0.14[d]	0.18[d]	0.029[d]	0	0.24[d]	**1.38[d]**	0.01[e]
Ba	0.11[d]	0.33[d]	**3.5[d]**	0	0.1[e]	0.01[e]	0.01[e]
La	0.4[e]	0.3[e]	0.3[e]	0	0.66[e]	0.01[e]	**20[e]**
Nd	0.6[e]	0.19[e]	0.19[e]	0	0.93[e]	0.01[e]	**57[e]**
Yb	0.91[e]	0.1[e]	0.1[e]	0	0.44[e]	0.01[e]	**24[e]**

Solid-compatible and neutral partition coefficients shown in bold. Note that $K_{s/H2O}$ and $K_{s/CO2}$ (and thus K_{sf}) are 1000 for all elements in all phases, except for the case with fluid mobility taken into account, where bulk D_{sf} values (uniform element-specific K_{sf} value input for all phases) are as follows (after Kessel et al., 2005): D_{sf}(Ni) = 100, D_{sf}(Sr) = 0.047, D_{sf}(Zr) = 2.56, D_{sf}(Ba) = 0.023, D_{sf}(La) = 0.088, D_{sf}(Nd) = 0.66, D_{sf}(Yb) = 91.

Mineral abbreviations: ol = olivine, cpx = clinopyroxene, plg = plagioclase, spl = spinel, opx = orthopyroxene, rhm = rhomboedral oxide, ksp = anorthoclase, qtz = quartz, apa = apatite.

Sources for the partition coefficients: [a]Boudreau (1999), [b]Norman et al. (2005), [c]Drake and Weill (1975), [d]Ewart and Griffin (1994), [e]Bacon and Druitt (1988).

[*] elevated $K^{M}_{ol/m}$(Ni) and $K^{M}_{cpx/m}$(Ni) values are only used in one FC trace element model.

[#] T-dependent $K_{plg/m}$(Sr) only used for one FC and one AFC trace element model (for calculation of $K_{plg/m}$(Sr) at a given temperature, see equations 6–8).

Electronic Appendices 11-15 contain the input data for each of five model cases performed here (same as Chapter 4) and Electronic Appendices 16-20 include fully tabulated output for both MCS tools (and input for *MCS-Traces*) in the five case-specific files. Electronic Appendices 21-25 contain the PAR files with different partition coefficients used throughout the five case studies. The results are discussed below and illustrated in Figs. 2–6. For more detailed discussion on the phase equilibria and major element evolution in the *MCS-Majors* models, the reader is referred to the companion paper (Bohrson et al., submitted); concise summaries of those results are presented herein.

3.1. Fractional Crystallization (FC)

In the primary MCS FC model, the melt composition evolves from basaltic (SiO_2 ≈ 49 wt.% at 1131 °C) to dacitic (SiO_2 ≈ 69 wt.% at 896 °C) by ~76% of crystallization. Because of the high H_2O content in the initial magma, a separate H_2O fluid phase forms after ~46%

crystallization and accumulates up to ~1% in total by the end of the run. The fractionated phases are in order of appearance: olivine (total of ~12%), clinopyroxene (~30%), plagioclase (~30%), spinel (~4%), and rhombohedral oxide (0.3%).

In terms of trace elements, Ni is compatible in the incremental solids almost throughout the default FC run (Fig. 2a), because all of the associated solid phases except plagioclase have K_{sm}^{M}(Ni) values of ≥ 1 (Table 1). D_{sm}^{M}(Ni) is slightly less than one only for two steps after the onset of plagioclase crystallization at ~50 wt.% of SiO_2.

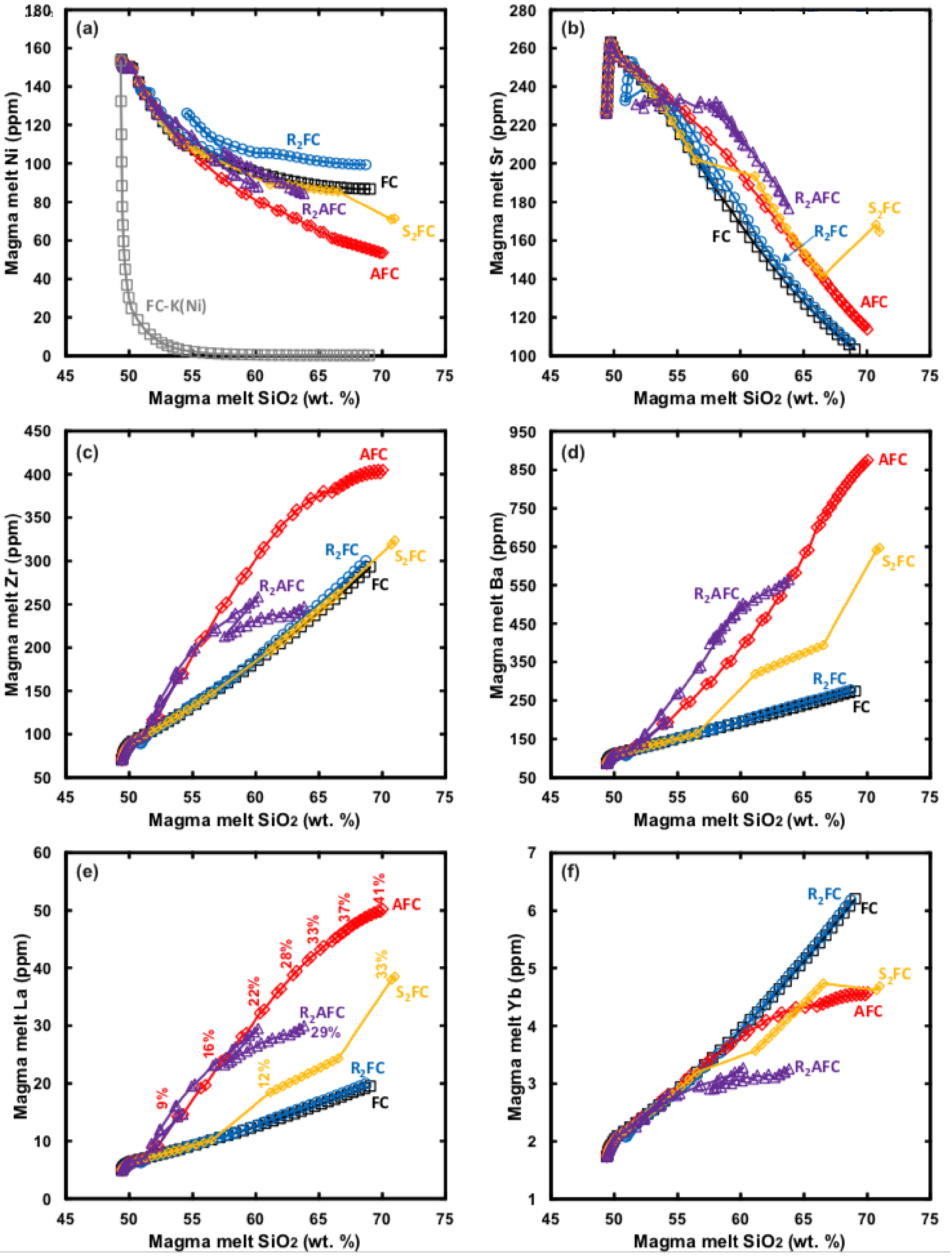

Figure 2. SiO_2 vs. Ni, Sr, Zr, Ba, La, and Yb (ppm) diagrams for the resident melt in the example case studies (FC, R_2FC, AFC, S_2FC, and R_2AFC). For Ni (a), in addition to the default FC simulation that is presented (FC-N), a FC model using higher $K^{M}_{ol/m}$(Ni) and $K^{M}_{cpx/m}$(Ni) is shown (Table 1). Percentages shown in SiO_2 vs. La for the cases involving assimilation (e) reflect the mass of assimilated material relative to the mass of the M subsystem; these are applicable for all diagrams at a given SiO_2, but are only shown in (e) to preserve clarity. Note that in AFC and S_2FC, assimilation begins when the trend diverges from the FC trend.

In the case of the run with elevated $K^M_{ol/m}$(Ni) of 38 and $K^M_{cpx/m}$(Ni) of 5.42, resident melt becomes considerably more depleted in Ni as fractionation proceeds (Fig. 2a), consistent with this extreme partitioning into the cumulates. Strontium is incompatible in the solids and enriched in the resident melt until the fractionation of plagioclase begins (Fig. 2b). All other elements are incompatible in the crystallizing phases and behave incompatibly throughout the run (Fig. 2c–f). Fractional crystallization has a negligible effect on rare earth element (REE) ratios, and isotope compositions obviously remain unchanged (Fig. 3).

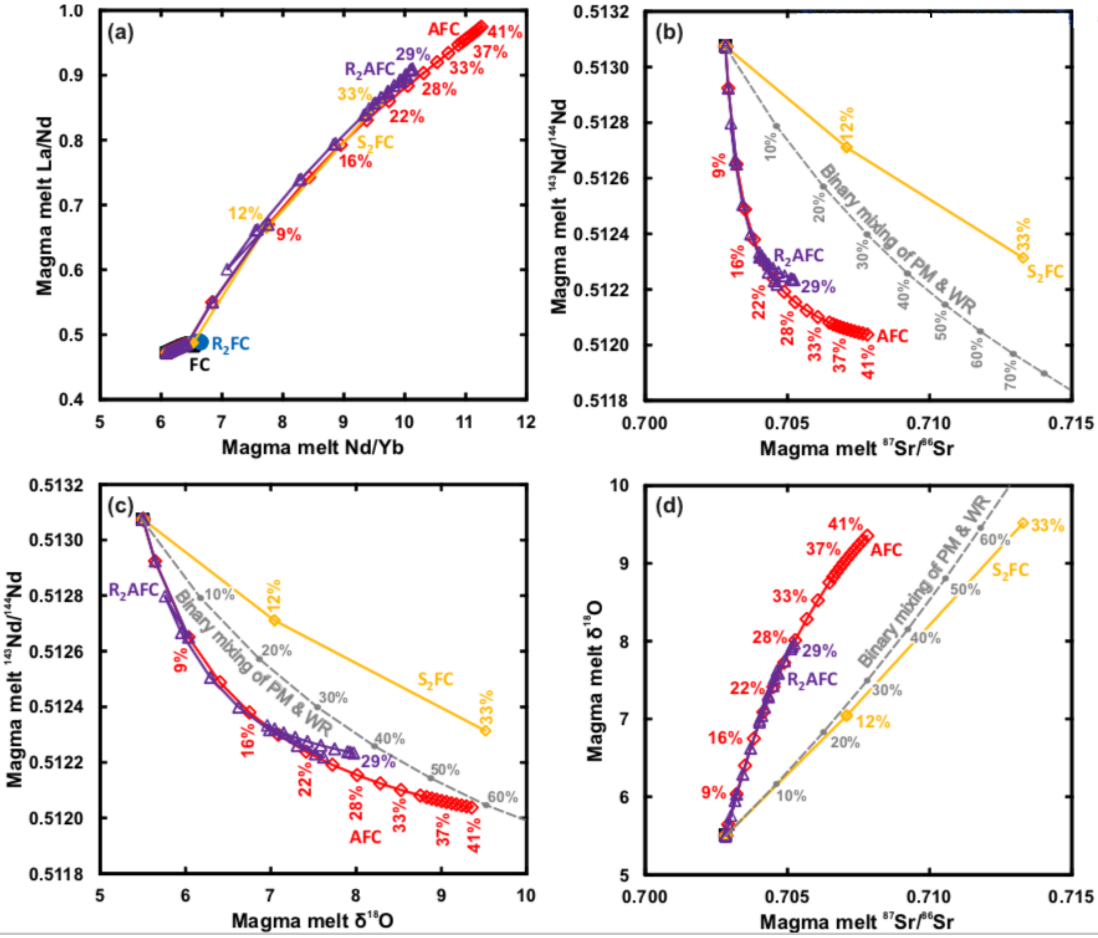

Figure 3. Nd/Yb vs. La/Nd diagram (a) and Sr, Nd, and O isotope diagrams (b–d) for the resident melt in the example case studies (FC, R₂FC, AFC, S₂FC, and R₂AFC). Note that FC and R₂FC are not shown in the isotopic diagrams because these models do not result in isotopic changes in the resident melt. Percentages given for the model curves involving assimilation reflect the mass of assimilated material relative to the mass of the M subsystem. Simple binary mixing models are also shown in the isotopic diagrams; percentages indicate the relative amount of WR in the mixture and are broadly comparable to the percentages in the MCS runs (there is no fractional crystallization in binary mixing, however).

The effect of using T-dependent $K_{plg/m}^{M}$(Sr) is illustrated in Fig. 4. Strontium concentration in the evolving resident melt is strongly controlled by plagioclase, which is reflected in D_{sm}^{M}(Sr) (Fig. 4b). First, Sr is compatible in bulk solids as soon as plagioclase begins to fractionate in both default and T-dependent runs. Whereas D_{sm}^{M}(Sr) remains rather constant (1–2) in the default run, in the T-dependent run at around 900 °C, D_{sm}^{M}(Sr) has increased to 9. This is naturally reflected in very low Sr contents in the final resident melt in the case of the T-dependent run (< 10 ppm) relative to the default run (Sr ≈ 100 ppm) (Fig. 4a).

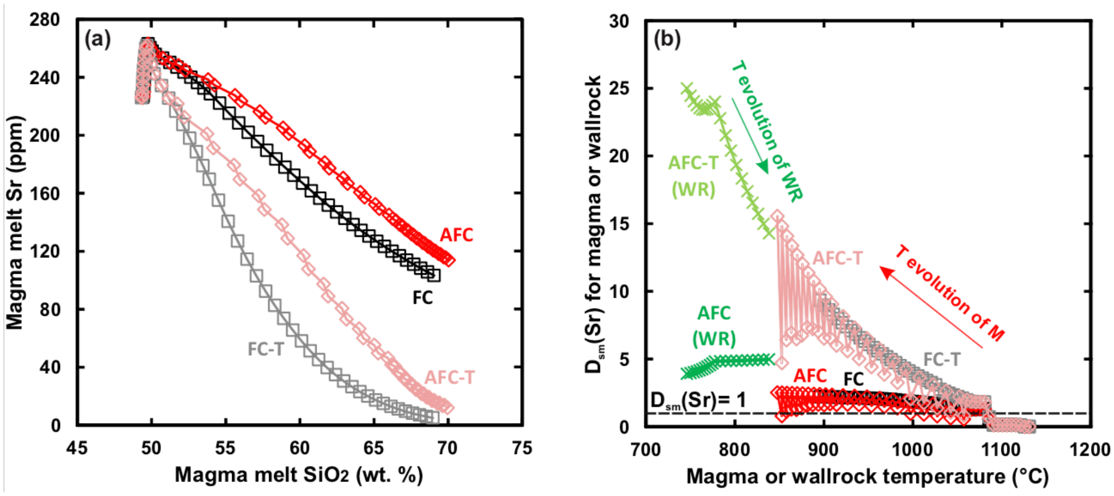

Figure 4. Comparison of the FC and AFC model runs using either constant $K_{plg/m}$(Sr) (FC-N, AFC-N) (same as in Fig. 2) or T-dependent $K_{plg/m}$(Sr) (FC-T, AFC-T) for M and WR. a) SiO2 vs. Sr diagram for the resident melt and b) temperature of the resident melt or WR vs. D_{sm}(Sr) in M or WR. In b, D_{sm}(Sr) of 1 is highlighted with a dashed line, and the thermal evolution of the resident melt and WR are indicated. The oscillating pattern for D_{sm}^{M}(Sr) in the AFC runs reflects the working principles of the primary MCS tool: low points in the pattern are first steps after assimilation of WR anatectic melt, whereas each high point in the diagram represents a normal 5 °C decrement FC step. See section 3.3 for more details.

The effect of adjusted D_{sf}^{M} values is negligible for elements with $D_{sf}^{M} \geq 1$ in the FC runs (Fig. 5a, b). However, the effect becomes more important for more soluble elements, such as Sr and Ba with $D_{sf}^{M} < 0.1$, even when the total mass of fractionated fluid in the FC run does not exceed 1% (Fig. 5c, d). The Sr and Ba contents at the end of the adjusted D_{sf}^{M} run are 60 % and 30 % lower, respectively, than at the end of the default run. Compared to Ba, the effect on Sr is more pronounced because it has a higher D_{sm}^{M} (1–2 after the onset of plagioclase fractionation at ~50 wt.% of SiO2) for most of the run, whereas D_{sm}^{M}(Ba) stays below 0.4 throughout.

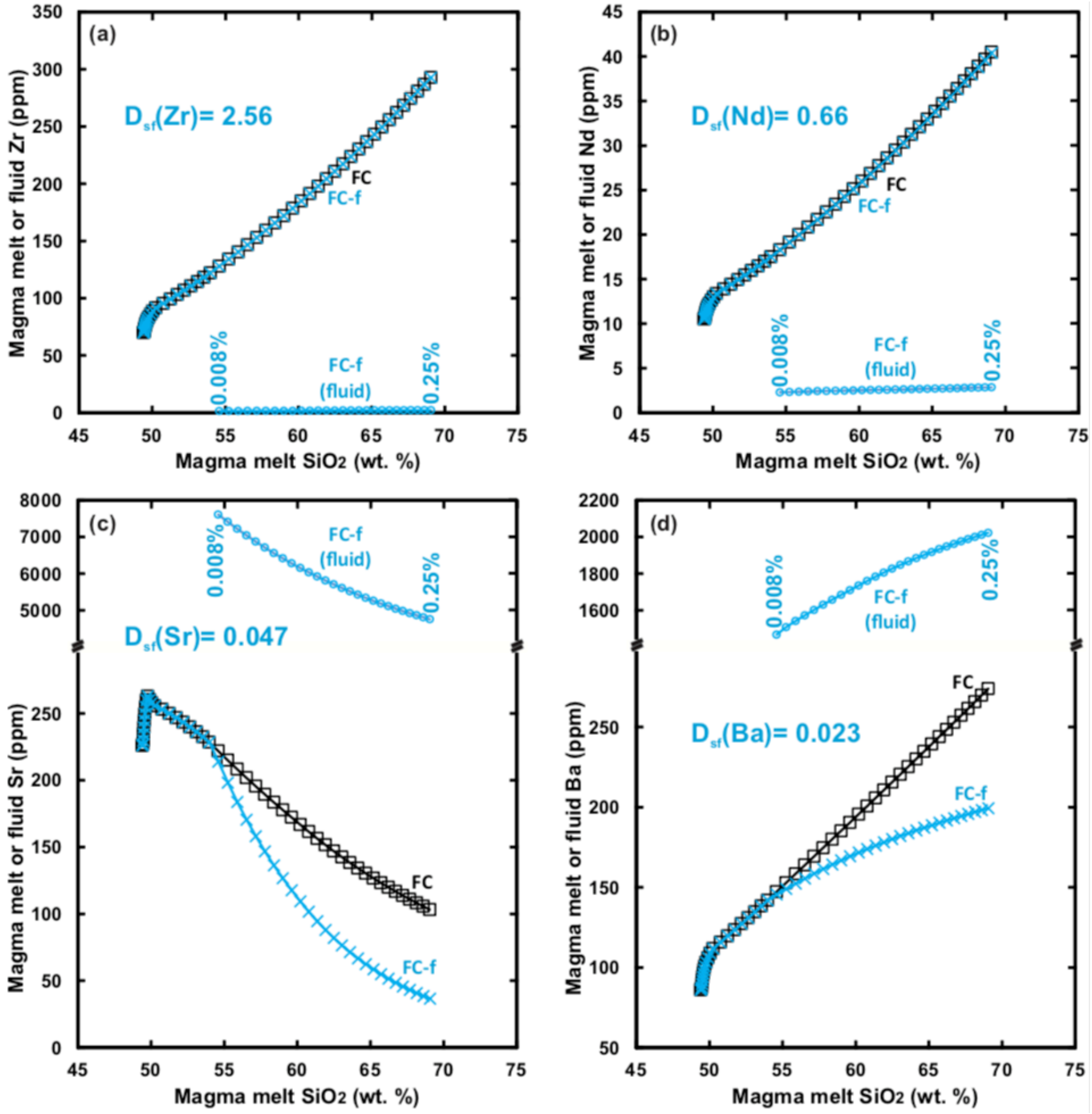

Figure 5. Comparison of resident melt concentrations of the FC model runs with elements considered incompatible in the fluid (i.e. D_{sf}^{M} = 1000; FC-N, same as in Fig. 2) and with element-specific D_{sf}^{M} employed (FC-f) (Table 1). Fluid composition is also shown; in a and b the fluid compositions are shown in the same diagram with the resident melt compositions and in c and d the highly enriched fluid compositions are shown in separate windows. The mass of separated fluid relative to the mass of the initial melt is indicated with percentages in the beginning of fluid separation and in the end of the run.

3.2. Recharge-Fractional Crystallization (R_2FC)

The primary R_2FC model simulates replenishment of the magma chamber with two batches of mantle–derived magma that are equivalent to the parental melt composition. The two R events of 75 mass units (m.u.) are introduced at ~1046 °C (resident melt $SiO_2 \approx 53$ wt.%) and at ~998 °C (resident melt $SiO_2 \approx 58$ wt.%). Because of the R events, the total magma chamber mass at the conclusion of the simulation is 250 m.u.. The second R magma is cooler than the first one and thus contains more crystal cargo; this does not affect the trace element run, however, as (bulk) R magmas (i.e., all crystals + melt ± fluid) are fully hybridized with the resident melt. The R_2FC model terminates with ~22% (~55 m.u.) of dacitic ($SiO_2 \approx$ 69 wt.% at 900 °C) melt and approximately 11% olivine, 31% clinopyroxene, 30% plagioclase, 4% spinel, 1% orthopyroxene, and <1% rhombohedral oxide fractionated (listed in the order of appearance), and ~1% of fluid separated.

At almost any given SiO_2 content, the concentrations and ratios of the modeled trace elements in the R_2FC run are very similar to those produced by the FC runs (Figs. 2, 3a). The only notable differences are in regard to Ni and Sr that show mostly compatible behavior (Fig. 2a, b). The resident melt is enriched in Ni due to the added primitive R pulses (that have higher Ni contents than the resident melt at the instance of R), especially the second R event (R2) that triggers considerable precipitation of clinopyroxene (14.5 m.u.), which has lower K_{sm}^{M}(Ni) than olivine (Table 1) that is the sole crystallizing phase one step after R1. In the case of Sr, R1 lowers the Sr content of the resident melt, whereas R2 increases it; this is because the recharge events take place when resident melt Sr concentrations are higher (before R1) and lower (before R2) than in the recharge magma. In addition, precipitation of clinopyroxene that has low K_{sm}^{M}(Sr) of 0.1283 after R2 enriches the resident melt in Sr considerably. In terms of fully incompatible elements (Fig. 2c–f), the recharge events do not cause deviation from the rather linear geochemical trends. The implications of these observations will be discussed in more detail later.

3.3. Assimilation of wallrock anatectic melts + Fractional Crystallization (AFC)

The AFC model is the first one involving assimilation of wallrock. The assimilation of WR partial melts begins when the temperature of the resident melt has dropped to ~1060 °C (~51 wt. SiO_2; ~30% crystallization at that point). The model terminates at a total magma chamber mass of ~168 m.u. (~68 m.u. of WR melt added) with ~56% of dacitic (nearly rhyolitic; $SiO_2 \approx 70$ wt.% at 844 °C) melt left. Approximately 4% olivine, 15% clinopyroxene, 17% plagioclase, 2% spinel, 5% orthopyroxene, and <1% rhombohedral oxide was fractionated (listed in the order of appearance), and <1% of fluid separated. Note that addition of felsic WR melts increases the stability of orthopyroxene at the expense of olivine relative to the FC run. The residual WR consists of varying amounts of orthopyroxene, plagioclase, alkali feldspar, quartz, spinel, rhombohedral oxide, and apatite. The WR phases that contribute most to the partial melting are alkali feldspar (disappears completely from the WR at ~783 °C) and quartz.

The default AFC run shows drastic differences relative to that of the default FC run. The compatible element Ni is diluted in the resident melt by WR assimilation (Fig. 2a). On the other hand, Sr is slightly enriched in the AFC resident melt (Fig. 2b) at any given SiO_2 content after assimilation begins even when D_{sm}^{WR}(Sr) remains relatively high (4–5; Fig. 4b) throughout the run (only ~90–100 ppm of Sr in WR melts that form). This enrichment in resident melt is primarily caused by subdued plagioclase crystallization in AFC relative to FC (see below; Bohrson et al., submitted).

Incompatible trace elements (K_{sm} < 1 in both M and WR) that are enriched in the WR (i.e., Zr, Ba, La) are considerably enriched in the AFC resident melt compared with the FC-only resident melt (after the onset of assimilation in the former; Fig. 2c–e). The contrary is true for Yb that is found in lower quantities in the WR (Fig. 2f). Assimilation has drastic effects on REE ratios and isotope compositions of the resident melt (Fig. 3). Note that compatibility of Sr in the WR (Fig. 4b) results in delayed enrichment in ^{87}Sr/^{86}Sr relative to ^{143}Nd/^{144}Nd in comparison to a simple binary mixing model (Fig. 3b). Similarly, the incompatibility of Nd and its enrichment in the WR anatectic melt enriches ^{143}Nd/^{144}Nd more efficiently than δ^{18}O in the resident melt (Fig. 3c). The opposite is true when comparing ^{87}Sr/^{86}Sr and δ^{18}O, the latter being more efficiently enriched in the resident melt (Fig. 3d).

The effects of using T-dependent $K^{M}_{plg/m}$(Sr) and $K^{WR}_{plg/m}$(Sr) on the Sr evolution of the resident melt in the AFC model are comparable to those for the FC model (Fig. 4a). Figure 4b illustrates a jigsaw pattern for D^{M}_{sm}(Sr) in the AFC runs. This pattern reflects the working principles of the primary MCS tool: low points in the jigsaw pattern are the result of crystallization in relation to assimilation of the WR melt that causes decreased plagioclase stability and thus low D^{M}_{sm}(Sr), whereas each high point in the diagram represents a normal 5 °C FC step with increased plagioclase stability and thus high D^{M}_{sm}(Sr). The reason for the continuous depletion of Sr in the resident melt in the default AFC run (Fig. 4a) – in spite of D^{M}_{sm}(Sr) being less than 1 at some temperatures (e.g., 1057–997 °C; Fig. 4b) – is due to the dilution effect of adding Sr-poor WR anatectic melt into the resident melt (Fig. 6). Note also that the major inflection point in AFC-T D^{WR}_{sm}(Sr) trend (Fig. 4b) is caused by the effect of WR temperature increase overcoming the effect of minor increase in the amount of residual plagioclase on D^{WR}_{sm}(Sr). The WR temperature rise is accelerated after alkali feldspar has been consumed at a WR temperature of ~780 °C (the consumption of alkali feldspar is also recorded in the default AFC D_{sm}^{WR}(Sr) trend). Again, these are examples of complex relationships between the different processes and variables included in MCS, and are natural consequences of open system behavior that are counterintuitive to reasoning that either implicitly or explicitly assumes closed system behavior.

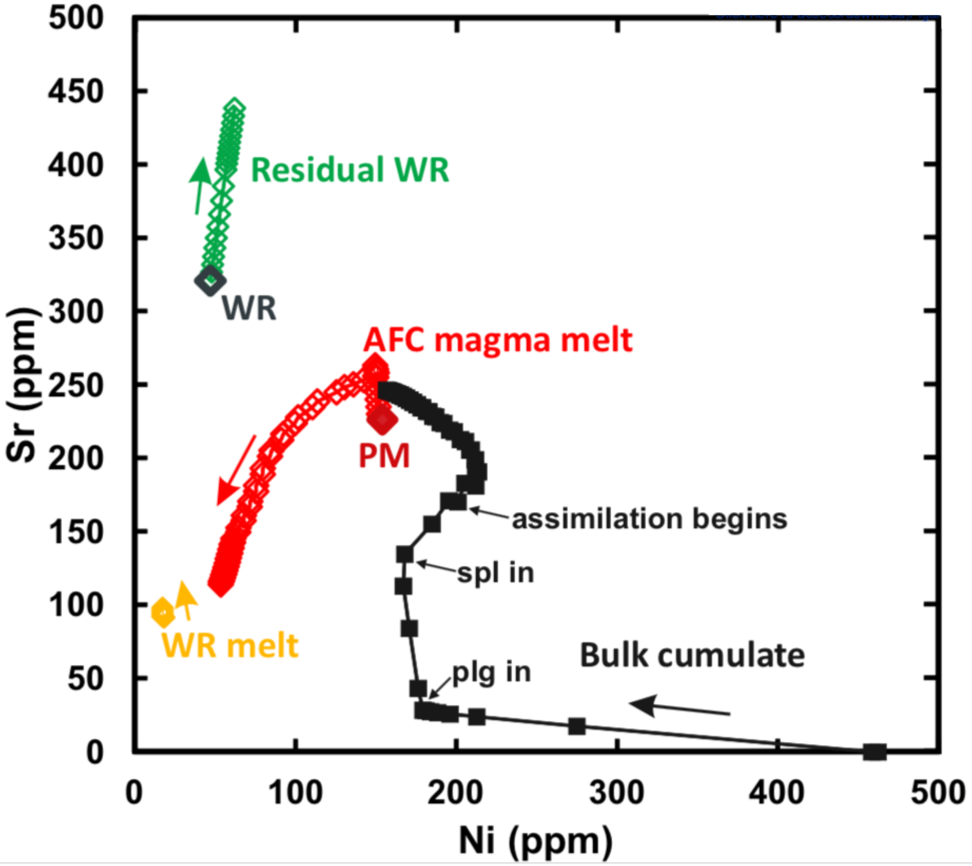

Figure 6. Ni (ppm) versus Sr (ppm) in resident melt, bulk cumulate, WR melt, and WR bulk residue (solid + melt + fluid) of the AFC model. Initial parental melt (PM) and WR compositions are labeled. Arrows indicate the direction of evolution in the MCS run. The causes for the major inflection points are marked for the bulk cumulate composition.

Figure 6 illustrates the compositional evolution of not only the resident melt, but also the bulk cumulate, WR melt, and WR residual (solid + melt + fluid) in the default AFC run. Nickel concentration in the bulk cumulate is highest in the beginning when olivine with high

K_{sm}^{M}(Ni) is the sole fractionating phase. Strontium content in the bulk cumulate begins to notably increase after the addition of plagioclase in the fractionating assemblage. Because Ni and Sr are compatible in WR solids, the WR partial melt shows little change in terms of trace element composition, whereas the WR residual gets progressively enriched in these elements. Note that all the data presented in Fig. 6 can be collected from *MCS-Traces* output with minimal effort. Correlating specific trends in trace element evolution is simple, as major element and phase abundances for each step of the scenario are output alongside the trace element concentrations.

3.4. Assimilation through Stoping-Fractional Crystallization (S$_2$FC)

The S$_2$FC model simulates complete assimilation of two stoped wallrock blocks by the resident melt. The stoped blocks are of WR composition, and are introduced into the magma using the recharge function at resident M temperatures of ~1015 °C and ~915 °C. The masses of the blocks are 14 and 36 m.u. and their temperatures at hybridization are 760 °C and 785 °C, respectively. These masses roughly correspond to the total mass of assimilated WR partial melts in the AFC model at the given magma temperatures.

The S$_2$FC model terminates at a total magma chamber mass of 150 m.u. (50 m.u. of stoped WR added) with ~33% of rhyolitic ($SiO_2 \approx 71$ wt.% at 850 °C) melt left. Approximately 6% olivine, 19% clinopyroxene, 31% plagioclase, 3% spinel, 7% orthopyroxene, and <1% rhombohedral oxide crystallized (listed in the order of appearance), and ~1% of fluid separated. Although WR blocks are composed of solids, melt, and fluid at hybridization, their phase identity is irrelevant for the outcome of the *MCS-Traces* modeling as the R function in MCS produces a new, completely hybridized equilibrated state. Similar to the AFC case, the addition of Si-rich WR increases orthopyroxene stability at the expense of olivine, relative to the FC run.

Relative to R_2FC and FC runs at a given SiO_2 content, S_2FC resident melt shows varying degrees of enrichment of Sr, Ba, and La (elements notably enriched in the WR), and depletion of Ni and Yb (elements depleted in the WR; Fig. 2). For most elements, the complete hybridization of a stoped WR block results in a significant compositional change for most elements immediately after each stoping event (Fig. 2 and 3). Interestingly, the SiO_2 vs. Zr trend of the S_2FC run does not differ from those of R_2FC or FC, because Zr and SiO_2 are equally enriched in the stoped WR blocks relative to the resident melt.

Relative to the AFC run, S_2FC shows some significant differences that are mostly related to the contamination process. In resident melt that has experienced assimilation by stoping, Sr and Ni, which are compatible during WR melting, are more enriched (Fig. 2a, b), whereas incompatible elements enriched in the WR (e.g., Zr, Ba, and La; Fig. 2c, d, e) are less enriched; the comparisons are again made at a given SiO_2 content after the beginning of assimilation. On the other hand, incompatible element Yb is depleted in the S_2FC resident melt relative to the AFC run right after the first stoping event because of the low concentration of Yb in the bulk WR (1.96 ppm) compared to that of resident melt at that point (3.19 ppm). The differences between AFC and S_2FC arise because contamination by stoping represents incorporation of the entire WR, rather than the assimilation of anatectic melt, in which compatible elements are relatively depleted and incompatible elements enriched in relation to bulk WR.

For isotopes, $^{87}Sr/^{86}Sr$ and $\delta^{18}O$ are more enriched at a given $^{143}Nd/^{144}Nd$ in the S_2FC resident melt than in the AFC run or in a binary mixing scenario (Fig. 3b, c). In the case of

^{87}Sr/^{86}Sr, this is both because Sr is progressively depleted from the resident melt by fractional crystallization of plagioclase, and because addition of bulk stoped WR adds more Sr to the resident melt (per unit addition of added mass) than relatively Sr-poor anatectic melt does. Strontium released from the stoped WR blocks thus changes the Sr isotopic composition of the melt more effectively than in the case of binary mixing or AFC. The explanation for the δ^{18}O enrichment at a given ^{143}Nd/^{144}Nd relative to the binary mixing scenario is less intuitive, but stems from the fact that Nd is enriched in the resident melt at the time of the stoping events relative to the parental melt used in the binary mixing model. Therefore, ^{143}Nd/^{144}Nd of the S$_2$FC resident melt is not as easily affected by assimilation of stoped WR. The higher δ^{18}O of S$_2$FC resident melt relative to that of the AFC model at similar degrees of contamination (e.g., 33%, Fig. 3c, d) can be associated with relatively higher resident melt mass in the latter (see Bohrson et al., submitted); δ^{18}O is more efficiently buffered by resident melt composition in a larger melt pool.

3.5. Recharge-Assimilation-Fractional Crystallization (R$_2$AFC)

In the exemplary R$_2$AFC model that combines magma replenishment with assimilation of WR partial melts, the R events are set as in the R$_2$FC model and WR parameters are set as in the AFC model.

The R$_2$AFC model terminates at a total magma chamber mass of ~351 m.u. (~101 m.u. of WR melt and 150 m.u. of R magma added) with ~60% of dacitic ($SiO_2 \approx 64$ wt.% at 960 °C) melt left. Approximately 3% olivine, 19% clinopyroxene, 11% plagioclase, 2% spinel, 5% orthopyroxene, and <1% rhombohedral oxide was fractionated (listed in the order of appearance), and <1% of fluid separated. The residual WR mineral composition and behavior is similar to the AFC model, although additional heat provided by the R magmas has melted the WR to a greater degree by the end of R_2AFC.

When assimilation is simulated together with recharge events, the composition of the resident melt begins to show non-linear characteristics in trace element geochemical trends (Fig. 2). These effects are the result of mass exchange between the resident melt and either "depleted" primitive R magmas or "enriched" WR partial melt batches and the resulting changes in phase equilibria and D values that can be reviewed in detail in the related model output. The effects of R events for contamination-sensitive trace element and radiogenic isotope ratios are less drastic, however, and the respective trends of the R_2AFC run closely parallel to those of the AFC run (Fig. 3). What is very different in these models, however, are the masses of the components. The final resident melt composition of the R_2AFC run is the result of assimilation of 101 m.u. of WR anatectic melt by 250 m.u. of initial and R magmas. The resulting compositions correspond to that of the AFC run with 30–40 m.u. assimilated by 100 m.u. of initial melt. Note that in both runs, the amount of assimilation relative the resident magma chamber mass is still around 30–40% at a given isotopic composition (Fig. 3). For more details on the mass balances of the different runs, the reader is referred to the companion paper (Bohrson et al., submitted).

4 Discussion

4.1. Selecting partition coefficients

For any reasonable trace element and radiogenic isotope model of a magmatic system, selection of feasible partition coefficients is crucial. Given the number of studies on partitioning of elements in different phases in different magma compositions and at different

P-T-conditions (see, e.g., GERM partition coefficient database), it is easy to get overwhelmed in the quest for such information.

For our example models presented here, we used a set of partition coefficients compiled from other modeling software or from individual publications of systems similar to the resident melt and WR partial melt compositions in the MCS models. Namely, for the initially basaltic resident melt, we used a set of partition coefficients compiled in the PELE software (Boudreau, 1999). However, using constant K_{sm}^{M}(Ni) values compiled from PELE in the FC and R_2FC runs results in anomalously high Ni concentrations (~90–100 ppm) in the final dacitic melts, whereas felsic igneous rocks usually have Ni contents of ≤10 ppm (Fig. 2a). Although we are not modeling a specific natural magma series here, this hints that the used K_{sm}^{M}(Ni) values (e.g., 3 in olivine and 1 in clinopyroxene; Table 1) are too low. K_{sm}^{M}(Ni) values for olivine and pyroxenes reported elsewhere are usually higher and have been shown to increase with decreasing temperature and more felsic magma composition (e.g., Duke 1976; Nabelek, 1980; Colson et al., 1988; Norman et al., 2005; Matzen et al., 2013). On the other hand, the reference FC run, in which we used high constant $K_{ol/m}^{M}$(Ni) of 38 and $K_{cpx/m}^{M}$(Ni) of 5.42 (Norman et al., 2005) depletes the resident melt from Ni excessively fast (Fig. 2a).

The Ni example demonstrates the issue of selecting feasible partition coefficients. In order to explore the effects of variable K values on MCS results for any modeled element, we recommend running *MCS-Traces* models with different sets of partition coefficients (e.g., using minimum and maximum reported K values for each phase). Temperature-dependent values should always be preferred, especially in runs that span large compositional and temperature ranges (for resident melt or WR melt or both), but such data may be scarce for particular settings or conditions. A multifaceted approach will provide a framework for the relative importance of reported K_{sm} variance and strengthen the presented models. The benefit of relying on highly compatible or incompatible elements is that possible magnitude-scale variations reported for K_{sm} values (e.g., from 100 to 10 or from 0.01 to 0.001) will have a minute effect on the resulting geochemical trends.

Finally, additional complexity in element partitioning in MCS models is caused by the appearance of a fluid phase, either in the resident magma or in the wallrock (Fig. 5). Unfortunately, K_{sf} values are highly underrepresented relative to K_{sm} values in experimental petrology and petrologic literature in general. This still is an important aspect of the modeling, because if an element is highly fluid-compatible, even small amounts of fluid separation may have drastic effects on its concentrations in the resident melt (e.g., Cs, Rb, Th; for Sr and Ba, see Fig. 5). Geochemical models based upon the assumption that trace elements are insoluble can lead to inaccurate source composition estimates if, in fact, appreciable amounts of trace elements are removed from the system by volatiles. Furthermore, assimilation of the fluid phase from the wallrock is not presently handled by MCS, so highly fluid-compatible elements may be primarily concentrated in the residual wallrock and not assimilated with the wallrock partial melts in AFC scenarios. We recommend using caution in selecting K_{sf} values for the resident magma and especially for the wallrock in modeling fluid-saturated systems.

4.2. Trace elements and isotopes as indicators of open-system processes

Trace elements and isotopes have traditionally been regarded as useful indicators of open-system processes in igneous systems. As major element and mineral compositional evolution is controlled by phase equilibria, and effects of recharge and assimilation processes on these may be minute or difficult to identify (as illustrated in the companion paper; Bohrson et al., submitted). In the sections below we review and, on the basis of *MCS-Traces* modeling, re-evaluate the usefulness of trace elements and isotopes as such indicators.

4.2.1. Identifying fingerprints of magma recharge

Identifying recharge (and complete homogenization) of magma pulses having the same composition with the initial resident melt (parental melt) based on major element evidence is challenging (Bohrson et al., submitted), and the same is true for incompatible trace elements: Zr, Ba, La, and Yb trends for both the FC and R_2FC scenarios are practically uniform (Fig. 2c–f). Some variation is evident in the case of Ni, which behaves mostly compatibly throughout the run, as well as Sr, which is incompatible before the onset of plagioclase fractionation (Fig. 2a, b). In both cases, slight offsets from the FC trend can be seen following recharge. In comparison to natural systems, however, such offsets may be difficult to distinguish from sample variation due to other factors (such as sample inhomogeneity) and analytical uncertainty.

Building on findings of Bohrson et al. (submitted), we conclude that magma recharge processes are very difficult to identify in differentiating magmatic systems on the basis of major or trace element trends alone if the recharge melts are of uniform composition. Instead, one or more of the following three premises should preferably be fulfilled: 1) the recharge magma has a distinct composition relative to earlier initial or parental melts of the system (e.g., Pietruszka and Garcia, 1999); 2) stratigraphic or other temporal sample control enables detection of “reverse” geochemical and/or mineral compositional trends (e.g., increase in MgO or Ni contents) that are best explained by addition of more primitive magma into the system (e.g., Cox, 1988; Blight et al., 2010; Yuan et al., 2017); and/or 3) there is a representative crystal cargo available in order to study crystalline microtextures and textural relationships, and major and trace element compositional variations. In the case of zoned crystals, this can be regarded as an intracrystalline stratigraphic control, and its importance in indicating magma recharge has been recognized in different magmatic environments, especially those related to subduction settings (e.g., Ginibre and Wörner, 2007; Streck, 2008; Ginibre and Davidson, 2014; Bouvet de Maisonneuve et al., 2016). However, evidence from *MCS-Majors* modeling suggests that recharge is not necessarily recorded similarly in all phases (e.g., in those that show varying stability in a replenishing system; Bohrson et al., submitted). In addition, post-crystallization re-equilibration of crystals by diffusion may readily erase some elemental zoning in certain minerals (see, e.g., Costa et al., 2008). Note that mineral major and trace element compositions are also recorded in MCS output.

4.2.2. Identifying fingerprints of crustal assimilation

Crustal assimilation was also surprisingly difficult to recognize based only on major element oxides from MCS model output in standard AFC and SFC scenarios (see Bohrson et al., submitted). Notable differences in the modeled AFC scenario relative to FC or R_2FC scenarios were only identified in terms of K_2O (5x enrichment relative to FC or R_2FC model due to melting of anorthoclase in the wallrock) with subtler differences also present in Al_2O_3, CaO, and Na_2O. These differences were even less obvious if contamination happened by wholesale incorporation of stoped blocks (S_2FC case).

In contrast, AFC, S_2FC, and R_2AFC cases are readily distinguished from FC and R_2FC cases in terms of incompatible elements and isotopic compositions (Figs. 2 and 3). These will be reviewed in case-specific sections below.

4.2.3 *Assimilation of wallrock anatectic melts*

Assimilation of wallrock anatectic melts will dominate in settings where wallrock xenoliths are not efficiently introduced into the resident melt, but assimilation takes place within a contact zone of the wallrock and the resident melt. Such conditions may prevail in middle to lower crustal magma chambers, where the wallrock is not highly fractured, behaves in ductile manner, and boundary temperatures are high (see Bohrson et al., 2014).

MCS modeling shows that partial melting of the wallrock considerably enriches the wallrock partial melt and thus the contaminated resident melt in incompatible elements that are found in high quantities in the wallrock (e.g., Zr, Ba, and La; Fig. 2c–e). This suggests that the relative amounts of assimilation in natural systems on the basis of incompatible trace element concentrations or their isotopes, without some kind of control on the thermodynamics, phase equilibria, and style of assimilation, may often be significantly overestimated (see Heinonen et al., 2016). The contrary is true if elements are incompatible but present in low quantities within the wallrock (e.g., Yb; Fig. 2f). Ytterbium is initially slightly enriched in the contaminated resident melt, because it effectively enters the assimilated wallrock partial melt (D_{sm}^{WR}(Yb) is 0.2–0.3 throughout the run). Because of the initially low concentration in the wallrock (1.96 ppm relative to 1.73 ppm in PM), the wallrock partial melts become depleted in Yb quite rapidly relative to SiO_2. The different degrees of enrichment/depletion shown by variably compatible elements in AFC resident melt underline the importance of evaluating the role of assimilation in natural systems based on several and not just one or two different elements (and their respective isotopes).

The isotopic effects of assimilation of wallrock partial melts are clear and most drastic for elements that show incompatible behavior in the wallrock and are relatively depleted in the resident melt (Fig. 4). If the partially melting wallrock contains residual plagioclase in significant proportions such that D_{sm}^{WR}(Sr) > 1, ^{144}Nd/^{143}Nd is expected to show more drastic changes than ^{87}Sr/^{86}Sr. Depending on the modal composition of the wallrock and the resulting D values, similar differences can also be expected for other radiogenic isotopic systems (Hf, Pb, and Os) that can be modeled with MCS. Oxygen isotopes have been considered as useful indicators of crustal contributions to mantle-derived magmatic systems, because usually O concentrations in magmas and wallrock are very similar whereas their O isotopic compositions are different. Therefore, binary mixing or traditional AFC curves (with O isotopes often considered together with radiogenic isotopes) have been used to estimate the relative amounts of mantle and crust end-members and importance of assimilation vs. source heterogeneity in such systems (e.g., Taylor, 1980; James, 1981; Martinez et al., 1996; Baker et al., 2000; France et al., 2016). The results of MCS modeling illustrated in Fig. 3 indicate that the differences in the compatibility of the trace elements (both in the magma and in wallrock), O budget of the crystallizing resident melt vs. assimilant, and style of assimilation have considerable effects on such isotopic comparisons in different contamination scenarios. It is evident from Fig. 3 that relative contributions from crustal sources may be considerably overestimated using binary mixing models even when relying on O isotopes.

If magma recharge is concurrent with anatectic wallrock assimilation, the latter process controls enrichment in incompatible elements and radiogenic. We emphasize, however, that this observation is highly dependent on the composition of the recharge magma and the wallrock, and the mass balances among the three subsystems. Finally, in addition to being able to follow the geochemical evolution of the resident melt, MCS records the geochemical evolution of the residual wallrock (Fig. 6). In cases where such information is available (e.g., contact zones of intrusions, inclusions of anatectic melt), MCS can be used in accordance with other information on the magmatic system to confirm or refine scenarios involving wallrock partial melting.

4.2.4 *Wholesale assimilation of stoped blocks*

Wholesale assimilation of stoped blocks will dominate in settings where wallrock xenoliths are efficiently introduced into the resident melt. Such conditions may prevail in upper crustal magma chambers or feeding channels, where the wallrock is highly fractured and behaves in brittle manner, and boundary temperatures are low (see Bohrson et al., 2014). The smaller the stoped blocks are, the higher the chance of rapid thermalization and partial or wholesale melting and, eventual equilibration with resident melt because small blocks heat up internally faster than larger ones (Carslaw and Jaeger, 1959).

When wallrock is completely equilibrated (i.e. bulk assimilation), partition coefficients for the wallrock phases do not play a role: i.e., the effect of assimilation on trace element contents of the resident melt is fully dictated by their concentration in the wallrock and the mass of the assimilated wallrock block. Therefore, in assimilation by stoping, any element that is relatively enriched in the assimilated wallrock block will also be enriched in the resident melt. Such effects may be diluted after stoping by subsequent fractional crystallization, however.

The isotopic model results very clearly illustrate the differences between assimilation by stoping (i.e., bulk incorporation of wallrock) and assimilation of anatectic melts (Fig. 3). Whereas Nd is incompatible and Sr compatible in wallrock in the case of wallrock partial melting (AFC; see previous section for details), in S_2FC, the isotopic composition of the resident melt is only controlled by bulk assimilation of the wallrock blocks into the resident melt. Depending on the compatibility of the associated elements and the process of contamination, the curves in isotope diagrams can be convex upwards or downwards (cf. Sr and Nd isotopes relative to $\delta^{18}O$ in Fig. 3b, c), making the distinction between wallrock contamination vs. source heterogeneity rather difficult (cf. Taylor, 1980; James, 1981).

If AFC and S_2FC are thought of as end-members of assimilation process, anything in between could take place in natural systems, where there is always a middle ground between wholesale melting of stoped blocks and partial melting of the wallrock. In most cases, MCS modeling would benefit from considering both options. Note that it is also possible to model SFC and AFC together in a single run to simulate such a system.

5 Model assumptions and limitations and future development of the *MCS-Traces*

MCS is a versatile, mass and energy balanced thermodynamic tool that can model complex scenarios that involve R_nAS_nFC. One of its shortcomings is that it is “only” an equilibrium thermodynamic model; it therefore does not account for time-dependent kinetic, diffusion, or transport phenomena, or other processes that may result in chemical disequilibrium – a well know feature of most igneous rocks. Many of these limitations have been discussed in the companion paper (Bohrson et al., submitted) and the reader is referred to it for more information, but we will further concentrate on those that are particularly relevant to modeling trace elements and their respective isotope systems.

A potentially important limitation in terms of trace element modeling is related to the MELTS engine. Current versions do not incorporate some minor phases such as zircon or monazite. Such phases are not usually important in terms of major element evolution of igneous systems, but they serve as important hosts for many otherwise incompatible trace elements (e.g., in the case of zircon and monazite, Zr and Th + REE, respectively). For example, Zr is modeled here as a generally incompatible trace element in the wallrock, but in an average crustal granitoid, zircon is almost always present, and its presence therefore will influence the behavior of Zr during its partial melting. If zircon remains in wallrock residue, wallrock partial melts will be relatively depleted in Zr, which will in turn affect the Zr evolution of the evolving resident melt. We recommend that the possibility of minor phases retaining some trace elements in the wallrock residue should be evaluated in MCS scenarios.

A designed future extension of *MCS-Traces* is to allow for isotopic disequilibrium during the partial melting of wallrock as demonstrated by Iles et al., (2018). In its current form, wallrock has an isotopic ratio that is the same as all phases in the wallrock. In the case of radiogenic isotopes, for example, this implies that differential ingrowth has not occurred in any of the minerals, and hence the isotopic ratio in anatectic melt does not change during assimilation. However, pre-magmatic in-growth of daughter isotopes in wallrock phases, dictated by phase-specific parent daughter ratios and time leads to variations in the respective isotopic ratios among mineral phases. In addition, although radiogenic ingrowth does not concern O isotopes, O isotopic heterogeneity between mineral phases in the same rock is also a common feature. It is easy to envision, for example, an Archean granitic wallrock where coexisting minerals (e.g., biotite, alkali feldspar, and plagioclase with distinct Rb/Sr) have distinct $^{87}Sr/^{86}Sr$. As wallrock undergoes partial melting, partial melt will have $^{87}Sr/^{86}Sr$ that is a function of the contribution each crystalline phase makes to the melt. Hence the isotopic composition of wallrock melt will change during the partial melt assimilation process. The potential effects of isotope fractionation between an isotopically heterogeneous wallrock and its partial melt batches can currently be approximated by, e.g., running two models using representative minimum and maximum radiogenic isotope ratios for the wallrock. Extension of MCS to include disequilibrium isotopes will allow a more quantitative and high-fidelity approach to this issue, and thus extends MCS's capabilities.

Similar to *MCS-Majors*, there is an urge to translate *MCS-Traces* to a programming language that would be platform-independent. While the advantages to the two-stage calculation presented here are many, merging the two tools would enable the Monte Carlo approach to trace element and isotope calculations, as has been proposed for the major element and phase equilibria calculations (see Bohrson et al., submitted). This modeling environment would allow users to produce a large number of models relatively rapidly, and with less human bias in choosing parameters. Future improvements will likely include the capacity for cross-platform use, as well as statistical tools to better constrain model results.

Finally, one of the most important things to realize as a petrologist and a potential user of MCS is the scale and the relative importance of the involved processes. If some crystals in the studied natural system are zoned, full of solid inclusions, or exhibit any disequilibrium textures, this does not instantly mean that MCS could not be used to constrain the general magmatic evolution of the system. Although current versions of MCS assume thermodynamic equilibration of a magma during open-system processes, the processes which produce such disequilibrium textures, such as recharge and magma mixing, are those which MCS was designed to model, and thus can reasonably approximate. In addition, with the ability to record trace element concentrations of melt, fluid, and each mineral in every step, MCS can provide important constraints on the thermal histories and geochemical conditions during the generation of crystal zoning; of course, interpretations of model results must be placed in context and compared with those derived from other data sources. In other words, when attempting to understand a natural system, one can search for the best MCS model by perturbing initial conditions and parameters iteratively, while remaining within the realm of reasonability. Such a 'best' model will, in all likelihood remain imperfect, perhaps in significant ways. Such imperfection should not be seen as a failure. Instead, by struggling with *the root cause* of the imperfections, valuable clues to the systems petrological and geochemical evolution may be elucidated. That is, the nature of the transport, kinetic and dynamic phenomena, precisely those ignored in thermodynamic models, may rise to the top to be addressed by 'beyond thermodynamic' analysis. This confrontation with reality and attempt to model complex systems is the ultimate goal of petrology. We close the MCS companion papers citing the final few words in N.L. Bowens 1928 opus on the *Evolution of the Igneous Rocks* (Bowen, 1928*):* "No implication is intended that our knowledge is all that could be desired. That can never be."

6 Summary

The Magma Chamber Simulator *MCS-Traces* computer program calculates the simultaneous evolution of 48 trace elements, seven radiogenic isotope systems (Sr, Nd, Hf, 3xPb, and Os), and O isotopes for a magma (melt + crystals ± fluid phase) in an igneous system influenced by magma recharge, assimilation (either of wallrock partial melts or stoped blocks), and fractional crystallization (R_nAS_nFC). In addition, the trace element evolution of the cumulate pile and residual wallrock is output. *MCS-Traces* works in Visual Basic in Macintosh Excel and requires output from the *MCS-Majors* computational tool (Bohrson et al., submitted) to perform the calculations. Our analysis of example case studies of depleted mantle melt assimilating average granodioritic crust, with or without recharge of the same parent magma reveals key characteristics of the different processes. For the case studies presented here, the effects of magma recharge are difficult to recognize from trace element or radiogenic isotope data alone; a temporal (e.g., stratigraphic or intracrystalline) reference frame is required and we also note that recharge may be more evident when there is greater contrast between resident melt and intruding magma(s). In contrast, assimilation (especially in the case of assimilation of wallrock anatectic melts) may have drastic effects on incompatible trace element and isotopic compositions of the resident melt. The magnitude of these effects depends predominantly on phase equilibria, element partitioning, style of contamination (wallrock partial melts vs. stoping) and the geochemical differences between the resident melt and the wallrock. In many cases, the effects of assimilation are counterintuitive and varied and considerable caution should be practiced in ruling out potential assimilation scenarios. The case studies presented here highlight the challenges that petrologists and geochemists face when diagnosing open-system processes. Discrepancies between observations and the 'best' open system model(s) have the potential to reveal details of the role of kinetic and transport phenomena (non-equilibrium) in petrogenesis. There are a plethora of ways to use MCS to solve petrogenetic questions related to magmatism in wide range of igneous environments.

Appendices

Appendix S1: Modeling the evolution of EM2 and the origin of trachytic liquids beneath Samoa

S1.1. Model scenario 1

Following the magma mixing model proposed by recent work (Edwards et al., 2019), the EM2 mixing endmember, proposed in this study to be trachytic in composition, is created by the generation of isotopically enriched, primitive mantle-derived partial melts that are then differentiated to an evolved, and high $^{87}Sr/^{86}Sr$ magma that is then mixed with a more primitive, low $^{87}Sr/^{86}Sr$ magma to form the ALIA-D115 lava mixing trend. The final mixed magma may contain crystal cargo inherited from either or both endmember magmas and, significantly, newly formed crystals can be the result of the mixing event itself. In this work, we take this model a step further by utilizing phase equilibria calculations to test this model. We suggest a scenario in which ancient subducted sediment (high in $^{87}Sr/^{86}Sr$) melts and fertilizes ambient peridotite to form a hybridized sediment + peridotite mixture. This mixture is subsequently partially melted at depths consistent with the lithosphere-asthenosphere boundary at Samoa, ~65 km (or 2-3 GPa) as well as Samoan mantle xenolith equilibration pressures of around 1-3.6 GPa using a Ca-in-olivine barometer (Hauri and Hart, 1994) and slightly lower than the 3-5 GPa pressures obtained using cpx-thermobarometry (Putirka, 2008). These melts are then transported to shallow levels in the lithosphere (≤ 1GPa) where they undergo fractionation.

Roughly 40 simulations were carried out using pMELTS (Ghiorso et al., 2002) and the Magma Chamber Simulator (MCS; Bohrson et al., 2014) to simulate the partial melting and fractionation described above (see Supplementary Dataset S3a and b for starting compositions and model parameterizations, respectively). Calculations of 5-20% equilibrium partial melting were performed at 2 and 3 GPa on various bulk compositions. Regardless of starting composition, at 2 and 3 GPa, the partial melts range from phonolites at low degree partial melts (5%) to dominantly basanitic at high degree partial melts (15-20%) with one partial melt composition reaching a picro-basalt. The 2 GPa partial melts are consistently more silicic by ~3 wt% than the 3 GPa partial melts, but their alkali contents seem to remain constant between the 2 and 3GPa simulations. Fractional crystallization of these partial melts consistently leads to phonolitic melts (see Supplementary Figure S7 for an example partial melting and fractionation calculation). The existence of evolved, low $^{87}Sr/^{86}Sr$ trachyte lavas erupted in Samoa show that highly differentiated magmas exist beneath Samoa and thus, EM2-like melts may undergo significant fractionation prior to mixing, but results from the above simulations are not consistent with the origin of the evolved, high $^{87}Sr/^{86}Sr$ trachytic liquids at Samoa being from partial melting of sediment contaminated peridotite followed by differentiation since we could only generate phonolitic to basanitic melts, not trachytic melts. Trachytic liquids are often thought to be derived through fractionation of alkali basalts (Le Roex, 1985; Renzulli and Santi, 2000; Thompson et al., 2001; Cousens et al., 2003; Berger et al., 2009). In the case of Samoa, the radiogenic nature of the EM2 mixing endmember requires a sediment component in the source and this sediment addition inevitably adds alkalis to the system. Thus, partial melting sediment-contaminated peridotite results in melts more enriched in the alkalis compared with typical primitive mantle melts driving any fractionation of these liquids to phonolitic compositions, consistent with our phase equilibria calculations.

Bearing in mind the discussion above, the parameter space that can be explored in these calculations is quite large – the following parameters are important: pressure of melting, pressure of fractionation, starting bulk composition, fO_2, water content, type of melting (i.e. equilibrium vs. batch), percentage of melting, to name the more salient ones. Considering these 7 variables, about 5000 models could be explored in this parameters space! Thus, further exploration of the model described above requires a Monte Carlo approach that we have not attempted, but should be explored.

S1.2. Model scenario 2

A second model is one in which the trachytic melts are created through partial melting of a sediment bulk composition. These partial or total melts may then mix with more primitive Samoan basaltic melt, perhaps generated by partial melting of an ultramafic or eclogitic source, to create the ALIA-D115 lava mixing trend. This scenario requires silicate melts derived by total or partial melting of sediments to remain isolated from ambient ultramafic mantle until the time of mixing with basaltic magmas. This is problematic because, as is well-known, siliceous melts are reactive with ultramafic bulk compositions. Nevertheless, there is evidence in mantle xenoliths found in alkali basalts of Tallante, Spain that show isolated high silica veins. These quartz-diorite veins (SiO_2=62 wt%, MgO=1.5 wt%, Na_2O+K_2O=3.9 wt%) are thought to be the result of slab melts interacting with the mantle wedge and remain isolated from the surrounding peridotite due to a reaction between the silicate melt and olivine creating an orthopyroxene reaction barrier (Arai et al., 2003; Shimizu et al., 2004; Bianchini et al., 2011; Bianchini et al., 2015). On a larger scale, perhaps this reaction could buffer the silicate melts allowing them to be transported through the mantle without completely reacting with surrounding peridotite. Alternatively, it’s possible that these xenoliths could be transported to the deeper mantle and sampled later by mantle plumes.

S1.3. Model scenario 3

Another scenario is that the primitive EM2 source has been contaminated not only by sediments, but also carbonatitic liquids. Evidence has been marshalled for carbonatitic metasomatism beneath Samoa (Hauri et al., 1993; Hauri and Hart, 1994; Ashley, 2019). Hauri et al. (1993) and Hauri and Hart (1994) suggest Samoan xenoliths show evidence of interaction with carbonatitic liquids based on enrichments in LREE and Zr and Ti depletions in cpx. More recently, Ashley (2019) performed an analysis of water contents and major and trace elements on Samoa peridotite xenoliths, particularly in orthopyroxene, showing trace element characteristics and variable depletions in water contents of nominally anhydrous minerals are reflective of both carbonatite and silicate melt metasomatism. Partial melting of mantle material contaminated with carbonatitic liquids has been suggested to produce phonolitic to trachytic liquids (Hauri et al., 1993; Ashwal et al., 2016; Loges et al., 2019) and Hauri et al. (1993) found trachytic glass in a Savai'i xenolith interpreted to be a partial melt of a carbonated peridotite. This glass is similar in composition to the inferred "EM2" endmember of this study and thus could be evidence for the origin of EM2. This model is currently difficult to explore by thermodynamic modeling calculations because no high pressure igneous thermodynamic model (that can handle ultramafic compositions) exists that includes CO_2.

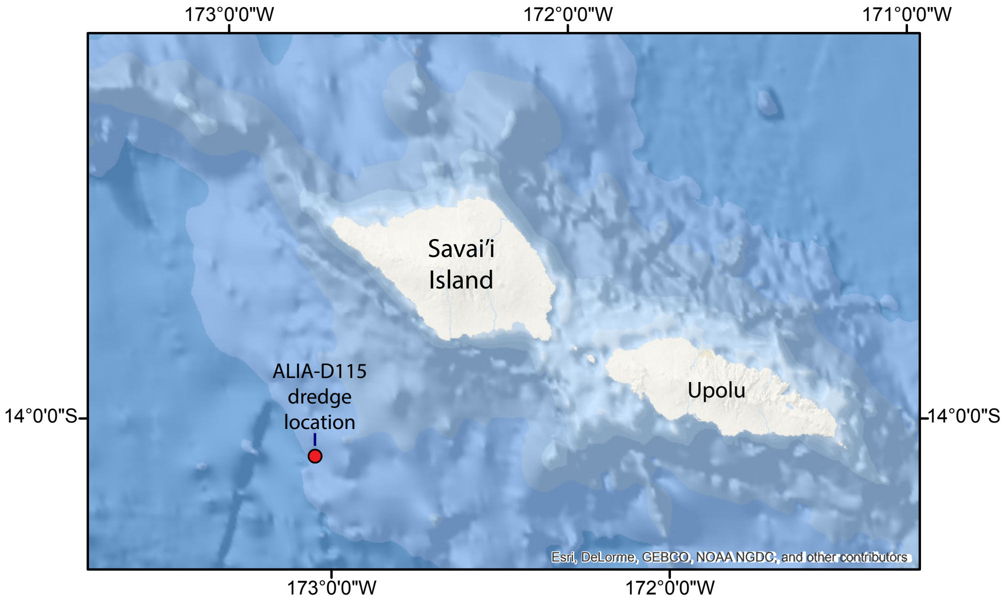

Figure S1: Location of Savai'i island, Western Samoa and the location of the samples discussed in this study. ALIA-D115 lavas were dredged off the coast of Savai'i Island at 3,220 m (Jackson et al., 2007) water depth (at the ALIA-D115 dredge sample site denoted with a red dot).

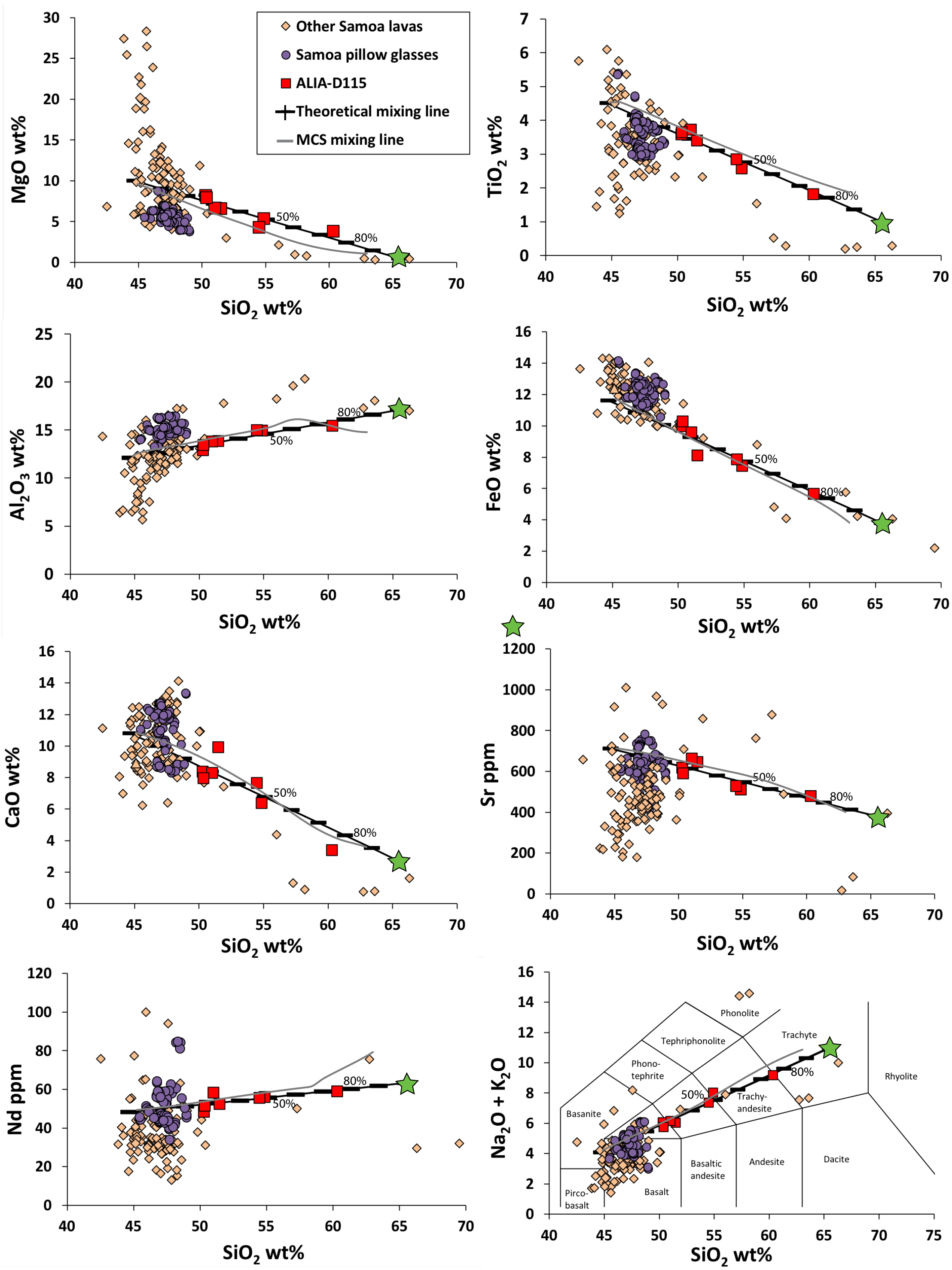

Figure S2: Theoretical and model mixing calculations in relation to other Samoan whole rock lavas. The black hatched line is the mixing curve calculated using binary mixing theory (see Methods for details) and each hatch represents 10% mixing increments. The green star denotes the silicic, high ^{87}Sr/^{86}Sr inferred endmember composition from one of the binary mixing calculations. The grey line is a Magma Chamber Simulator (MCS) magma mixing simulation that incorporates the thermodynamics of combined magma mixing and fractional crystallization processes between the calculated mixing endmembers of this study. The mixing line represents the *melt* evolution as a result of mixing and crystallization (where crystals are removed from the system), thus mass is not conserved (unlike theoretical binary mixing) and the mixing line is not expected to end at the *inferred* EM2 endmember (see Methods for more detail). Since the grey line represents a real thermodynamically constrained simulation, in this case the simulation terminated when the melt reached ~63% crystallization meaning no solution could be found past this point. This highlights the differences between using simple binary mixing calculations that do not take into account thermodynamics compared to the MCS simulation, which, although not perfect, represents a more realistic view of these open system processes.

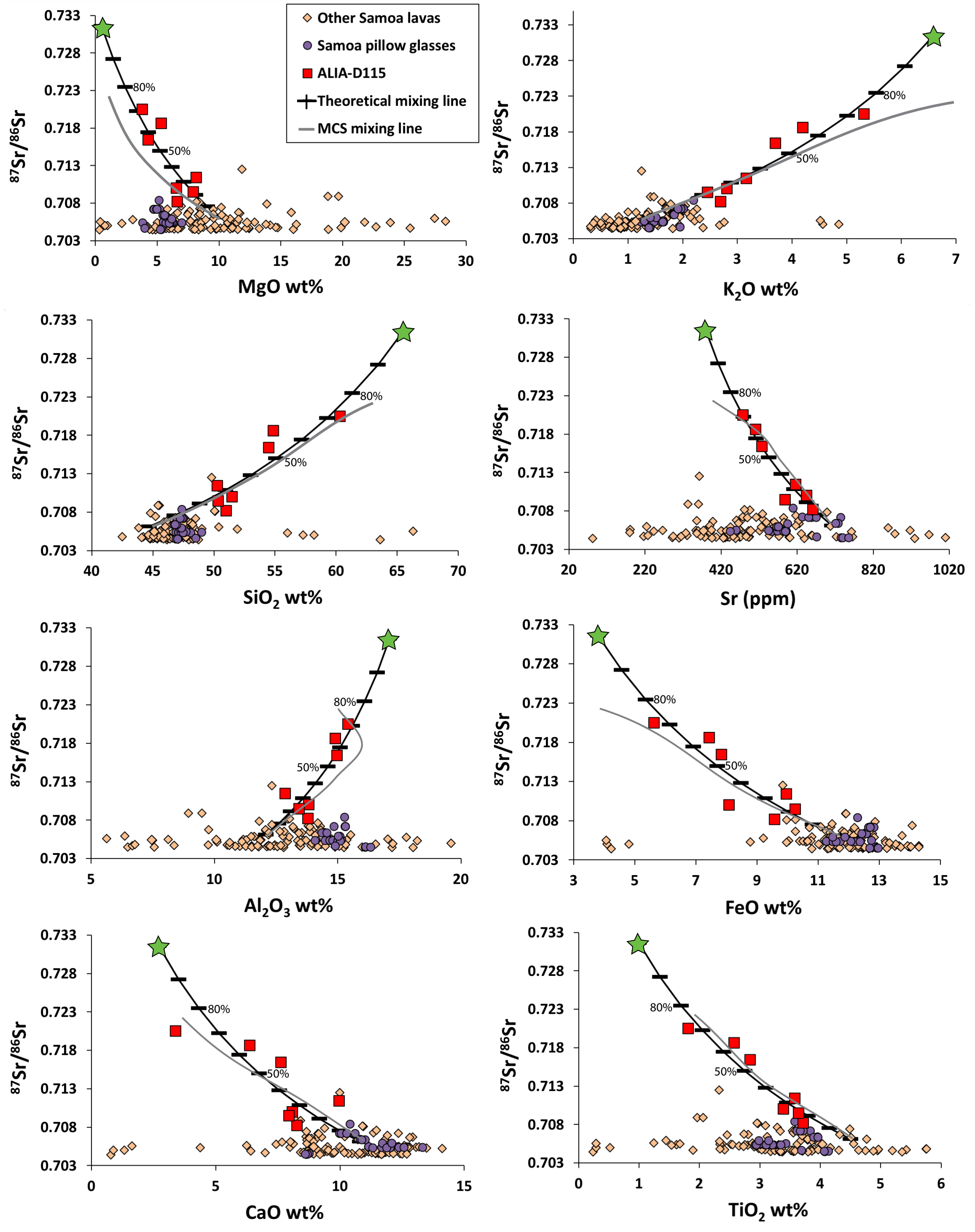

Figure S3: Theoretical and model mixing calculations in relation to other Samoan whole rock lavas in $^{87}Sr/^{86}Sr$ vs. element concentration plots. Mixing is theoretically hyperbolic in ratio versus element space. The green star denotes the composition of the silicic, high $^{87}Sr/^{86}Sr$ EM2-derived endmember. See Figure S1 caption for description of mixing lines.

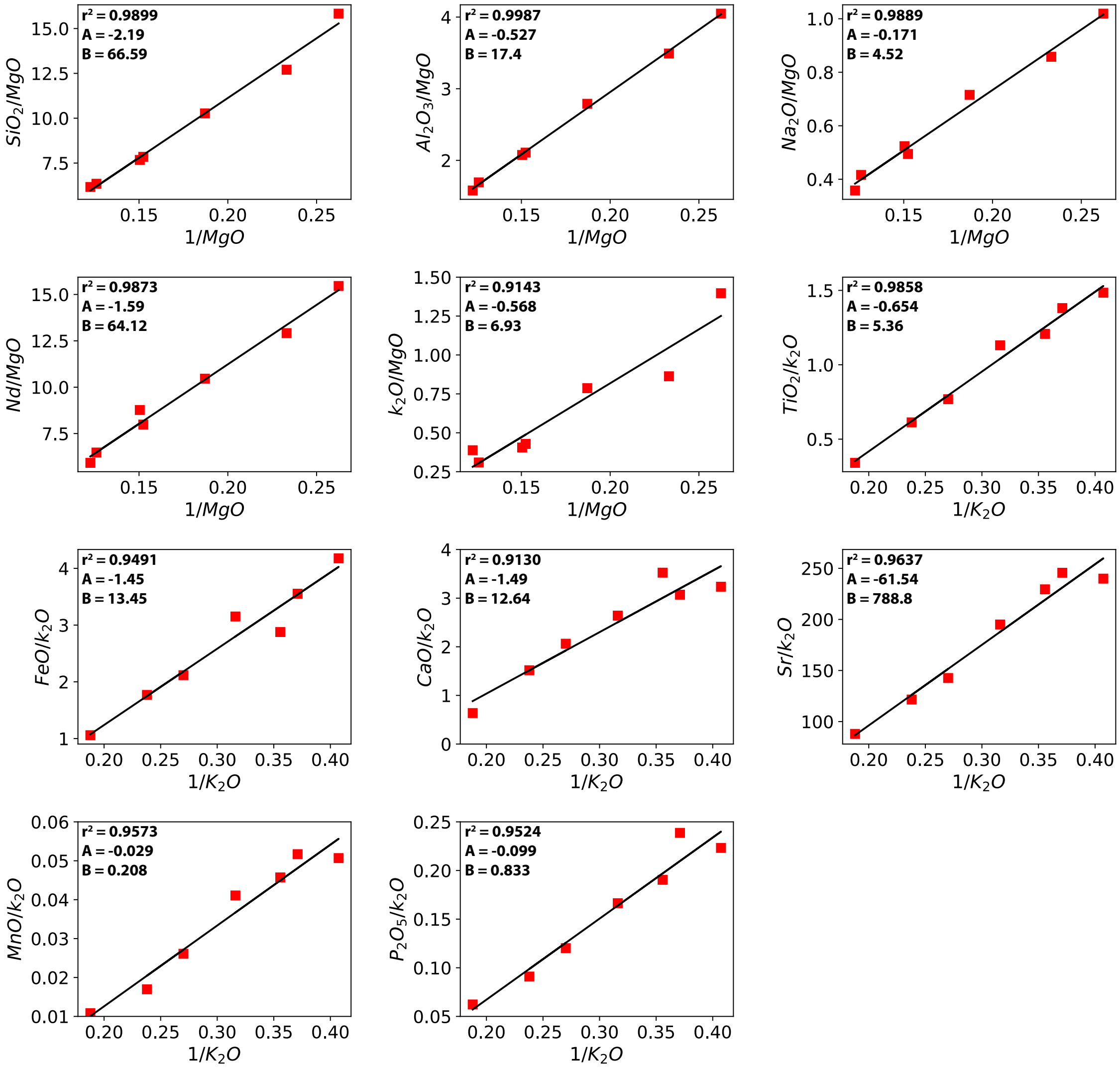

Figure S4: Ordinary least squares regression (ODR) for all ratio-ratio plots used to infer both the mafic (M), low ^{87}Sr/^{86}Sr and silicic (S), high ^{87}Sr/^{86}Sr mixing endmembers. The red squares are the ALIA-D115 whole rock lavas. The black line is the modeled regression fit which is of the form $\frac{C_2^H}{C_1^H} = A + \frac{B}{C_1^H}$, where C_1^H and C_2^H are the concentrations of chemical species 1 and 2 the mixed (**H**ybrid) magma. *A* can be thought of as the y-intercept and is of the form $A = \frac{C_2^M - C_2^S}{C_1^M - C_1^S}$ and *B* represents the slope given by the equation $B = \frac{(C_1^M C_2^S - C_1^S C_2^M)}{C_1^M - C_1^S}$, , where C_1^M and C_2^M are concentrations of chemical species 1 and 2 in M and C_1^S and C_2^S are the concentrations in S. The *A* and *B* values are derived from the ODR, thus given *A* and *B* and the known value of MgO in C_1^M and C_1^S, then C_2^M and C_2^S can be calculated, given some re-arranging of the above equations (see Methods for more details), for all of the other major elements.

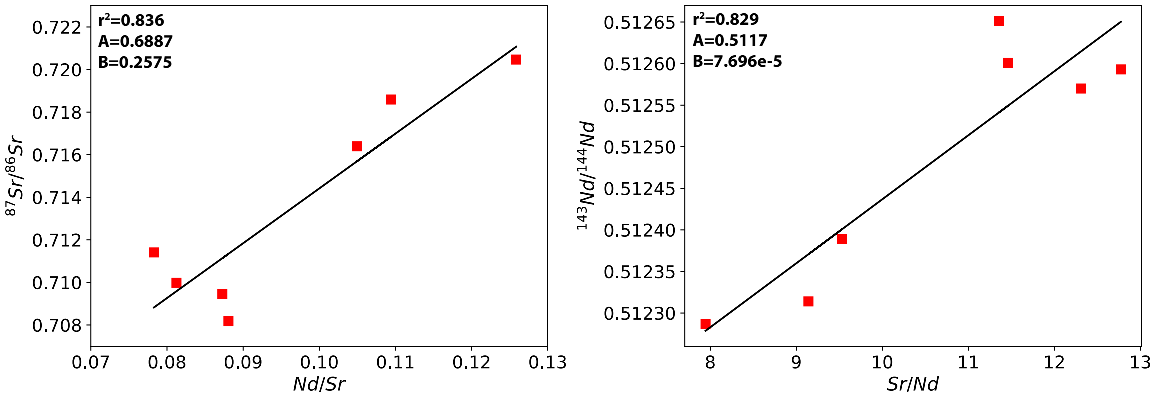

Figure S5: Ordinary least squares regressions for isotope ratio vs. element ratio mixing plots. The red squares are the ALIA-D115 whole rocks. The black line is the modeled regression fit and the A and B values describe the equation for the fit – these values are summarized briefly in Supplementary Figure 4 and more thoroughly in the Methods section. The Sr and Nd concentrations used in these plots are from the regressions of Supplementary Figure 4. Thus, if the Sr and Nd concentrations are known, then using the equation for the linear regression described on isotope ratio versus element ratio space, one can calculate the ^{87}Sr/^{86}Sr and ^{143}Nd/^{144}Nd.

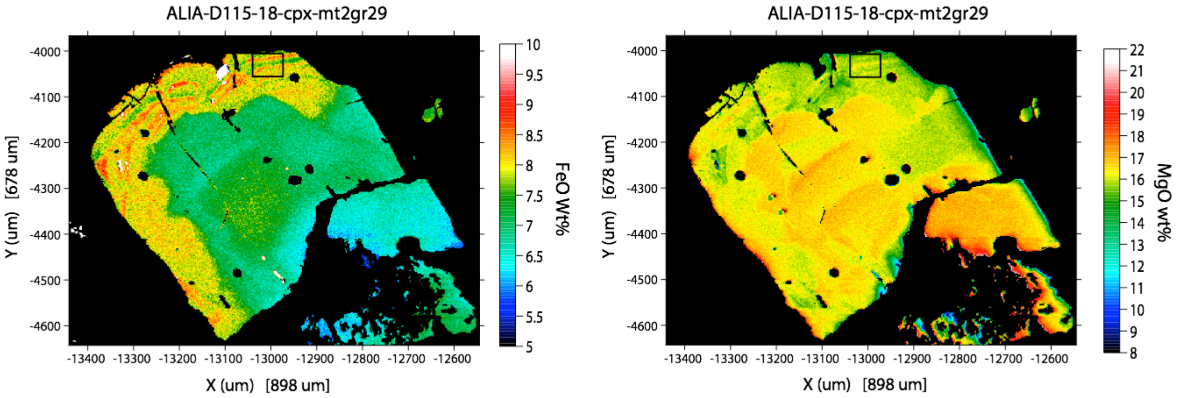

Figure S6: Example of clinopyroxene major element oxide maps performed on the electron microprobe at UC Santa Barbara using 2 µm pixel size. Mg and Fe chemical zonation show irregular zoning patterns indicative of magmatic mixing and are also the fastest diffusing elements that have preserved chemical zoning in the ALIA-D115-18 clinopyroxenes. Mg-Fe inter-diffusion is particularly fast and the smallest compositional band thicknesses (lamella) are used to estimate magmatic residence times. Magma residence time calculations are described in detail in the Methods section. The smallest lamella thicknesses that exist in these clinopyroxenes are shown in the black box below measuring about 15 µm thick.

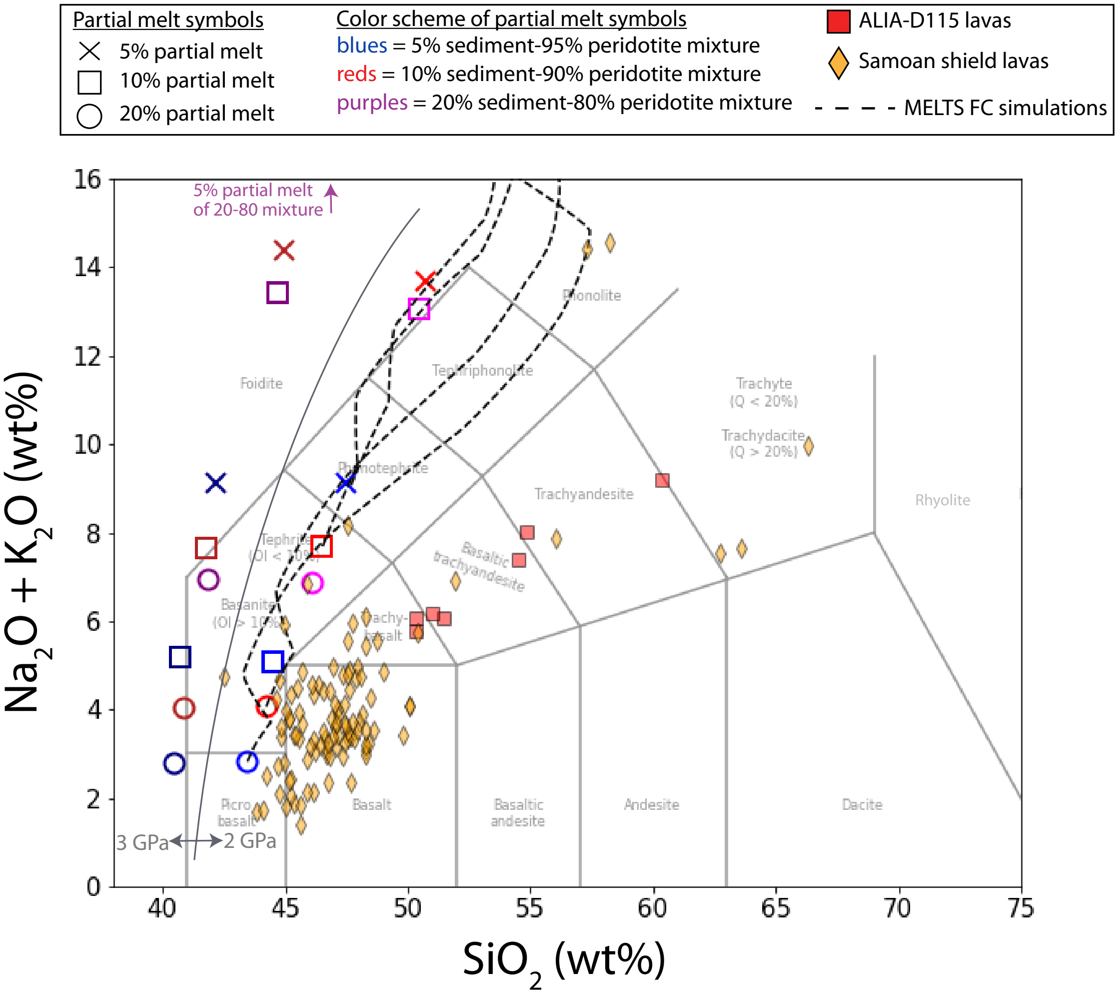

Figure S7: Representative partial melting and fractional crystallization (FC) simulations of mixed peridotite+sediment bulk compositions. Simulations were performed using pMELTS showing that the origin of the EM2-derived, trachytic mixing endmember calculated in this study likely does not originate from partial melting of a sediment contaminated peridotite source that subsequently undergoes differentiation, as suggested by other workers[4,12]. The differentiation of the partial melts consistently lead to phonolites, not trachytes (see Supplementary text for further discussion). The bulk starting mixture used for these simulations was MSCS-3G (see Supplementary Table 3 for ref.) sediment + peridotite with mixture proportions ranging from 5-20% MSCS-3G and 95-80% peridotite. "X" symbols indicate 5% partial melt compositions, squares indicate 10% melt compositions, and circles indicate 20% partial melt compositions. The light grey line divides the 2 and 3 GPa partial melt simulations (3 GPa partial melts to the left of the line and 2 GPa partial melts to the right). Blue colors on either side of the grey line indicate a mixture of 5% MSCS-3G and 95% peridotite, reds indicate a 10% MSCS-3G and 90% peridotite mixture, and purples indicate a 20% MSCS-3G and 80% peridotite. In addition, 0.5 GPa FC simulations (dashed lines) using different 2 GPa partial melt compositions as starting compositions are plotted. Only the FC simulations performed on the partial melts performed at 2 GPa are shown as FC of the 3GPa partial melts look very similar. FC simulations were also run at 1 GPa and 0.3 GPa and show minute differences in their evolutionary paths, thus only the 0.5 GPa simulations are plotted for clarity. ALIA-D115 whole rock lavas and other Samoan shield lavas are also plotted for reference. Similar results as those presented below are found using any of the compositions outlined in Supplementary Table 3a under any of the parameterizations outlined in Supplementary Table 3b, thus only one set of simulations is shown below for clarity.

Appendix S2: Test of post-entrapment crystallization using geochemical gradients

S2.1 Compositional gradients as a result of post-entrapment crystallization

Here we test post-entrapment crystallization of clinopyroxene as the mechanism generating the unusual melt inclusion compositions observed here. If we assume that the melt inclusions (MIs) represent a residual liquid from which host clinopyroxene grew after entrapment, we can consider a hypothetical model, as seen in Figure S1, that can be tested. In this model, the initial state of the MI is entrapment within the host clinopyroxene grain as shown in Figure S1a. After cooling proceeds, the MI begins to react with the host clinopyroxene and crystallize a compositionally distinct clinopyroxene at the MI edge (Figure S1b). If we assume no diffusive re-equilibration has occurred (the diffusion assumption is tested in Figures S2-S9), then we should observe major and trace element compositional gradients going away from the MI and into the host clinopyroxene (see Figure S1b A-A'). If crystallization is in equilibrium, we would expect compositional profiles to differ based on their partition coefficients (K_d) between clinopyroxene and melt. At location 1 along the A-A' transect in Figure S1c, we would expect compatible elements to have elevated concentrations (as this was the first clinopyroxene to grow from the melt), and low concentrations at location 2 (as this was the last clinopyroxene to grow from the melt). The incompatible elements will show the opposite behavior. We have measured 17 compositional profiles in 4 clinopyroxenes hosting melt inclusions and we can use this data to test if our incompatible and compatible element profiles are consistent with the model behavior.

S2.2 Major element profiles

Figures S2-S9 show 2-6 compositional profiles across each of the 4 clinopyroxene grains tested. Although we assume here no diffusive re-equilibration has occurred, it behooves us to focus on the elements that diffuse the slowest as these are least affected by diffusion and preserve gradients (if any) resulting from the proposed PEC model (as shown in Figure S1). Compatible major elements within clinopyroxene that diffuse slowly are Si, Ca, and Cr. Slowly diffusing incompatible elements are Al and Ti. Figures S2-S5 show major element compositional profiles (termed line segments, or LS) going in different directions away from the MI edge and into the host clinopyroxene. Our model above predicts that Si, Ca, and Cr concentrations should increase going away from the MI, while Al and Ti concentrations should decrease. It's important to note that a measure of inconsistency with the model for the gradients is if they show opposite trends for what the model predicts *or* if they are flat (within relevant uncertainty). Thus, of the 17 line segments across four clinopyroxenes, 4 (~24%) Si profiles are consistent with the PEC model and 13 (76%) are not consistent (11 of which are flat), 5 (~29%) Ca profiles are consistent with the model and 12 (~71%) are not (9 of which are flat), and finally 1 (~6%) Cr profile is consistent with the model and 16 (~94%) are not (12 of which are flat). As for the incompatible major elements, 4 (~24%) Ti profiles are consistent with the model, while 13 (~76%) are not (8 of which are flat), and 7 (~41%) Al profiles are consistent with the model, while 10 (~59%) are not (7 of which are flat).

S1.3 Trace element profiles

Thirteen of the 17 profiles analyzed for major elements by electron microprobe were later analyzed for trace elements by LA-ICP-MS. Figures S6-S9 show trace element compositional profiles for the same clinopyroxene as described for the major elements, but not all line segments were measured given the laser spot size and available space on the clinopyroxene. We can test our model again for incompatible (i.e., Y, Zr, La, Ce, Dy) and compatible elements (i.e., Sc). For the profiles presented in Figures S6-S9. The compatible element, Sc, should increase going away from the MI and 2 (~15%) out of the 13 transects are consistent with this hypothesis while 11 (~85%) do not (with 8 being flat within uncertainty). For the following incompatible elements: Zr, Y, La, Ce, Dy, and Nd, about 31-38% of the 13 profiles show agreement with the model (decreasing gradients going away from the MI) and 62-69% do not conform to the model. For Gd, Sm, and Ho, ~8-15% of the profiles are consistent with the model while 85-92% of the profiles are not consistent. For Yb, none of the profiles are consistent with the PEC model. It should be noted that many of the non-model conforming line profiles were either going in the opposite direction of the predicted model gradient or were ambiguous due to oscillatory zoning or were flat within uncertainty.

S1.4 Conclusions

Considering the combined major and trace element transect data (13 profiles total were measured for both), only 2 out of the 13 (~15%) profiles completely conform to the PEC model presented here, meaning of all of the elements (major and trace; including compatible and incompatible), that were not flat or had oscillatory zoning, for both profiles were consistent with the model gradients for PEC. Considering only the 17 major element profiles, again 2 out of the 17 (~12%) are consistent with PEC. Given the few number of profiles consistent with the PEC model presented here, we suggest PEC has not played a role in controlling these gradients and thus the MI compositions. Additionally, there is much ambiguity in interpreting some of these chemical gradients because some profiles within a single clinopyroxene can exhibit opposite behavior, as in some profiles will increase in concentration of compatible elements going away from the MI and some will decrease (e.g., see the four Cr_2O_3 profiles in Figure S5 in which profiles LS2 and LS4 increase going away from the MI and LS1 and LS3 decrease). The same feature is seen with the incompatible elements as well (see example in Figure S7 in which LS1 and LS3 of the Y and Zr profiles are decreasing going away from the MI while LS2 is increasing). Much of this behavior could be due to clinopyroxene anisotropy, which has been previously observed (e.g., Biedermann et al., 2015). Alternatively, if new clinopyroxene did grow from the MIs post-entrapment, the only other way to reconcile the ambiguous data is that there has been sufficient time for diffusion to redistribute elements and smooth out or alter the gradients in some way. If this were the case, we can calculate the time in which it would take to smooth out gradients for certain elements. Elements like Ca and Si, for example, diffuse quite slowly, yet show flat compositional profiles in many of the clinopyroxenes. For illustration, consider a distance into the crystal of 30 μm in which gradients exist. Using a clinopyroxene diffusivity (log D; m^2/s) at 1200 °C for Ca and Si of -19.2 (Cherniak and Dimanov, 2010) and -21.6 (Cherniak and Dimanov, 2010), respectively, we would expect the gradients to be smoothed out in ~452 years (for Ca) to ~110,000 years (for Si). These times are not consistent with the much shorter magma residence timescales calculated in a recent study by Adams et al. (in review) that used the thickness of Mg and Fe compositional zones and diffusivities in the clinopyroxenes from the ALIA-D115-18 sample to calculate magmatic residence times of less that 45 to less than 2 years. In addition, if significant diffusion had occurred to smooth out the gradients, we would expect to see that process reflected in the MI morphology as discussed in the main text (section 4.1.1), which is not the case for these

MIs, thus, diffusion and PEC seem to have had little effect on modifying the MI compositions.

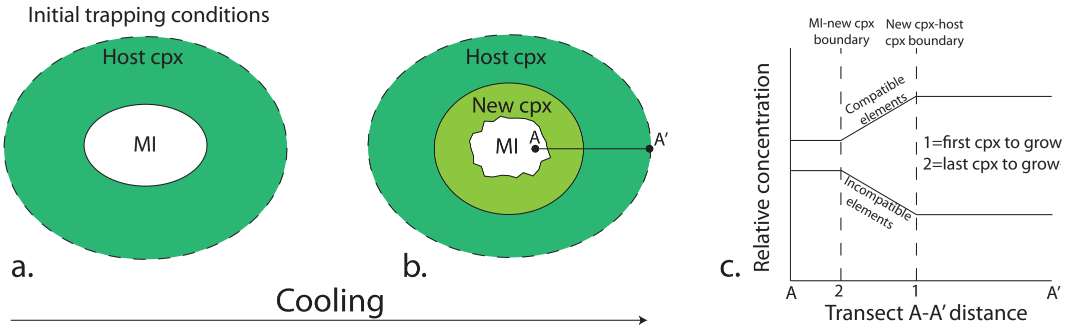

Figure S1. The evolution of post-entrapment crystallization (PEC) and a model for hypothetical chemical gradients. (a) Conditions of initial trapping of MI prior to any PEC. The MI has a rounded shape. (b) As cooling proceeds, the MI begins to react with the host clinopyroxene and precipitate a compositionally distinct clinopyroxene directly from the melt, resulting in changes in the chemistry of the MI and will also leave behind distinct chemical gradients between the MI and the newly-crystallized clinopyroxene (gradients shown in panel c). A chemical profile along the A-A’ line should reveal these gradients if diffusion has not been an important process in modifying them. (c) Schematic representation of the predicted behavior of chemical gradients from the MI edge through the host clinopyroxene. The location of the A-A’ transect can be seen in panel (b) and is represented on the x-axis of panel (c). Relative concentrations of incompatible and compatible elements is represented on the y-axis. Locations 1 and 2 correspond to the boundary between the MI and newly-crystallized clinopyroxene and original host clinopyroxene, respectively. The relative concentrations of compatible elements should show an increasing trend between the edge of the MI and the host clinopyroxene while the incompatible elements should show the opposite trend. These gradients are not confirmed in the data (see Supporting Figures S2-S9), indicating that PEC processes are not important in the petrogenetic evolution of these inclusions (i.e., the compositions of the inclusions are quite close to the compositions of the original trapped melts).

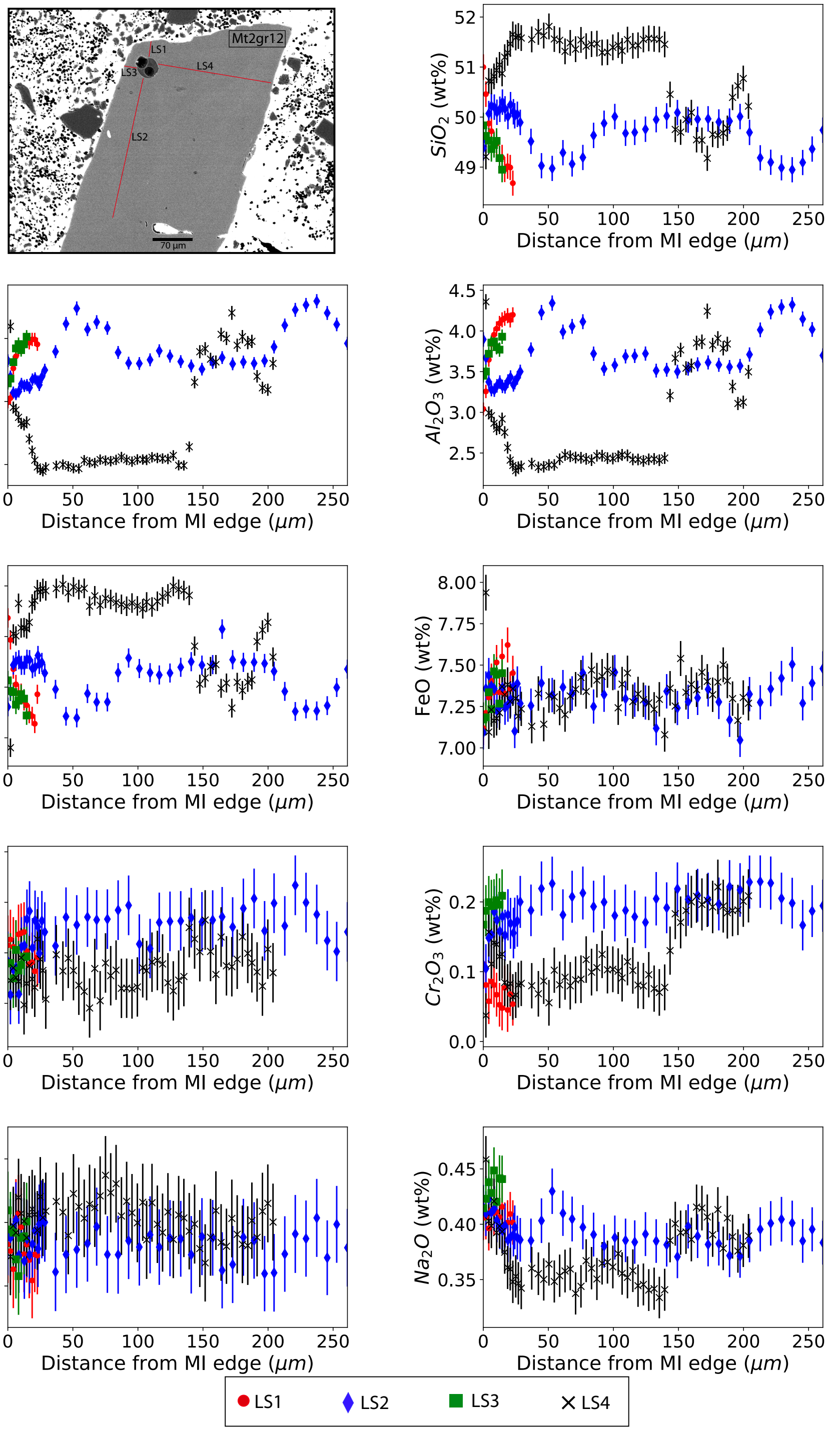

Figure S2: Major element transects through the mt2gr12 host clinopyroxene (the mt2gr12 melt inclusion was also analyzed in this study for major and trace elements). The transects, termed line segments (LS) 1 through 4, are shown in the BSE image (1st panel) of the clinopyroxene where each red line denotes the extent of each line segment that can be seen in the major element plots. Each line segment extends from the MI edge out into the clinopyroxene grain. Major element data was collected via EPMA using a 2 µm spot size and error bars are 2σ.

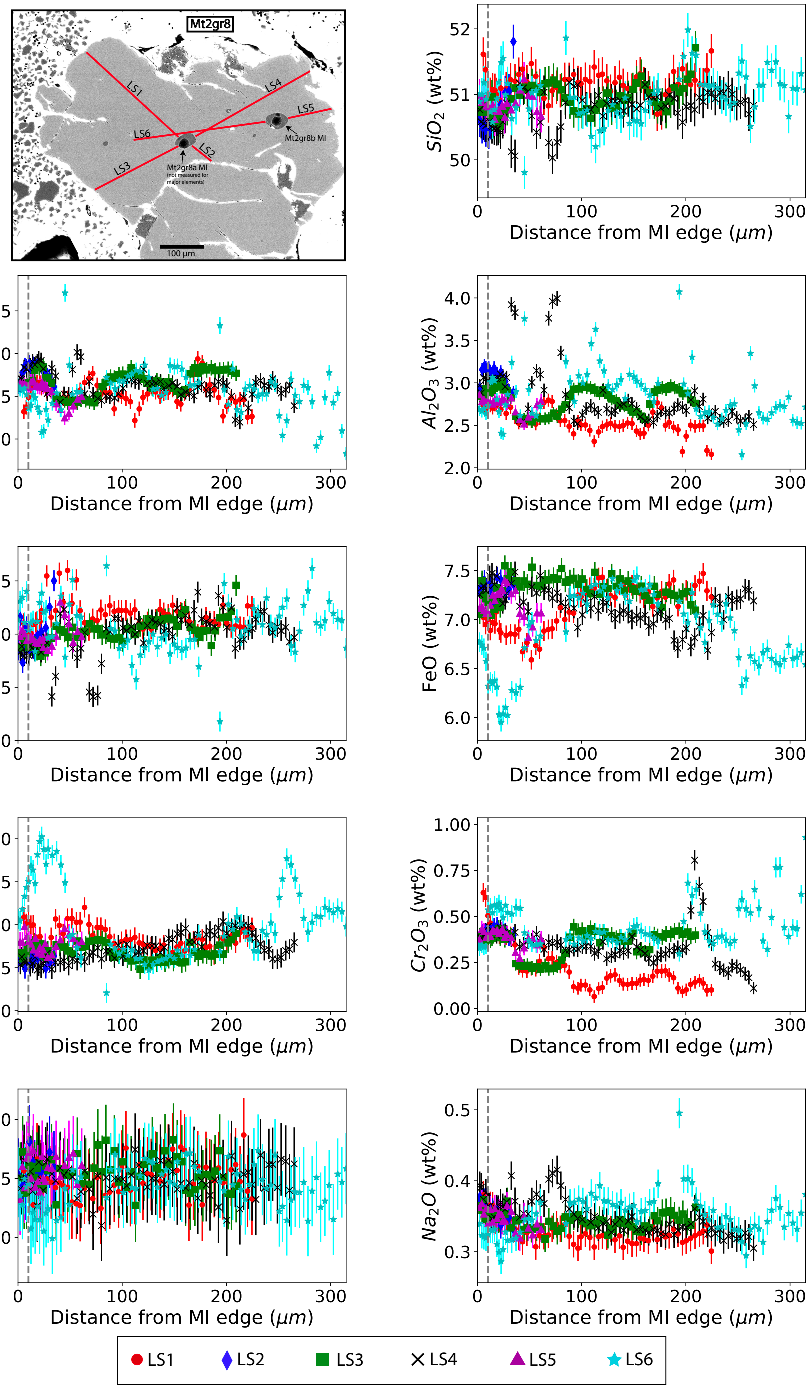

Figure S3. Major element transects through the mt2gr8 host clinopyroxene (the mt2gr8b MI was analyzed for major and trace elements in this study as denoted in the BSE image). The transects, termed line segments (LS) 1 through 6, are shown in the BSE image (1st panel) of the clinopyroxene where each red line denotes the extent of each line segment that can be seen in the major element plots. Each line segment extends from the MI edge out into the clinopyroxene grain. Major element data was collected via EPMA using a 2 µm spot size and error bars are 2σ. Some of the data points of LS6 have been removed as they were contaminated in passing by the central melt inclusion. The grey dashed line denotes the average distance from the MI edge to the edge of the "halo" feature that can be seen around the mt2gr8b MI (see Figure S10h).

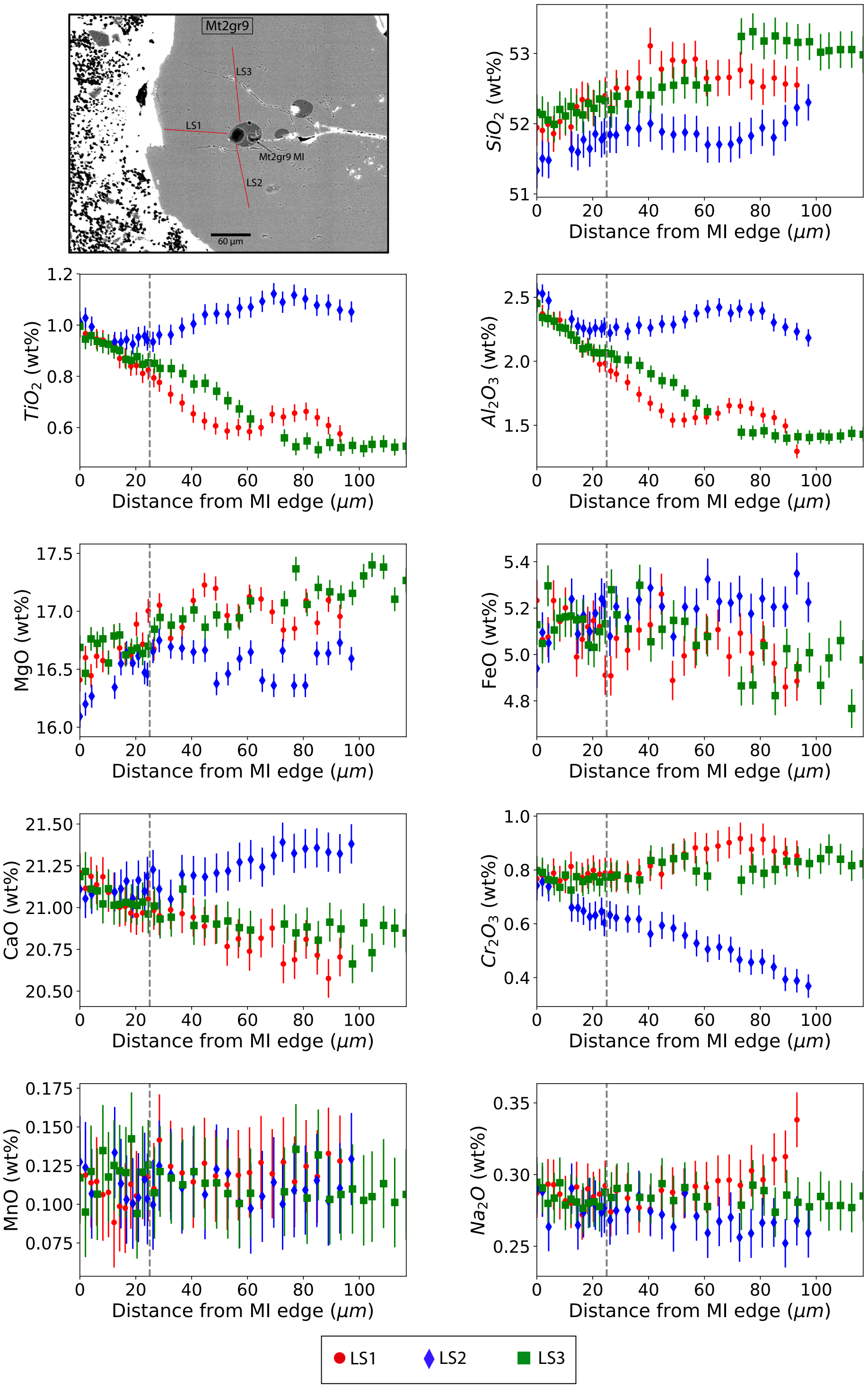

Figure S4. Major element transects through the mt2gr9 host clinopyroxene (the mt2gr9 MI was analyzed for major and trace elements in this study). The transects, termed line segments (LS) 1 through 3, are shown in the BSE image (1st panel) of the clinopyroxene where each red line denotes the extent of each line segment that can be seen in the major element plots. Each line segment extends from the MI edge out into the clinopyroxene grain. Major element data was collected via EPMA using a 2 µm spot size and error bars are 2σ. The grey dashed line denotes the average distance from the MI edge to the edge of the "halo" feature that can be seen around the mt2gr8b MI (see Figure S10i).

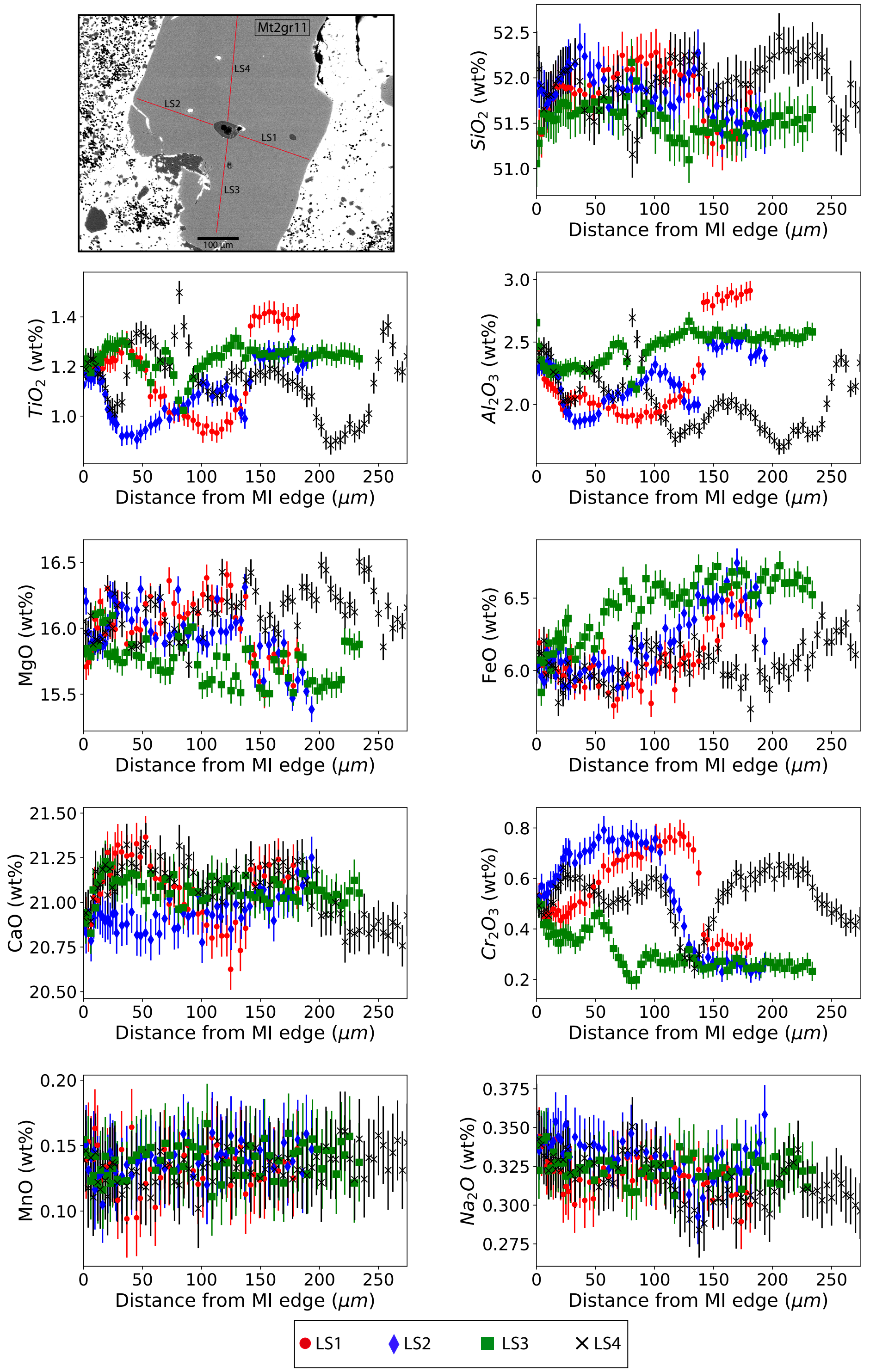

Figure S5. Major element transects through the mt2gr11 host clinopyroxene (the mt2gr9 MI was analyzed for major and trace elements in this study). The transects, termed line segments (LS) 1 through 4, are shown in the BSE image (1st panel) of the clinopyroxene where each red line denotes the extent of each line segment that can be seen in the major element plots. Each line segment extends from the MI edge out into the clinopyroxene grain. Major element data was collected via EPMA using a 2 µm spot size and error bars are 2σ.

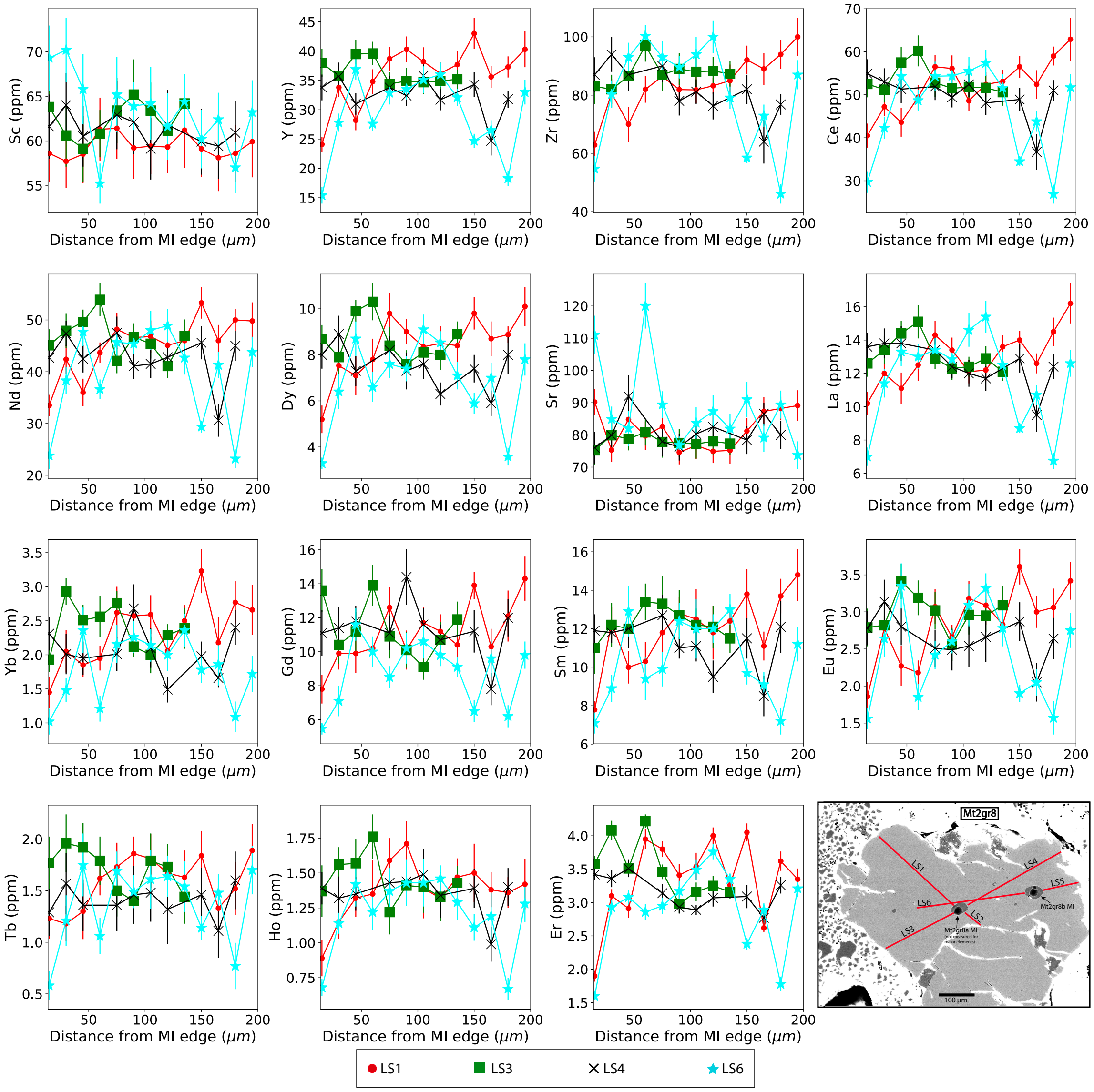

Figure S6: Trace element transects through the mt2gr8 host clinopyroxene (the mt2gr8b MI was analyzed for major and trace elements in this study, as denoted in the BSE image in the last panel). The transects, termed line segments (LS) 1 through 6, are shown in the BSE image (last panel) of the clinopyroxene where each red line denotes the extent of each line segment that can be seen in the major element plots. Each line segment extends from the MI edge out into the clinopyroxene grain. Trace element data was collected via LA-IC-PMS using a 15 μm spot size and error bars are 2 SE. Trace elements were not measured for each of the line segments that were measured for major elements and therefore that are shown in the BSE image due to space available on the clinopyroxene grain and the large laser spot size.

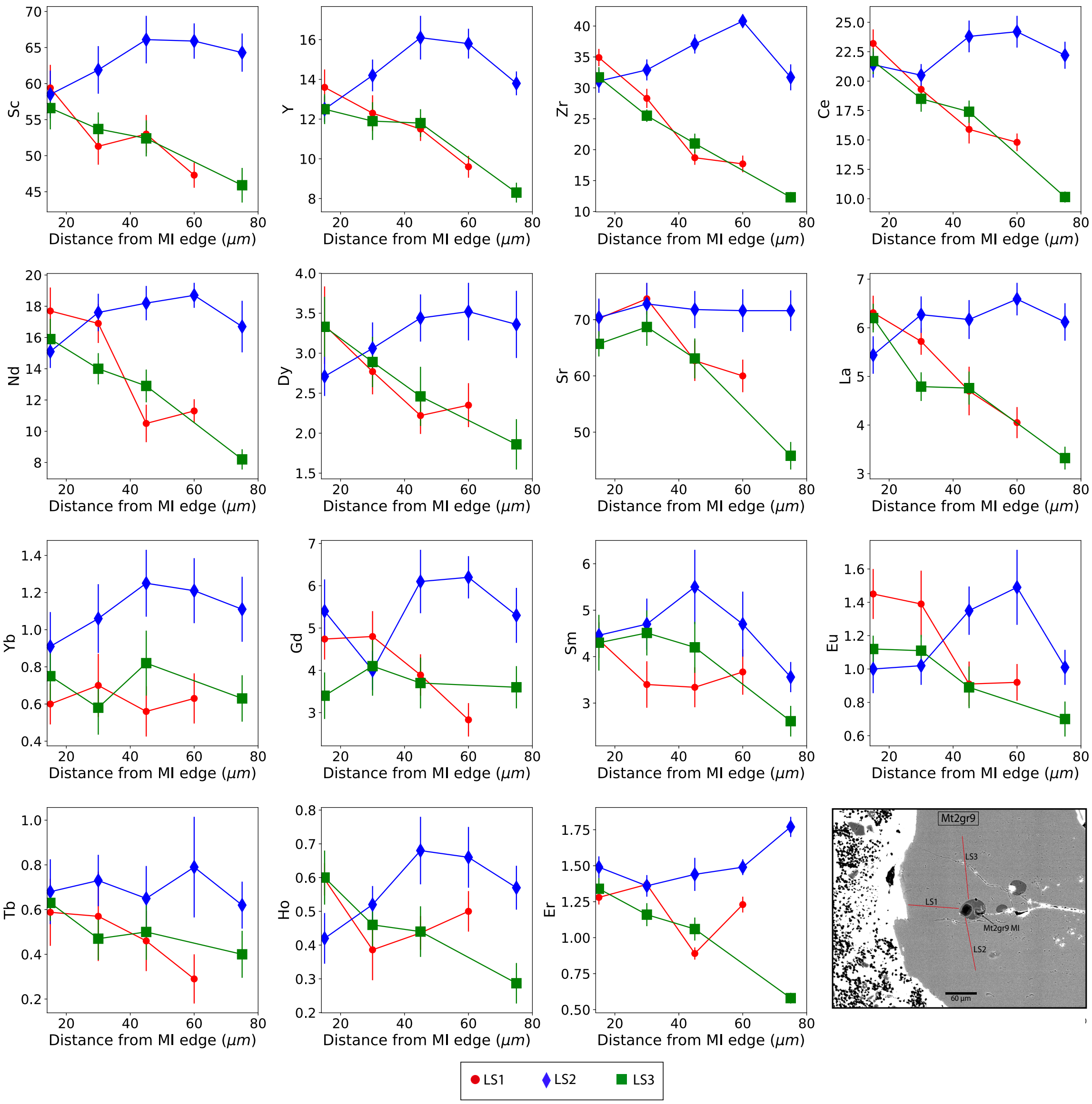

Figure S7. Trace element transects through the mt2gr9 host clinopyroxene (the mt2gr9 MI was analyzed for major and trace elements in this study, and can be seen in the BSE image in the last panel). The transects, termed line segments (LS) 1 through 3, are shown in the BSE image (last panel) of the clinopyroxene where each red line denotes the extent of each line segment that can be seen in the major element plots. Each line segment extends from the MI edge out into the clinopyroxene grain. Trace element data was collected via LA-IC-PMS using a 15 µm spot size and error bars are 2 SE.

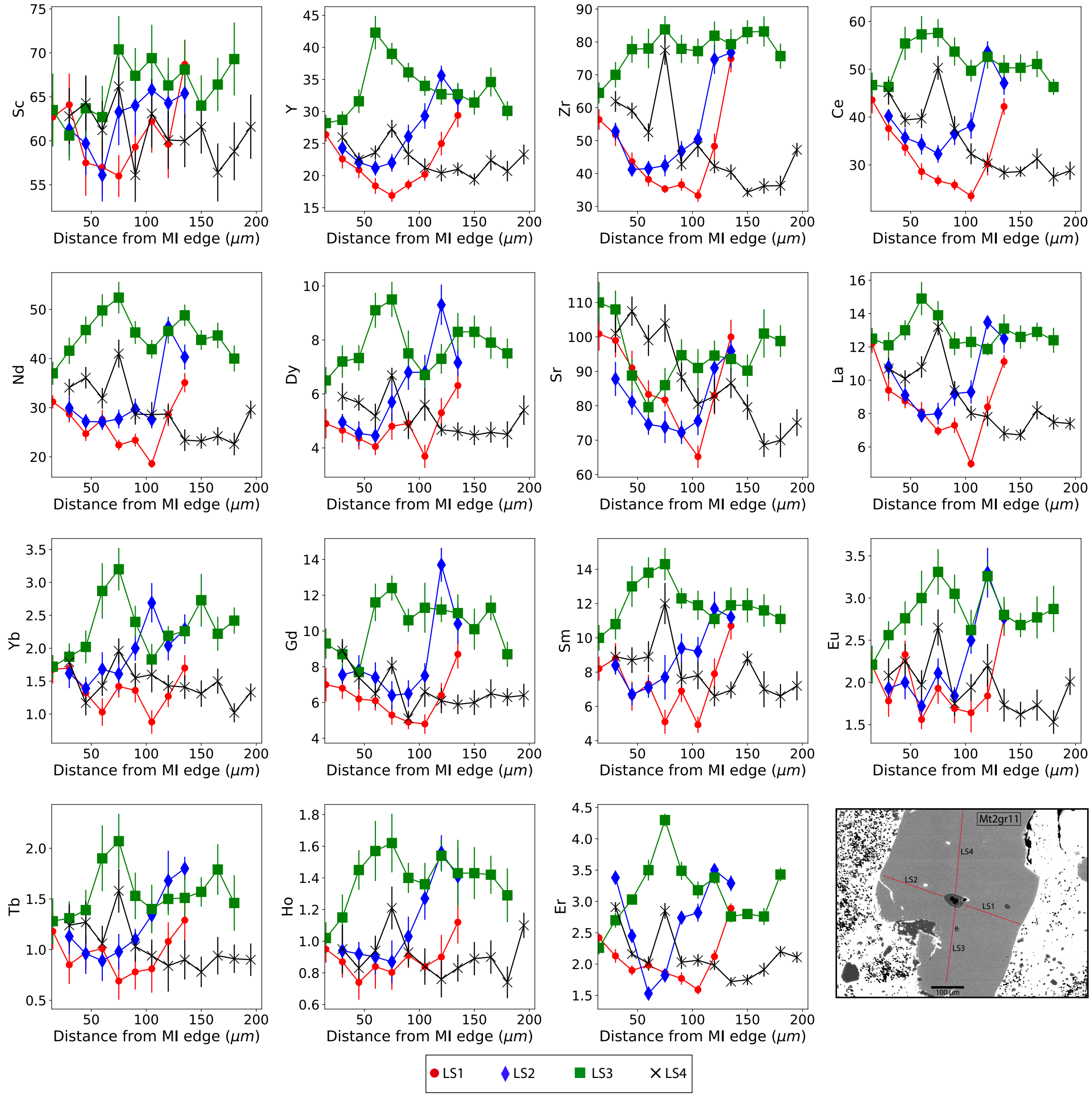

Figure S8 Trace element transects through the mt2gr11 host clinopyroxene (the mt2gr11 MI was analyzed for major and trace elements in this study, and can be seen in the BSE image in the last panel). The transects, termed line segments (LS) 1 through 4, are shown in the BSE image (last panel) of the clinopyroxene where each red line denotes the extent of each line segment that can be seen in the major element plots. Each line segment extends from the MI edge out into the clinopyroxene grain. Trace element data was collected via LA-IC-PMS using a 15 μm spot size and error bars are 2 SE.

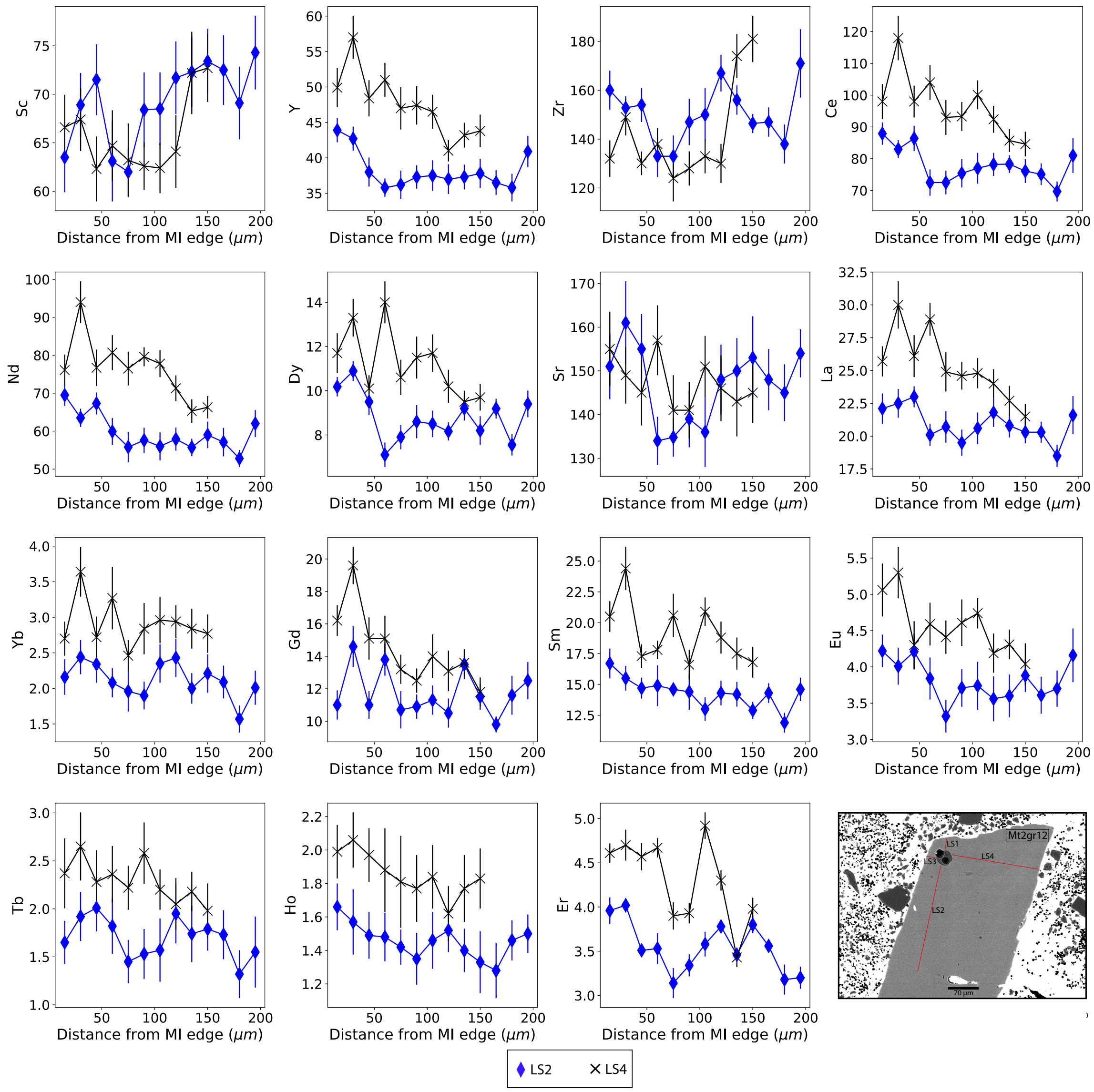

Figure S9. Trace element transects through the mt2gr12 host clinopyroxene (the mt2gr12 MI was analyzed for major and trace elements in this study, and can be seen in the BSE image in the last panel). The transects, termed line segments (LS) 2 and 4, are shown in the BSE image (last panel) of the clinopyroxene where each red line denotes the extent of each line segment that can be seen in the major element plots. Each line segment extends from the MI edge out into the clinopyroxene grain. Trace element data was collected via LA-IC-PMS using a 15 µm spot size and error bars are 2 SE. Trace elements were not measured for each of the line segments that were measured for major elements and therefore that are shown in the BSE image due to space available on the clinopyroxene grain and the large laser spot size.

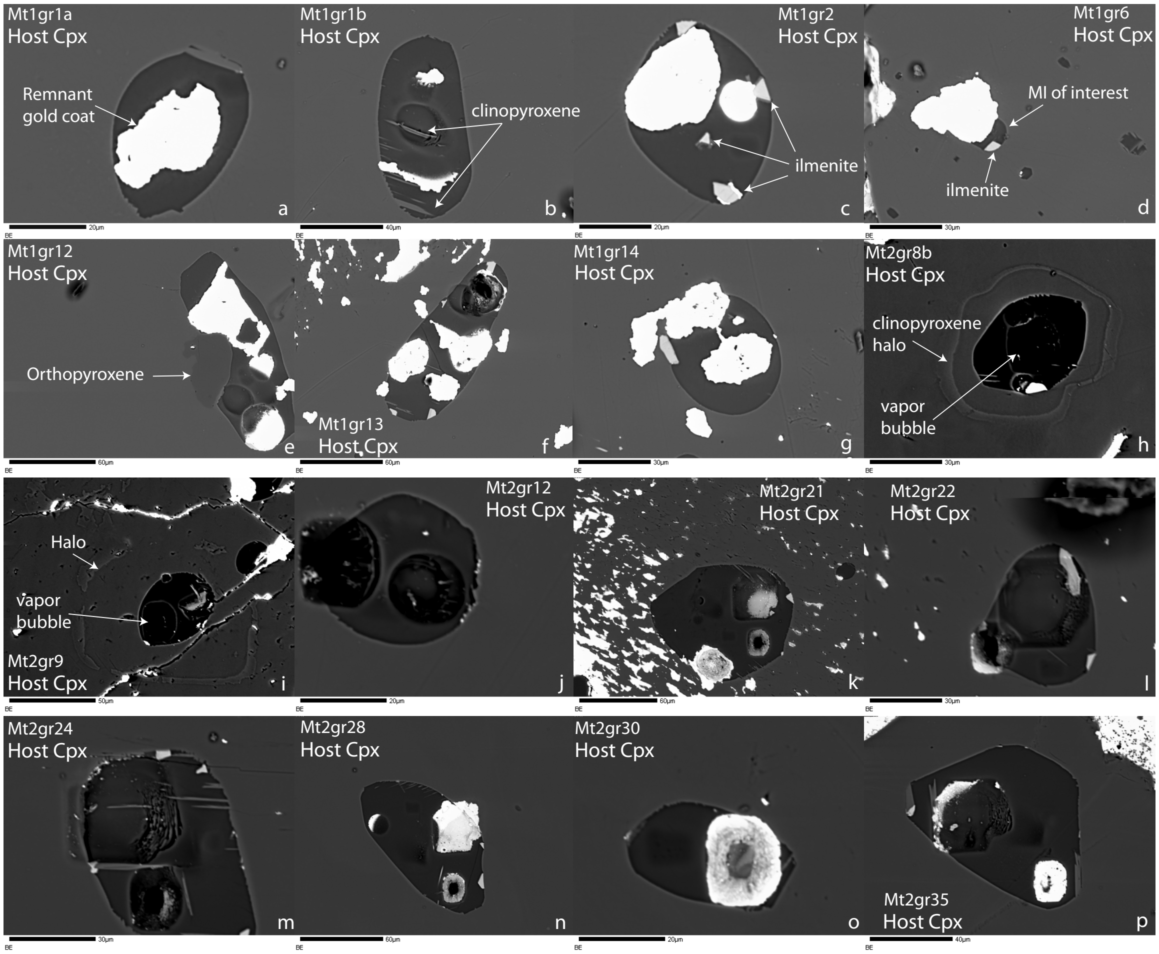

Figure S10. Melt inclusion back-scatter electron images of those melt inclusions not presented in the main text. Many inclusions show bright white splotches that is gold coat that was not completely removed prior to imaging (see panel a for example). Due to the delicate nature of these inclusions and their size, care was taken during polishing to remove very little melt inclusion material, thus some gold coat was left behind. The pitted features are ion probe or laser ablation spot analyses. Panels h and i show the two melt inclusions exhibiting the “halo” feature, as described in the text, and additionally are the two melt inclusions with vapor phases. The cracks seen in panel i occurred during sample preparation. Panel e shows the clinopyroxene-melt inclusion pair that contains the only orthopyroxene observed in these samples. Panels a, b, f, k, m, and p show needle-like clinopyroxene crystallization (see labeled example in panel b). Panels c, d, g, l, m, n, and p, show variable amounts of ilmenite crystals (see labeled example in panel c).

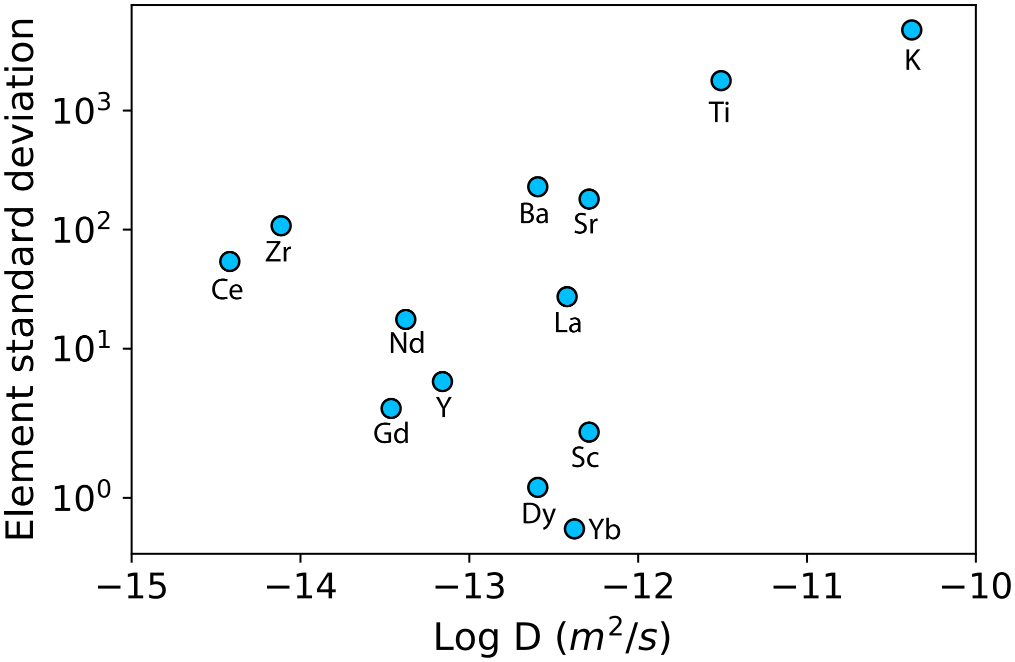

Figure S11: Diffusivity vs trace element standard deviation. Log diffusivities for a trachytic melt at 1150 ºC are from Cherniak (2008) and references therein. When diffusivities are plotted against their respective element concentration standard deviation (i.e., 1 standard deviation calculated using all of the melt inclusions for each element indicated on the plot beneath the data points), a correlation should be seen if diffusion has played a role in controlling MI element variability in which the faster diffusing elements should show little variation and the slowest diffusing elements should show the most variability. If such a correlation is seen, diffusion has played a minor role in re-distributing and modifying MI trace element chemistry (Michael et al., 2002; Kent, 2008). The element used here are Sc, Y, Zr, Ba, Ce (slowest diffusing of the group), Nd, Dy, Sr, La, Yb, Gd, Ti, and K (fastest diffusing of the group).

Appendix S3

Following formulations by Berman and Brown (1994) and Ghiorso and Evans (2008), a generalized formulation of the excess Gibbs free energy (G^{XS}) for a ternary, asymmetric (sub-regular) solution model can be written as follows:

$$G^{Xs} = \sum_{i=1}^{nc-1} \sum_{j=i}^{nc} \sum_{k=j,k\neq i}^{nc} W_{ijk}\left(X_i X_j X_k\right) \qquad (1),$$

where *nc* is the number of components. The expanded version pertaining to a ternary solution is:

$$G^{XS} = X_1X_2(W_{112}X_1 + W_{122}X_2) + X_1X_3(W_{113}X_1 + W_{133}X_3) + X_2X_3(W_{223}X_2 + W_{233}X_3) + X_1X_2X_3W_{123} \quad (2),$$

where subscripts 1, 2, and 3, equivalent to i, j, and k in equation (1), refer to the almandine (Fe), grossular (Ca), and pyrope (Mg) garnet endmembers and X refers to the mole fraction of the specified endmember. The W's refer to the interaction parameters, or Margules parameters. Following the formulation of Jackson (1989) and Helffrich and Wood (1989), the W's can then be related to the activity coefficients in the following way (setting ternary parameters to zero, consistent with the final model formulation of this study):

$$RT\ln\gamma_1 = 2W_{122}X_1X_2(1-X_1) + W_{112}X_2^2(1-2X_1) + 2W_{133}X_1X_3(1-X_1) + W_{113}X_3^2(1-2X_1) - 2X_2X_3(X_3W_{223} + X_2W_{233})$$

$$RT\ln\gamma_2 = 2W_{233}X_2X_3(1-X_2) + W_{223}X_3^2(1-2X_2) + 2W_{112}X_2X_1(1-X_2) + W_{122}X_1^2(1-2X_2) - 2X_2X_1(X_1W_{133} + X_3W_{113})$$

$$RT\ln\gamma_3 = 2W_{113}X_3X_1(1-X_3) + W_{133}X_1^2(1-2X_3) + 2W_{223}X_3X_2(1-X_3) + W_{233}X_2^2(1-2X_3) - 2X_3X_2(X_2W_{112} + X_1W_{122})$$

Using ΔW notation, we can transform the above G^{XS} equation into a slightly simpler form using the following mapping:

$$W_{12} = \frac{W_{112}+W_{122}}{2} \quad (3)$$

and

$$\Delta W_{12} = \frac{W_{112} - W_{122}}{2} \quad (4)$$

thus,

$$W_{112} = W_{12} + \Delta W_{12} \quad (5)$$

and

$$W_{122} = W_{12} - \Delta W_{12} \quad (6)$$

and therefore, G^{XS} can be re-written in the form:

$$G^{XS} = X_1X_2[W_{12} + \Delta W_{12}(X_1 - X_2)] + X_1X_3[W_{13} + \Delta W_{13}(X_1 - X_3)] + X_2X_3[W_{23} + \Delta W_{23}(X_2 - X_3)] \quad (7).$$

Parameters reported in this study are of the form W_{12} and ΔW_{12} (denoted as dW12 in Table 1) and can be transformed to their binary pairs using equations (5) and (6).

Table A1. Final uncertainties imposed on prior values of this study to arrive at the best fit model. The full range of uncertainties test can be found in Table 1 of the main text. The uncertainties reported below are the final values prior to any scaling by the chi-square, which gives the absolute uncertainties.

Prior	Prior value	Uncertainty (or range of values tested)
Exchange reaction affinities	N/A	100 kJ
Saturation reaction affinities	N/A	10 kJ
Wh_{ij}[a]	N/A	10 kJ/mol
ΔWh_{ij}	N/A	1 kJ/mol
Wv_{12}[b]	0.1073 J/bar	0.0893 J/bar
Wv_{13}	0 J/bar	0.005 J/bar
Wv_{23}	0.1 J/bar	0.05 J/bar
Critical point temperature	873 K	10 K
Critical point almandine composition	0	0.03 (3% almandine endmember)
Univariant reaction temperature	1173 K	10 K
Univariant reaction slope	0.14	0.001

References

Adams, J.V., Spera, F.J., Jackson, M.G., and Schmidt, J. (2017). A petrogenetic evaluation of clinopyroxene-hosted melt inclusions from an enriched submarine lava of the Samoan hotspot track: a phase equilibria and diffusion modeling study. *In Review*. https://doi.org/2017AGUFM.V33G0593A

Albarede, F. (1995). *Introduction to Geochemical Modeling*. Cambridge University Press. https://doi.org/10.1017/CBO9780511622960

Ambler, E. P., & Ashley, P. M. (1977). Vermicular orthopyroxene-magnetite symplectites from the Wateranga layered mafic intrusion, Queensland, Australia. *Lithos*, *10*(3), 163–172. https://doi.org/10.1016/0024-4937(77)90044-5

Anderson, A.T. and Wright, T. L. (1972). Phenocrysts and glass inclusions and their bearing on oxidation and mixing of basaltic magmas, Kilauea Volcano, Hawaii. *American Mineralogist*, *57*, 188–216.

Arai, B.S., Shimizu, Y., and Gervilla, F. (2003). Quartz diorite veins in a peridotite xenolith from Tallante, Spain: implications for reaction and survival of slab-derived SiO2-oversaturated melt in the upper mantle. *Proc. Japan Acad.*, *79*(Ser. B).

Arndt, N. T., Czamanske, G. K., Wooden, J. L., & Fedorenko, V. A. (1993). Mantle and crustal contributions to continental flood volcanism. *Tectonophysics*, *223*(1–2), 39–52. https://doi.org/10.1016/0040-1951(93)90156-E

Ashley, A. W. (2019). Water Systematics of Samoan Peridotite Xenoliths. *University of South Caorlina.*

Ashley, A. W., Bizimis, M., Peslier, A. H., & Jackson, M. (2020). Metasomatism and Hydration of the Oceanic Lithosphere: A Case Study of Peridotite Xenoliths from Samoa. *Journal of Petrology*. https://doi.org/10.1093/petrology/egaa028

Ashwal, L., Torsvik, T., Horváth, P., Harris, C., Webb, S., Werner, S., & Corfu, F. (2016). A mantle-derived origin for mauritian trachytes. *Journal of Petrology*, *57*(9), 1645–1676. https://doi.org/10.1093/petrology/egw052

Asmerom, Y., Patchett, P. J., & Damon, P. E. (1991). Crust-mantle interaction in continental arcs: inferences from the Mesozoic arc in the southwestern United States. *Contributions to Mineralogy and Petrology*, *107*(1), 124–134. https://doi.org/10.1007/BF00311190

Bacon, C. R., & Druitt, T. H. (1988). Compositional evolution of the zoned calcalkaline magma chamber of Mount Mazama, Crater Lake, Oregon. *Contributions to Mineralogy and Petrology*, *98*(2), 224–256. https://doi.org/10.1007/BF00402114

Baker, D. R. (2008). The fidelity of melt inclusions as records of melt composition. *Contributions to Mineralogy and Petrology*, *156*(3), 377–395. https://doi.org/10.1007/s00410-008-0291-3

Baker, J. A. (2000). Resolving Crustal and Mantle Contributions to Continental Flood Volcanism, Yemen; Constraints from Mineral Oxygen Isotope Data. *Journal of Petrology*, *41*(12), 1805–1820. https://doi.org/10.1093/petrology/41.12.1805

Becerril, L., Galindo, I., Gudmundsson, A., & Morales, J. M. (2013). Depth of origin of magma in eruptions. *Scientific Reports*, *3*, 1–6. https://doi.org/10.1038/srep02762

Berger, J., Ennih, N., Mercier, J.-C. C., LiéGeois, J.-P., & Demaiffe, D. (2009). The role of fractional crystallization and late-stage peralkaline melt segregation in the mineralogical evolution of Cenozoic nephelinites/phonolites from Saghro (SE

Morocco). *Mineralogical Magazine*, *73*(1), 59–82. https://doi.org/10.1180/minmag.2009.073.1.59

Berman, R. G. (1988). Internally consistent thermodynamic data for minerals in the system Na2O-K2O-CaO-MgO-FeO-Fe2O-SiO2-TiO2-H2O-CO2. *Journal of Petrology*, *29*, 445–552. https://doi.org/10.1127/ejm/9/1/0175

Berman, R. G. (1990). Mixing Properties of Calcium-Magnesium-Iron-Manganese Garnets. *Am. Mineral.*, *75*(3–4), 328–344.

Berman, R. G., & Aranovich, L. Y. (1997). Optimized standard state and solution properties of minerals I. Model calibration for olivine, orthopyroxene, cordierite, garnet, and ilmenite in the system FeO-MgO-CaO-Al2O3-TiO2-SiO2. *Contributions to Mineralogy and Petrology*, *126*(1–2), 1–24. https://doi.org/10.1007/s004100050232

Berman, R. G., & Koziol, A. M. (1991). Ternary excess properties of grossular-pyrope-almandine garnet and their influence in geothermobarometry. *American Mineralogist*, *76*(7–8), 1223–1231.

Bianchini, G., Beccaluva, L., Nowell, G. M., Pearson, D. G., & Siena, F. (2011). Mantle xenoliths from Tallante (Betic Cordillera): Insights into the multi-stage evolution of the south Iberian lithosphere. *Lithos*, *124*(3–4), 308–318. https://doi.org/10.1016/j.lithos.2010.12.004

Bianchini, G., Braga, R., Langone, A., Natali, C., & Tiepolo, M. (2015). Metasedimentary and igneous xenoliths from Tallante (Betic Cordillera, Spain): Inferences on crust-mantle interactions and clues for post-collisional volcanism magma sources. *Lithos*, *220–223*, 191–199. https://doi.org/10.1016/j.lithos.2015.02.011

Blight, J. H. S., Petterson, M. G., Crowley, Q. G., & Cunningham, D. (2010). The Oyut Ulaan Volcanic Group: Stratigraphy, magmatic evolution and timing of Carboniferous arc development in SE Mongolia. *Journal of the Geological Society*, *167*(3), 491–509. https://doi.org/10.1144/0016-76492009-094

Blundy, J., & Wood, B. (2003). Partitioning of trace elements between crystals and melts. *Earth and Planetary Science Letters*, *210*(3–4), 383–397. https://doi.org/10.1016/S0012-821X(03)00129-8

Blundy, J. D., & Wood, B. J. (1991). Crystal-chemical controls on the partitioning of Sr and Ba between plagioclase feldspar, silicate melts, and hydrothermal solutions. *Geochimica et Cosmochimica Acta*, *55*(1), 193–209. https://doi.org/10.1016/0016-7037(91)90411-W

Bohlen, S. R., Wall, V. J., & Boettcher, A. L. (1983). Experimental investigation and application of garnet granulite equilibria. *Contributions to Mineralogy and Petrology*, *83*(1–2), 52–61. https://doi.org/10.1007/BF00373079

Bohrson, W. a., Spera, F. J., Ghiorso, M. S., Brown, G. a., Creamer, J. B., & Mayfield, a. (2014). Thermodynamic Model for Energy-Constrained Open-System Evolution of Crustal Magma Bodies Undergoing Simultaneous Recharge, Assimilation and Crystallization: the Magma Chamber Simulator. *Journal of Petrology*, *0*(0). https://doi.org/10.1093/petrology/egu036

Bohrson, W. A., Spera, F. J., Heinonen, J. S., Brown, G. A., Scruggs, M. A., Adams, J. V., et al. (2020). Diagnosing open-system magmatic processes using the Magma Chamber Simulator (MCS): Part I-Major elements and phase equilibria. *Contributions to Mineralogy and Petrology*, in press.

Borisova, A. Y., Bohrson, W. A., & Gregoire, M. (2017). Origin of primitive ocean island basalts by crustal gabbro assimilation and multiple recharge of plume-derived melts. *Geochemistry, Geophysics, Geosystems*, *18*. https://doi.org/10.1002/2017GC006986

Bosenick, A., Geiger, C. A., Schaller, T., & Sebald, A. (1995). A 29Si MAS NMR and IR spectroscopic investigation of synthetic pyrope-grossular garnet solid solutions. *American Mineralogist*, *80*(7–8), 691–704. https://doi.org/10.2138/am-1995-7-806

Bosenick, A., Dove, M. T., & Geiger, C. A. (2000). Simulation studies on the pyrope-grossular garnet solid solution. *Physics and Chemistry of Minerals*, *27*(6), 398–418. https://doi.org/10.1007/s002690000088

Bosenick, A., Dove, M. T., Heine, V., & Geiger, C. A. (2001). Scaling of thermodynamic mixing properties in garnet solid solutions. *Physics and Chemistry of Minerals*, *28*(3), 177–187. https://doi.org/10.1007/s002690000141

Bosenick, Anne, Geiger, C. A., & Cemič, L. (1996). Heat capacity measurements of synthetic pyrope-grossular garnets between 320 and 1000 K by differential scanning calorimetry. *Geochimica et Cosmochimica Acta*, *60*(17), 3215–3227. https://doi.org/10.1016/0016-7037(96)00150-0

Bosenick, Anne, Geiger, C. A., & Phillips, B. L. (1999). Local Ca-Mg distribution of Mg-rich pyrope-grossular garnets synthesized at different temperatures revealed by 29Si MAS NMR spectroscopy. *American Mineralogist*, *84*(9), 1422–1432. https://doi.org/10.2138/am-1999-0921

Boudreau, A. E. (1999). PELE-a version of the MELTS software program for the PC platform. *Computers and Geosciences*, *25*(2), 201–203. https://doi.org/10.1016/S0098-3004(98)00117-4

Bouvet de Maisonneueve, C., Costa, F., Huber, C., Vonlanthen, P., Bachmann, O., & Dungan, M. A. (2016). How do olivines record magmatic events? Insights from major and trace element zoning. *Contributions to Mineralogy and Petrology*, *171*(56), 1–20. https://doi.org/10.1007/s00410-016-1264-6

Bouvier, A., Vervoort, J. D., & Patchett, P. J. (2008). The Lu – Hf and Sm – Nd isotopic composition of CHUR : Constraints from unequilibrated chondrites and implications for the bulk composition of terrestrial planets, *273*, 48–57. https://doi.org/10.1016/j.epsl.2008.06.010

Bowen, N. L. (1928). *The evolution of igneous rocks*. New York: Dover Publications.

Bucholz, C. E., Gaetani, G. A., Behn, M. D., & Shimizu, N. (2013). Post-entrapment modification of volatiles and oxygen fugacity in olivine-hosted melt inclusions. *Earth and Planetary Science Letters*, *374*, 145–155. https://doi.org/10.1016/j.epsl.2013.05.033

Carslaw, H.S. and Jaeger, J. C. (1959). *Conduction of heat in solids* (2nd ed.). London: Oxford University Press.

Castillo, P., & Batizat, R. (1989). Strontium, neodymium, and lead isotope constraints on near-ridge seamount production beneath the South Atlantic. *Nature*, *342*(November), 262–265.

Colson, R. O., McKay, G. A., & Taylor, L. A. (1988). Temperature and composition dependencies of trace element partitioning: Olivine/melt and low-Ca pyroxene/melt. *Geochimica et Cosmochimica Acta*, *52*(2), 539–553. https://doi.org/10.1016/0016-7037(88)90109-3

Coogan, L. A., Saunders, A. D., & Wilson, R. N. (2014). Aluminum-in-olivine thermometry of primitive basalts: Evidence of an anomalously hot mantle source for large igneous provinces. *Chemical Geology*, *368*, 1–10. https://doi.org/10.1016/j.chemgeo.2014.01.004

Costa, F., Dohmen, R., & Chakraborty, S. (2008). Time scales of magmatic processes from modeling the zoning patterns of crystals. *Reviews in Mineralogy and Geochemistry*, *69*(April 2016), 545–594. https://doi.org/10.2138/rmg.2008.69.14

Cottrell, E., Spiegelman, M., & Langmuir, C. H. (2002). Consequences of diffusive reequilibration for the interpretation of melt inclusions. *Geochemistry Geophysics Geosystems*, *3*(5), 1–26. https://doi.org/10.1029/2001GC000205

Couch, S., Sparks, R. S. J., & Carroll, M. R. (2001). Mineral disequilibrium in lavas explained by convective self-mixing in open magma chambers. *Nature*, *411*(6841), 1037–1039. https://doi.org/10.1038/35082540

Cousens, B.L., Clague, D.A., and Sharp, W. D. (2003). Chronology, chemistry, and origin of trachytes from Hualalai Volcano, Hawaii. *Geochemistry Geophysics Geosystems*, *4*(9). https://doi.org/10.1029/2003GC000560

Cox, K. G., & Hawkesworth, C. J. (1984). Relative contribution of crust and mantle to flood basalt magmatism, Mahabaleshwar area, Deccan Traps. *Philosophical Transactions of the Royal Society of London*, *641*(A310(1514)), 627–641. https://doi.org/10.1098/rsta.1984.0011

Cressey, G. (1978). Exsolution in almandine-purope-grossular garnet. *Nature*, *271*.

Dachs, E., & Geiger, C. A. (2006). Heat capacities and entropies of mixing of pyrope-grossular (Mg3Al2Si3O12 -Ca3Al2Si3O12) garnet solid solutions: A low-temperature calorimetric and a thermodynamic investigation. *American Mineralogist*, *91*(5–6), 894–906. https://doi.org/10.2138/am.2006.2005

Danyushevsky, L. v., Della-Pasqua, F. N., & Sokolov, S. (2000). Re-equilibration of melt inclusions trapped by magnesian olivine phenocrysts from subduction-related magmas: Petrological implications. *Contributions to Mineralogy and Petrology*, *138*(1), 68–83. https://doi.org/10.1007/PL00007664

Danyushevsky, Leonid v., McNeill, A. W., & Sobolev, A. v. (2002). Experimental and petrological studies of melt inclusions in phenocrysts from mantle-derived magmas: An overview of techniques, advantages and complications. *Chemical Geology*, *183*(1–4), 5–24. https://doi.org/10.1016/S0009-2541(01)00369-2

Dasgupta, R., Hirschmann, M. M., & Withers, A. C. (2004). Deep global cycling of carbon constrained by the solidus of anhydrous, carbonated eclogite under upper mantle conditions. *Earth and Planetary Science Letters*, *227*(1–2), 73–85. https://doi.org/10.1016/j.epsl.2004.08.004

Dasgupta, R., Jackson, M. G., & Lee, C. T. A. (2009). Major element chemistry of ocean island basalts - Conditions of mantle melting and heterogeneity of mantle source. *Earth and Planetary Science Letters*, *289*(3–4), 377–392. https://doi.org/10.1016/j.epsl.2009.11.027

Davidson, Jon P., & Tepley, F. J. (1997). Recharge in volcanic systems: Evidence from isotope profiles of phenocrysts. *Science*, *275*(5301), 826–829. https://doi.org/10.1126/science.275.5301.826

Davidson, J.P., Morgan, D. J., Charlier, B. L. A., Harlou, R., & Hora, J. M. (2007). Microsampling and Isotopic Analysis of Igneous Rocks: Implications for the Study of Magmatic Systems. *Annual Review of Earth and Planetary Sciences*, *35*(1), 273–311. https://doi.org/10.1146/annurev.earth.35.031306.140211

Depaolo, D. J. (1981). Trace element and isotopic effects of combined wallrock assimilation and fractional crystallization. *Earth and Planetary Science Letters*, *53*, 189–202.

Dimanov, A., & Wiedenbeck, M. (2006). (Fe,Mn)-Mg interdiffusion in natural diopside: Effect of pO2. *European Journal of Mineralogy*, *18*(6), 705–718. https://doi.org/10.1127/0935-1221/2006/0018-0705

Drake, M. J., & Weill, D. F. (1975). Partition of Sr, Ba, Ca, Y, Eu2+, Eu3+, and other REE between plagioclase feldspar and magmatic liquid: an experimental study. *Geochimica et Cosmochimica Acta*, *39*(5), 689–712. https://doi.org/10.1016/0016-7037(75)90011-3

Du, W. (2011). Excess volume and exsolution in pyrope-grossular garnet. *Columbia University*.

Du, W., Clark, S. M., & Walker, D. (2015). Thermo-compression of pyrope-grossular garnet solid solutions: Non-linear compositional dependence. *American Mineralogist*, *100*, 215–222. https://doi.org/10.1377/hlthaff.2013.0625

Du, W., Clark, S. M., & Walker, D. (2016). Excess mixing volume, microstrain, and stability of pyrope-grossular garnets. *American Mineralogist*, *101*(1), 193–204.

Duke, J. M. (1976). Distribution of the period four transition elements among olivine, calcic clinopyroxene and mafic silicate liquid: Experimental results. *Journal of Petrology*, *17*(4), 499–521. https://doi.org/10.1093/petrology/17.4.499

Edwards, M. A., Jackson, M. G., Kylander-Clark, A. R. C., Harvey, J., Hagen-Peter, G. A., Seward, G. G. E., et al. (2019). Extreme enriched and heterogeneous ^{87}Sr/ ^{86}Sr ratios recorded in magmatic plagioclase from the Samoan hotspot. *Earth and Planetary Science Letters*, *511*. https://doi.org/10.1016/j.epsl.2019.01.040

Eiler, J. M. (2001). Oxygen Isotope Variations of Basaltic Lavas and Upper Mantle Rocks. *Reviews in Mineralogy and Geochemistry*, *43*, 319–364. https://doi.org/10.2138/gsrmg.43.1.319

Eiler, John M., Schiano, P., Kitchen, N., & Stolper, E. M. (2000). Oxygen-isotope evidence for recycled crust in the sources of mid-ocean- ridge basalts. *Nature*, *403*, 530–534. https://doi.org/10.1038/35000553

Erdmann, S., Scaillet, B., & Kellett, D. A. (2012). Textures of peritectic crystals as guides to reactive minerals in magmatic systems: New insights from melting experiments. *Journal of Petrology*, *53*(11), 2231–2258. https://doi.org/10.1093/petrology/egs048

Ewart, A., & Griffin, W. L. (1994). Application of proton-microprobe data to trace-element partitioning in volcanic rocks. *Chemical Geology*, *117*(1–4), 251–284. https://doi.org/10.1016/0009-2541(94)90131-7

Faure, G. and Mensing, T. M. (2004). *Isotopes: Principles and Applications*. Wiley.

France, L., Demacon, M., Gurenko, A. A., & Briot, D. (2016). Oxygen isotopes reveal crustal contamination and a large, still partially molten magma chamber in Chaîne des Puys (French Massif Central). *Lithos*, *260*, 328–338. https://doi.org/10.1016/j.lithos.2016.05.013

Freeman, C. L., Allan, N. L., & van Westrenen, W. (2006). Local cation environments in the pyrope-grossular Mg3Al2Si3O12 - Ca3Al2Si3O12 garnet solid solution. *Physical Review B - Condensed Matter and Materials Physics*, *74*(13), 1–9. https://doi.org/10.1103/PhysRevB.74.134203

Frezzotti, M. L. (2001). Silicate-melt inclusions in magmatic rocks: Applications to petrology. *Lithos*, *55*(1–4), 273–299. https://doi.org/10.1016/S0024-4937(00)00048-7

Gaetani, G. A., & Watson, E. B. (2000). Open system behavior of olivine-hosted melt inclusions. *Earth and Planetary Science Letters*, *183*(1–2), 27–41. https://doi.org/10.1016/S0012-821X(00)00260-0

Gaetani, G. A., & Watson, E. B. (2002). Modeling the major-element evolution of olivine-hosted melt inclusions. *Chemical Geology*, *183*(1–4), 25–41. https://doi.org/10.1016/S0009-2541(01)00370-9

Gaetani, G. A., O'Leary, J. A., Shimizu, N., Bucholz, C. E., & Newville, M. (2012). Rapid reequilibration of H2O and oxygen fugacity in olivine-hosted melt inclusions. *Geology*, *40*(10), 915–918. https://doi.org/10.1130/G32992.1

Gale, A., Dalton, C. A., Langmuir, C. H., Su, Y., & Schilling, J. G. (2013). The mean composition of ocean ridge basalts. *Geochemistry, Geophysics, Geosystems*, *14*(3), 489–518. https://doi.org/10.1029/2012GC004334

Ganguly, J., & Saxena, S. K. (1984). Mixing properties of aluminosilicate garnets: constraints from natural and experimental data, and applications to geothermo-barometry. *American Mineralogist*, *69*(1–2), 88–97.

Ganguly, J., Weiji Cheng, & O'Neill, H. S. C. (1993). Syntheses, volume, and structural changes of garnets in the pyrope- grossular join: implications for stability and mixing properties. *American Mineralogist*, *78*(5–6), 583–593.

Ganguly, Jibamitra. (2010). Cation diffusion kinetics in aluminosilicate garnets and geological applications. *Reviews in Mineralogy and Geochemistry*, *72*(November 2010), 559–601. https://doi.org/10.2138/rmg.2010.72.12

Ganguly, Jibamitra, & Kennedy, G. C. (1974). The energetics of natural garnet solid solution. *Contributions to Mineralogy and Petrology*, *48*(2), 137–148. https://doi.org/10.1007/bf00418615

Ganguly, Jibamitra, Cheng, W., & Tirone, M. (1996). Thermodynamics of aluminosilicate garnet solid solution: New experimental data, an optimized model, and thermometric applications. *Contributions to Mineralogy and Petrology*, *126*(1–2), 137–151. https://doi.org/10.1007/s004100050240

Gao, M., Xu, H., Zhang, J., & Foley, S. F. (2019). Experimental interaction of granitic melt and peridotite at 1.5 GPa: Implications for the origin of post-collisional K-rich magmatism in continental subduction zones. *Lithos*, *350–351*(October), 105241. https://doi.org/10.1016/j.lithos.2019.105241

Garçon, M., Boyet, M., Carlson, R. W., Horan, M. F., Auclair, D., & Mock, T. D. (2018). Factors influencing the precision and accuracy of Nd isotope measurements by thermal ionization mass spectrometry. *Chemical Geology*, *476*(December 2017), 493–514. https://doi.org/10.1016/j.chemgeo.2017.12.003

Geiger, C. A. (1999). Thermodynamics of (Fe2+, Mn2+, Mg, Ca)3- Al2Si3O12 garnet: A review and analysis. *Mineralogy and Petrology*, *66*(4), 271–299. https://doi.org/10.1007/BF01164497

Geiger, C. A., Newton, R. C., & Kleppa, O. J. (1987). Enthalpy of mixing of synthetic almandine-grossular and almandine-pyrope garnets from high-temperature solution calorimetry. *Geochimica et Cosmochimica Acta*, *51*(6), 1755–1763. https://doi.org/10.1016/0016-7037(87)90353-X

Geiger, Charles A., & Feenstra, A. (1997). Molar volumes of mixing of almandine-pyrope and almandine-spessartine garnets and the crystal chemistry and thermodynamic-mixing properties of the aluminosilicate garnets. *American Mineralogist*, *82*(5–6), 571–581. https://doi.org/10.2138/am-1997-5-617

Geiger, Charles A., Stahl, A., & Rossman, G. R. (2000). Single-crystal IR- and UV/VIS-spectroscopic measurements on transition-metal-bearing pyrope: the incorporation of hydroxide in garnet. *European Journal of Mineralogy*, *12*(2), 259–271. https://doi.org/10.1127/0935-1221/2000/0012-0259

Ghiorso, Mark S., & Evans, B. W. (2008). Thermodynamics of rhombohedral oxide solid solutions and a revision of the Fe-Ti two-oxide geothermometer and oxygen-barometer. *American Journal of Science*, *308*(9), 957–1039. https://doi.org/10.2475/09.2008.01

Ghiorso, Mark S., & Gualda, G. A. R. (2015). An H2O–CO2 mixed fluid saturation model compatible with rhyolite-MELTS. *Contributions to Mineralogy and Petrology*, *169*(6), 1–30. https://doi.org/10.1007/s00410-015-1141-8

Ghiorso, Mark S, & Sack, R. O. (1995). Chemical mass transfer in magmatic processes IV. A revised and internally consistent thermodynamic model for the interpolation and extrapolation of liquid-solid equilibria in magmatic systems at elevated temperatures and pressures. *Contributions to Mineralogy and Petrology*, *119*, 197–212.

Ghiorso, Mark S., Hirschmann, M., Reiners, P., & Kress, V. (2002a). The pMELTS: A revision of MELTS for improved calculation of phase relations and major element partitioning related to partial melting of the mantle to 3 GPa. *Geochemistry Geophysics Geosystems*, *3*(5). https://doi.org/10.1029/2001GC000217

Ghiorso, Mark S., Hirschmann, M. M., Reiners, P. W., & Kress, V. C. (2002b). The pMELTS: A revision of MELTS for improved calculation of phase relations and major element partitioning related to partial melting of the mantle to 3 GPa. *Geochemistry, Geophysics, Geosystems*, *3*(5), 1–35. https://doi.org/10.1029/2001gc000217

Ghiorso, M.S. (2013). A globally convergent saturation state algorithm applicable to thermodynamic systems with a stable or metastable omni-component phase. *Geochimica Et Cosmochimica Acta*, *103*, 295–300.

Ginibre, C., & Davidson, J. P. (2014). Sr isotope zoning in plagioclase from parinacota volcano (Northern Chile): Quantifying magma mixing and crustal contamination. *Journal of Petrology*, *55*(6), 1203–1238. https://doi.org/10.1093/petrology/egu023

Ginibre, Catherine, & Wörner, G. (2007). Variable parent magmas and recharge regimes of the Parinacota magma system (N. Chile) revealed by Fe, Mg and Sr zoning in plagioclase. *Lithos*, *98*(1–4), 118–140. https://doi.org/10.1016/j.lithos.2007.03.004

Ginibre, Catherine, Wörner, G., & Kronz, A. (2007). Crystal zoning as an archive for magma evolution. *Elements*, *3*(4), 261–266. https://doi.org/10.2113/gselements.3.4.261

Goldstein, S. L., & Jacobsen, S. B. (1988). Nd and Sr isotopic systematics of river water suspended material: implications for crustal evolution. *Earth and Planetary Science Letters*, *87*, 249–265.

Green, E. C. R., Holland, T. J. B., Powell, R., & White, R. W. (2012). Garnet and spinel lherzolite assemblages in MgO-Al 2O 3-SiO 2 and CaO-MgO-Al 2O 3-SiO 2:

Thermodynamic models and an experimental conflict. *Journal of Metamorphic Geology*, *30*(6), 561–577. https://doi.org/10.1111/j.1525-1314.2012.00981.x

Grove, T. L., Kinzler, R. J., & Bryan, W. B. (1992). Fractionation of Mid-Ocean Ridge Basalt (MORB). *Mantle Flow and Melt Generation at Mid-Ocean Ridges: Geophysical Monograph*, *71*.

Gualda, G. a R., Ghiorso, M. S., Lemons, R. v., & Carley, T. L. (2012). Rhyolite-MELTS: A modified calibration of MELTS optimized for silica-rich, fluid-bearing magmatic systems. *Journal of Petrology*, *53*(0), 875–890. https://doi.org/10.1093/petrology/egr080

Hamecher, E. A. (2013). Studies of the equation of state and elasticity of mantle minerals. *California Institute of Technology.*

Hamecher, E. A., Antoshechkina, P. M., Ghiorso, M. S., & Asimow, P. D. (2013). The molar volume of FeO-MgO-Fe2O3-Cr2O3-Al2O3-TiO2 spinels. *Contributions to Mineralogy and Petrology*, *165*(1), 25–43. https://doi.org/10.1007/s00410-012-0790-0

Harlou, R., Pearson, D. G., Nowell, G. M., Ottley, C. J., & Davidson, J. P. (2009). Combined Sr isotope and trace element analysis of melt inclusions at sub-ng levels using micro-milling, TIMS and ICPMS. *Chemical Geology*, *260*(3–4), 254–268. https://doi.org/10.1016/j.chemgeo.2008.12.020

Hart, S. R. (1988). Heterogeneous mantle domains: signatures, genesis and mixing chronologies. *Earth and Planetary Science Letters*, *90*(3), 273–296. https://doi.org/10.1016/0012-821X(88)90131-8

Hauri, E. (2002). SIMS analysis of volatiles in silicate glasses, 2: Isotopes and abundances in Hawaiian melt inclusions. *Chemical Geology*, *183*(1–4), 115–141. https://doi.org/10.1016/S0009-2541(01)00374-6

Hauri, E. H. (1996). Major-element variability in the Hawaiian mantle plume. *Nature*, *382*(6590), 415–419. Retrieved from http://cat.inist.fr/?aModele=afficheN&cpsidt=3169729

Hauri, E. H., & Hart, S. R. (1994). Constraints on melt migration from mantle plumes: a trace element study of peridotite xenoliths from Savai'i, Western Samoa. *Journal of Geophysical Research*, *99*(B12). https://doi.org/10.1029/94jb01553

Hauri, Erik H., Shimizu, N., Dieu, J. J., & Hart, S. R. (1993). Evidence for hotspot-related carbonatite metasomatism in the oceanic upper mantle. *Nature*, *365*(6443), 221–227. https://doi.org/10.1038/365221a0

Heinonen, J. S., Luttinen, A. v., & Bohrson, W. A. (2016). Enriched continental flood basalts from depleted mantle melts: modeling the lithospheric contamination of Karoo lavas from Antarctica. *Contributions to Mineralogy and Petrology*, *171*(1), 1–22. https://doi.org/10.1007/s00410-015-1214-8

Heinonen, J. S., Luttinen, A. v., Spera, F. J., & Bohrson, W. A. (2019). Deep open storage and shallow closed transport system for a continental flood basalt sequence revealed with Magma Chamber Simulator. *Contributions to Mineralogy and Petrology*, *174*(11), 1–18. https://doi.org/10.1007/s00410-019-1624-0

Heinonen, J. S., Bohrson, W. A., Spera, F. J., Brown, G. A., Scruggs, M. A., & Adams, J. V. (2020). Diagnosing open-system magmatic processes using the Magma Chamber Simulator (MCS): Part II-Trace elements and isotopes. *Contributions to Mineralogy and Petrology*, in press.

Hensen, B. J., Schmid, R., & Wood, B. J. (1975). Activity-composition relationships for pyrope-grossular garnet. *Contributions to Mineralogy and Petrology*, *51*(3), 161–166. https://doi.org/10.1007/BF00372076

Hildreth, W., & Moorbath, S. (1988). Crustal contributions to arc magmatism in the Andes of Central Chile. *Contributions to Mineralogy and Petrology*, *98*(4), 455–489. https://doi.org/10.1007/BF00372365

Hofmann, A. W., & White, W. M. (1982). Mantle plumes from ancient oceanic crust. *Earth and Planetary Science Letters*, *57*(2), 421–436. https://doi.org/10.1016/0012-821X(82)90161-3

Holdaway, M. J. (2000). Application of new experimental and garnet Margules data to the garnet-biotite geothermometer. *American Mineralogist*, *85*(7–8), 881–892.

Holland, T. B., Hudson, N. F. C., Powell, R., & Harte, B. (2013). Newthermodynamic models and calculated phase equilibria in NCFMAS for basic and ultrabasic compositions through thetransition zone into the uppermost lower mantle. *Journal of Petrology*, *54*(9), 1901–1920. https://doi.org/10.1093/petrology/egt035

Holland, T. J. B., & Powell, R. (1998). An internally consistent thermodynamic data set for phases of petrological interest. *Journal of Metamorphic Geology*, *16*(3), 309–343. https://doi.org/10.1111/j.1525-1314.1998.00140.x

Holland, T. J. B., & Powell, R. (2011). An improved and extended internally consistent thermodynamic dataset for phases of petrological interest, involving a new equation of state for solids. *Journal of Metamorphic Geology*, *29*(3), 333–383. https://doi.org/10.1111/j.1525-1314.2010.00923.x

Iles, K. A., Hergt, J. M., & Woodhead, J. D. (2018). Modelling isotopic responses to disequilibrium melting in granitic systems. *Journal of Petrology*, *59*(1), 87–114. https://doi.org/10.1093/petrology/egy019

Jackson, M. G., Becker, T. W., & Konter, J. G. (2018). Evidence for a deep mantle source for EM and HIMU domains from integrated geochemical and geophysical constraints. *Earth and Planetary Science Letters*, *484*, 154–167. https://doi.org/10.1016/j.epsl.2017.11.052

Jackson, Matthew G., & Hart, S. R. (2006). Strontium isotopes in melt inclusions from Samoan basalts: Implications for heterogeneity in the Samoan plume. *Earth and Planetary Science Letters*, *245*(1–2), 260–277. https://doi.org/10.1016/j.epsl.2006.02.040

Jackson, Matthew G., Hart, S. R., Koppers, A. A. P., Staudigel, H., Konter, J., Blusztajn, J., et al. (2007). The return of subducted continental crust in Samoan lavas. *Nature*, *448*(7154), 684–687. https://doi.org/10.1038/nature06048

Jackson, Matthew G., Hart, S. R., Shimizu, N., & Blusztajn, J. S. (2009). The 87Sr/86Sr and 143Nd/144Nd disequilibrium between Polynesian hot spot lavas and the clinopyroxenes they host: Evidence complementing isotopic disequilibrium in melt inclusions. *Geochemistry, Geophysics, Geosystems*, *10*(3). https://doi.org/10.1029/2008GC002324

James, D. E. (1981). The combined use of oxygen and radiogenic isotopes as indicators of crustal contamination. *Annual Review of Earth and Planetary Sciences*, *9*, 311–344.

Jennings, E. S., & Holland, T. J. B. (2015). A simple thermodynamic model for melting of peridotite in the system NCFMASOCr. *Journal of Petrology*, *56*(5), 869–892. https://doi.org/10.1093/petrology/egv020

Juteau, M., Michard, A., & Albarede, F. (1986). The Pb-Sr-Nd isotope geochemistry of some recent circum-Mediterranean granites. *Contributions to Mineralogy and Petrology*, *92*(3), 331–340. https://doi.org/10.1007/BF00572162

Kamenetsky, V. (1996). Methodology for the study of melt inclusions in Cr-spinel, and implications for parental melts of MORB from FAMOUS area. *Earth and Planetary Science Letters*, *142*(3–4), 479–486. https://doi.org/10.1016/0012-821x(96)00117-3

Kamenetsky, V. S., Crawford, A. J., Eggins, S., & Mühe, R. (1997). Phenocryst and melt inclusion chemistry of near-axis seamounts, Valu Fa Ridge, Lau Basin: Insight into mantle wedge melting and the addition of subduction components. *Earth and Planetary Science Letters*, *151*(3–4), 205–223. https://doi.org/10.1016/s0012-821x(97)81849-3

Kent, A. J. R. (2008). Melt inclusions in basaltic and related volcanic rocks. *Reviews in Mineralogy and Geochemistry*, *69*, 273–332.

Kent, A. J. R., & Elliott, T. R. (2002). Melt inclusions from Marianas arc lavas: Implications for the composition and formation of island arc margins. *Chemical Geology*, *183*(1–4), 263–286. https://doi.org/10.1016/S0009-2541(01)00378-3

Kent, A. J. R., Norman, M. D., Hutcheon, I. D., & Stolper, E. M. (1999). Assimilation of seawater-derived components in an oceanic volcano: Evidence from matrix glasses and glass inclusions from Loihi seamount, Hawaii. *Chemical Geology*, *156*(1–4), 299–319. https://doi.org/10.1016/S0009-2541(98)00188-0

Kessel, R., Schmidt, M. W., Ulmer, P., & Pettke, T. (2005). Trace element signature of subduction-zone fluids, melts and supercritical liquids at 120–180 km depth. *Nature*, *437*(7059), 724–727. https://doi.org/10.1038/nature03971

Konter, J. G., & Jackson, M. G. (2012). Large volumes of rejuvenated volcanism in Samoa: Evidence supporting a tectonic influence on late-stage volcanism. *Geochemistry, Geophysics, Geosystems*, *13*(1). https://doi.org/10.1029/2011GC003974

Koornneef, J. M., Nikogosian, I., van Bergen, M. J., Smeets, R., Bouman, C., & Davies, G. R. (2015). TIMS analysis of Sr and Nd isotopes in melt inclusions from Italian potassium-rich lavas using prototype $10^{13}\Omega$ amplifiers. *Chemical Geology*, *397*, 14–23. https://doi.org/10.1016/j.chemgeo.2015.01.005

Koziol, A M, & Newton, R. C. (1987). Experimental determination of spessartine-grossular solid solution relations. *EOS*, *68*(46).

Koziol, Andrea M, & Newton, R. C. (1989). Grossular activity-composition relationships in ternary garnets determined by reversed displaced-equilibrium experiments, 423–433.

Kress, V. C., & Ghiorso, M. S. (2004). Thermodynamic modeling of post-entrapment crystallization in igneous phases. *Journal of Volcanology and Geothermal Research*, *137*(4), 247–260. https://doi.org/10.1016/j.jvolgeores.2004.05.012

Lambart, S., Koornneef, J. M., Millet, M. A., Davies, G. R., Cook, M., & Lissenberg, C. J. (2019). Highly heterogeneous depleted mantle recorded in the lower oceanic crust. *Nature Geoscience*, *12*(6), 482–486. https://doi.org/10.1038/s41561-019-0368-9

Langmuir, C.H., Vocke, R.D., Hanson, G.N., and Hart, S. R. (1978). A general mixing equation with applications to icelandic basalts. *Earth and Planetary Science Letters*, *37*, 380–392.

Lavrentiev, M. Y., van Westrenen, W., Allan, N. L., Freeman, C. L., & Purton, J. A. (2006). Simulation of thermodynamic mixing properties of garnet solid solutions at high temperatures and pressures. *Chemical Geology*, *225*(3–4), 336–346. https://doi.org/10.1016/j.chemgeo.2005.08.026

Lesher, C. E., & Spera, F. J. (2015). *Thermodynamic and Transport Properties of Silicate Melts and Magma*. *The Encyclopedia of Volcanoes* (Second Edi). Elsevier Inc. https://doi.org/10.1016/B978-0-12-385938-9.00005-5

Loges, A., Schultze, D., Klügel, A., & Lucassen, F. (2019). Phonolitic melt production by carbonatite Mantle metasomatism: evidence from Eger Graben xenoliths. *Contributions to Mineralogy and Petrology*, *174*(11). https://doi.org/10.1007/s00410-019-1630-2

Lowenstern, J. B. (1995). Applications of silicate-melt inclusions to the study of magmatic volatiles. *Magmas, Fluids and Ore Deposits. Mineralogical Association of Canada Short Course*, *23*(January 1995), 71–99.

Luttinen, A. v., Rämö, O. T., & Huhma, H. (1998). Neodymium and strontium isotopic and trace element composition of a Mesozoic CFB suite from Dronning Maud Land, Antarctica: Implications for lithosphere and asthenosphere contributions to Karoo magmatism. *Geochimica et Cosmochimica Acta*, *62*(15), 2701–2714. https://doi.org/10.1016/S0016-7037(98)00184-7

Luttinen, Arto v., & Furnes, H. (2000). Flood basalts of Vestfjella: Jurassic magmatism across an Archaean-Proterozoic lithospheric boundary in Dronning Maud Land, Antarctica. *Journal of Petrology*, *41*(8), 1271–1305. https://doi.org/10.1093/petrology/41.8.1271

Mangiacapra, A., Moretti, R., Rutherford, M., Civetta, L., Orsi, G., & Papale, P. (2008). The deep magmatic system of the Campi Flegrei caldera (Italy). *Geophysical Research Letters*, *35*(21), 6–11. https://doi.org/10.1029/2008GL035550

Martinez, I. A., Harris, C., le Roex, A. P., & Milner, S. C. (1996). Oxygen isotope evidence for extensive crustal contamination in the Okenyenya igneous complex, Namibia. *Geochimica Et Cosmochimica Acta*, *60*(22), 4497–4508.

Matzen, A. K., Baker, M. B., Beckett, J. R., & Stolper, E. M. (2013). The temperature and pressure dependence of nickel partitioning between olivine and silicate melt. *Journal of Petrology*, *54*(12), 2521–2545. https://doi.org/10.1093/petrology/egt055

Melson, W. G. (1983). Monitoring the 1980-1982 eruptions of Mount St. Helens: Composition and Abundance of glass. *Science*, *221*(4618), 1387–1391.

Menzer, G. (1928). The crystal structure of garnet. *Z. Krist.*, *69*, 300–396.

Michael, P. J., McDonough, W. F., Nielsen, R. L., & Cornell, W. C. (2002). Depleted melt inclusions in MORB plagioclase: Messages from the mantle or mirages from the magma chamber? *Chemical Geology*, *183*(1–4), 43–61. https://doi.org/10.1016/S0009-2541(01)00371-0

Moore, N. E., Grunder, A. L., & Bohrson, W. A. (2018). The three-stage petrochemical evolution of the Steens Basalt (southeast Oregon, USA) compared to large igneous provinces and layered mafic intrusions. *Geosphere*, *14*(6), 2505–2532. https://doi.org/10.1130/GES01665.1

Mukhopadhyay, B., Holdaway, M. J., & Koziol, A. M. (1997). A statistical model of thermodynamic mixing properties of Ca-Mg-Fe2+ garnets. *American Mineralogist*, *82*(1–2), 165–181. https://doi.org/10.2138/am-1997-1-219

Müller, T., Dohmen, R., Becker, H. W., ter Heege, J. H., & Chakraborty, S. (2013). Fe-Mg interdiffusion rates in clinopyroxene: Experimental data and implications for Fe-Mg exchange geothermometers. *Contributions to Mineralogy and Petrology*, *166*(6), 1563–1576. https://doi.org/10.1007/s00410-013-0941-y

Nabelek, P. I. (1980). Nickel partitioning between olivine and liquid in natural basalts: Henry's Law behavior. *Earth and Planetary Science Letters*, *48*(2), 293–302. https://doi.org/10.1016/0012-821X(80)90193-4

Neave, D. A., & Putirka, K. D. (2017). A new clinopyroxene-liquid barometer, and implications for magma storage pressures under Icelandic rift zones. *American Mineralogist*, *102*(4), 777–794. https://doi.org/10.2138/am-2017-5968

Newton, R. C., Charlu, T. v., & Kleppa, O. J. (1977). Thermochemistry of high pressure garnets and clinopyroxenes in the system CaO-MgO-Al2O3-SiO2. *Geochimica et Cosmochimica Acta*, *41*(3), 369–377. https://doi.org/10.1016/0016-7037(77)90264-2

Nielsen, R. L., Michael, P. J., & Sours-Page, R. (1998). Chemical and physical indicators of compromised melt inclusions. *Geochimica et Cosmochimica Acta*, *62*(5), 831–839. https://doi.org/10.1016/S0016-7037(98)00024-6

Norman, M., Garcia, M. O., & Pietruszka, A. J. (2005). Trace-element distribution coefficients for pyroxenes, plagioclase, and olivine in evolved tholeiites from the 1955 eruption of Kilauea Volcano, Hawai'i, and petrogenesis of differentiated rift-zone lavas. *American Mineralogist*, *90*(5–6), 888–899. https://doi.org/10.2138/am.2005.1780

Oldenburg, C. M., Spera, F. J., Yuen, D. A., & Sewell, G. (1989). Dynamic mixing in magma bodies: theory, simulations, and implications. *Journal of Geophysical Research*, *94*(B7), 9215–9236. https://doi.org/10.1029/JB094iB07p09215

Pamukcu, A. S., Gualda, G. A. R., Bégué, F., & Gravley, D. M. (2015). Melt inclusion shapes: Timekeepers of short-lived giant magma bodies. *Geology*, *43*(11), 947–950. https://doi.org/10.1130/G37021.1

Peterson, M. E., Saal, A. E., Kurz, M. D., Hauri, E. H., Blusztajn, J. S., Harpp, K. S., et al. (2017). Submarine basaltic glass from the Galapgos Archipelago: determining the volatile budget of the manlte plume. *Journal of Petrology*, *58*(7), 1419–1450. https://doi.org/10.1093/petrology/egx059

Pietruszka, A. J., & Garcia, M. O. (1999). A rapid fluctuation in the mantle source and melting history of Kilauea Volcano inferred from the geochemistry of its historical summit lavas (1790-1982). *Journal of Petrology*, *40*(8), 1321–1342. https://doi.org/10.1093/petroj/40.8.1321

Plank, T., Kelley, K. A., Zimmer, M. M., Hauri, E.H., A., & Wallace, P. J. (2013). Why Do Mafic Arc Magmas Contain ~ 4 wt % Water on Average? How Much Water Comes Out Arc Volcanoes? *Earth and Planetary Science Letters*, *364*, 168–179.

Portnyagin, M., Almeev, R., Matveev, S., & Holtz, F. (2008). Experimental evidence for rapid water exchange between melt inclusions in olivine and host magma. *Earth and Planetary Science Letters*, *272*(3–4), 541–552. https://doi.org/10.1016/j.epsl.2008.05.020

Pownceby, M. I., Wall, V. J., & O'Neill, H. S. C. (1987). Fe-Mn partitioning between garnet and ilmenite: experimental calibration and applications. *Contributions to Mineralogy and Petrology*, *97*(1), 116–126. https://doi.org/10.1007/BF00375219

Putirka, K. (2008). Excess temperatures at ocean islands: Implications for mantle layering and convection. *Geology*, *36*(4), 283–286. https://doi.org/10.1130/G24615A.1

Putirka, K. D. (2008). Thermometers and barometers for volcanic systems. *Reviews in Mineralogy and Geochemistry*, *69*, 61–120. https://doi.org/10.2138/rmg.2008.69.3

Putirka, K. D. (2017). Geothermometry and Geobarometry. In: White WM (ed) Encyclopedia of Geochemistry. *A Comprehensive Source on the Chemistry of the Earth. Springer International Publishing, Cham*, 1–19. https://doi.org/10.1007/978-3-319-39193-9_322-1

Qin, Z., Lu, F., & Anderson, A. T. (1992). Diffusive reequilibration of melt and fluid inclusions. *American Mineralogist*, *77*(5–6), 565–576.

Reinhard, A. A., Jackson, M. G., Harvey, J., Brown, C., & Koornneef, J. M. (2016). Extreme differences in 87Sr/86Sr between Samoan lavas and the magmatic olivines they host: Evidence for highly heterogeneous 87Sr/86Sr in the magmatic plumbing system sourcing a single lava. *Chemical Geology*, *439*, 120–131. https://doi.org/10.1016/j.chemgeo.2016.05.017

Reinhard, A. A., Jackson, M. G., Koornneef, J. M., Rose-Koga, E. F., Blusztajn, J., Konter, J. G., et al. (2018). Sr and Nd isotopic compositions of individual olivine-hosted melt inclusions from Hawai'i and Samoa: Implications for the origin of isotopic heterogeneity in melt inclusions from OIB lavas. *Chemical Geology*, *495*(August), 36–49. https://doi.org/10.1016/j.chemgeo.2018.07.034

Renzulli, A., & Santi, P. (2000). Two-stage fractionation history of the alkali basalt-trachyte series of Sete Cidades volcano (Sao Miguel Island, Azores). *European Journal of Mineralogy*, *12*(2), 469–494. https://doi.org/10.1127/0935-1221/2000/0012-0469

Roedder, E. (1984). Fluid Inclusions. *Reviews in Mineralogy*, *12*, 1–644.

le Roex, A. P. (1985). Geochemistry, mineralogy and magmatic evolution of the basaltic and trachytic lavas from Gough Island, South Atlantic. *Journal of Petrology*, *26*(1), 149–186. https://doi.org/10.1093/petrology/26.1.149

Rollinson, H. (2015). Slab and sediment melting during subduction initiation: granitoid dykes from the mantle section of the Oman ophiolite. *Contributions to Mineralogy and Petrology*, *170*(3), 32. https://doi.org/10.1007/s00410-015-1177-9

Rudnick, R. L., & Gao, S. (2003). Composition of the continental crust. *Treatise on Geochemistry*, *3*, 1–64.

Saal, A. E., Hart, S. R., Shimizu, N., Hauri, E. H., & Layne, G. D. (1998). Pb isotopic variability in melt inclusions from oceanic Island Basalts, Polynesia. *Science*, *282*(5393), 1481–1484. https://doi.org/10.1126/science.282.5393.1481

Schiano, P., & Bourdon, B. (1999). On the preservation of mantle information in ultramafic nodules: Glass inclusions within minerals versus interstitial glasses. *Earth and Planetary Science Letters*, *169*(1–2), 173–188. https://doi.org/10.1016/S0012-821X(99)00074-6

Scruggs, M. A., & Putirka, K. D. (2018). Eruption triggering by partial crystallization of mafic enclaves at Chaos Crags, Lassen Volcanic Center, California. *American Mineralogist*, *103*(10), 1575–1590. https://doi.org/10.2138/am-2018-6058

Shimizu, Y., Arai, S., Morishita, T., Yurimoto, H., & Gervilla, F. (2004). Petrochemical characteristics of felsic veins in mantle xenoliths from Tallante (SE Spain): An insight into activity of silicic melt within the mantle wedge. *Special Paper of the Geological Society of America*, *389*, 265–276. https://doi.org/10.1130/0-8137-2389-2.265

Sobolev, A. v. (1996). Melt inclusions in minerals as a source of principle petrological information. *Petrology*, *4*(3), 209–220.

Sobolev, A. V. (2007). Melt inclusions and host olivines: what do they tell about mantle processes and sources. *Geochimica et Cosmochimica Acta*.

Sobolev, A. V., & Shimizu, N. (1993). The Origin of Typical NMORB: The Evidence from a Melt Inclusions Study. *Mineralogical Magazine*, *58A*(2), 862–863. https://doi.org/10.1180/minmag.1994.58a.2.184

Sobolev, Alexander v., Hofmann, A. W., & Nikogosian, I. K. (2000). Recycled oceanic crust observed in `ghost plagioclase' within the source of Mauna Loa lavas. *Nature*, *404*(April), 986–90. https://doi.org/10.1038/35010098

Sobolev, Alexander v., Hofmann, A. W., Sobolev, S. v., & Nikogosian, I. K. (2005). An olivine-free mantle source of Hawaiian shield basalts. *Nature*, *434*(7033), 590–597. https://doi.org/10.1038/nature03411

Sobolev, Alexander v., Hofmann, A. W., Jochum, K. P., Kuzmin, D. v., & Stoll, B. (2011). A young source for the Hawaiian plume. *Nature*, *476*(7361), 434–439. https://doi.org/10.1038/nature10321

Soldati, A. (2011). Studio Geochimico delle inclusion vetrose nei clinopirosseni. *Universita degli Studi di Pavia.*

Sours-Page, R., Johnson, K. T. M., Nielsen, R. L., & Karsten, J. L. (1999). Local and regional variation of MORB parent magmas: Evidence from melt inclusions from the Endeavour Segment of the Juan de Fuca Ridge. *Contributions to Mineralogy and Petrology*, *134*(4), 342–363. https://doi.org/10.1007/s004100050489

Spandler, C., O'Neill, H. S. C., & Kamenetsky, V. S. (2007). Survival times of anomalous melt inclusions from element diffusion in olivine and chromite. *Nature*, *447*(7142), 303–306. https://doi.org/10.1038/nature05759

Spera, F.J. (2001). Energy-Constrained Open-System Magmatic Processes I: General Model and Energy-Constrained Assimilation and Fractional Crystallization (EC-AFC) Formulation. *Journal of Petrology*, *42*(5), 999–1018. https://doi.org/10.1093/petrology/42.5.999

Spera, Frank J., Bohrson, W. a., Till, C. B., & Ghiorso, M. S. (2007). Partitioning of trace elements among coexisting crystals, melt, and supercritical fluid during isobaric crystallization and melting. *American Mineralogist*, *92*(1999), 1881–1898. https://doi.org/10.2138/am.2007.2326

Spera, Frank J, Schmidt, J. S., Bohrson, W. A., & Brown, G. A. (2016). Dynamics and thermodynamics of magma mixing: Insights from a simple exploratory model. *American Mineralogist*, *101*(3), 627–643. https://doi.org/9443/10.2138/am-2016-5305

Spera, Frank J., Schmidt, J. S., Bohrson, W. A., & Brown, G. A. (2016). Dynamics and thermodynamics of magma mixing: Insights from a simple exploratory model. *American Mineralogist*, *101*(3), 627–643. https://doi.org/10.2138/am-2016-5305

Streck, M. J. (2008). Mineral textures and zoning as evidence for open system processes. *Reviews in Mineralogy and Geochemistry*, *69*, 595–622. https://doi.org/10.2138/rmg.2008.69.15

Swalin, R. A. (1972). Century of development in metallurgical physical chemistry. *Journal of Metals*, *35*, 35–41. https://doi.org/10.1007/bf03355756

Tanaka, T., Togashi, S., Kamioka, H., Amakawa, H., Kagami, H., Hamamoto, T., et al. (2000). JNdi-1: A neodymium isotopic reference in consistency with LaJolla neodymium. *Chemical Geology*, *168*(3–4), 279–281. https://doi.org/10.1016/S0009-2541(00)00198-4

Taylor, H. P. (1980). The effects of assimilation of country rocks by magmas on 18O/16O and 87Sr/86Sr systematics in igneous rocks. *Earth and Planetary Science Letters*, *47*(2), 243–254. https://doi.org/10.1016/0012-821X(80)90040-0

Tepley, F. J., Davidson, J. P., Tilling, R. I., & Arth, J. G. (2000). Magma mixing, recharge and eruption histories recorded in plagioclase phenocrysts from El Chichon Volcano, Mexico. *Journal of Petrology*, *41*(9), 1397–1411. https://doi.org/10.1093/petrology/41.9.1397

Tepley, Frank J., de Silva, S., & Salas, G. (2013). Magma dynamics and petrological evolution leading to thevei 5 2000 BP Eruption of EL mistivolcano, southern Peru. *Journal of Petrology*, *54*(10), 2033–2065. https://doi.org/10.1093/petrology/egt040

Thompson, G., Smith, I., & Malpas, J. (2001). Origin of oceanic phonolites by crystal fractionation and the problem of the Daly gap: An example from Rarotonga. *Contributions to Mineralogy and Petrology*, *142*(3), 336–346. https://doi.org/10.1007/s004100100294

Thompson, J. B., & Waldbaum, D. R. (1969). Mixing properties of sanidine crystalline solutions: III. Calculations based on two-phase data1. *American Mineralogist*, *54*(5–6), 811–838.

Tikoff, B., & Teyssier, C. (1992). Crustal-scale, en echelon “P-shear” tensional bridges: A possible solution to the batholithic room problem. *Geology*, *20*, 927–930.

Tirone, M., Ganguly, J., Dohmen, R., Langenhorst, F., Hervig, R., & Becker, H. W. (2005). Rare earth diffusion kinetics in garnet: Experimental studies and applications. *Geochimica et Cosmochimica Acta*, *69*(9), 2385–2398. https://doi.org/10.1016/j.gca.2004.09.025

Ubide, T., & Kamber, B. S. (2018). Volcanic crystals as time capsules of eruption history. *Nature Communications*, *9*(1), 1–12. https://doi.org/10.1038/s41467-017-02274-w

Ubide, T., Mollo, S., Zhao, J. xin, Nazzari, M., & Scarlato, P. (2019). Sector-zoned clinopyroxene as a recorder of magma history, eruption triggers, and ascent rates. *Geochimica et Cosmochimica Acta*, *251*, 265–283. https://doi.org/10.1016/j.gca.2019.02.021

Ungaretti, L., Leona, M., Merli, M., & Oberti, R. (1995). Non-ideal solid-solution in garnet: crystal-structure evidence and modelling. *European Journal of Mineralogy*, *7*(6), 1299–1312.

Villiger, S., Müntener, O., & Ulmer, P. (2007). Crystallization pressures of mid-ocean ridge basalts derived from major element variations of glasses from equilibrium and fractional crystallization experiments. *Journal of Geophysical Research: Solid Earth*, *112*(1), 1–18. https://doi.org/10.1029/2006JB004342

Vinograd, V. L., & Sluiter, M. H. F. (2006). Thermodynamics of mixing in pyrope-grossular, Mg3Al2Si3O12- Ca3Al2Si3O12, solid solution from lattice dynamics calculations and Monte Carlo simulations. *American Mineralogist*, *91*(11–12), 1815–1830. https://doi.org/10.2138/am.2006.2140

Wade, J. A., Plank, T., Hauri, E. H., Kelley, K. A., Roggensack, K., & Zimmer, M. (2008). Prediction of magmatic water contents via measurement of H2O in clinopyroxene phenocrysts. *Geology*, *36*(10), 799–802. https://doi.org/10.1130/G24964A.1

Walker, J. A., Williams, S. N., Kalamarides, R. I., & Feigenson, M. D. (1993). Shallow open-system evolution of basaltic magma beneath a subduction zone volcano: The Masaya Caldera Complex, Nicaragua. *Journal of Volcanology and Geothermal Research*, *56*(4), 379–400. https://doi.org/10.1016/0377-0273(93)90004-B

Wallace, P. J. (2005). Volatiles in subduction zone magmas: Concentrations and fluxes based on melt inclusion and volcanic gas data. *Journal of Volcanology and Geothermal Research*, *140*(1–3), 217–240. https://doi.org/10.1016/j.jvolgeores.2004.07.023

Wang, Y., Prelević, D., Buhre, S., & Foley, S. F. (2017). Constraints on the sources of post-collisional K-rich magmatism: The roles of continental clastic sediments and terrigenous blueschists. *Chemical Geology*, *455*, 192–207. https://doi.org/10.1016/j.chemgeo.2016.10.006

Wark, D. A., Hildreth, W., Spear, F. S., Cherniak, D. J., & Watson, E. B. (2007). Pre-eruption recharge of the Bishop magma system. *Geology*, *35*(3), 235–238. https://doi.org/10.1130/G23316A.1

Weber, G., & Castro, J. M. (2017). Phase petrology reveals shallow magma storage prior to large explosive silicic eruptions at Hekla volcano, Iceland. *Earth and Planetary Science Letters*, *466*, 168–180. https://doi.org/10.1016/j.epsl.2017.03.015

Weis, D., Kieffer, B., Maerschalk, C., Barling, J., de Jong, J., Williams, G. A., et al. (2006). High-precision isotopic characterization of USGS reference materials by TIMS and MC-ICP-MS. *Geochemistry, Geophysics, Geosystems*, *7*(8). https://doi.org/10.1029/2006GC001283

White, R. W., Powell, R., Holland, T. J. B., Johnson, T. E., & Green, E. C. R. (2014). New mineral activity-composition relations for thermodynamic calculations in metapelitic systems. *Journal of Metamorphic Geology*, *32*(3), 261–286. https://doi.org/10.1111/jmg.12071

White, W. (2015). Probing the Earth's Deep Interior Through Geochemistry. *Geochemical Perspectives*, *4*(2), 95–251. https://doi.org/10.7185/geochempersp.4.2

White, W. M., & Hofmann, A. W. (1982). Sr and Nd isotope geochemistry of oceanic basalts and mantle evolution. *Nature*, *296*(5860), 821–825. https://doi.org/10.1038/296821a0

White, William M. (2015). Isotopes, DUPAL, LLSVPs, and Anekantavada. *Chemical Geology*, *419*, 10–28. https://doi.org/10.1016/j.chemgeo.2015.09.026

Wiebe, R. A. (1968). Plagioclase stratigraphy: A record of magmatic conditions and events in a granite stock. *American*, 690–703.

Wood, B. J. (1988). Activity Measurements and Excess Entropy-Volume Relationships for Pyrope-Grossular Garnets. *The University of Chicago Press Journals*, *96*(6), 721–729.

Wooden, J. L., Czamanske, G. K., Fedorenko, V. A., Arndt, N. T., Chauvel, C., Bouse, R. M., et al. (1993). Isotopic and trace-element constraints on mantle and crustal contributions to Siberian continental flood basalts, Noril'sk area, Siberia. *Geochimica et Cosmochimica Acta*, *57*(15), 3677–3704. https://doi.org/10.1016/0016-7037(93)90149-Q

Workman, R. K., Hart, S. R., Jackson, M., Regelous, M., Farley, K. A., Blusztajn, J., et al. (2004). Recycled metasomatized lithosphere as the origin of the Enriched Mantle II (EM2) end-member: Evidence from the Samoan Volcanic Chain. *Geochemistry, Geophysics, Geosystems*, *5*(4), 1–44. https://doi.org/10.1029/2003GC000623

Wortis, M. (1988). Equilibrium crystal shapes and interfacial phase transitions. In *In: Vanselow R., Howe R. (eds) Chemistry and Physics of Solid Surfaces VII. Springer Series in Surface Sciences.* (10th ed., pp. 367–405). Springer, Berlin, Heidelberg.

Yaxley, G. M., & Sobolev, A. v. (2007). High-pressure partial melting of gabbro and its role in the Hawaiian magma source. *Contributions to Mineralogy and Petrology*, *154*(4), 371–383. https://doi.org/10.1007/s00410-007-0198-4

Yoder, H. S., & Tilley, C. E. (1962). Origin of basalt magmas: An experimental study of natural and synthetic rock systems. *Journal of Petrology*, *3*(3), 342–532. https://doi.org/10.1093/petrology/3.3.342

Yuan, Q., Namur, O., Fischer, L. A., Roberts, R. J., Lü, X., & Charlier, B. (2017). Pulses of plagioclase-laden magmas and stratigraphic evolution in the Upper Zone of the Bushveld Complex, South Africa. *Journal of Petrology*, *58*(8), 1619–1644. https://doi.org/10.1093/petrology/egx067

Zhang Y. and Cherniak, D. J. (2010). Diffusion in minerals and melts. *Reviews in Mineralogy and Geochemistry*, *72*.

Zindler, A., & Hart, S. R. (1986). Chemical Geodynamics. *Annual Review of Earth and Planetary Sciences*, *14*(1), 493–571. https://doi.org/10.1146/annurev.earth.14.1.493